JOURNAL OF RESEARCH

OF THE U.S. GEOLOGICAL SURVEY

JANUARY–FEBRUARY 1978
VOLUME 6, NUMBER 1

Scientific notes and summaries of investigations in geology, hydrology, and related fields

U.S. DEPARTMENT OF THE INTERIOR

UNITED STATES DEPARTMENT OF THE INTERIOR
CECIL D. ANDRUS, Secretary
GEOLOGICAL SURVEY
V. E. McKelvey, Director

For sale by Superintendent of Documents, U.S. Government Printing Office, Washington, DC 20402. Annual subscription rate, $18.90 (plus $4.75 for foreign mailing). Make check or money order payable to Superintendent of Documents. Send all subscription inquiries and address changes to Superintendent of Documents at above address.

Purchase single copy ($3.15) from Branch of Distribution, U.S. Geological Survey, 1200 South Eads Street, Arlington, VA 22202. Make check or money order payable to U.S. Geological Survey.

Library of Congress Catalog-card No. 72-600241.

The Journal of Research is published every 2 months by the U.S. Geological Survey. It contains papers by members of the Geological Survey and their professional colleagues on geologic, hydrologic, topographic, and other scientific and technical subjects.

Correspondence and inquiries concerning the Journal (other than subscription inquiries and address changes) should be directed to Anna M. Orellana, Managing Editor, Journal of Research, Publications Division, U.S. Geological Survey, 321 National Center, Reston, VA 22092.

Papers for the Journal should be submitted through regular Division publication channels.

The Secretary of the Interior has determined that the publication of this periodical is necessary in the transaction of the public business required by law of this Department. Use of funds for printing this periodical has been approved by the Director of the Office of Management and Budget through June 30, 1980.

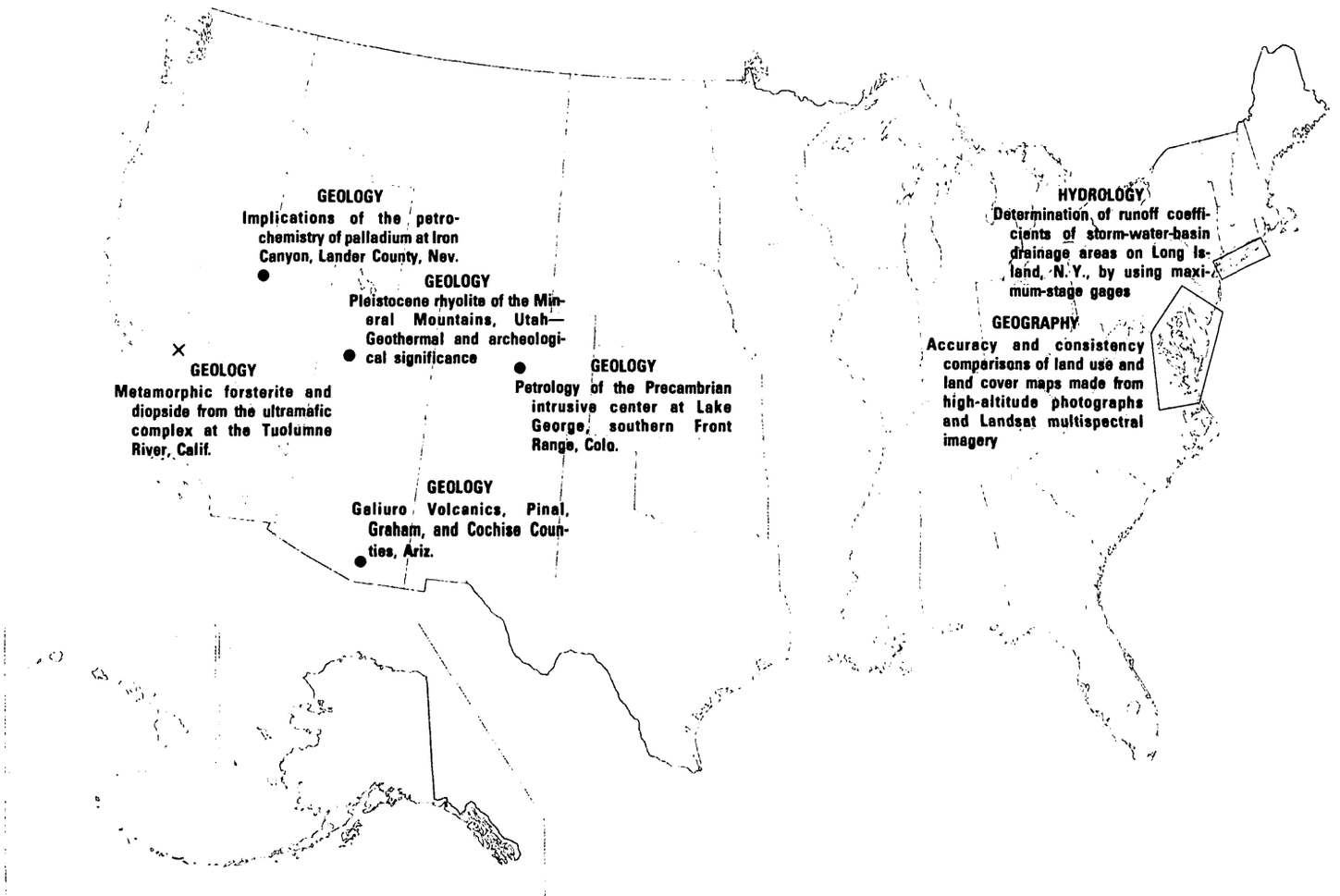

GEOGRAPHIC INDEX TO ARTICLES

See "Contents" for articles concerning areas outside the United States and articles without geographic orientation.

JOURNAL OF RESEARCH

of the

U.S. Geological Survey

Vol. 6 No. 1 Jan.–Feb. 1978

CONTENTS

SI UNITS AND U.S. CUSTOMARY EQUIVALENTS

[SI, International System of Units, a modernized metric system of measurement. All values have been rounded to four significant digits except 0.01 bar, which is the exact equivalent of 1 kPa. Use of hectare (ha) as as alternative name for square hectometer (hm^2) is restricted to measurement of land or water areas. Use of liter (L) as a special name for cubic decimeter (dm^3) is restricted to the measurement of liquids and gases; no prefix other than milli should be used with liter. Metric ton (t) as a name for megagram (Mg) should be restricted to commercial usage, and no prefixes should be used with it. Note that the style of meter^2 rather than square meter has been used for convenience in finding units in this table. Where the units are spelled out in text, Survey style is to use square meter]

SI unit		U.S. customary equivalent	
Length			
millimeter (mm)	=	0.039 37	inch (in)
meter (m)	=	3.281	feet (ft)
	=	1.094	yards (yd)
kilometer (km)	=	0.621 4	mile (mi)
	=	0.540 0	mile, nautical (nmi)
Area			
centimeter^2 (cm^2)	=	0.155 0	inch^2 (in^2)
meter^2 (m^2)	=	10.76	feet^2 (ft^2)
	=	1.196	yards^2 (yd^2)
	=	0.000 247 1	acre
hectometer^2 (hm^2)	=	2.471	acres
	=	0.003 861	section (640 acres or 1 mi^2)
kilometer^2 (km^2)	=	0.386 1	mile^2 (mi^2)
Volume			
centimeter^3 (cm^3)	=	0.061 02	inch^3 (in^3)
decimeter^3 (dm^3)	=	61.02	inches^3 (in^3)
	=	2.113	pints (pt)
	=	1.057	quarts (qt)
	=	0.264 2	gallon (gal)
	=	0.035 31	foot^3 (ft^3)
meter^3 (m^3)	=	35.31	feet^3 (ft^3)
	=	1.308	yards^3 (yd^3)
	=	264.2	gallons (gal)
	=	6.290	barrels (bbl) (petroleum, 1 bbl=42 gal)
	=	0.000 810 7	acre-foot (acre-ft)
hectometer^3 (hm^3)	=	810.7	acre-feet (acre-ft)
kilometer^3 (km^3)	=	0.239 9	mile^3 (mi^3)
Volume per unit time (includes flow)			
decimeter^3 per second (dm^3/s)	=	0.035 31	foot^3 per second (ft^3/s)
	=	2.119	feet^3 per minute (ft^3/min)
decimeter^3 per second (dm^3/s)	=	15.85	gallons per minute (gal/min)
	=	543.4	barrels per day (bbl/d) (petroleum, 1 bbl=42 gal)
meter^3 per second (m^3/s)	=	35.31	feet^3 per second (ft^3/s)
	=	15 850	gallons per minute (gal/min)
Mass			
gram (g)	=	0.035 27	ounce avoirdupois (oz avdp)
kilogram (kg)	=	2.205	pounds avoirdupois (lb avdp)
megagram (Mg)	=	1.102	tons, short (2 000 lb)
	=	0.984 2	ton, long (2 240 lb)
Mass per unit volume (includes density)			
kilogram per meter^3 (kg/m^3)	=	0.062 43	pound per foot^3 (lb/ft^3)
Pressure			
kilopascal (kPa)	=	0.145 0	pound-force per inch^2 (lbf/in^2)
	=	0.009 869	atmosphere, standard (atm)
	=	0.01	bar
	=	0.296 1	inch of mercury at 60°F (in Hg)
Temperature			
temp kelvin (K)	=	[temp deg Fahrenheit (°F)+459.67]/1.8	
temp deg Celsius (°C)	=	[temp deg Fahrenheit (°F)−32]/1.8	

The policy of the "Journal of Research of the U.S. Geological Survey" is to use SI metric units of measurement except for the following circumstance:

When a paper describes either field equipment or laboratory apparatus dimensioned or calibrated in U.S. customary units and provides information on the physical features of the components and operational characteristics of the equipment or apparatus, then dual units may be used. For example, if a pressure gage is calibrated and available only in U.S. customary units of measure, then the gage may be described using SI units in the dominant position with the equivalent U.S. customary unit immediately following in parentheses. This also applies to the description of tubing, piping, vessels, and other items of field and laboratory equipment that normally are described in catalogs in U.S. customary dimensions.

S. M. LANG, *Metrics Coordinator,*
U.S. Geological Survey

Jour. Research U.S. Geol. Survey
Vol. 6, No. 1, Jan.–Feb. 1978, p. 1–9

HYDROCHEMISTRY AND HYDRODYNAMICS OF INJECTING AN IRON-RICH PICKLING LIQUOR INTO A DOLOMITIC SANDSTONE–A LABORATORY STUDY

By STEPHEN E. RAGONE, FRANCIS S. RILEY, and ROBERT J. DINGMAN,
Syosset, N.Y., Denver, Colo., Albany, N.Y.

Work done in cooperation with the New York State Geological Survey

Abstract.—Waste pickling liquor containing high concentrations of iron salts was injected into cores of quartzite, sandstone, and dolomite in a laboratory study to determine what effect this procedure might have on the permeability of these rock types. Experiments were performed at field conditions—40°C and 13.8 MPa (megapascals)—in a high-pressure triaxial chamber similar to that used in rock-mechanics testing but modified to allow downstream sample collection of effluent liquids and direct visual monitoring at in-situ conditions. Five samples were tested, ranging in effective porosity from 2.9 to 13 percent and in lithology from a quartzite to a dolomite. Hydraulic conductivity of the quartzitic samples remained unchanged during injection of over 50 pore volumes of pickling liquor, but significant decreases in the hydraulic conductivity of dolomitic samples were observed. Chemical analyses of effluents from a dolomitic sample suggest that carbonate minerals were dissolving and iron was precipitating. Clogging of pore space by CO_2 entrapment or by $CaCl_2$ precipitation did not seem to play a role in decreasing hydraulic conductivity because injection into a dolomitic core of more than 140 pore volumes of HCl at a concentration similar to that of the pickling liquor caused only a slight decrease in hydraulic conductivity compared with the decrease observed when an additional 30 pore volumes of pickling liquor were subsequently injected.

The U.S. Geological Survey, in cooperation with the New York State Geological Survey, is studying the feasibility of injecting an iron-rich waste pickling liquor (henceforth called pickling liquor) by well into a relatively impermeable dolomitic sandstone in Lackawanna, N.Y.

The pickling liquor, a waste product from a steel plant, contains high concentrations of iron (140 000 to 180 000 mg/L) and has a pH of 0 to 0.01. The receiving formations for the pickling liquor are the Cambrian Theresa Formation and underlying Potsdam Sandstone, at a depth of 1158 to 1311 m below land surface. At this depth the in-situ overburden pressure is typically 27.6 MPa (megapascals) and the pore pressure is about 12.4 MPa. Formation temperature is 40°C. The injection zone is composed of dolomitic sandstone grading from nearly pure quartzite to nearly pure dolomite, with permeabilities ranging from 0 to 41.80 m/s. The interstitial pore space is occupied by a brine containing about 330 000 mg/L NaCl (sodium chloride) and 30 000 mg/L $CaCl_2$ (calcium chloride).

Under these conditions, several kinds of reactions (eqs 1–5 and possibly others) might occur between the pickling liquor, the native fluid, and the receiving rock, and would directly or indirectly affect permeability. Many of these reactions have been observed in field studies. Acid dissolution of dolomitic rocks (eq 1) has been used to increase yields from oil wells (Smith and others, 1970; van Poolen and Jargon, 1943; Chamberlain and Boyer, 1939) and has been observed to occur during injection of acidic wastes into limestone or dolomite (Donaldson and Bayazeed, 1971; Goolsby, 1971; Donaldson, 1964) and sandstone (Bayazeed and Donaldson, 1973). Precipitation of iron carbonate or calcium salts (eqs 3–5)) has also been reported (Bayazeed and Donaldson, 1973; Chamberlain and Boyer, 1939).

$$Ca\,Mg(CO_3)_2 + 4HCL = CaCl_2 + MgCl_2 + 2H_2O + 2CO_{2(g)} \quad (1)$$

$$CO_{2(g)} + H_2O = H_2CO_3 \quad (2)$$

$$FeCl_2 + H_2CO_3 = FeCO_{3(s)} + 2HCl \quad (3)$$

$$Ca^{+2} + 2HCl = CaCl_2 + 2H^+ \quad (4)$$

$$Ca^{+2} + H_2SO_4 + 2H_2O = CaSO_4 \cdot 2H_2O + 2H^+ \quad (5)$$

Because of the variability in dissolution rates of carbonate rocks (van Poolen and Jargon, 1943), the

uncertainties about the material that may precipitate from solution, and the effect of CO_2 formation and viscosity changes on permeability, a series of laboratory experiments was performed. The purpose of this report is to summarize the techniques used to simulate field conditions and to describe the results obtained from injection of pickling liquor through cores of quartzite, sandstone, and dolomite from the proposed injection site.

CHEMISTRY OF PICKLING LIQUOR AND NATIVE FLUID

Pickling liquor used in the study was filtered through a 0.45μm filter. The liquor is characterized by its high iron concentration and acidity (table 1). The iron is predominantly in the ferrous form. Hydrochloric acid is the predominant acid, but some sulfuric acid is also present.

The native brine is characterized by its high sodium chloride concentration (table 2). The pH is 7. The kinematic viscosity of the native brine and pickling liquor is 1.55 mm^2/s (centistokes) and 1.95 mm^2/s, respectively, at 25°C and decreases with increasing temperature (fig. 1). At formation temperature (40°C), the viscosities are 1.15 and 1.42 mm^2/s, respectively. A synthetic brine was prepared for the laboratory study containing 290 000 mg/L NaCl and 22 500 mg/L $CaCl_2$.

TABLE 1.—*Chemical and physical characteristics of pickling liquor*
[Concentrations in milligrams per liter unless otherwise noted]

Constituents and characteristics	Sample 1 [1] (collected 7–8–70)	Sample 2 (collected 12–5–72)	Sample 3 [2] (collected 12–14–72)	Sample 4 [3] (collected 1–8–73)
Iron (Fe) (unfiltered sample):				
Total	181 000	180 000	----------	------
Ferrous	----------	160 000	151 000	------
Iron (Fe) (filtered through 0.45-μm filter):				
Total	----------	170 000	----------	143 000
Ferrous	----------	150 000	----------	------
Iron (Fe) (centrifuged sample):				
Total	----------	180 000	----------	------
Ferrous	----------	160 000	----------	------
Manganese (Mn)	820	----------	----------	550
Silica (SiO_2)	90	----------	----------	------
Calcium (Ca)	7.0	----------	----------	------
Magnesium (Mg)	4.0	----------	----------	------
Sodium (Na)	1.7	----------	----------	26
Potassium (K)	.7	----------	----------	------
Bicarbonate (HCO_3)	0	0	----------	------
Carbonate (CO_3)	0	0	----------	------
Sulfate (SO_4)	792	----------	----------	------
Chloride (Cl)	224 000	----------	----------	------
Fluoride (F)	2.0	----------	----------	------
Normality	----------	4.56	----------	------
Acidity, as $CaCO_3$	----------	228 000	----------	------
Acidity, as H^+	1 080	4 600	----------	------
Total alkalinity, as $CaCO_3$	0	----------	----------	------
Carbon dioxide	0	----------	----------	------
Color (platinum-cobalt)	800	----------	----------	------
Specific conductance (millisiemen per meter at 25°C)	12 300	----------	----------	------
Density at 20°C (g/mL)	1.33	----------	----------	------
Specific gravity at 25°C	----------	1.2182	[4] 1.26	------
Viscosity at 40°C (mPa·s)	----------	1.4023	----------	------
Dissolved solids at 180°C	261 000	----------	----------	------
Dissolved solids (sum)	407 000	----------	----------	------
Hardness (noncarbonate)	34	----------	----------	------
Hardness (total)	34	----------	----------	------
Methylene blue active substances (MBAS)	7.5	----------	----------	------
Nitrite (NO_2)	15	----------	----------	------
pH	0	0	0.01	------
Cadmium (Cd)	----------	810	----------	------
Chromium (Cr), μg/L dissolved	----------	81 000	----------	------
Cobalt (Co), μg/L	----------	220 000	----------	------
Copper (Cu), μg/L	----------	14 000	----------	------
Lead (Pb), μg/L	----------	2 600	----------	------
Lithium (Li), μg/L	----------	0	----------	------
Nickel (Ni), μg/L	----------	250 000	----------	------
Oil-grease, μg/L	----------	3.0	----------	------
Silver (Ag), μg/L	----------	300	----------	------
Strontium (Sr), μg/L	----------	30	----------	------
Zinc (Zn), μg/L	----------	3 600	----------	------

[1] Analyses performed by U.S. Geological Survey laboratory, Albany, N.Y.
[2] Analyses performed by E. R. Bauer, Bethlehem Steel Corp.
[3] Analyses performed by U.S. Geological Survey laboratory, Denver, Colo.
[4] About 20°C.

TABLE 2.—*Chemical and physical characteristics of native brine*
[Analyses performed by U.S. Geological Survey laboratory, Albany, N.Y.]

Chloride (mg/L)	204 000
Sodium chloride (mg/L)	336 000
Calcium chloride (mg/L)	30 000
pH	7.0

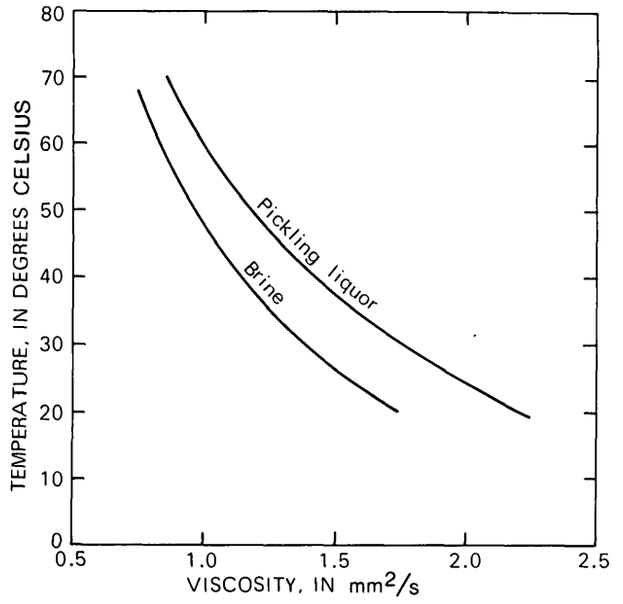

FIGURE 1.—Change in viscosity with temperature of pickling liquor and brine.

TEST PROCEDURES

The apparatus constructed to test hydraulic conductivity was designed to satisfy, insofar as possible, the following principal criteria:

1. The rock core being tested should be maintained under temperature, pore pressure, and effective stress conditions that approximate those prevailing in situ. The testing apparatus should incorporate devices to indicate applied confining stress and pore pressure.
2. The flow system should permit (a) saturation of the core with native fluid (synthetic brine was used), (b) determination of the hydraulic conductivity after saturation with brine, (c) displacement of the brine in the core with pickling liquor, and (d) observation of whatever changes in hydraulic conductivity occur as pickling liquor flows through the core. Devices should be incorporated to record the very slow flow rates through the core and the small differential pressures across the core during permeability testing.
3. Provision should be made for visually observing the effluent permeant fluid at the downstream end of the core under in-situ pressure and for sampling the effluent liquid and gas at atmospheric pressure.
4. Provision should be made for storage of the effluent liquid under in-situ pressure in a back-pressure accumulator.
5. The sample holder should allow orientation of the core so that either vertical or horizontal conductivity can be observed.
6. Because of the extremely corrosive nature of the pickling liquor and the relatively high test pressures involved, special precautions should be taken to minimize experimentation hazards and possible interference between corrosion reactions and the processes under study.

The apparatus developed to meet the above criteria is illustrated schematically in figure 2. The test chamber is a high-pressure stainless-steel triaxial chamber of the type used in rock-mechanics testing. During testing, the annulus between the rubber-jacketed core sample and the chamber wall is filled with water and is pressurized to the calculated geostatic (total overburden) load.

Moderately elevated temperatures can be maintained within the chamber by means of an electric heating tape wrapped around the outside of the chamber. Power to the tape is regulated by a proportional controller actuated by a thermistor that senses the water temperature in the annulus adjacent to the core. A second sensor provides a readout of chamber temperature.

Two permeant fluids—in most cases[1] a synthetic brine solution containing 290 000 mg/L NaCl and 22 500 mg/L $CaCl_2$ and a pickling liquor—are stored and pressurized in a pair of stainless-steel cylinders (hydraulic separators). In each cylinder, a free piston separates the permeant fluid from the pressurizing fluid. A piston rod extends through one end of the cylinder to maintain piston alinement and to provide a visual indicator of the piston's position. A linear-motion transducer clamped to the piston rod generates a voltage proportional to the position of the rod. This voltage is recorded during testing as a continuous line whose slope defines the rate of flow of permeant fluid. Bottled nitrogen controlled through a precision regu-

[1] In one experiment, the permeant liquids were hydrochloric acid and pickling liquor.

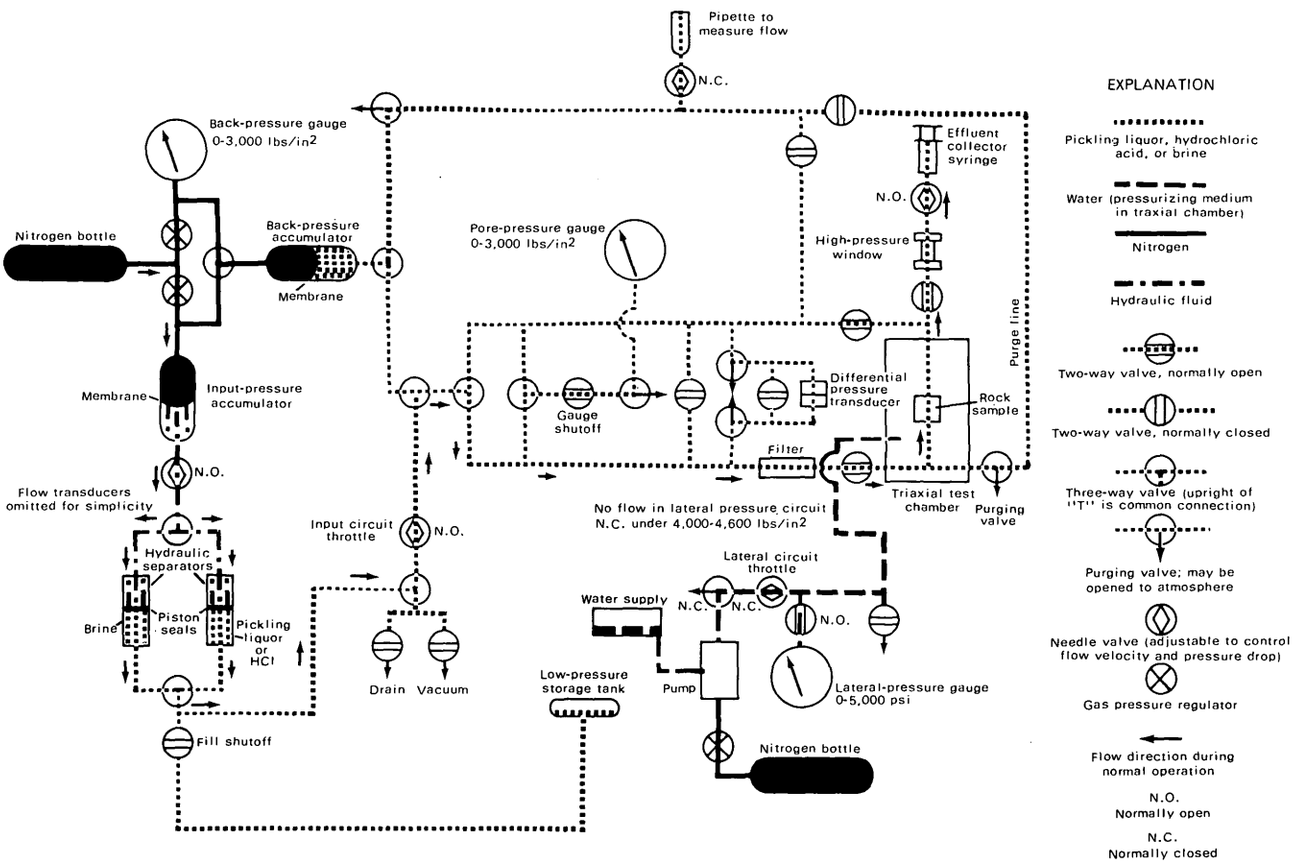

FIGURE 2.—High-pressure permeability-testing apparatus. (1 lb/in² or psi=6.895 kPa.)

lator provides the pressure source to the separators. To minimize the hazard of a corrosion-induced, high-pressure failure in some component of the system, the nitrogen pressure is transmitted to the separator piston through an intermediary fluid—a viscous hydraulic oil. The maximum possible flow rate of the oil in case of a downstream failure is restricted to a low value by a needle valve in the oil line between the separators and the hydraulic accumulator. Additional safety features include the use of conservatively rated stainless-steel lines, fittings, and valves throughout, the routing of all pressurized lines behind panels, and the sinking of the separators in heavy-walled steel wells.

In preparation for testing, each core sample was trimmed to a cube 50 mm on a side, flushed with distilled water, and saturated with synthetic brine in a vacuum jar. Sintered metal filter plates shaped to fit opposite faces of the cube were used to provide a smooth transition from the rectangular section of the sample to the cylindrical section of the sample-mounting heads. Samples were oriented for either vertical or horizontal flow between the mounting heads, and the entire assembly (sample, filter plates, and mounting heads) was loosely sleeved in a length of heat-shrinkable polyolefin tubing. A hot-air gun was used to shrink the tubing to a snug fit around the assembly. Finally, a length of heavy rubber tubing (a section from a motorcycle tire innertube) was stretched over the entire assembly, which was then ready for mounting in the test chamber.

Standard testing procedures were as follows: After the rubber-jacketed assembly of sample and mounting heads had been sealed into the triaxial chamber, the chamber was filled with water and pressurized to about 13.8 MPa. This placed the sample under an effective stress approaching in-situ conditions (although the pore pressure was still near atmospheric level) and provided a test of the integrity of the sample jacket. The chamber was then brought up to in-situ temperature (about 40°C). After all lines had been flushed with synthetic brine and purged of air, the chamber pressure and pore pressure were increased approximately in parallel until both were stabilized at in-situ values, typically about 27.6 MPa for chamber pressure and 12.4 MPa for pore pressure. During this process, the sample-bypass valve remained open, so that no

net flow occurred through the sample, although a small quantity of synthetic brine entered each end because of the compression of the contained fluids. Pressure was delivered to the back-pressure accumulator from the same regulator that pressurized the synthetic brine and pickling-liquor cylinders, so that all parts of the permeant-fluid circuit were pressurized uniformly. The back-pressure regulator was then adjusted to provide for a moderate pressure drop of typically 13.7 to 344.2 kPa across the sample, the sample-bypass valve was closed, and flow of synthetic brine through the sample was initiated by switching back-pressure control from the input-pressure regulator to the back-pressure regulator. After complete saturation of the sample was assured and steady-flow conditions attained, the hydraulic conductivity was determined by referring to the continuously recorded outputs of the flow-volume transducer and the differential-pressure transducer that sensed the pressure drop across the sample.

When consistently repeatable values of hydraulic conductivity had been attained for synthetic brine, in some cases over a range of flow rates, the permeant-fluid selector valve was switched from brine to pickling liquor and all lines were thoroughly flushed, while the sample was isolated and maintained at in-situ pore pressure. The final step in preparation for testing with pickling liquor was to flush the pickling liquor through the lower sample-mounting head to establish a pickling liquor–brine interface at the base of the lower filter plate.

Procedures for testing hydraulic conductivity with pickling liquor were generally similar to those used in testing with synthetic brine. However, significant differences arose out of the need to obtain frequent samples of the effluent permeant fluid for chemical analysis. A sampling assembly was attached directly to the top of the test chamber in order to minimize the volume of plumbing between the core and the sampling point. The assembly consisted of a shutoff valve, a high-pressure window of transparent polycarbonate plastic, a needle valve, and a 20- to 50-mL glass medical syringe to receive the effluent sample.

When effluent samples were being collected, the line to the back-pressure accumulator was closed, and the pressure drop across the sample was controlled manually by adjusting the needle valve immediately below the sampling syringe. As the in-situ pore pressure dropped to atmospheric level across this valve, gas tended to be evolved within the metering annulus of the valve, thus causing erratic variations in flow characteristics. Experience showed that concentrated monitoring of the output from the differential-pressure transducer would enable the operator to hold the fluctuations of differential pressure within narrow limits and to maintain an essentially constant flow rate by making minute, but nearly continuous, adjustments of the needle valve.

RESULTS AND DISCUSSION

Five samples were tested that ranged in effective porosity from 2.9 to 13 percent and in lithology from a quartzite to a dolomite (table 3). The hydraulic conductivity of the quartzitic sample, 73NY34, remained unchanged during injection of over 50 pore volumes of

TABLE 3.—*Description of selected core samples*

Sample	Depth (m)	Lithology[1]	Mineralogy[2] (weight percent)					Dolomite equivalent[3] (weight percent)	Specific gravity	Porosity (percent)	
			Quartz	Dolomite	Calcite	Potassium feldspar	Total			Total	Effective
73NY10	1164.3	Microcrystalline dolomite -------	2	98	0	0	100	92	2.77	7.1	2.9
73NY13	1166.5	Oolithic dolomite-	1	99	0	0	100	94	2.83	8.1	7.0
73NY14	1167.5	Cryptocrystalline dolomite -------	5	89	0	6	100	82	2.84	14	13
73NY30	1250.7	Coarse, dense sandstone-------	43	42	0	7	92	30	2.67	7.4	6.8
73NY34	1261.9	Quartzite --------	57	0	0	32	89	0	2.7	13	11

[1] Determined with binocular microscope.

[2] Estimated from X-ray diffraction patterns.

[3] Calculated from volumes of CO_2 gas evolved in wet-chemical analyses.

TABLE 4.—*Injection data for samples of dolomite, dolomite- cemented sandstone, and quartzite*
[Dolomite percentages were estimated from X-ray diffraction patterns]

Sample	Flow	Confining pressure (MPa)	Nominal pore pressure (MPa)	Hydraulic gradient (m/m)	Hydraulic conductivity at 40°C (m/d)		
					Brine	Pickling liquor	
						Initial	Final
73NY34 (quartzite)	Horizontal --	33.9	13.6	20.2	7.0×10^{-3}	--------	--------
	-----do------	33.5	13.5	555.0	--------	4.9×10^{-3}	4.9×10^{-3}
73NY13 (99 percent	-----do------	31.3	12.4	118.0	1.0×10^{-3}	--------	--------
dolomite)	-----do------	31.4	12.2	112.0	--------	6.3×10^{-4}	--------
	Vertical ----	31.1	10,0	282.0	--------	--------	3.1×10^{-7}
73NY14 (89 percent	Horizontal --	-----	-----	-----	--------	5×10^{-4}	2.5×10^{-6}
dolomite)							
73NY30 (42 percent	Horizontal --	-----	-----	-----	7.0×10^{-6}	1.4×10^{-6}	4.0×10^{-7}
dolomite)					to		
					4.8×10^{-6}		
73NY10 (98 percent	----------	-----	-----	-----	--------	3.0×10^{-7}	5.7×10^{-8}
dolomite)							

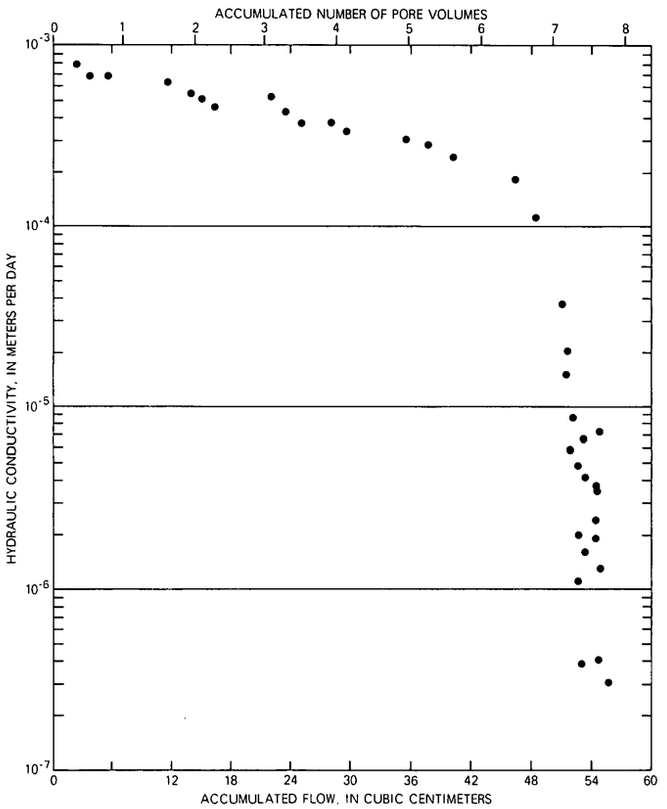

FIGURE 3.—Change in hydraulic conductivity of sample 73NY13 during injection of pickling liquor. (From Waller and others, 1977.)

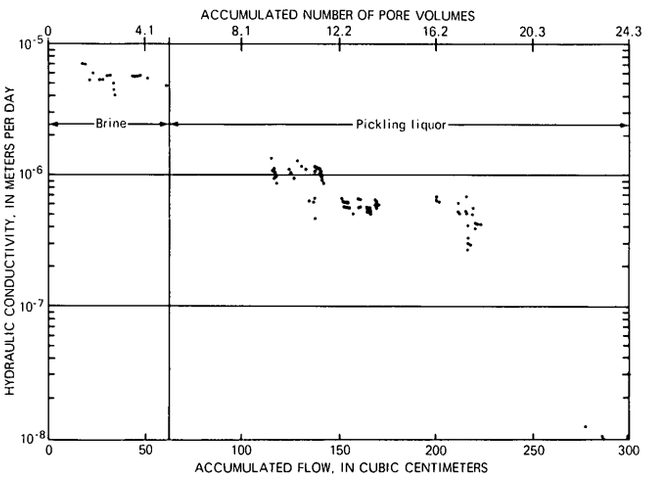

FIGURE 4.—Change in hydraulic conductivity of sample 73NY30 during injection of brine and then pickling liquor. (From Waller and others, 1977.)

pickling liquor, but decreases of from one to three orders of magnitude were observed in the dolomitic samples (table 4). Dolomitic samples having relatively high effective porosity, 73NY13 (fig. 3) and 73NY14, showed marked decreases in hydraulic conductivity after several pore volumes[2] were injected. Hydraulic

[2] The pore-volume scale was arbitrarily but consistently set at the point at which the pickling liquor–brine interface was initially displaced upward from the base of the sample holder.

conductivity in the less porous dolomite, 73NY10, and in the sandstone with dolomite cement, 73NY30 (fig. 4), decreased at a more gradual rate over a larger pore volume.

Results from the quartzite experiment indicate that, under in-situ conditions, injection of pickling liquor does not produce reactions with the silicate matrix of the rock or the brine. It also indicates that the pickling liquor does not cause precipitation of iron salts, for instance, under the pressure and temperature conditions in the receiving formation.

The decrease in hydraulic conductivity of the dolomitic samples and sample of sandstone with dolomite cement probably results from interaction between constituents in the pickling liquor and the carbonate matrix. Chemical analysis of effluent pickling liquor from dolomitic sample 73NY14 support this hypothesis. Injection of pickling liquor began at "0" on the pore-volume scale (fig. 5). The origin of this scale was arbitrarily set at the point at which the pickling liquor–brine interface in the base of the sample holder was initially displaced upward toward the rock core. To travel from this point to the point of sample collection, an idealized, planar (nondispersed) interface would pass successively through the porous filter disk at the bottom of the core (volume 17.9 mL), the rock core (volume 16.3 mL for sample 73NY14), the upper porous disk (volume 17.9 mL), and several inches of plumbing (volume 7.2 mL). These data show that the effective zero point on the pore-volume scale is displaced to the right about 3+ pore volumes. The breakthrough curve for Na^+, presumably a conservative constituent in light of the reactions that were anticipated to occur, supports this. The midpoint of this curve indicates that pickling liquor displaces brine at just over 3 pore volumes.

The breakthrough curve for Na^+ (fig. 5) indicates that virtually all the brine in the core has been displaced by pickling liquor by the time the last sample aliquot was collected at 9.4 pore volumes. However, Ca^{+2} and Mg^{+2} concentrations for this sample are significantly in excess of the input concentrations of 7.0 and 4.0 mg/L, respectively, in the pickling liquor, and Fe^{+2} concentrations are lower than expected.[3]

Net differences between the amount of Na^+, Ca^{+2}, Mg^{+2}, and Fe^{+2} in the influent and effluent pickling liquor were calculated. Effluent amounts of these constituents were calculated from the area under the curves in figure 5. Influent amounts had to be corrected to include the volume of brine in the test apparatus and in the core at the start of injection because this fluid would be collected along with the pickling-liquor effluent. The following equation was used to calculate influent amounts:

$$I = 50(B) + 104(P) \quad (6)$$

[3] The iron concentration of pickling liquor used for this experiment was not determined, but iron concentration of other, filtered samples of pickling liquor ranged from 143 000 to 170 000 mg/L.

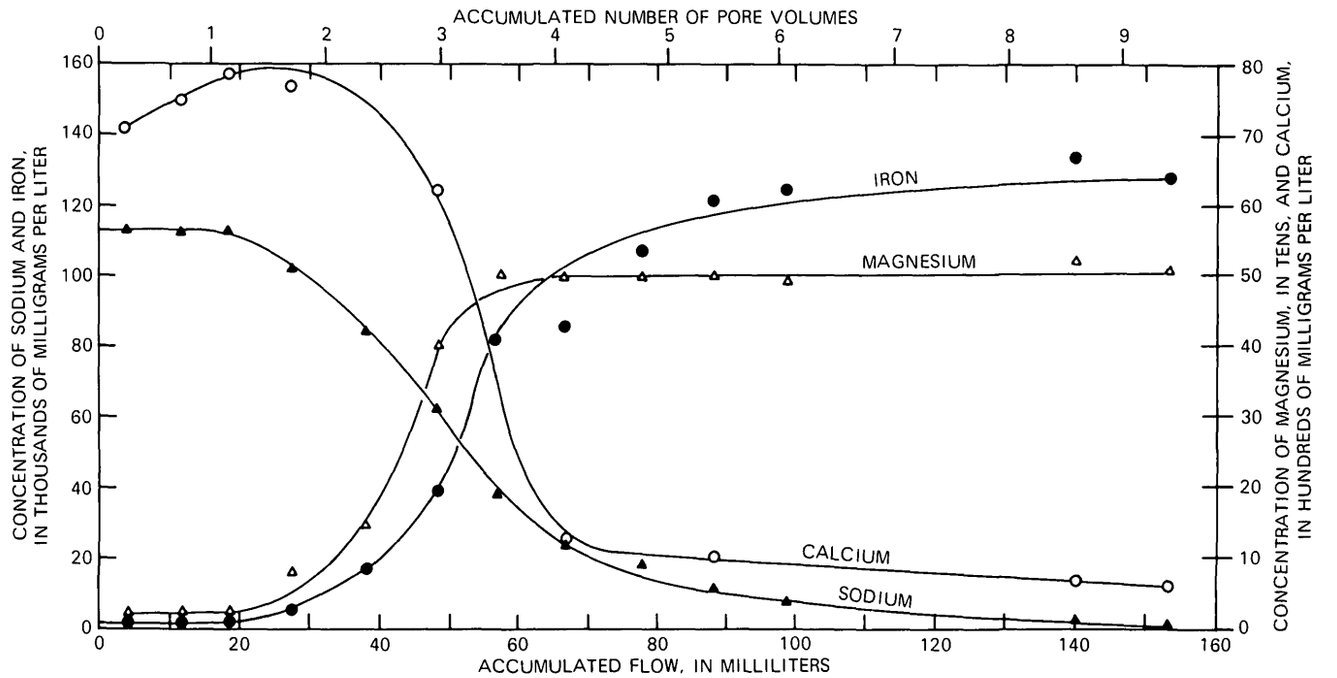

FIGURE 5.—Change in concentrations of sodium, calcium, magnesium, and iron in effluent pickling liquor from dolomitic sample 73NY14.

where I = the influent amount, in milligrams;

B = the concentration of a given constituent (Na^+, Ca^{+2}, Mg^{+2}, or Fe^{+2}) in the brine, in milligrams per milliliter; slight adjustments in the concentration of these constituents were made to account for impurities in the reagent salts used to prepare the synthetic brine;

P = the concentration of a given constituent (Na^+, Ca^{+2}, Mg^{+2}, or Fe^{+2}) in pickling liquor, in milligrams per milliliter.

The number in the first term of the equation is the volume, in milliliters, in the apparatus and core (about 3 pore volumes, as estimated earlier). The number in the second term of the equation is the difference between total volume of influent (about 154 mL) and the volume of the apparatus and core.

The close balance between the amount of effluent and influent Na^+ (table 5)—a nonreactive constituent in light of the anticipated reactions (eqs 1–5)—indicates that equation 6 is accurate in approximating influent concentrations.

The data (table 5) show that, as pickling liquor moves through the sample core, it gains significant amounts of Ca^{+2} and Mg^{+2} and loses iron.[4] This suggests that dolomite is being dissolved by acid and that iron is precipitating. Two general observations of the pickling-liquor effluent from dolomitic samples also indicate that dolomite is being dissolved: (1) pH of the pickling liquor that passed through the sample was about 3, as compared to 0 for the influent liquor, which indicates that some neutralization of acid had occurred, and (2) CO_2 effervesced from the effluent pickling liquor as pressure dropped to atmospheric levels. Consequently, CO_2 was being produced but remained in solution rather than in a separate gaseous phase under in-situ conditions. The volume of CO_2 approximately equaled the volume of pickling-liquor effluent in the early part of injection, but the ratio of CO_2 volume to pickling-liquor volume decreased over the course of injection.

It is not clear what iron compound was precipitating from solution. From the data in table 5, it is calculated that a minimum of about 36 millimoles of Fe^{+2} was lost from solution, presumably as a ferrous salt. If $FeCO_3$ were the salt, then it would require dissolution of 18 millimoles of dolomite (to produce 36 millimoles CO_3^{-2}) and would also add 18 millimoles of Ca^{+2} and Mg^{+2} to solution. However, the data in table 5 indicate that only about 2.3 millimoles of Mg^{+2} and 1.4 millimoles Ca^{+2} have been added to the effluent pickling liquor. Consequently, other noncarbonate iron species, such as $Fe(OH)_2$ or mixed hydroxy-carbonate species, for instance, may be precipitating.

Another possibility is that colloidal-size iron that passes through the 0.45-μm filter may be entrapped in the smaller pore spaces of the core. This would clog the core and cause the observed decrease in iron.

A thin section was taken through the center of the plugged core and was examined by binocular microscope for gross physical changes and by electron microprobe for changes in chemistry, particularly iron distribution. No physical or chemical changes were observed, presumably because the sawing procedure for preparing the rock section used water as lubricating fluid and caused the iron to be dissolved or because clogging took place at or near the upstream end of the core sample.

Clogging by $CaCl_2$ precipitation (eq 4) or by CO_2 entrapment (eq 2) did not seem to play a role in decreasing hydraulic conductivity. Perfusion of more than 140 pore volumes of HCl at a concentration comparable to that of pickling liquor had only a minor effect on hydraulic conductivity of sample 73NY10, compared with the decrease observed when an additional 30 pore volumes of pickling liquor was subsequently injected (fig. 6). Also, as mentioned before, no CO_2 was observed as a separate gas phase when seen through the high-pressure window until pressure was dropped to atmospheric levels.

TABLE 5.—*Comparison of influent and effluent amounts of sodium, calcium, magnesium, and iron for sample 73NY14, in milligrams*

	Na^+	Ca^{+2}	Mg^{+2}	Fe^{+2}
Effluent -----	5 680	465	57	12 600
Influent -----	5 700	408	1	[1]14 600 to 18 700
Difference[2] --	-20	+57	+56	-2 000 to -6 100

[1] Based on input concentrations of 140,000 and 180,000 mg/L, respectively.

[2] Positive number indicates gain to effluent pickling liquor; negative number indicates loss from effluent pickling liquor.

[4] The loss of iron from the effluent pickling liquor shown in table 5 is a small difference between two large numbers; consequently, the values may be greatly in error.

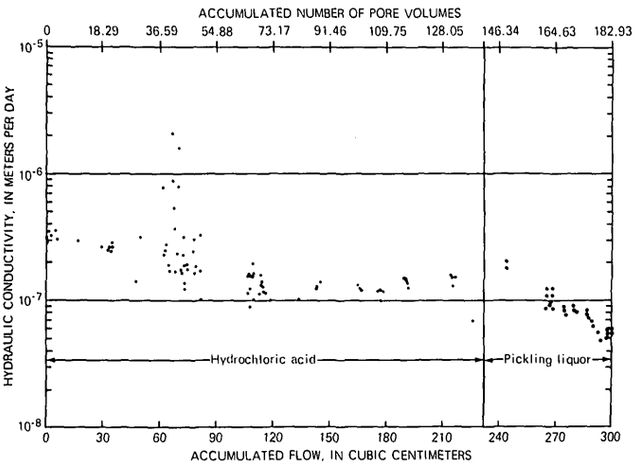

FIGURE 6.—Change in hydraulic conductivity of dolomitic sample 73NY10 during injection of HCl and then pickling liquor.

SUMMARY

A laboratory experiment was designed to study, at in-situ field conditions, the kinds of chemical reactions that occur when an iron-rich waste pickling liquor is injected into dolomitic and quartzitic core samples.

The apparatus developed for the experiment was a high-pressure, stainless-steel triaxial chamber of the type used in rock-mechanics testing but modified to allow downstream sample collection of effluent liquids and direct visual monitoring at in-situ temperature and pressure. Pickling liquor was injected into quartzitic and dolomitic cores, and changes in hydraulic conductivity and in the chemical and physical characteristics of the effluent liquids were determined.

The data presented here support the contention that the predominant chemical effects that occur during injection are dissolution of the dolomite and precipitation of iron from the pickling liquor.

It is emphasized that this conclusion was reached on the basis of data for specific samples. Other carbonate rocks having different chemical and physical properties might not react in the same fashion.

REFERENCES CITED

Bayazeed, A. F., and Donaldson, E. C., 1973, Subsurface disposal of pickle liquor: U.S. Bur. Mines Rept. Inv. 7804, 31 p.

Chamberlain, L. C., Jr., and Boyer, R. F., 1939, Acid solvents for oil wells: Indus. Eng. Chemistry, v. 31, no. 4, p. 400–406.

Donaldson, E. C., 1964, Subsurface disposal of industrial wastes in the United States: U.S. Bur. Mines Inf. Circ. 8212, 34 p.

Donaldson, E. C., and Bayazeed, A. F., 1971, Reuse and subsurface injection of municipal sewage effluent—two case histories: U.S. Bur. Mines Inf. Circ. 8522, 34 p.

Goolsby, D. A., 1971, Hydrogeochemical effects of injecting wastes into a limestone aquifer near Pensacola, Florida: Ground Water, v. 9, no 1., p. 355–368.

Smith, C. F., Crowe, C. W., and Wieland, D. R., 1970, Fracture acidizing in high temperature limestone: Am. Inst. Mining Engineers, Soc. Petroleum Engineers, Ann. Mtg., 45th, Houston, Texas, 1970, Preprint SPE 3008, 9 p.

van Poolen, H. K., and Jargon, J. R., 1943, How conditions affect reaction rate of well-treating acids: Oil and Gas Jour., v. 66, no. 43, p. 84–88, 90–91.

Waller, R. M., Turk, J. T., and Dingman, R. J., 1977, Potential effects of deep-well waste disposal in western New York: U.S. Geol. Survey Prof. Paper 1053. (In press.)

Jour. Research U.S. Geol. Survey
Vol. 6, No. 1, Jan.-Feb. 1978, p. 11-21

DETERMINATION OF RUNOFF COEFFICIENTS OF STORM-WATER-BASIN DRAINAGE AREAS ON LONG ISLAND, NEW YORK, BY USING MAXIMUM-STAGE GAGES

By D. A. ARONSON, Syosset, N.Y.

Prepared in cooperation with the Nassau County Department of Public Works

Abstract.—A method for determining runoff coefficients indirectly—without direct measurement of volume of runoff—was developed for drainage areas of selected storm-water basins on Long Island, N.Y., to expedite evaluation of basin performance. The method requires a maximum-stage gage to record the maximum water level attained in the basin during the storm, and a precipitation gage to record storm intensity at regular intervals. The maximum volume of runoff impounded in the basin during a storm is calculated from precipitation data, an arbitrarily estimated runoff coefficient, and the basin's dimensions and infiltration rate. The calculated result is then compared with the recorded maximum water level, and the process is repeated with increased or decreased coefficients on a trial basis until two of the resulting water-storage maxima closely bracket the recorded maximum. The runoff coefficient in effect during that storm is then interpolated or derived graphically from the calculated water-storage maxima. Results of data analyses suggest that a close approximation of a basin's infiltration rate may be used instead of a measured infiltration rate to calculate the runoff coefficient. Differences between measured and calculated runoff coefficients averaged less than 20 percent when based on average infiltration rates adjusted for water temperature and less than 10 percent when based on measured infiltration rates. Accuracy of the calculated runoff coefficient tends to decline as the interval between precipitation measurements increases. Precipitation data collected at 5- and 15-minute intervals gave accurate runoff coefficients regardless of storm duration, but data collected at 30- or 60-minute intervals gave widely varying results.

Use of existing storm-water basins on Long Island, N.Y., for infiltration of reclaimed water (highly treated sewage effluent) is receiving increasing attention as an efficient and economical means of recharging the ground-water reservoir, the sole source of freshwater for more than 2.5 million residents of Nassau and Suffolk Counties (fig. 1.) Many of the more than 2100 basins in Nassau and Suffolk Counties are potential sites for infiltration of reclaimed water for supplemental recharge, provided that such use does not interfere with the disposal of storm runoff and that the geologic material underlying the basins can accept and transmit the additional water.

A method of evaluating the suitability of storm-water basins for infiltration of reclaimed water has been described by Aronson and Prill (1977). The procedure involves analysis of basin performance during inflow of both reclaimed water and runoff from large-magnitude storms when the basin's ability to accommodate large volumes of water is under greatest stress. Of the several factors that must be evaluated prior to a basin-performance analysis, the most difficult to determine is the volume of storm runoff entering the basin because it requires (1) knowledge of the storm's areal extent, duration, and intensity and (2) the runoff coefficient [1] of the basin's drainage area.

Seaburn and Aronson (1974) determined runoff coefficients for the drainage areas of three representative test basins by direct measurement of precipitation and volume of runoff into the basins; however, the instrumentation required to obtain volume of inflow was expensive to install and was subject to frequent breakdowns. Because direct measurement of inflow is not expedient and because a great many basins must be investigated before those most suitable for infiltration of reclaimed water can be selected, a simplified procedure was devised whereby the runoff coefficient could be determined from measurements of precipitation and maximum volume of storm runoff within the basin so that direct measurement of storm-water inflow is not required.

PURPOSE AND SCOPE

The purpose of this report is to (1) describe a method for determining the runoff coefficient of a

[1] The runoff coefficient is defined as the ratio of volume of runoff to volume of precipitation within a basin's drainage area during a storm (Jens and McPherson, 1964, p. 20-20–20-28).

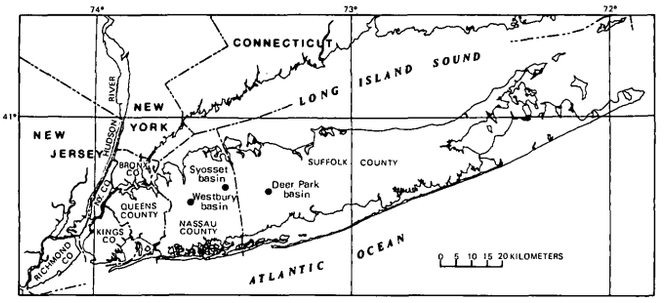

FIGURE 1.—Location of test basins in Nassau and Suffolk Counties, Long Island, N.Y.

basin's drainage area during a given storm without direct measurements of storm-water inflow to the basin, (2) discuss how the accuracy of the infiltration rate and the frequency of precipitation measurements can affect results, and (3) discuss the method's application to present and future studies of storm-water basins on Long Island.

GENERAL DESCRIPTION OF STORM-WATER BASINS

In general, storm-water basins on Long Island are open pits of various shapes and sizes in moderately to highly permeable sand and gravel deposits of glacial origin. The basins' primary function is to collect storm runoff from highways and from residential, industrial, and commercial areas. The area of individual basins ranges from 405 to 121 000 square meters and averages between 4050 and 8100 m². Most basins are between 3.0 and 4.6 meters deep, but some are as deep as 12 m. In 1969, 2124 basins in Nassau and Suffolk Counties returned approximately 2.67 cubic meters per second of storm runoff to the ground-water reservoir (Seaburn and Aronson, 1974).

DESCRIPTION OF TEST BASINS

Three storm-water basins were used to develop the simplified method for determining runoff coefficients. The basins are in the villages of Westbury, Syosset, and Deer Park (fig. 1). For convenience, each basin is referred to in this report by the name of the village in which it is located. Pertinent information on the basins is summarized in table 1. The unsaturated zone beneath the three test basins consists of generally similar deposits of light-brown, medium to very coarse sand and gravel with thin lenses of silt and fine sand. A detailed description of each of the basins is given in Seaburn and Aronson (1974).

Determination of runoff coefficients by the method described in this report requires knowledge of the relationships between depth, volume, and infiltration area of stored water for each basin. The graphs in figure 2 depict these relationships for the Westbury, Syosset, and Deer Park basins, respectively. The graphs were derived from topographic maps that were prepared by the method described in Aronson and Prill (1977) for each basin.

TABLE 1.—*Summary of data on Westbury, Syosset, and Deer Park basins*

[Modified from Seaburn and Aronson, 1974]

Basin	Date of construction	Contributing drainage area (hectares)	Storage capacity [1] (cubic meters)	Maximum infiltration area [2] (square meters)	Altitude of basin floor above sea level (meters)	Water depth at overflow level (meters)
Westbury	1954	6.1	2 660	1 160	29.6	3.0
Syosset	1957	11.7	7 870	2 420	58.2	3.7
Deer Park	1967	47.8	10 480	4 420	22.2	3.0

[1] Storage capacity is the volume of water the basin can obtain without overflowing.
[2] Maximum infiltration area is the horizontal projected plan area at the overflow level.

SOURCE OF DATA

A detailed study of storm-water basins on Long Island was made by Seaburn and Aronson (1974). The major results of the study were (1) a compilation of basic data on physical features of the basins, (2) a record of the areal extent, duration, and intensity of precipitation during 30 selected storms, with measurements of storm runoff into each basin, (3) measurement of infiltration rates at three selected basins, and (4) evaluation of hydrologic effects of storm-water basins on the regional ground-water systems of Long Island. As part of the study, precipitation, storm runoff, and volume of impounded water were measured during numerous storms at each of three typical storm-water basins—those at Westbury, Syosset, and Deer Park. The storm and basin data analyzed in the present report were derived from the study of Seaburn and Aronson (1974).

Features measured by Seaburn and Aronson (1974) that are required for determining runoff coefficients include precipitation characteristics as well as the basin's infiltration rate, maximum depth of stored runoff, and water temperature during storms. Precipitation was recorded at 5-minute intervals by an automatic digital recorder, and maximum depth of impounded storm runoff was monitored by a digital water-level recorder, although any type of maximum-stage gage would have been adequate. Infiltration rates were measured by Seaburn and Aronson (1974) during individual storms at each of the test basins. However, it will be explained in following sections that the average infiltration rate of a basin, or a reasonable estimate thereof, determined by standard field techniques, may

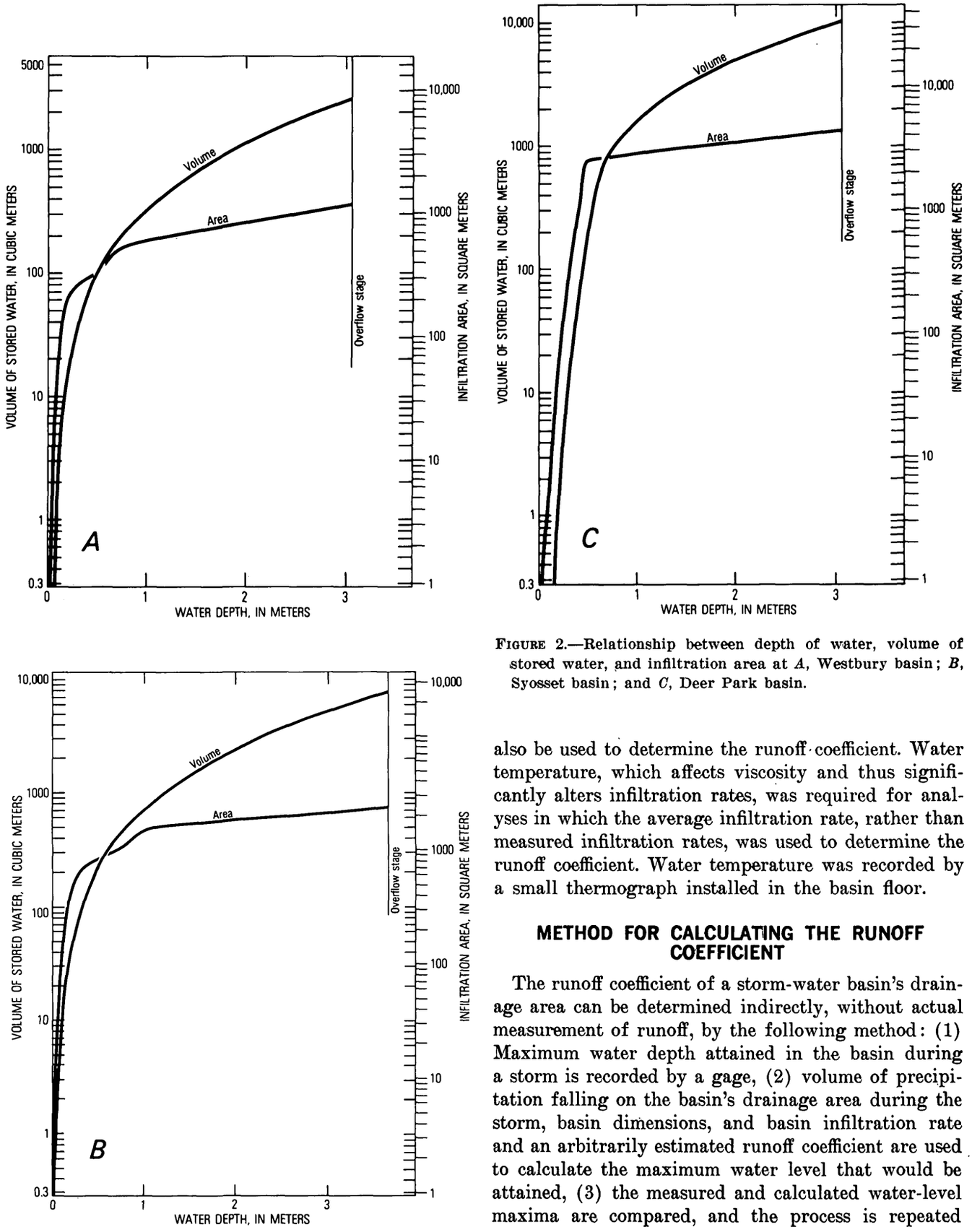

FIGURE 2.—Relationship between depth of water, volume of stored water, and infiltration area at *A*, Westbury basin; *B*, Syosset basin; and *C*, Deer Park basin.

also be used to determine the runoff coefficient. Water temperature, which affects viscosity and thus significantly alters infiltration rates, was required for analyses in which the average infiltration rate, rather than measured infiltration rates, was used to determine the runoff coefficient. Water temperature was recorded by a small thermograph installed in the basin floor.

METHOD FOR CALCULATING THE RUNOFF COEFFICIENT

The runoff coefficient of a storm-water basin's drainage area can be determined indirectly, without actual measurement of runoff, by the following method: (1) Maximum water depth attained in the basin during a storm is recorded by a gage, (2) volume of precipitation falling on the basin's drainage area during the storm, basin dimensions, and basin infiltration rate and an arbitrarily estimated runoff coefficient are used to calculate the maximum water level that would be attained, (3) the measured and calculated water-level maxima are compared, and the process is repeated

with the trial runoff coefficient increased or decreased in increments until two of the resulting water-level maxima closely bracket the recorded value, and (4) the runoff coefficient is then interpolated or derived graphically from the two approximate values.

The method for calculating maximum depth of stored runoff in a basin is basically the same as that given by Aronson and Prill (1977), except that they used precipitation data for idealized storms, whereas, in the present study, precipitation data from actual storms were used. Calculation of the runoff coefficient requires that, during the period of inflow and infiltration, precipitation measurements be taken at short enough intervals that the sum of the incremental changes in volume of storage is equivalent to the maximum recorded value of stored water.

Volume of water in storage at any time during simultaneous inflow and infiltration of storm runoff can be defined by the continuity equation

$$S_t = \sum_{i=1}^{n} (V_i - I_i), \qquad (1)$$

where S_t is the volume of water in storage at a specified time after start of inflow, in cubic meters,
i is the number of the time interval since the start of inflow,
n is the number of time intervals used to determine S_t,
V_i is the volume of storm runoff entering the basin during the ith time interval, in cubic meters, and
I_i is the volume of water that infiltrates the basin during the ith time interval, in cubic meters.

Volume of storm runoff entering the basin is determined by the equation

$$V_i = D \cdot C \cdot P_i / 1000, \qquad (2)$$

where D is the contributing drainage area, in square meters,
C is the preliminary, estimated runoff coefficient, and
P_i is the amount of precipitation during the ith time interval, in millimeters.

Volume of infiltration is determined by the equation

$$I_i = A_i \cdot R \cdot t_i, \qquad (3)$$

where A_i is the average infiltration area during the ith time interval, in square meters,
R is the infiltration rate, in meters per hour, and
t_i is the duration of the ith time interval, in hours.

The computational procedure for solving equation 1 requires that cumulative storage (S_t) be determined for the start of each time interval. Infiltration area at the start of a time interval can be determined from graphs that relate infiltration area to depth of impounded water (storage volume) (fig. 2). If this value is used as the infiltration area during the ith time interval, equation 1 can be expressed as

$$S_x = S_o + V_i - (A_o \cdot R \cdot t_i), \qquad (4)$$

where S_x is the volume of water in storage (S_t) at the end of the ith time interval, in cubic meters,
S_o is the volume of water in storage at the beginning of the ith time interval, in cubic meters, and
A_o is the infiltration area for S_o, in square meters.

S_x is a preliminary estimate of S_t in equation 1. When stage is rising, the value of S_x is an overestimate of maximum storage for a selected interval, because the infiltration area and, correspondingly, the volume of infiltration are increasing. Similarly, during intervals of declining stage, the value of S_x is an underestimate of maximum storage because the infiltration area is decreasing. Thus, in order to calculate S_t in equation 1, the average infiltration area (A_i) during the selected time interval must first be determined and then computed from the equation

$$A_i = (A_o + A_x)/2 \qquad (5)$$

where A_x is the infiltration area for the volume of stored water for S_x, in square meters.

Calculation of incremental changes in basin storage and determination of the runoff coefficient are demonstrated by the following analysis of a storm at the Westbury basin. Changes in basin storage for the storm of July 28, 1969, are given in table 2, which is a facsimile of a computer printout. The precipitation was measured at 5 min intervals with an automatic digital recorder (Seaburn and Aronson, 1974). An average infiltration rate of 0.43 meter per hour was measured during this storm. The maximum depth of stored water was 0.55 m, which corresponds to a storage volume of 122.7 cubic meters. With a preliminary runoff coefficient of 18 percent, the maximum volume of stored water (in the last column of table 2) that would be attained is 124.0 m^3—a value greater than that actually measured. Calculations were then repeated with a slightly lower runoff coefficient (16 percent), and this yielded a lower volume of runoff and, hence, a lower maximum volume of stored water. (If the first calculated maximum volume of stored water had been lower than that actually measured,

TABLE 2.—*Tabulation of calculated changes in water storage at Westbury basin during storm of July 28, 1969*

CHANGES IN VOLUME OF STORED WATER AT AN INFILTRATION RATE OF 0.433 METER PER HOUR AND A RUNOFF COEFFICIENT OF 0.18.
MAXIMUM MEASURED VOLUME OF STORED WATER, 123 CUBIC METERS.
TIME INTERVAL, 5 MINUTES.
DRAINAGE AREA, 60,700 SQUARE METERS.

DATE JULY 28, 1969
BASIN 263

TIME[1]	PREC[2]	CUM RUNOFF[3]	RUN INCR[4]	SO[5]	AO[6]	AORT[7]	SX[8]	AX[9]	AXRT[10]	AVG[11]	FINAL[12]
0.0	0.25	2.7	2.7	0.0	0.0	0.0	2.8	82.9	3.0	1.5	1.3
0.08	0.0	2.7	0.0	1.3	43.8	1.6	0.0	0.0	0.0	0.8	0.5
0.17	2.03	24.9	22.2	0.5	22.1	0.8	21.9	228.0	8.2	4.5	18.2
0.25	4.32	72.1	47.2	18.2	214.1	7.7	57.7	290.2	10.5	9.1	56.3
0.33	3.56	111.0	38.9	56.3	289.2	10.4	84.8	309.0	11.2	10.8	84.4
0.42	3.81	152.6	41.6	84.4	308.7	11.1	114.9	339.9	12.3	11.7	114.3
0.50	2.03	174.8	22.2	114.3	339.1	12.2	124.3	355.3	12.8	12.5	124.0
0.58	0.76	183.1	8.3	124.0	354.7	12.8	119.5	347.0	12.5	12.7	119.6
0.67	0.25	185.8	2.7	119.6	347.3	12.5	109.8	333.4	12.0	12.3	110.0
0.75	0.0	185.8	0.0	110.0	333.8	12.0	98.0	321.4	11.6	11.8	98.2
0.83	0.25	188.5	2.7	98.2	321.6	11.6	89.3	313.2	11.3	11.4	89.4
0.92	0.51	194.1	5.6	89.4	313.4	11.3	83.7	308.3	11.1	11.2	83.8
1.00	0.25	196.8	2.7	83.8	308.4	11.1	75.4	302.3	10.9	11.0	75.5
1.08	0.51	202.4	5.6	75.5	302.4	10.9	70.2	299.0	10.8	10.8	70.3
1.17	0.25	205.1	2.7	70.3	299.0	10.8	62.2	293.7	10.6	10.7	62.3
1.25	0.25	207.8	2.7	62.3	293.8	10.6	54.4	288.1	10.4	10.5	54.6
1.33	0.25	210.5	2.7	54.6	288.2	10.4	46.9	281.7	10.2	10.3	47.0
1.42	0.51	218.1	5.6	47.0	281.8	10.2	42.4	276.8	10.0	10.1	42.5
1.50	0.76	224.4	8.3	42.5	276.9	10.0	40.8	275.0	9.9	10.0	40.8
1.58	0.25	227.1	2.7	40.8	275.1	9.9	33.6	265.4	9.6	9.7	33.8
1.67	0.76	235.4	8.3	33.8	265.6	9.6	32.5	263.0	9.5	9.5	32.6
1.75	0.76	243.7	8.3	32.6	263.1	9.5	31.4	260.2	9.4	9.4	31.5
1.83	0.76	252.0	8.3	31.5	260.3	9.4	30.4	257.2	9.3	9.3	30.5
1.92	0.76	260.3	8.3	30.5	257.4	9.3	29.5	254.5	9.2	9.2	29.6
2.00	2.54	288.1	27.8	29.6	254.6	9.2	48.2	283.0	10.2	9.7	47.7
2.08	0.76	296.4	8.3	47.7	282.5	10.2	45.8	280.6	10.1	10.2	45.8
2.17	0.25	299.1	2.7	45.8	280.6	10.1	38.4	271.9	9.8	10.0	38.5
2.25	0.25	301.8	2.7	38.5	272.1	9.8	31.4	260.5	9.4	9.6	31.6

MAXIMUM CALCULATED VOLUME OF STORED WATER, 124.0 CUBIC METERS

[1]Time since start of precipitation, in hours.

[2]Amount of precipitation, in millimeters.

[3]Cumulative volume of runoff with an 18-percent runoff coefficient, in cubic meters.

[4]Incremental increase in runoff during time interval t_i, in cubic meters (V_i in equation 2).

[5]Volume of water stored in basin at start of time interval t_i, in cubic meters (S_O in equation 4).

[6]Infiltration area of S_O, in square meters (A_O in equation 4, see figure 2).

[7]First estimate of volume of water infiltrated during t_i, in cubic meters, equal to $R \cdot A_O \cdot t_i$.

[8]Preliminary estimate of volume of water stored in basin at end of time interval t_i, in cubic meters (S_X in equation 4).

[9]Infiltration area of S_X, in square meters (A_X in equation 5).

[10]Second estimate of volume of water infiltrated during t_i, in square meters, equal to $R \cdot A_X \cdot t_i$.

[11]Average volume of water infiltrated during t_i, in cubic meters (I_i in equation 3, equivalent to $\frac{R \cdot A_O \cdot t_i + R \cdot A_X \cdot t_i}{2}$).

[12]Volume of water in storage at end of time interval t_i, in cubic meters (S_t in equation 1. Value becomes S_O for next time interval).

the runoff coefficient would have increased for the second calculation). The effective runoff coefficient, which lies between the two calculated values, can be determined by interpolation, although a slightly more precise solution can be obtained by graphing maximum calculated water storage in relation to the runoff coefficient for several sets of calculations. At least three different runoff coefficients should be used to define the graph. The effective runoff coefficient is the point where the graph crosses the line representing observed maximum water storage (fig. 3). The difference between coefficients obtained by interpolation and those obtained graphically averaged less than 2 percent for 10 storms selected at random. Accordingly, the interpolated values for runoff coefficient, which take less time to derive, are reported here.

By the preceding method, an average runoff coefficient of 17.8 percent was calculated for the storm of July 28, 1969, at the Westbury basin. (See fig. 3). This value is only slightly smaller than the 18.6-percent coefficient measured by Seaburn and Aronson (1974, p. 35) during the same storm.

The method described in this report for calculating the runoff coefficient is based on the premise that the volume of storm runoff entering a basin is proportional to the volume of precipitation falling on the contributing drainage area. The relationships among precipitation, resulting inflow to the basin, and changes in water storage in the basin are illustrated by the following analysis of data obtained during a representative storm at a test basin.

To allow comparison of results, inflow to the basin and changes in water storage were measured and also calculated for the storm of July 28, 1969, at the Westbury basin. Figure 4 depicts graphs on which are plotted measured and calculated volume of storage, measured and calculated volume of inflow, and precipitation rate during the storm. Values for calculated inflow and volume of stored water were derived from a runoff coefficient of 18 percent. Values for measured inflow and volume of stored water result from a measured runoff coefficient of 18.6 percent.

The graphs of incremental precipitation and calculated incremental flow are characterized by several peaks; peaks in the graph of calculated incremental inflow correspond to peaks in precipitation. The graph

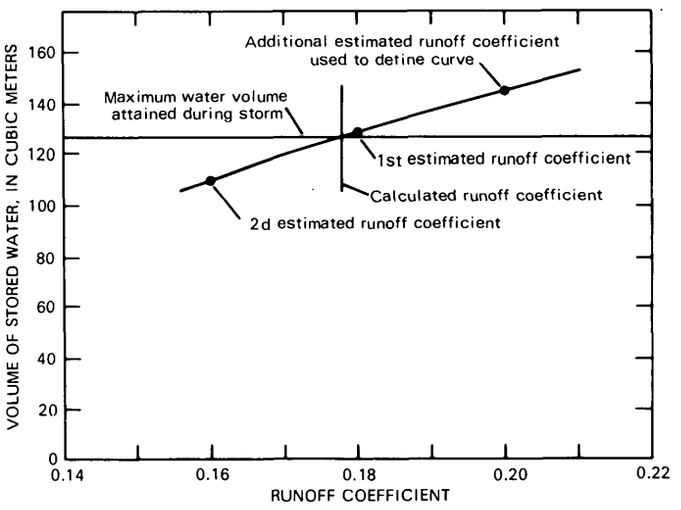

FIGURE 3.—Graphical determination of runoff coefficient for storm of July 28, 1969, at Westbury basin.

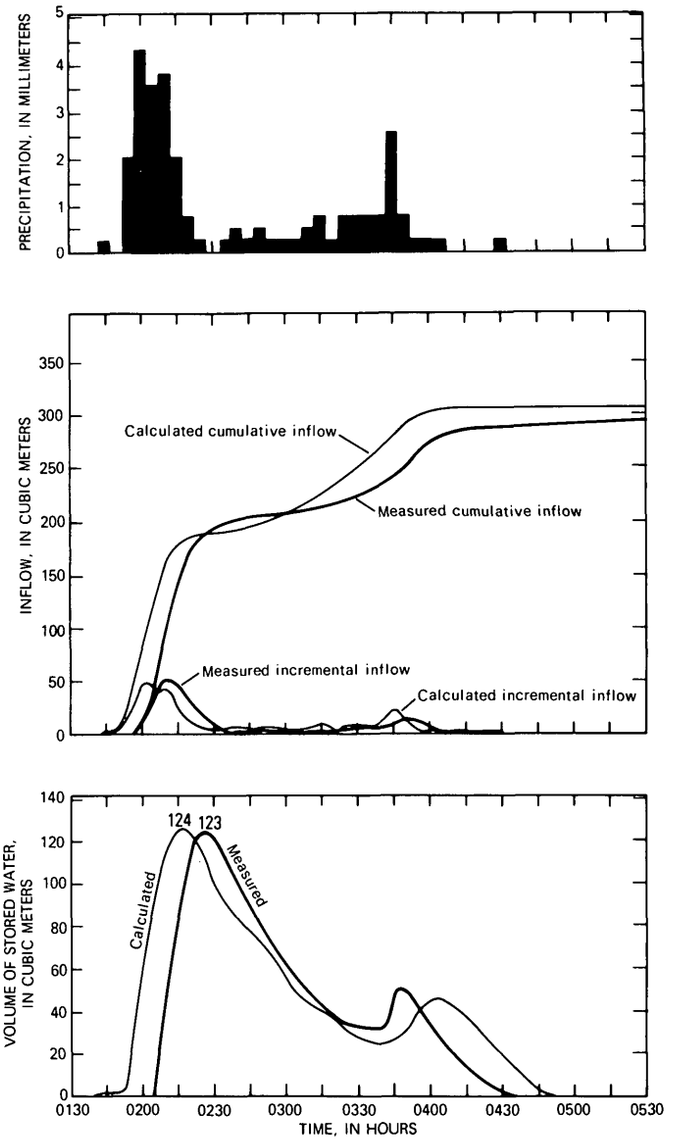

FIGURE 4.—Relationships between precipitation, measured and calculated volume of inflow, and measured and calculated volume of stored water at Westbury basin during storm of July 28, 1969.

of measured incremental inflow, however, has two peaks, probably because the effects of small precipitation peaks on the resulting inflow generally are reduced during traveltime between precipitation and inflow to the basin. (Lag times between precipitation, inflow, and water storage need not be known and are not incorporated in the determination of the runoff coefficient.) The curves for cumulative measured and calculated inflow are in general very similar, as are curves of measured and calculated volume of stored water in the basin. Peak values of measured and calculated incremental inflow are also similar, as are the peak values of measured and calculated volume of stored water. Although the graph of calculated incremental inflow has several peaks and exhibits a double peak during initial inflow, calculated volume of stored water exhibits a single peak during initial water storage. Changes in water storage generally do not vary in direct proportion to changes in inflow because inflow and infiltration occur simultaneously, which tends to reduce the magnitude of changes in volume of stored water.

The relationships depicted in figure 4 are typical of other storms analyzed for the Westbury, Syosset, and Deer Park basins. The similarity between measured and calculated volumes of inflow and between measured and calculated volumes of water storage indicate that the method for determining runoff coefficients is reliable.

In this study, each of the three test basins was analyzed during 10 selected storms. Precipitation was measured at 5-min intervals, and the runoff coefficients were calculated from measurements taken 5, 15, 30, and 60 min apart to evaluate the effect of time interval on the accuracy of the calculated coefficient. Precipitation data for each storm are given in table 3.

Infiltration rates at the three test basins were measured by Seaburn and Aronson (1974) and ranged from 0.15 to 0.43 m/h at the Westbury basin, from 0.08 to 0.34 m/h at the Syosset basin, and from 0.03 to 0.12 m/h at the Deer Park basin. These ranges reflect variations in water temperature, depth of stored water, antecedent soil-moisture conditions at the basin floor, and length of the flooding period, among other factors. The infiltration rates used to calculate runoff coefficients in the present study were the rates measured by Seaburn and Aronson (1974) during the same storms.

RESULTS OF ANALYSES

Results of analyses for 30 storms are listed in table 3; runoff coefficients obtained from measured infiltration rates are given in analysis 1, and those obtained from estimated infiltration rates are given in analysis 2.

In analysis 1, calculated runoff coefficients ranged from 21 percent below to 17 percent above measured coefficients at the three test basins. Absolute error between measured and calculated coefficients averaged 5.5 percent at the Westbury basin, 9.1 percent at the Syosset basin, and 8.2 percent at the Deer Park basin. The storm in which the maximum difference between calculated and measured runoff coefficients occurred was at Syosset on April 2, 1970, when the measured coefficient was 30.2 percent and the calculated coefficient was 24.0 percent, a difference of 21 percent.

The runoff coefficient during a storm is determined by two major groups of factors—those related to precipitation and those related to characteristics of the drainage area. Major factors relating to precipitation include intensity, duration, and areal distribution of the storm; direction of storm travel; antecedent soil-moisture content; and season of the year. Major factors relating to characteristics of the drainage area include land use; soil type; amount and type of ground cover; size, shape, and slope of drainage area; type and extent of storm-water sewering; and season of the year. Because these factors are numerous and highly variable, their combined effects on the runoff coefficient during a storm is complex and difficult to evaluate. Seaburn and Aronson (1974) have shown that, in general, the runoff coefficient tends to be higher during storms of large magnitude because more runoff is contributed from lawns and sidewalks during these storms than during storms of lesser magnitude. However, this relationship is not readily apparent from data in table 3; for example, the storm of March 3, 1970 at the Westbury basin had an average precipitation intensity of 5.8 millimeters per hour, during which time a 7.8-percent runoff coefficient was measured. In contrast, the storm of April 2, 1970, at the same basin, had an average precipitation intensity of 2.8 mm/h, only half as large, and a runoff coefficient of 21.1 percent, more than twice as large as that of the first storm. This and similar examples of a seemingly inverse relationship between precipitation intensity and volume of storm runoff illustrate the complexity of the many factors that determine the runoff coefficient of a basin's drainage area.

The calculated runoff coefficients given in analysis 1, table 3, were obtained from infiltration rates measured during impoundment of storm runoff and those in analysis 2, table 3, were obtained from estimated infiltration rates. It was theorized that if infiltration rates could be estimated accurately, the need to measure them during each storm would be avoided. There-

TABLE 3.—*Characteristics of selected storms at Westbury, Syosset, and Deer Park basins*

[Runoff coefficients in analysis 1, calculated from infiltration rate measured during storm; runoff coefficients in analysis 2, calculated from basins' average infiltration rates, adjusted for temperature of impounded water during storm. Precipitation measurements taken at 5-minute intervals]

Date of storm	Amount of precipitation (mm)	Duration of precipitation (h)	Average precipitation intensity (mm/h)	Maximum water depth (m)	Maximum volume of stored runoff (m^3)	Measured runoff coefficient (percent)	Water temperature (°C)	Analysis 1			Analysis 2		
								Measured infiltration rate (m/h)	Calculated runoff coefficient (percent)	Error[1] (percent)	Adjusted average infiltration rate[2] (m/h)	Calculated runoff coefficient (percent)	Error[1] (percent)
Westbury basin													
July 18, 1969	8.1	0.33	24.6	0.36	47.3	15.9	25.6	0.43	16.1	+1	0.35	15.0	+6
July 28, 1969	30.2	2.25	13.5	.43	122.7	18.6	21.1	.43	17.8	-4	.31	16.4	-12
July 29, 1969	8.9	2.00	4.6	.30	20.7	17.0	23.9	.30	18.0	+6	.34	19.1	+12
Aug. 26, 1969	9.1	.83	10.9	.32	28.6	17.2	24.4	.42	18.1	+5	.34	15.8	-8
Mar. 4, 1970	7.9	3.25	2.6	.26	9.2	15.0	1.7	.15	15.4	+3	.18	17.6	+14
Mar. 12, 1970	7.4	2.42	3.0	.24	6.7	12.4	1.7	.20	11.7	-6	.18	11.1	-10
Mar. 26, 1970	7.6	1.75	4.3	.31	24.8	18.0	3.3	.20	17.3	-4	.19	16.9	-6
Mar. 30, 1970	16.5	2.83	5.8	.31	23.4	7.8	.6	.15	6.7	-14	.18	7.0	-10
Mar. 31, 1970	5.8	5.58	1.0	.20	2.6	10.5	.6	.15	9.9	-6	.18	11.0	+5
Apr. 2, 1970	24.1	8.33	2.8	.39	75.2	21.1	3.9	.16	22.1	+5	.20	24.9	+18
							Average absolute percentage error			5.5	----	----	10.1
Syosset basin													
July 20, 1969	8.1	0.92	8.9	0.29	81.7	13.6	20.0	0.19	12.9	-5	0.24	12.2	-10
Sept. 3, 1969	13.2	7.17	1.8	.20	28.8	11.5	20.0	.30	10.8	-6	.24	9.5	-17
Sept. 4, 1969	44.2	13.17	3.3	.49	233.5	30.1	20.0	.25	33.6	+12	.24	32.7	+9
Oct. 2, 1969	45.7	9.42	4.8	.24	48.9	15.7	21.1	.18	15.6	-1	.24	18.6	+18
Oct. 3, 1969	15.2	1.08	14.0	.56	295.0	19.1	21.1	.14	22.3	+17	.24	25.2	+32
Dec. 22, 1969	28.7	9.58	3.0	.68	410.8	37.0	12.8	.14	39.5	+7	.20	46.2	+25
Mar. 27, 1970	9.4	3.25	2.8	.20	30.0	9.2	3.3	.08	7.8	-15	.15	11.0	+20
Apr. 2, 1970	44.2	16.00	2.8	.33	111.9	30.2	3.9	.30	24.0	-21	.15	22.0	-27
Apr. 20, 1970	12.4	2.25	5.6	.26	67.3	15.1	5.0	.11	14.4	-5	.16	19.2	+27
Sept. 27, 1970	11.9	2.25	5.3	.23	45.9	5.7	21.1	.34	5.6	-2	.24	5.0	-12
							Average absolute percentage error			9.1	----	----	19.7
Deer Park basin													
Mar. 19, 1970	7.9	5.25	1.5	0.33	48.2	7.3	0.6	0.09	7.6	+4	0.05	5.8	-21
Mar. 20, 1970	11.7	5.08	2.3	.85	260.5	11.6	2.8	.06	11.3	-3	.05	10.3	-11
Apr. 2, 1970	45.5	16.83	2.8	1.33	565.7	12.7	3.9	.08	14.6	+15	.05	11.5	-9
Apr. 24, 1970	12.4	.67	18.8	1.07	393.0	11.3	11.7	.08	9.4	-17	.07	9.2	-19
May 26, 1970	14.5	5.17	2.8	.72	197.9	8.9	16.7	.12	8.8	-1	.08	7.4	-17
June 12, 1970	6.6	1.92	3.6	.39	65.8	5.1	26.1	.09	5.8	+14	.09	6.0	+18
July 4, 1970	8.6	.67	13.0	.52	108.2	4.2	23.3	.07	3.9	-7	.09	4.0	-5
July 16, 1970	21.1	3.17	6.6	1.30	525.0	6.7	22.2	.05	7.2	+7	.09	8.1	+21
Aug. 17, 1970	9.9	.67	15.0	.95	323.1	8.7	23.9	.04	9.5	+9	.09	10.4	+20
Aug. 31, 1970	8.6	3.17	2.8	.42	75.2	4.4	22.8	.03	4.2	-5	.09	5.3	+21
							Average absolute percentage error			8.2	----	----	16.2

[1] Percentage difference between measured and calculated runoff coefficients.

[2] Average infiltration rates of 0.28 m/h, 0.21 m/h, and 0.07 m/h at Westbury, Syosset, and Deer Park basins, respectively, adjusted to prevailing water temperature.

fore, runoff coefficients were calculated both from estimated infiltration rates and from the measured infiltration rates of the three test basins to determine whether the estimated rates would give comparable results. The estimated values were obtained by adjusting the infiltration rates measured during the 10 storms at each basin to reflect a uniform temperature of 15.6°C because the variation in viscosity resulting from temperature difference would significantly affect the infiltration rate. (A basin's average infiltration rate could also be estimated by any of several other standard field methods.)

The averages of the adjusted infiltration rates measured at the Westbury, Syosset, and Deer Park basins were 0.28 m/h, 0.21 m/h, and 0.07 m/h, respectively. These average rates were then converted to reflect the water temperature prevailing during each of the 30 analyzed storms. For example, temperature of impounded runoff during the storm of July 28, 1969, at the Westbury basin averaged 21°C (table 3). If the average infiltration rate of 0.28 m/h at 15.6°C is corrected for a temperature of 21°C, it increases to 0.31 m/h, which, although less than the measured infiltration rate of 0.43 m/h during that storm, results in a calculated runoff coefficient of 16.4 percent, only 12 percent lower than the measured runoff coefficient of 18.6 percent.

The relatively small range in percentage error (−12 to +18, −27 to +32, and −21 to +21 percent at the Westbury, Syosset, and Deer Park basins, respectively) for runoff coefficients calculated from the adjusted average infiltration rate is related, in part, to the relatively small variation in infiltration rates among the 10 storms at each of the three test basins, when adjusted for temperature. The adjusted average infiltration rates varied by a factor of 2.0 at the Westbury basin, by a factor of 1.6 at the Syosset basin, and by a factor of 2.1 at the Deer Park basin (analysis 2, table 3). These relatively narrow ranges of infiltration rate are typical of other basins studied on Long Island (Prill and Aaronson, 1973; R. C. Prill, written commun., 1976), which suggests that if a reasonably accurate estimate of infiltration rate can be obtained for a basin on Long Island or any hydrogeologically similar region, that rate may be used as a factor in determining the runoff coefficient for any storm in that basin's drainage area.

Runoff coefficients were calculated for three storms at each of the three test basins to determine whether reasonably accurate coefficients could be obtained when precipitation measurements were taken at intervals longer than 5 min. As shown in table 4, runoff coefficients calculated from precipitation measurements taken at 5-min intervals are similar to those taken at 15-min intervals, regardless of storm duration. Measurements taken at intervals of 30 or 60 min did not give accurate runoff coefficients, however, because short variations in inflow and corresponding variations in volume of infiltration were not detected. Over a 5-min interval, differences between volume of inflow and volume of infiltration generally are sufficiently small to permit accurate determination of incremental changes in volume of water stored in the basin so that the maximum volume of stored water can be readily determined. During longer intervals, however, differences between volume of inflow and volume of infiltration can vary, especially if rainfall decreases or ceases intermittently during the storm. If the volume of inflow is small or 0, the volume of infiltration may remain large, depending on the volume of water already impounded. Thus, in most instances, measurements taken at 30- or 60-min intervals cannot be used to calculate small changes in volume of water stored in the basin. The maximum permissible time interval between measurements depends on several factors, including storm duration, distribution and amount of precipitation with respect to time, infiltration rate of the basin, and geometry of the basin. Collectively, these factors tend to obscure the relationships between individual factors and lessen the accuracy of the calculated runoff coefficient. The only apparent relationship between the runoff coefficient and the interval at which precipitation measurements are taken (table 4) is that the feasibility of using 30- and 60- min intervals between measurements improves as storm duration increases. This applies regardless of whether the measured or estimated infiltration rate is used to calculate the runoff coefficient.

APPLICATION OF METHOD

The procedure for determining the runoff coefficient of a basin's drainage area should be of interest to those involved in water-resource management and in the design and operation of storm-water basins on Long Island and especially to those concerned with potential use of storm-water basins for infiltration of reclaimed water.

If runoff coefficients of a basin's drainage area are known, then that basin's suitability for infiltration of both storm runoff and reclaimed water can be evaluated by the method of Aronson and Prill (1977). Knowledge of the runoff coefficient also enables determination of the volume of storm runoff entering the basin and, hence, the volume of water recharging the ground-water reservoir. In addition, comparison of runoff coefficients for different basins during the

TABLE 4.—*Runoff coefficients for storms at Westbury, Syosset, and Deer Park basins with precipitation measured at 5-, 15-, 30-, and 60-minute intervals.*

Date of storm	Duration of storm (h)	Measured runoff coefficient (percent)	Time interval (min)	Analysis 1			Analysis 2		
				Measured infiltration rate (m/h)	Calculated runoff coefficient (percent)	Error[1] (percent)	Adjusted average infiltration rate[2] (m/h)	Calculated runoff coefficient (percent)	Error[1] (percent)
Westbury basin									
July 29, 1969	2.00	17.0	5	0.30	18.0	+6	0.34	19.1	+12
			15		18.1	+6		18.5	+9
			30		19.2	+13		(3)	--
			60		(3)	--		(3)	--
Mar. 31, 1970	5.58	10.5	5	.15	9.9	-6	.18	11.0	+5
			15		10.9	+4		11.1	+6
			30		(3)	--		(3)	--
			60		(3)	--		(3)	--
Apr. 2, 1970	8.33	21.1	5	.16	22.1	+5	.20	24.9	+18
			15		22.2	+5		25.4	+20
			30		21.8	+3		24.4	+16
			60		19.9	-6		22.0	+4
Syosset basin									
Oct. 3, 1969	1.08	19.1	5	0.14	22.3	+17	0.24	25.3	+32
			15		23.0	+20		26.3	+38
			30		22.6	+18		26.9	+41
			60		(3)	--		(3)	--
Apr. 2, 1970	16.0	30.2	5	.30	24.0	-21	.15	22.0	-27
			15		26.1	-14		22.3	-26
			30		27.2	-10		22.0	-27
			60		(3)	--		(3)	--
Sept. 3, 1970	7.17	11.5	5	.30	10.8	-6	.24	9.5	-17
			15		11.0	-4		10.0	-13
			30		(3)	--		8.1	-30
			60		(3)	--		(3)	--
Deer Park basin									
Apr. 2, 1970	16.83	12.7	5	0.08	14.6	+15	0.05	11.5	-9
			15		14.7	+16		11.5	-9
			30		14.8	+17		11.6	-9
			60		13.7	+8		12.1	-5
May 26, 1970	5.17	8.9	5	.12	8.8	-1	.08	7.4	-17
			15		8.9	0		7.4	-17
			30		10.8	+21		8.3	-7
			60		11.7	+31		10.1	+13
June 12, 1970	1.92	5.1	5	.09	5.8	+14	.09	6.0	+18
			15		5.8	+14		6.1	+20
			30		6.0	+18		6.2	+22
			60		(3)	--		(3)	--

[1] Percentage difference between measured and calculated runoff coefficients.

[2] Average infiltration rates of 0.28, 0.21, and 0.07 m/h at Westbury, Syosset, and Deer Park basins, respectively, adjusted to temperature of impounded water during storm.

[3] Time interval too long to calculate runoff coefficient.

same storm period could be useful in determining the runoff characteristics of specific types of surfaces within a basin's drainage area, which would provide basin designers on Long Island with a method for assigning a more precise runoff coefficient to future basin drainage areas than is currently employed.

SUMMARY

1. Determination of the runoff coefficient of a stormwater basin's drainage area without measuring inflow into the basin requires knowledge of the relationships between the depth of impounded water and the basin's volume, infiltration area, and infiltration rate, all of which can be measured or determined by established field techniques. Precipitation must be recorded at regular intervals, and the maximum stage attained in the basin during the storm must be measured by a gage. The runoff coefficient that would produce this maximum depth is then determined from the volume of inflow into the basin (determined from the precipitation data) and from the basin's dimensions and infiltration rate.
2. The runoff coefficient is determined by the following procedure: The maximum volume of water

received in a basin during inflow of storm runoff is calculated from an arbitrarily estimated runoff coefficient. The resulting maximum is compared with the value recorded by the gage, and the process is repeated by trial and error, raising or lowering the coefficient in increments until the resulting water-storage maxima for two slightly different coefficients bracket the measured value. The runoff coefficient in effect during the storm is then interpolated or derived graphically from the two calculated water-storage maxima.

3. The runoff coefficients were both measured and calculated for 10 storms at each of three test basins to evaluate the accuracy of the method of calculation. Calculated coefficients were derived twice, from measured infiltration rates and from average infiltration rates adjusted for temperature. Analysis of results showed that calculated runoff coefficients ranged between −21 and +17 percent of the measured coefficients when derived from measured infiltration rates and between −27 and +32 percent when derived from the average infiltration rates. In general, absolute percentage differences between measured coefficients and those calculated from measured infiltration rates averaged less than 10 percent, and the corresponding differences resulting from adjusted average infiltration rates averaged less than 20 percent.
4. The runoff coefficient of a basin's drainage area can be calculated accurately if a reasonably correct estimate of the basin's average infiltration rate is obtained. The relatively small difference between measured and adjusted average infiltration rates is typical of many storm-water basins on Long Island; this difference supports the conclusion that a reasonable estimate of the infiltration rate may be used in place of actual measurement in the determination of runoff coefficients.
5. Accuracy of calculated runoff coefficients tends to decline as the time interval between precipitation measurements is increased. Coefficients calculated from measurements taken at 5- and 15-min intervals were similar regardless of storm duration, but measurement intervals of 30 and 60 min resulted in wide variation of runoff coefficients.

REFERENCES CITED

Aronson, D. A., and Prill, R. C., 1977, Analysis of the recharge potential of storm-water basins on Long Island, New York: U.S. Geol. Survey Jour. Research, v. 5, no. 3, p. 307–318.

Jens, S. W., and McPherson, M. B., 1964, Hydrology of urban areas, *in* Chow, V. T., ed., Handbook of applied hydrology: New York, McGraw-Hill Book Co., p. 20–1 to 20–45.

Prill, R. C., and Aaronson, D. B., 1973, Flow characteristics of a subsurface-controlled recharge basin on Long Island, New York: U.S. Geol. Survey Jour. Research, v. 1, no. 6, p. 735–744.

Seaburn, G. E., and Aronson, D. A., 1974, Influence of recharge basins on the hydrology of Nassau and Suffolk Counties, Long Island, New York: U.S. Geol. Survey Water-Supply Paper 2031, 66 p.

Jour. Research U.S. Geol. Survey
Vol. 6, No. 1, Jan.–Feb. 1978, p. 23–40

ACCURACY AND CONSISTENCY COMPARISONS OF LAND USE AND LAND COVER MAPS MADE FROM HIGH-ALTITUDE PHOTOGRAPHS AND LANDSAT MULTISPECTRAL IMAGERY

By KATHERINE FITZPATRICK-LINS
Reston, Va.

Abstract.—Accuracy analyses for land use and land cover maps of the 74 712-km² Central Atlantic Regional Ecological Test Site were performed for a 1-percent sample of the area. Researchers compared Level II land use and land cover maps produced at three scales, 1:24 000, 1:100 000, and 1:250 000 from high-altitude photographs, with point data obtained in the field. The same procedures were employed to determine the accuracy of the Level I land use and land cover produced at 1:250 000 scale from high-altitude photographs and color composite Landsat imagery.

The accuracy of the Level II maps was 85 percent at 1:24 000, 77 percent at 1:100 000, and 73 percent at 1:250 000. The accuracy of the Level I 1:250 000 maps produced from high-altitude photographs was 77 percent and for those produced from Landsat multispectral imagery was 70 percent. The accuracy of the Level I land use maps produced using Landsat imagery is approximately that of the Level I land use maps produced from high-altitude photography with the exception of urban and built-up land. No built-up land was identified from Landsat imagery in the non-urban areas.

The Central Atlantic Regional Ecological Test Site (CARETS) project was sponsored jointly by NASA and the U.S. Geological Survey to evaluate Landsat and high-altitude aircraft data as inputs to a regional land resources information system. The study area includes the District of Columbia, 18 independent cities, and 74 counties within the Chesapeake Bay and Delaware Bay regions.

The CARETS map format was based on the Universal Transverse Mercator (UTM) grid system, and 50×50-km photomosaics were constructed at a scale of 1:100 000 from high-altitude photographs at a scale of 1:120 000. Researchers used these photomosaics as the mapping base for the 1970 land use and land cover maps and for the 1972 land use change maps. The land use classification system proposed by the Interagency Steering Committee on Land Use Information and Classification is presented in USGS Circular 671 (Anderson, 1972) and shown here in table 1. The revision of this classification, based on user response and actual mapping experience, is presented in table 2 (Anderson and others, 1976). The land use classification system used for the CARETS project, table 3, is an earlier version of the two above. Researchers also compiled Level I land use maps at 1:250 000 scale, corresponding to the standard 1°×2° USGS topographic

TABLE 1.—*Land use classification system for use with remote sensor data*[1]

Level I		Level II	
01.	Urban and built-up land	01	Residential.
		02	Commercial and services.
		03	Industrial.
		04	Extractive.
		05	Transportation, communications, and utilities.
		06	Institutional.
		07	Strip and clustered settlement.
		08	Mixed.
		09	Open and other.
02.	Agricultural land	01	Cropland and pasture.
		02	Orchards, groves, bush, fruits, vineyards, and horticultural areas.
		03	Feeding operations.
		04	Other.
03.	Rangeland	01	Grass.
		02	Savannas (Palmetto prairies).
		03	Chaparral.
		04	Desert shrub.
04.	Forest land	01	Deciduous.
		02	Evergreen (coniferous and other).
		03	Mixed.
05.	Water	01	Streams and waterways.
		02	Lakes.
		03	Reservoirs.
		04	Bays and estuaries.
		05	Other.
06.	Nonforested wetland	01	Vegetated.
		02	Bare.
07.	Barren land	01	Salt flats.
		02	Beaches.
		03	Sand other than beaches.
		04	Bare exposed rock.
		05	Other.
08.	Tundra	01	Tundra.
09.	Permanent snow and icefields	01	Permanent snow and icefields.

[1] Source: U.S. Geological Survey Circular 671, p. 6.

TABLE 2.—*U.S. Geological Survey land use and land cover classification system for use with remote sensor data*[1]

Level I		Level II	
1	Urban or built-up land	11	Residential.
		12	Commercial and services.
		13	Industrial.
		14	Transportation, communications, and utilities.
		15	Industrial and commercial complexes.
		16	Mixed urban or built-up land.
		17	Other urban or built-up land.
2	Agricultural land	21	Cropland and pasture.
		22	Orchards, groves, vineyards, nuseries, and ornamental.
		23	Confined feeding operations.
		24	Other agricultural land.
3	Rangeland	31	Herbaceous rangeland.
		32	Shrub and brush rangeland.
		33	Mixed rangeland.
4	Forest land	41	Deciduous forest land.
		42	Evergreen forest land.
		43	Mixed forest land.
5	Water	51	Streams and canals.
		52	Lakes.
		53	Reservoirs.
		54	Bays and estuaries.
6	Wetland	61	Forested wetland.
		62	Nonforested wetland.
7	Barren land	71	Dry salt flats.
		72	Beaches.
		73	Sandy areas other than beaches.
		74	Bare exposed rock.
		75	Strip mines, quarries, and gravel pits.
		76	Transitional areas.
		77	Mixed barren land.
8	Tundra	81	Shrub and brush tundra.
		82	Herbaceous tundra.
		83	Bare ground tundra.
		84	Wet tundra.
		85	Mixed tundra.
9	Perennial snow or ice	91	Perennial snowfields.
		92	Glaciers.

[1] Source: U.S. Geological Survey Professional Paper 964.

TABLE 3.—*Land use categories in CARETS data base*

Level I categories		Level II categories and map notation used	
1	Urban and built-up land	11	Residential.
		12	Commercial and services.
		13	Industrial.
		14	Extractive.
		15	Transportation, communications, and utilities.
		16	Institutional.
		17	Strip and clustered settlement.
		18	Mixed.
		19	Open and other.
2	Agricultural land	21	Cropland and pasture.
		22	Orchards, groves bush fruits, vineyards, and horticultural areas.
		23	Feeding operations.
		24	Other.
4	Forest land	41	Heavy crown cover (40 percent and over).
		42	Light crown cover (10–40 percent.)
5	Water	51	Streams and waterways.
		52	Lakes.
		53	Reservoirs.
		54	Bays and estuaries.
		55	Other.
6	Nonforested wetland	61	Vegetated.
		62	Bare.
7	Barren land	72	Sand other than beaches.
		73	Bare exposed rock.
		74	Beaches.
		75	Other.

map format, using color-composite Landsat imagery enlarged to 1:250 000 scale.

Researchers outlined various land use and land cover polygons on stable base film overlaid on each base map, after refering to the aerial photographs or Landsat multispectral imagery at or near map scale. The minimum mapping unit at all scales was 2×2 mm. Where the land use was an intermixture of several land use and land cover types, all below the minimum mapping size, only one classification code for the dominant land use and land cover was assigned. When interpreters found an area that could not be classified from the photography, they checked auxiliary source material such as topographic or State and county maps. If they were still not able to assign a land use and land cover category with confidence the polygon was marked for field verification.

Field verifications were made several times during the map compilation process between 1971 and 1973. This fieldwork was designed to correct the land use maps, where possible, and to provide an indication of those land use and land cover categories that would require revision and redefinition. Various field methodologies were employed to obtain field data, both to verify the land use maps and to provide needed information about the applicability of the two-level land use and land cover classification system for use with remotely sensed data. During the field verification process, no overall measure of the accuracy of the land use and land cover as mapped, vis-a-vis the classification system, was achieved.

The purpose of this report is to present the findings of an evaluation of the accuracy of the CARETS land use and land cover maps as well as an evaluation of the usefulness of the two-level land use and land cover classification system. The results of this study were originally reported in the CARETS final report to NASA (Fitzpatrick, 1975).

Acknowledgments

The CARETS project was sponsored jointly by NASA and the U.S. Geological Survey through Memorandum of Understanding S–70243–AG, Earth Resources Technology Satellite Investigation SR–125 (IN–002). For this accuracy study, we give particular thanks and acknowledgments to Brian J. L. Berry of the Harvard Center for Computer Graphics for his recommendations and direction in the research design.

THE PROBLEM

Several questions emerged during experimental mapping of land use and land cover at medium and small scales using high-altitude photographs and Landsat multispectral imagery.

The land use and land cover classification system used by the CARETS project (table 3) was a proto-

type developed for use with remotely sensed data. The first question is whether the classes of this system can be validly discriminated using the high-altitude photographs and Landsat multispectral imagery.

Another question relates to the reliability and accuracy of the land use and land cover maps. Several variables are relevant here: the number of land use and land cover classes to be identified, the scale of the maps, and the size of the uniformly coded polygon chosen as the minimum mapping unit. Generally, one may assume that mapping accuracy at any one level is greater for land use and land cover mapped from high altitude photography at large scales; and accuracy decreases as scale decreases, or as detail is diminished by increasing the area of the minimum mapping unit.

A third question relates to the difference between the accuracy and consistency of maps based on the high-altitude photographs and the Landsat imagery at a common scale (1:250 000). The data retrievable per unit area from high-altitude aerial photographs far exceed those obtainable from Landsat multispectral imagery. The slight difference in detail that can be shown on a map at 1:250 000 scale compiled from Landsat multispectral data compared to one compiled from aerial photographs, however, causes one to question the use of the more costly high-altitude aerial photographs.

This paper addresses the questions outlined above, using data from the Central Atlantic Regional Ecological Test Site (CARETS), previously interpreted by Geography Program staff of the U.S. Geological Survey. The Level I mapping accuracy is evaluated for maps compiled at 1:250 000 from high-altitude photographs and from Landsat multispectral imagery. Level II mapping accuracy is evaluated at three scales: 1:24 000, 1:100 000, and 1:250 000 mapped from high-altitude photographs. The original scale of the high-altitude photographs was 1:120 000, and the Level II mapping was originally at 1:100 000 for all of CARETS. Enlargements of the same photographs were used to interpret the land use and land cover on a 1:24 000 topographic map base as a basis for testing the accuracy at 1:24 000. The 1:120 000 scale photographs were interpreted and compiled on a 1:250 000 scale mosaic. The resulting map served as a basis for testing the accuracy at 1:250 000.

RESEARCH DESIGN

Sampling Procedure

The study was restricted to a 1-percent sample of the 74 712-km² area of CARETS. A random stratified sampling technique was used to select the sample sites (Berry and Baker, 1968), after prior separation of the area into urban and non-urban parts to assure proper representation of both urban and non-urban land use. A 5×5-km sampling unit was used in non-urban areas and a 2×2-km unit was used within urban areas where land use and land cover are more complex and parcels are smaller. The random stratified sampling techniques was chosen with the assumption that there were no regular repetitious land use patterns in the CARETS area.

The 5×5-km non-urban sample sites were selected at random for each mosaic using a 5-km UTM grid overlay. Numbers selected from a random number table were considered to be the coordinates of the lower left corner of the sample site. Selected sample sites that fell more than 50 percent outside of the CARETS boundary or totally in water areas were discarded. Sample sites that fell on the boundary but more than 50 percent within the CARETS area were moved inside. The rule followed was that those extending over the northern boundary be moved south, those extending over the eastern or western boundary be moved west or east, respectively, and those extending over the southern boundary be moved north along the UTM grid lines. Sample sites falling in the urbanized areas were not used in the sampling of non-urban areas.

A total of 28 non-urban sites was selected for 1-percent sample of the non-urban area. A regular grid of 25 points located at 1-km intervals was registered to each sample site for use in a point sample of the land use.

The 2×2-km urban sample sites with a regular grid of four 1-km points were selected from the urbanized areas as defined by the U.S. Bureau of the Census, 1972. The sizes of all the urbanized areas in CARETS are presented in table 4. Fifteen 2×2-km urban sample sites, comprising 1 percent of the total

TABLE 4.—*CARETS urbanized areas*[1] *and allocation of urban sample sites*

	Mile²	Km²	Acres	Percent of total	No. of sites
Atlantic City	67.1	173.9	42 944	3	0
Baltimore	309.6	802.5	198 144	13	2
Newport News—Hampton.	143.3	371.4	91 712	6	1
Norfolk—Portsmouth.	299.0	775.0	191 360	12	2
Petersburg—Colonial Heights.	42.4	109.9	27 136	2	0
Philadelphia	751.8	1948.7	481 152	31	5
Richmond	144.6	374.8	92 544	6	1
Vineland—Millville.	85.3	221.1	54 592	3	0
Washington, D.C.	494.5	1281.7	316 480	20	3
Wilmington	109.8	284.5	70 272	4	1
Total	2447.4	6343.6	1 566 336	100	15

[1] Source: U.S. Bureau of the Census, 1972.

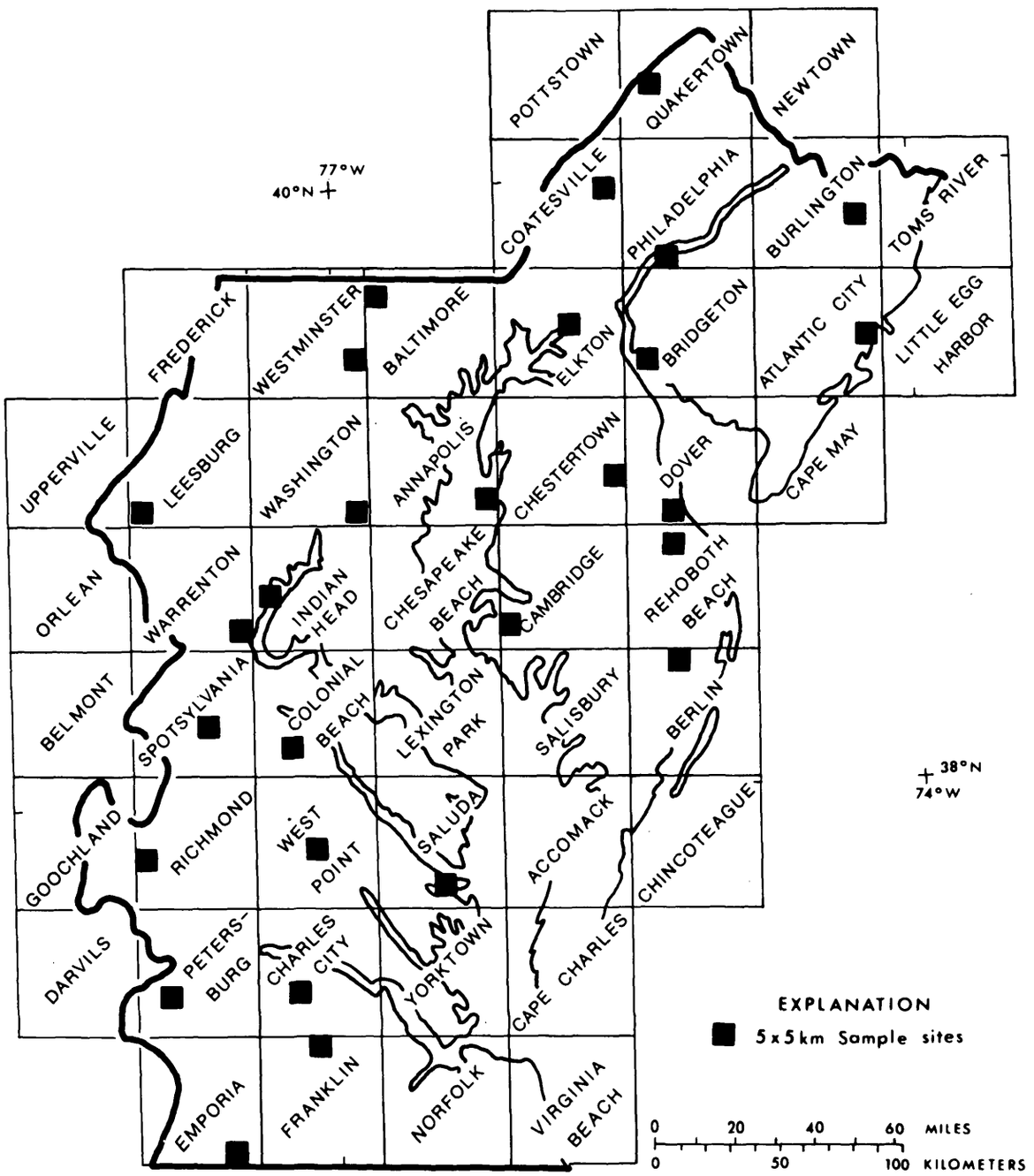

FIGURE 1.—Locations of 5×5-km sample sites within non-urban areas of the CARETS, and index to the 48 1:100 000-scale photomosaics.

CARETS urbanized area, were distributed among urbanized areas according to the ratio of each urbanized area to the total. Within each urbanized area the sample sites were chosen using a 2-km UTM grid cell overlay and a random number table. As before, sites falling more than 50 percent outside the area were discarded; however, those on the boundaries were retained in order to include the urban-rural fringe in the sample.

A total of 760 km² (700 non-urban and 60 urban) thus was selected to evaluate the 74 712-km² area of the CARETS region. Figure 1 shows the locations of the non-urban sample sites, and figure 2 shows the locations of the urban sample sites.

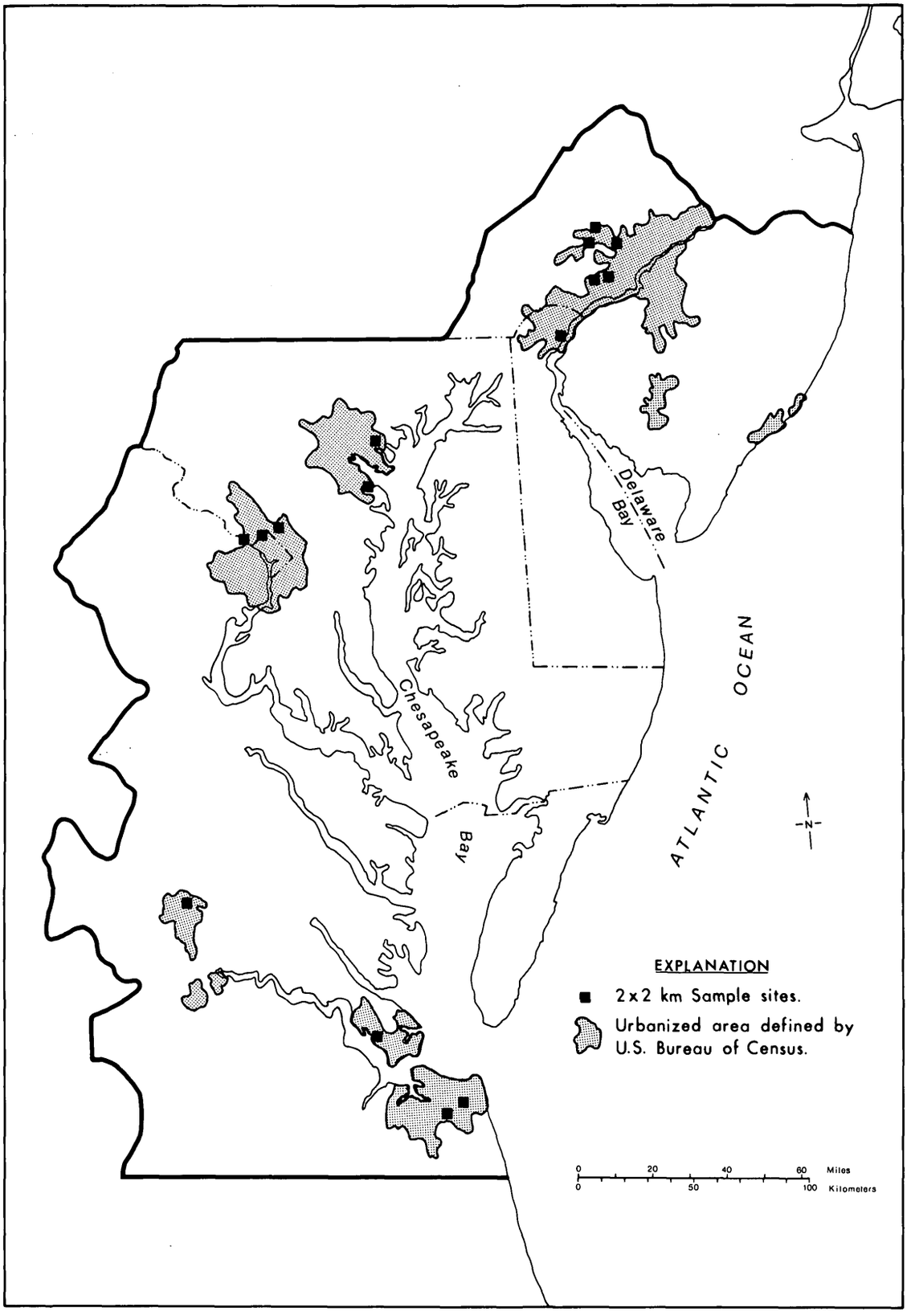

FIGURE 2.—Location of 2×2-km sample sites within urban areas.

It is neccessary to have a method of selecting an appropriate sample size to validate the experimental inference or the accuracy determination. One such selection method is presented by Natrella (1963). In accordance with this method, the 760-point sample size will allow estimation of the standard deviation within 5 percent of its true value with confidence coefficient of 0.95.

Methods of Deriving Accuracy Measures of Land Use and Land Cover Data

For each of the sampling sites, three methods for determining accuracy were developed. The first involved the measurement and tabulation of the area of each land use and land cover category at each scale mapped. Assuming that the most nearly correct land use and land cover map is the one prepared at the largest scale and with the smallest minimum mapping unit, one can then attempt to determine the reduction of accuracy resulting from reduced resolution and areal aggregation at the smaller scales. In some cases it also was possible to identify land use categories that had been most frequently misinterpreted and therefore had little or no reliability.

A second procedure involved determining Level II land use and land cover at the center of each kilometer square. A grid of evenly spaced points, representing the center of each 1-km cell was superimposed on the land use map at each sample site to locate the points of land use and land cover to be identified. Land use and land cover, identified by direct observation of these points from a low-flying aircraft, was compared to the land use and land cover of the same points interpreted from the high-altitude photography and mapped at three scales: 1:250 000, 1:100 000, and 1:24 000. In this way the accuracy of interpretations of the aerial photographs could be checked.

Accuracy percentages of the Level 1 interpretations at 1:250 000, from both high-altitude photographs and and Landsat multispectral imagery were also determined by comparing the interpretations to the field points. These accuracy figures for the two Level I land use and land cover maps were also compared

RESEARCH PROCEDURES

Area Comparisons from Larger to Smaller Scales

Each sample site was masked off on the Landsat multispectral imagery, on the high-altitude photographs, on the Level I land use and land cover maps at 1:250 000 scale, and on the Level II land use and land cover maps at 1:100 000 scale. Level II land use and land cover maps of the sample sites were then prepared by using an enlarged image of the photographs at a scale 1:24 000 for remapping. Level II maps at 1:250 000 scale were prepared by transferring data from the 1:120 000 scale high-altitude photographs to a reduced photomosaic base.

The dot planimeter, which has been found to be an accurate tool for manual measurement of small areas such at those on the CARETS land use and land cover maps (Yuill, 1970), was used to determine the area for each land use and land cover within the sample sites mapped The dot planimeter is basically a uniform grid of dots. Each dot represents a portion of the area of the cell in which it is located. Researchers measured areas on the polygon map by laying the grid on the map and counting the number of dots within the polygon and every other dot on the boundary between polygons. They then converted the number of dots counted to an equivalent ground measure by multiplying this number by a conversion factor determined by the scale of the map being measured.

An identical dot grid having 25 dots per square centimeter was used at all three mapping scales. A single dot thus represented 4 mm^2. This unit was the size of the smallest land use and land cover polygon identified at each scale. At a scale of 1:24 000, each dot or 4 mm^2 area represented 0.23 ha (hectares); at a scale of 1:100 000, each dot represented 4 ha; and at a scale of 1:250 000, each dot represented 25 ha.

The total area of each non-urban site was 25 km^2 and of each urban site, 4 km^2. When the sum of polygon measurements for a sample site deviated by more than 2 percent from the total area, the areas were remeasured. The small discrepancies that did occur are believed to be the cumulative errors resulting from the occasional miscount of dots, errors in outlining a 5×5-km square, and errors resulting from the use of dot grids made on a nonstable base material.

Areas of each land use and land cover were tabulated for each scale map (1:24 000, 1:100 000, and 1:250 000). The tables listing the area for each of the sample sites were summed to give a single tabulation for all the sample sites. Next, tabular summaries were prepared to compare the land use and land cover data at the different scales and to show the effect of generalization from larger scales to smaller scales. Table 5 is one such summary comparing the area in each land use category at 1:24 000, 1:100 000 and 1:250 000 as mapped from the high-altitude photographs. Table 6 gives an indication, at the scale of 1:250 000, of the effects of the reduced resolution of Landsat multispectral imagery in comparison to the high-altitude photographs. The actual measurements obtained were adjusted to total 76 000 ha to compensate for errors

TABLE 5.—*Comparison of area, in hectares, for various categories of land use and land cover at three scales from high-altitude photographs*

	Land use and land cover code	Mapping scale		
		1:24 000	1:100 000	1:250 000
Urban and built-up				
Residential	11	4 069	3 441	4 950
Commercial and services	12	340	464	300
Industrial	13	38	48	
Extractive	14	33	112	
Transportation, etc	15	259	132	225
Institutional	16	961	1 289	875
Strip and clustered	17	60	48	
Mixed	18	-----	16	
Open and other	19	409	400	325
Subtotal	1	6 169	5 950	6 675
Agricultural				
Cropland and pasture	21	21 544	23 156	23 875
Orchards, etc	22	10	404	
Other	24	95	92	
Subtotal	2	21 649	23 652	23 875
Forest land				
Heavy crown cover	41	33 740	31 550	30 950
Light crown cover	42	1 217	1 906	1 900
Subtotal	4	34 957	33 456	32 850
Water				
Streams and waterways	51	334	404	75
Lakes	52	-----	108	
Reservoirs	53	224	92	125
Bays and estuaries	53	9 316	9 150	8 850
Subtotal	5	9 874	9 754	9 050
Nonforested wetland				
Vegetated	61	3 273	3 088	3 500
Subtotal	6	3 273	3 088	3 500
Barren land				
Sand other than beaches	72	6	-----	
Beaches	74	10	-----	
Other	75	62	100	50
Subtotal	7	78	100	50
Total	--	76 000	76 000	76 000

TABLE 6.—*Comparison of area, in hectares, of Level I land use and land cover at 1:250 000 scale compiled from high-altitude photographs and Landsat multispectral imagery*

	Land-use and land cover code	From aerial photographs	From Landsat multispectral imagery
Urban and built-up	1	6 675	4 109
Agricultural	2	23 875	24 154
Forest land	4	32 850	35 432
Water	5	9 050	9 687
Nonforested wetland	6	3 500	2 618
Barren land	7	50	0
Total	------	76 000	76 000

in manual processing, necessarily less than 2 percent as described above.

Referring to table 5, one can calculate the total area at each scale that differs in land use and land cover classification from the next larger scale. By assuming that the land use and land cover is correctly mapped within the limitations of the minimum mapping unit for each scale, one can then consider that the discrepancy in area among three scales is due to generalizing the land use and land cover mapped to the smallest mapping unit for each scale. This discrepancy value of the area may then be expressed as a percentage of the total area mapped.

For instance, the difference between category 11 at 1:24 000 and 1:100 000 is 628 ha (4069–3441 ha) and for category 12 this difference is −124 ha (340–464 ha). Only the absolute value of the difference is important here; whether the difference is an increase or decrease is irrelevant. An absolute summation of these differences (that is, disregarding the sign) for categories 11 through 19 would give the total area in the urban category mapped differently at 1:24 000 and 1:100 000. By continuing this summation through all 22 Level II land use and land cover categories mapped, one would obtain the total area on both maps of differences in classification between the two scales. To calculate the total area on only one of these two maps, it is necessary to divide the total by 2.

The equation for this calculation of the area of difference between maps at two scales is:

$$\sum_{i=1}^{22} \frac{|h_{i1} - h_{i2}|}{2} \qquad (1)$$

Where h_{i1} = hectares of land use i at one scale,
h_{i2} = hectares of land use i at the next scale,
and 22 = the number of land use categories mapped.

Therefore the difference due to generalization between 1:24 000 and 1:100 000 is 3468 ha or 5 percent of the 76 000 total hectares measured. The difference due to generalization between 1:100 000 and 1:250 000, is 2766 ha or 4 percent of the 76 000 total hectares measured. Notice, however, that the percent of difference is not cumulative; some of the differences due to generalization in proceeding from 1:100 000 to 1:250 000 cancel out differences that arise in generalization from 1:24 000 to 1:100 000. In consequence, the difference due to generalization between 1:24 000 and 1:250 000 is 4122 ha or 5 percent of the 76 000 total hectares measured.

One of the major land use and land cover categories that was not mapped consistently is urban land. At 1:24 000 small parcels of built-up land may be distinguishable, whereas at 1:100 000, many of the smaller parcels are aggregated into the background of other uses, resulting in a lower total. At 1:250 000, parcels of agricultural and forest land within and at the periphery of the urban setting are mapped as urban residential, accounting for the total greater than at the larger scales.

The main cause of the discrepancies in the assignments of areas to urban land is the visual appearance of residential land on the photographs at the various scales. At 1:24 000, residential land appears as a cluster of individual homesteads, excluding the surrounding land. At 1:100 000, residential developments,

as well as linear residential settlements, are discernable on the photographs. At this scale, clusters of residential lots are seldom separated from agricultural land, resulting in the significant decrease in area mapped as residential. At 1:250 000, several tracts of urban developments merge to form a single land use and land cover including much land that would be interpreted as forest or agricultural land, and so mapped at a larger scale.

As scale decreased, the area mapped as agricultural land increased, and the area mapped as forest land decreased. This indicates that an increase in the area on the ground mapped as a 2×2-mm polygon allows fewer small forest patches (and small patches of all other uses) to be mapped, resulting in their inclusion in the surrounding agricultural or urban categories.

The area of difference between Level I land use and land cover maps at 1:250 000 scale mapped from high-altitude photographs and Landsat multispectral imagery is 3498 ha by the formula:

$$\sum_{i=1}^{6} \left| \frac{h_{i3} - h_{i4}}{2} \right| \qquad (2)$$

Where h_{i3} = hectares of land use and land cover i mapped at 1:250 000 scale from high-altitude photographs,

h_{i4} = hectares of land use and land cover i mapped at 1:250 000 scale from Landsat multispectral imagery.

and 6 = the number of land use and land cover categories mapped.

From table 6, it is apparent that the percentage of area mapped differently from the two sources is 3498 divided by 76 000 or 5 percent. This generalization could be the result of sensor resolution differences rather than mapping scale differences as in the previous comparison because, in this case, the maps are at the same scale.

The above values for the percentage difference between the three scales and betwen the two types of images should be viewed with reservations. This analysis is empirical and presents no statistical tests of the observations. The statistical technique, analysis of variance, did not furnish valid results using the area data. Further research would be needed to validate geographical analysis based upon areal data.

One of the land use and land cover categories in which the interpretation of Landsat multispectral imagery differed noticably from the interpretation of high-altitude photographs was urban land: 1556 ha of built-up land as interpreted from high-altitude photographs were mapped as cropland and pasture or forestland using Landsat multispectral imagery. In the urbanized areas, urban land was more readily identified from the Landsat multispectral imagery, indicating that where the settlement pattern is dense the signature is distinct. The Landsat false-color composite images do not reveal the distinction between dispersed settlement and dissected agricultural patterns at the periphery of the urbanized areas because of the predominant vegetative response in the near-infrared wavelengths. Likewise, the Landsat multispectral sensor response for heavily wooded residential areas is nearly identical to that for forest.

In numerous instances, particularly in wetland areas, either totally or partially submerged, nonforested wetlands were mapped as water. This condition seems most likely attributable to the opaqueness of water in the infrared wavelengths.

Comparison with Field Data

An additional measure of accuracy was obtained by comparing the Level II land use or land cover obtained from the high-altitude photographs at the center of each 1-km grid for each site at the three scales, 1:24 000, 1:100 000, and 1:250 000 with observation of land use and land cover at the same points in the field.

A 1-km grid cell overlay was prepared for each sample site for each scale of land use and land cover map and the center of each cell marked by a dot. When this overlay was registered to the land use and land cover map, the land use or land cover at each point was tabulated on a computer coding sheet having a separate column for the land use and land cover at each scale of map. The field observations were made from a low-flying aircraft. The 25 points to be identified were plotted on a topographic map and the land use and land cover was recorded on this map as the plane passed over the field points. If there were any obvious differences between the patterns seen in the field and those on the map, the field researcher would look for signs of recent change and note it on the topographic map. It was not possible to conduct field interviews to determine if change had occurred since 1972, and so only the rather obvious changes were noted. No estimate of the total amount of change that had occurred is possible. However, based on field observation it is concluded that any such change was insignificant.

Figure 3 is an example of the field points of the Dover site, one of the 28 non-urban sites chosen. The field-determined land use and land cover then was entered in its column on the coding sheet. The tabulation of land use and land cover for the Dover site is given in table 7. Figures 4, 5, and 6 matrices com-

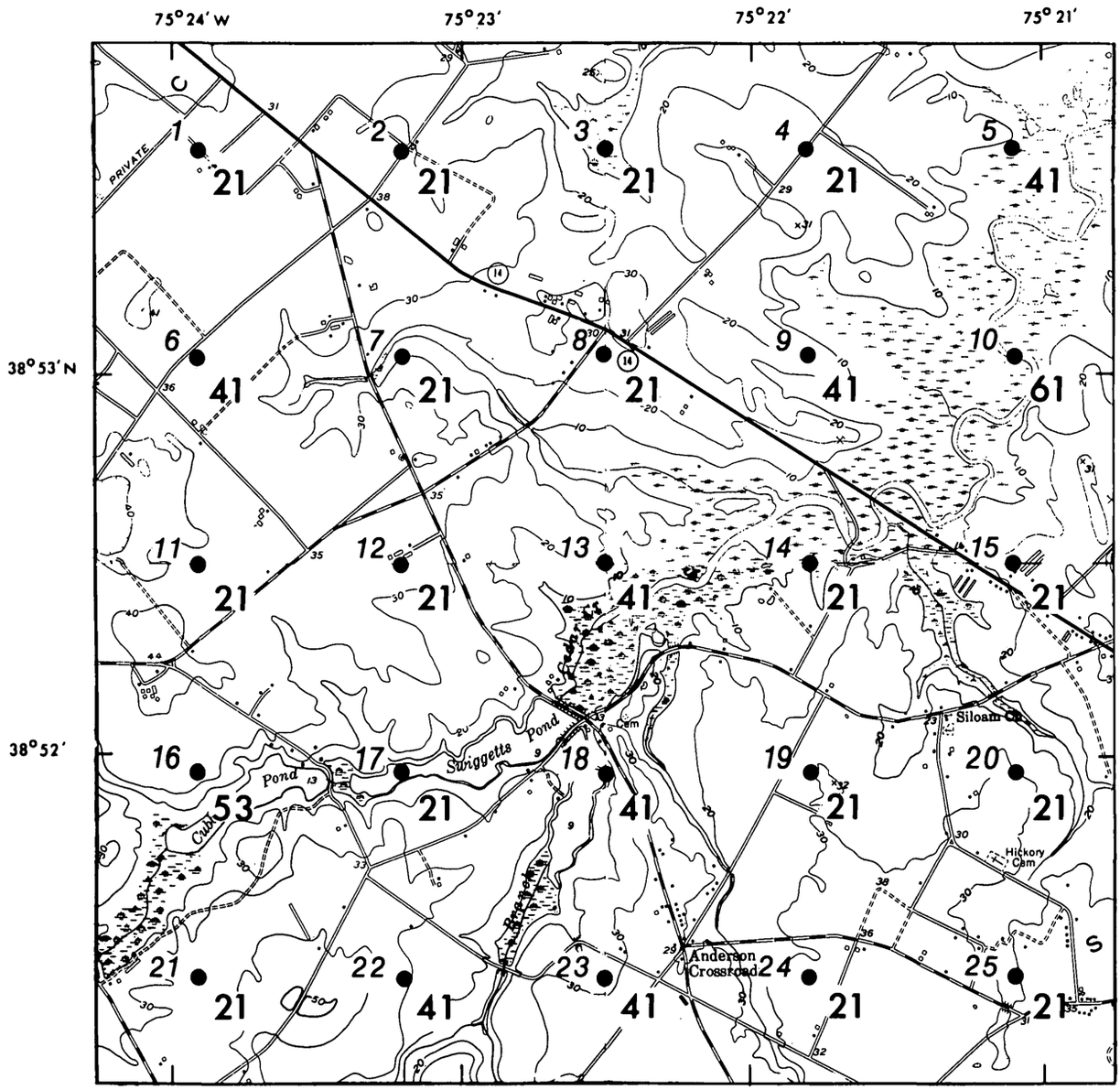

FIGURE 3.—Center points of 1-km grid cells plotted on the 1:24 000-scale topographic map labeled with the observed land use and land cover for the Dover site.

TABLE 7.—*Land use and land cover categories identified at field points and on land use maps of various scales for the Dover site*

Point	Field observation	1:24 000 map from aerial photographs	1:100 000 map from aerial photographs	1:250 000 from aerial photographs	1:250 000 map from Landsat multispectral imagery
1	21	21	21	21	2
2	21	21	21	21	2
3	21	21	41	21	2
4	21	21	21	21	4
5	41	41	41	41	6
6	41	21	41	21	2
7	21	21	21	21	2
8	21	21	21	41	4
9	41	41	41	41	4
10	61	41	61	21	2
11	21	21	21	21	2
12	21	21	21	21	2
13	41	41	41	41	4
14	21	21	21	21	2
15	21	21	21	21	2
16	53	54	53	21	2
17	21	21	41	21	2
18	41	41	21	21	2
19	21	21	21	21	2
20	21	21	21	21	2
21	21	21	21	21	2
22	41	21	21	41	4
23	41	21	41	41	2
24	41	21	21	21	2
25	21	21	21	21	2

pare the field-determined land use and land cover with the classification at each scale as determined from photographs and Landsat multispectral imagery for the 15 urban and 28 non-urban sample sites for a total of 760 points for Level II.

Results of Comparisons at Level II

Figures 4, 5, and 6 reveal that the predominant Level II land uses are mapped with a higher degree of accuracy than those occurring less frequently. By comparing the number of correct occurrences of a given category with the number of field-identified occurrences of that category, one can determine the corresponding percent of accuracy. This can be drawn from the tables by dividing the number of points for each category along the diagonal by the total number of points at the base of each column. Specifically in the case of the land use and land cover map at 1:100 000 scale, the accuracies of the four major land use and land cover categories, residential land (11), cropland and pasture (21), heavy crown cover forest (41), and bays and estuaries (54) are 75 percent, 84 percent, 80 percent, and 90 percent, respectively (see table 8 for development). The greatest accuracy at this scale is in the bays and estuaries category (54), where the photographic signature is easy to delineate. The least accurate of the four major land use categories, residential land (11), is also the category with the most complex signatures.

TABLE 8.—*Accuracies of separate Level II land use and land cover categories at 1:100 000 scale*

Category	Total number of points	Correct	
		Number correct	Percent correct
11	51	38	75
21	214	179	84
41	316	253	80
54	89	80	90

As can be seen from table 9, the accuracy percentage is highest at a scale of 1:24 000 and appears to decrease as the scale decreases. The overall accuracy is 85 percent at 1:24 000, 77 percent at 1:100 000, and 73 percent at 1:250 000. For three land use categories specific interpretation difficulties occur at all three scales. Residential land (11) is often interpreted as cropland and pasture (21) or heavy crown cover forest (41). Light crown cover forest (42), the most inaccurately interpreted land use type, is often interpreted as either heavy crown cover forest (42) or cropland and pasture (21). Nonforested wetland (61) is frequently incorrectly mapped as heavy crown cover forest (41), bays and estuaries (54), or as some other land use and land cover types on high-altitude photographs.

Residential land (11) was misclassified as cropland and pasture (21) or heavy crown cover forest (41) for 20 percent of the points at 1:24 000, 19 percent at 1:100 000, and 35 percent at 1:250 000. In the rural areas this may be due to the tendency to see the area being mapped in terms of the general background land use and land cover type (a hypothesis that could be tested by comparing the location of the errors within the overall CARETS map).

Category 42, light crown cover forest, is a poorly defined land use category, and as borne out by the field verification statistics, it is rarely mapped correctly. Light crown cover forest includes all transition stages of forest from brushland to a 40-percent crown forest and is therefore difficult to define and identify. It is best to consider category 42 on the land use and land cover CARETS maps as Level I Forest, especially since the category of light crown cover forest has been dropped from the classification system.

TABLE 9.—*Comparison of land use and land cover identification accuracy at three scales — 1:24 000, 1:100 000, and 1:250 000*

Scale	Total number of points	Correct	
		Number	Percent
1:24 000	760	645	85
1:100 000	760	588	77
1:250 000	760	555	73

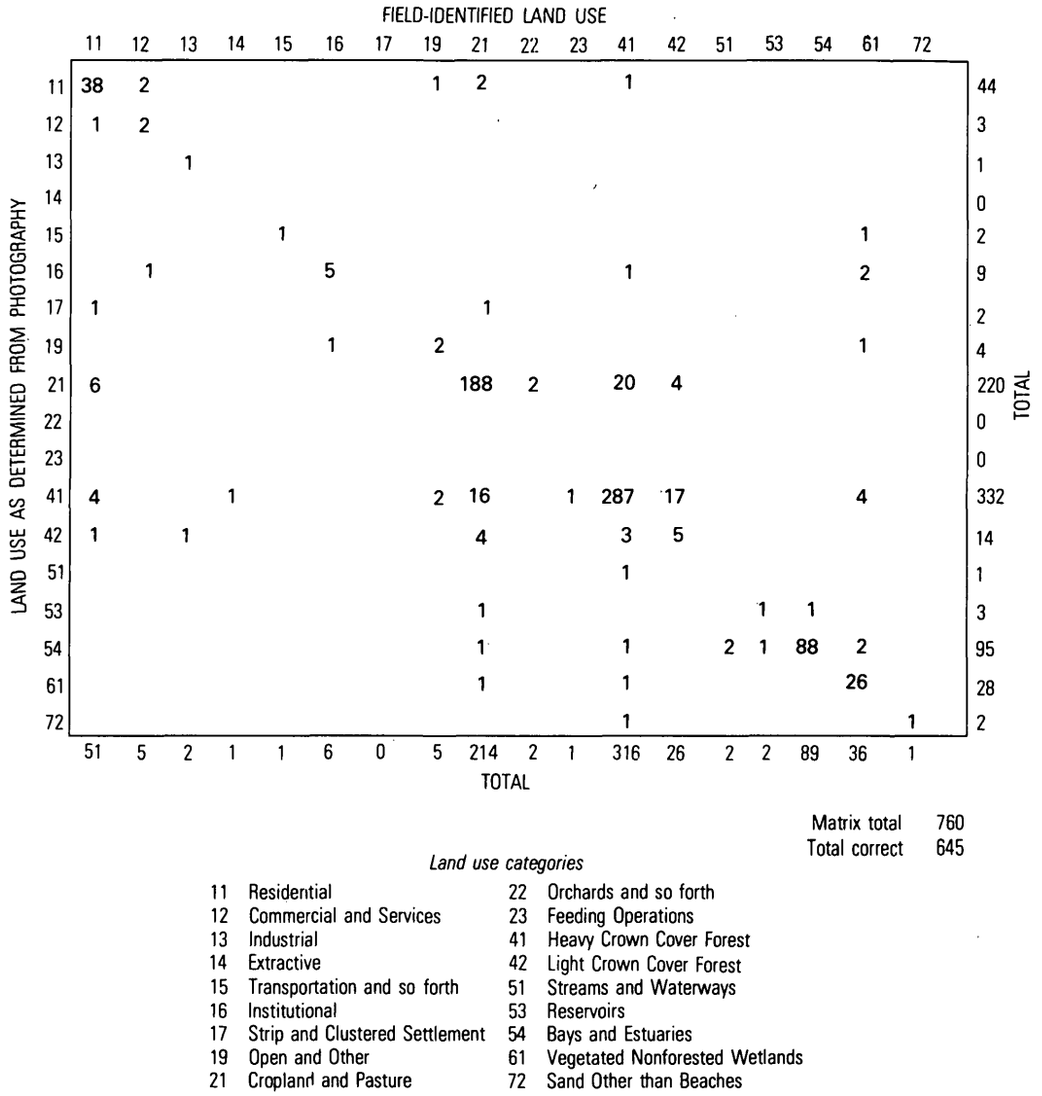

FIGURE 4.—Matrix comparing field-identified land use and land cover with that determined from high-altitude photographs enlarged to 1:24 000 scale, mapped at 1:24 000 scale.

Category 61, vegetated nonforested wetlands, is frequently confused with adjacent land use categories, such as bays and estuaries (54), or heavy crown cover forest (41). Nonforested wetlands are often subject to tidal fluctuations and change their appearance daily and seasonally. To utilize high-altitude color-infrared photographs properly in mapping wetlands, seasonal coverage should be obtained. It is reasonable to question whether the large decrease in accuracy for the wetland category at all three scales is entirely due to errors of misclassification. For a land use category such as wetland, subject to any periodic or seasonal variations, the conditions observed in the field at a later date could be inconsistent with the conditions noticeable on the source material. Therefore, field data should be collected at the time of data acquisition.

The overall accuracy of the Level I land use maps from the maps at the three scales is plotted by the land use categories in figure 7. Generally, it appears that the accuracy decreases as the scale decreases. Exceptions to this trend, however, can be singled out from figure 7. For instance, nonforested wetlands are mapped most accurately at scales of 1:24 000 and 1:250 000. Urban and built-up land is below the average accuracy at a scale of 1:250 000 and is most accurately mapped at a scale of 1:100 000. These exceptions to the general trend are the result of only one or two sample points and show the 1:100 000 scale to be neither significantly more accurate for urban land nor significantly less accurate for the nonforested category.

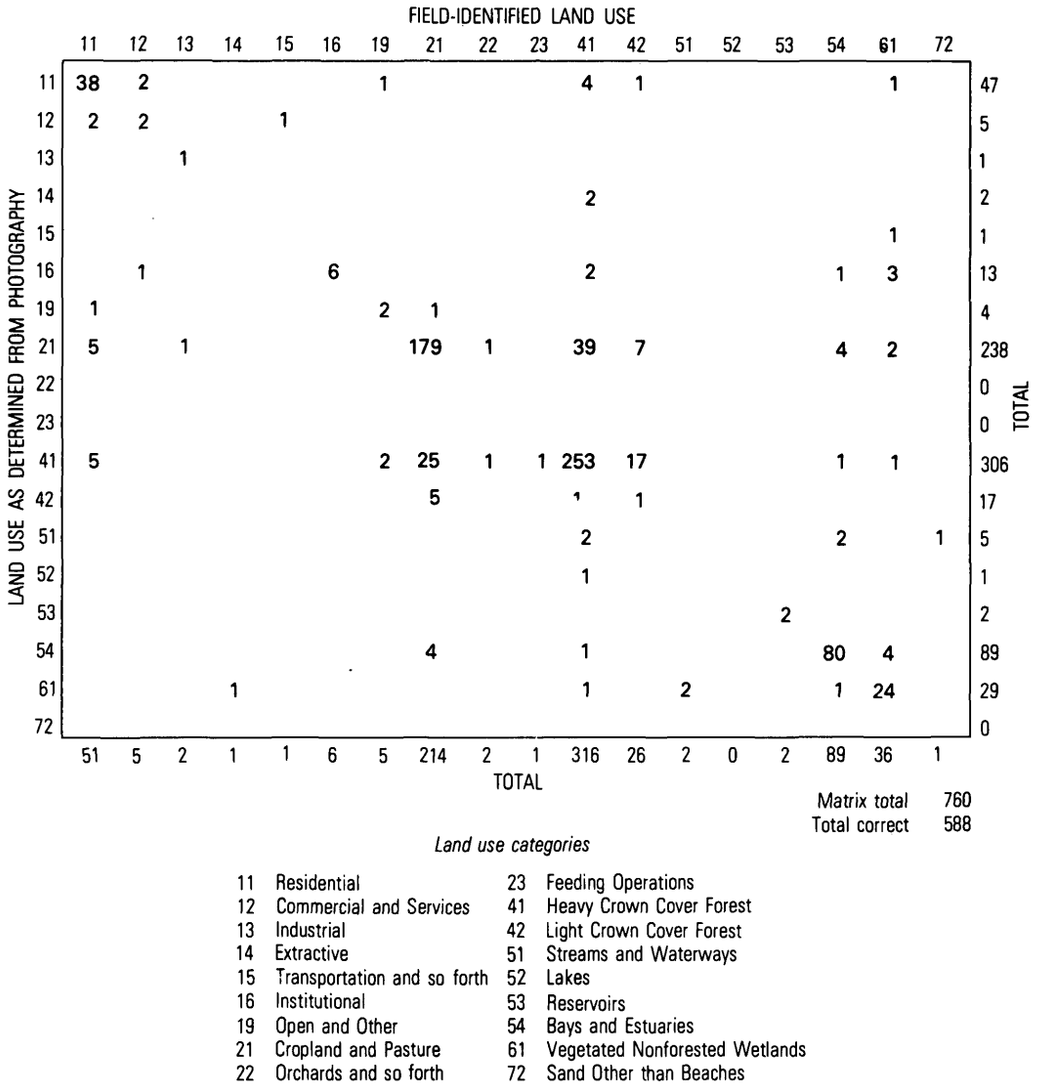

FIGURE 5.—Matrix comparing field-identified land use and land cover determined from high-altitude photographs at compilation scale of 1:120 000, mapped at 1:100 000 scale.

These data for overall accuracy among the three scales should be regarded with reservation. A further analysis of the data was performed using the method of two-way analysis of variance with one observation per cell. The variables of scale were used as the other factor. The analysis of variance indicated that there was no statistically significant difference at the 0.95 percent confidence level between the data at the three scales, when considering differences due to classes and differences due to changes in scale.

Test for statistical significance

Using a two-way analysis of variance, the results of the above accuracy comparison were analyzed for significant differences either between scales or between categories of land use. For this analysis of variance the proportion of points in agreement are transformed using $\theta = \arcsin \sqrt{p}$, where p is the percent of points in agreement. This makes the distribution of percentages more nearly normal by stretching the tails of the distribution and compressing the middle. The null hypothesis is that the population of percentages is the same among the three scales and the land use categories. The analysis of variance was run using data from all categories except those having only one or two points in either Level I or Level II. The results showed with a 95-percent level of confidence that there was no significant difference between the data at the three scales for both Level I and Level II land use. At Level II only, was there a significant difference in the variance between land use categories.

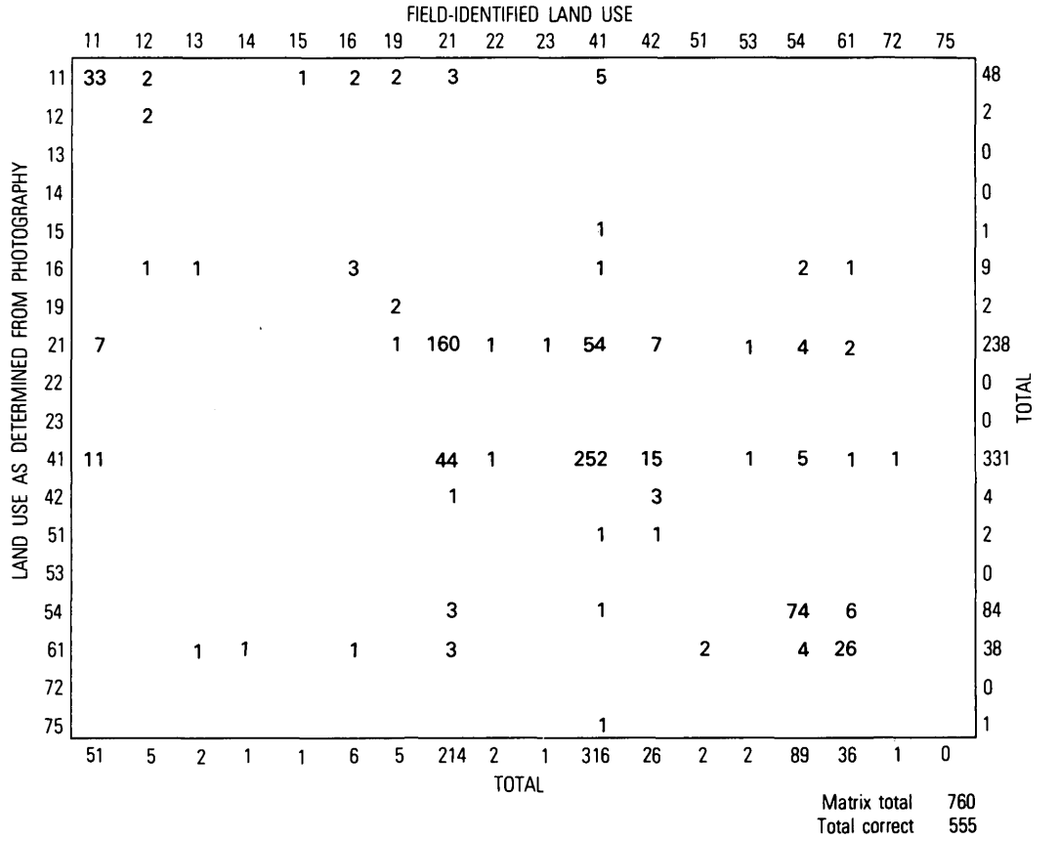

FIGURE 6.—Matrix comparing field-identified land use and land cover determined from high altitude photographs at compilation scale of 1:120 000 mapped at 1:250 000 scale.

The input data for the analysis of variance of Level II data at three scales, excluding those categories with only one or two points, is as follows:

Land use code	No. of pts.	Map scale 1:24 000 No. agreed	Per-cent	arc-sin $\sqrt{p}$	1:100 000 No. agreed	Per-cent	arc-sin $\sqrt{p}$	1:250 000 No. agreed	Per-cent	arc-sin $\sqrt{p}$
11	51	38	74.5	59.67	38	74.5	59.67	33	64.7	53.55
12	5	2	40.0	39.23	2	40.0	39.23	2	40.0	39.23
16	6	5	83.3	65.88	6	100.0	90.00	3	50.0	45.0
19	5	2	40.0	39.23	2	40.0	39.23	2	40.0	39.23
21	214	188	87.9	69.64	179	83.6	66.11	160	74.8	59.87
41	316	287	90.8	72.34	253	80.1	63.51	252	79.7	63.22
42	26	5	19.2	25.99	1	3.8	11.24	3	11.5	19.82
54	89	88	98.9	83.98	80	89.9	71.47	74	83.1	65.73
61	36	26	72.2	58.18	24	66.7	54.76	26	72.2	58.18

The summary of the results of the two-tailed analysis of variance of the arcsin $\sqrt{p}$ values of the above Level II land use data is as follows:

Source	Degrees of freedom	Sum of the squares	Mean square	F
A (9 categories)	8	7552.955	944.119	13.257
B (3 scales)	2	294.162	147.081	2.065
Error	16	1139.466	71.216	
Total	26	8986.583		

With $\alpha = 0.05$ in the two-tailed test:
A = $F[8, 16] = 3.12$. Difference among categories is significant.
B = $F[2, 16] = 4.69$. Difference among scales is not significant.

The input data for the analysis of variance of the Level I land use at three scales is as follows:

Land use code	No. of pts.	Map scale 1:24 000 No. agreed	Per-cent	arc-sin $\sqrt{p}$	1:100 000 No. agreed	Per-cent	arc-sin $\sqrt{p}$	1:250 000 No. agreed	Per-cent	arc-sin $\sqrt{p}$
1	71	56	78.9	62.65	57	80.3	63.65	49	69.0	56.17
2	217	190	87.6	69.38	180	82.9	65.57	162	74.7	59.80
4	342	312	91.2	72.74	282	82.5	65.27	270	78.9	62.65
5	93	93	100.0	90.00	84	90.3	71.85	74	79.6	63.15
6	36	26	72.2	58.18	24	66.7	54.76	26	72.2	58.18

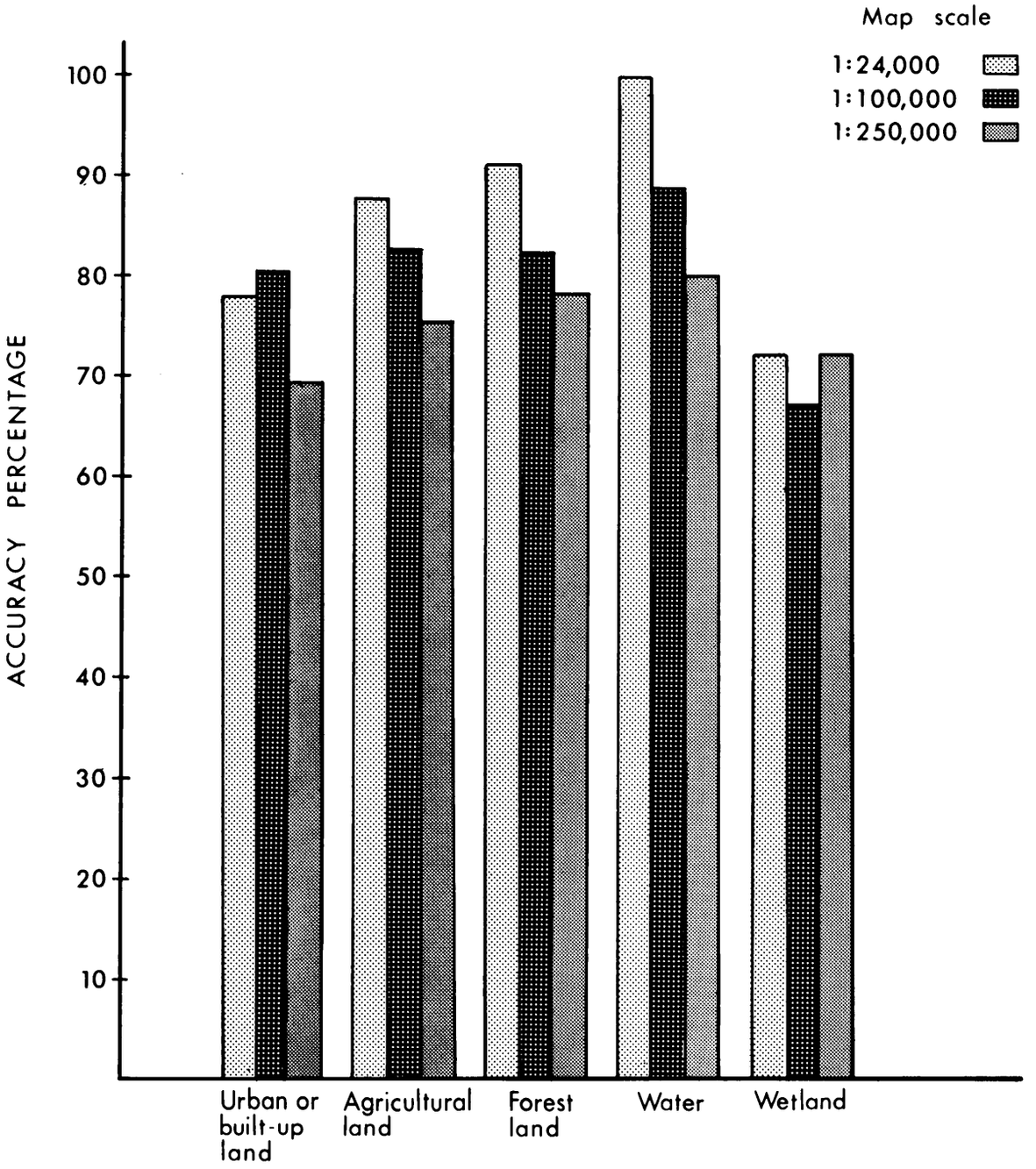

FIGURE 7.—A comparison of the accuracy of Level I land use and land cover interpretations derived from aerial photographs for each land use category at three scales. Percentages derived from field check.

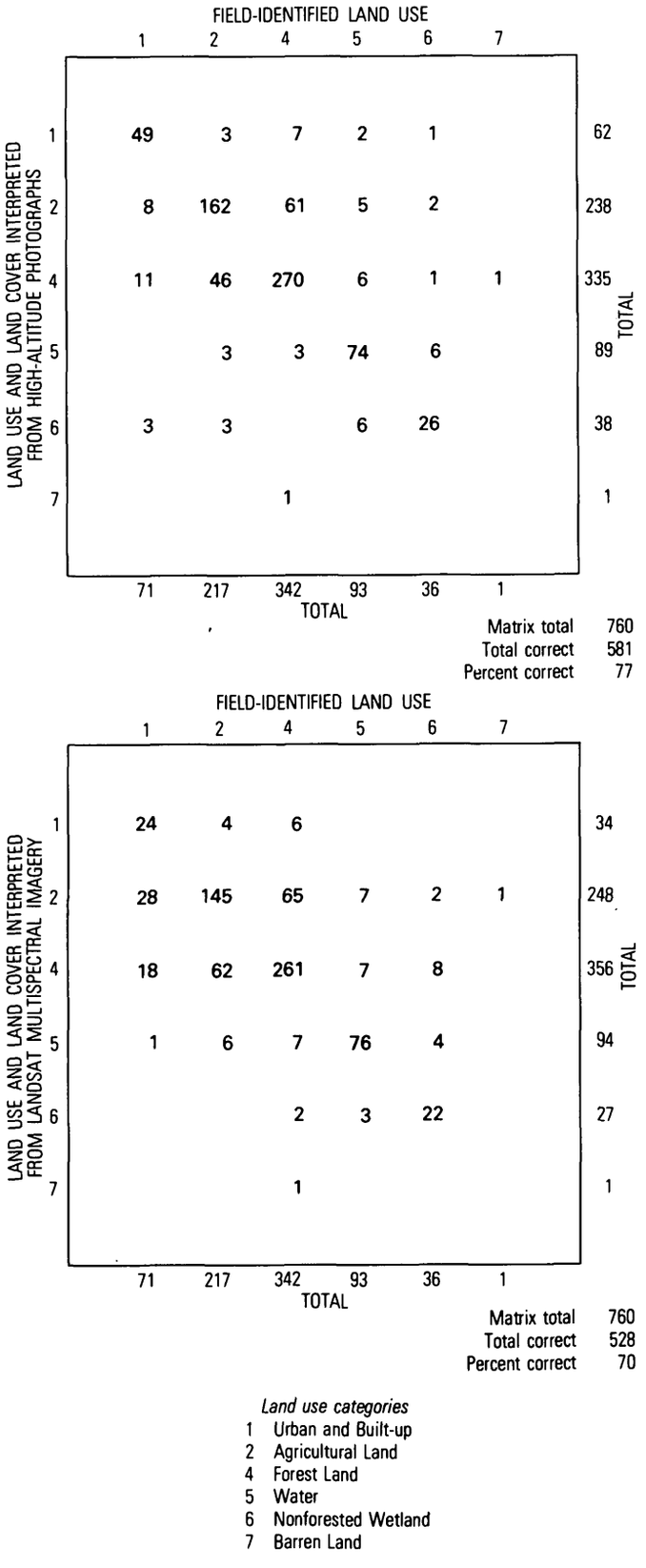

FIGURE 8.—Matrices of land use and land cover identified in the field and mapped at 1:250 000 scale from high-altitude photographs and Landsat multispectral imagery.

The summary of the results of the two-tailed analysis of variance of the arcsin $\sqrt{p}$ values of the above Level I land use data is as follows:

Source	Degrees of freedom	Sum of the squares	Mean square	F
A (5 categories)	4	553.051	138.262	4.752
B (3 scales)	2	284.716	142.358	4.892
Error	8	232.759	29.094	
Total	14	1070.526		

Where $\alpha = 0.05$ in the two-tailed test:
$A = F[4, 8] = 5.05$. Difference among categories is not significant.
$B = F[2, 8] = 6.06$. Difference among scales is not significant.

Comparison of 1:250 000-Scale Land Use and Land Cover Maps Derived from Landsat Multispectral Imagery and High-Altitude Photographs

The accuracy of Level I land use and land cover identified on high-altitude photographs and mapped at 1:250 000 scale was compared with the accuracy of the Level I land use mapped from the Landsat multispectral imagery at 1:250 000 scale. The Level I land use at the center points of each 1-km cell within each sample site was identified on the map produced from multispectral imagery and entered in a separate column on the computer coding sheets. It was then possibly to generate matrices by computer, comparing the Level I land use identified on each map at a scale of 1:250 000 with the field data. Figure 8 shows the matrix of data obtained for all the field sites.

The overall accuracy of the multispectral imagery derived land use and land cover maps was found to be 70 percent as compared to 77 percent accuracy for the maps at a scale of 1:250 000 derived from high-altitude photographs. The major discrepancy between the two maps was in the identification of urban land (1). The accuracy of land use and land cover mapped from multispectral imagery and high-altitude photographs at 1:250 000 are compared in figure 9.

The two-way analysis of variance used to analyze these data indicated that there was no statistically significant difference at the 0.95-percent confidence level between the two sources.

Test for statistical significance

The two-way analysis of variance of Level I land use from high-altitude photographs and Landsat multispectral imagery showed no significant difference between either source material or between land use categories. The input data for the analysis of variance is as follows:

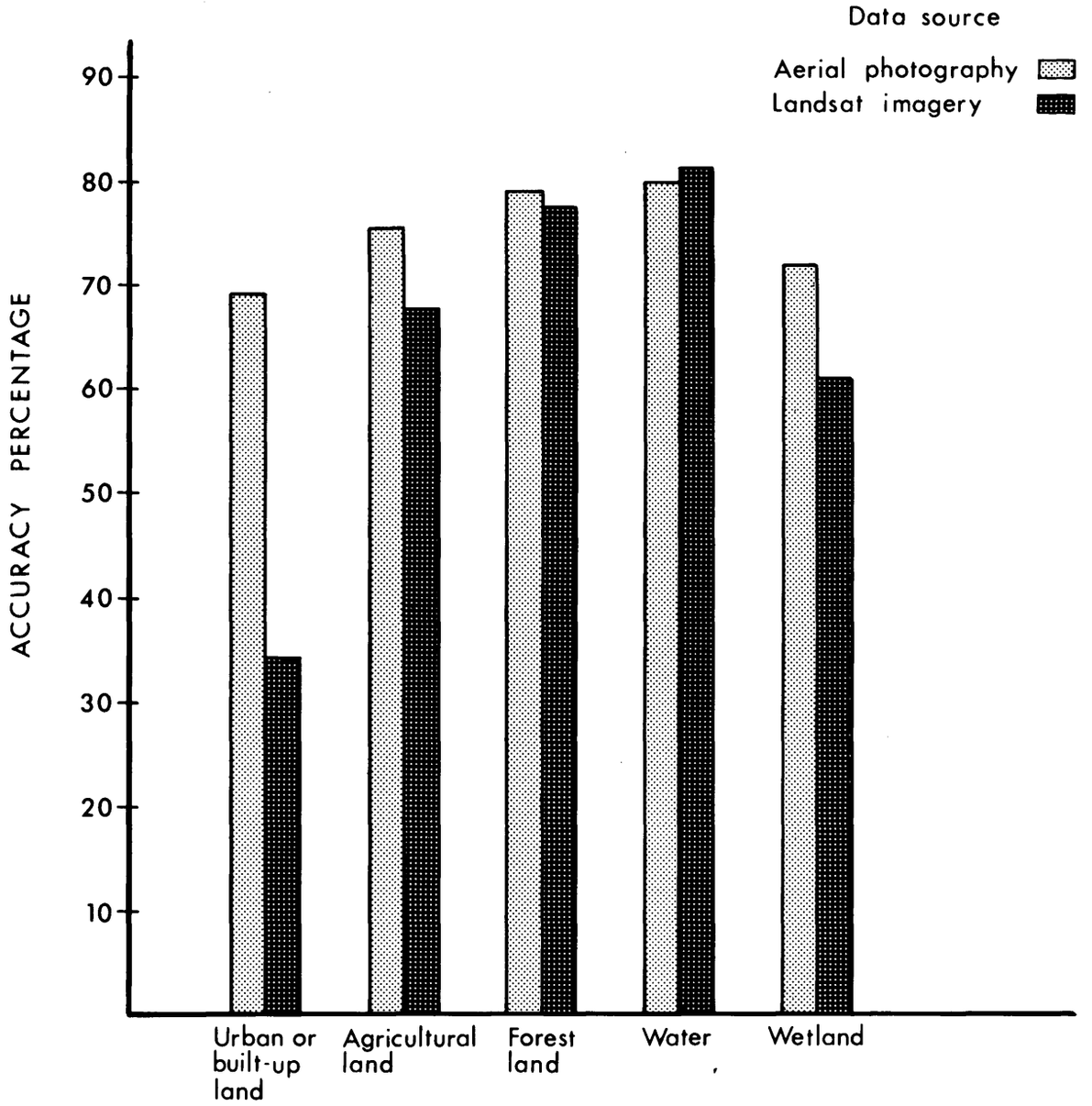

FIGURE 9.—A comparison of the accuracy of land use and land cover interpretations for each Level I land use category mapped at a scale of 1:250 000 from Landsat multispectral imagery and high-altitude photographs.

Land use codes	No. of pts.	High-altitude photographs			Landsat multispectral imagery		
		No. agreed	Percent	arc-sin $\sqrt{p}$	No. agreed	Percent	arc-sin $\sqrt{p}$
1 ---	71	49	69.0	56.17	24	33.8	35.55
2 ---	217	162	74.7	59.80	145	65.8	54.21
4 ---	342	270	78.9	62.65	261	76.3	60.87
5 ---	93	74	79.6	63.15	76	81.7	64.67
6 ---	36	26	72.2	58.18	22	61.1	51.41

Source	Degrees of freedom	Sum of the squares	Mean squares	F
A (5 categories ---	4	397.619	99.404	2.773
B (2 sources) ----	1	110.489	110.489	3.082
Error ----------	4	143.382	35.845	
Total --------	9	651.490		

Where $\alpha = 0.05$ in the two-tailed test:

$A = F[4, 4] = 9.60$. Difference between categories is not significant.

$B = F[1, 4] = 12.2$. Difference between high-altitude photographs and Landsat multispectral imagery is not significant.

The summary of the results of analysis of variance of the arcsin $\sqrt{p}$ values of the above Level I land use data is as follows:

Results of Comparison of Level I

The category with the largest apparent discrepancy is the built-up land category. Interpreters were not able to detect any built-up land (1) in the non-urban sample sites using Landsat multispectral imagery. In the field, however, 29 points were identified as built-up land. Using high-altitude photographs, interpreters correctly mapped 17 of these 29 points of built-up land; of those points incorrectly mapped, 6 were mapped as agricultural land, 5 as forest land, and 1 as wetland. Using Landsat multispectral imagery, interpreters misclassified the built-up land as agricultural land in 22 cases, as forest land in 6 cases, and as water in 1 case. In these non-urban areas, the response of a small built-up area on Landsat multispectral imagery is lost in the stronger vegetative response and is mapped as agricultural land. Of these same points identified on high-altitude photographs, 17 were mapped correctly as urban land, and 6 were incorrectly interpreted as agricultural land and 4 as forest land.

Within the urban sample sites, more than half of the points identified as urban during field verification had been classified correctly as urban on the Landsat multispectral imagery (24 of a possible 42, or 57 percent). By comparison, an interpreter, using high-altitude photographs at 1:120 000 scale as source material and mapping on a mosaic base at 1:250 000, identified 32 of a possible 42 points (76 percent) correctly as urban.

Color-composite prints or transparencies of Landsat multispectral imagery show a distinct spectral response for urban areas. Where older residential areas have a predominance of tall trees or residential lots are larger than 0.4 hectare, the vegetative cover dominates, giving a forest or agricultural signature. The forest signature had higher reflectance value than the urban residential signature in the more central urbanized areas, where one would expect older residential neighborhoods. The agricultural signature was predominant at the periphery of the urbanized areas where population density is less and either large estate homes or new residential communities are adjacent to agricultural areas. Occasionally, forest or agricultural land within an urban setting was not identified on the Landsat imagery because of low resolution and the small size of the forest or agricultural parcel.

Color-composite Landsat multispectral imagery is most useful for interpreting forest and water categories, because band 5 shows the greatest contrasts between forest areas and other cover types, and band 7 shows water as an easily interpreted dark signature on the imagery. Where an intermixture of agricultural and forest land occurs, some agricultural land may be mapped as forest since the forest returns the stronger signature. Wetland is often misclassified as water when the land is submerged. In this case both wetland vegetation and water are present and either of these two categories defines only part of the existing conditions. By definition, however, both nonforested wetland and the water categories are mutually exclusive.

CONCLUSIONS

Field verification indicates that three of the four major Level II land use and land cover categories occurring in the CARETS area—cropland and pasture, heavy crown cover forest, and bays and estuaries—were mapped with a high degree of accuracy, using high-altitude photographs. Land use and land cover categories frequently mapped incorrectly from the aerial photographs are commercial land (12) and light crown cover forest (42). These categories have subsequently been removed from the classification system.

Category 12 has been revised to include institutional land use and land cover within the limitation of commercial and services, and a separate land use category was created for commercial and industrial complexes. Category 42, light crown cover forest, was removed from the classification scheme after the CARETS area had been mapped. Even as the mapping was in progress, the definition of light crown cover forest was being modified. Category 42, therefore, cannot be considered a reliable land use category as compiled on the CARETS maps.

Greater accuracy is possible at all scales by deleting category 42, light crown cover forest, from the land use and land cover classification—it was almost never mapped correctly and resulted in 3 percent of the experimental error at each scale. By mapping light crown cover forest as either pasture land or forest land, the accuracy would be increased by 3 percent for each scale.

Category 61, vegetated nonforested wetland, was not mapped as accurately as the other non-urban land use and land cover categories. This could result from the inability of the sensor (either multispectral or photograph) to distinguish consistently the signature of wetland, or, more likely, from seasonal fluctuations so that the water level differed from the time of remote sensing to the time of field verification.

In general, the accuracy of the land use and land cover maps appears to increase as mapping scale increases; however these results must be interpreted with reservations. Comparisons of the area mapped in each category revealed apparent differences only. No

statistically significant differences were found between the data at the three scales of mapping.

The accuracy of 1:250 000 scale Level I maps interpreted from both high altitude photographs and Landsat multispectral imagery was similar in all categories except for urban and built-up land (see fig. 9). Landsat multispectral imagery interpreters detected less Level I urban or built-up land than did the interpreters of high-altitude photographs when mapping at 1:250 000 scale. Of the 760 points sampled there were 24 points of built-up land identified on the maps from Landsat multispectral imagery and 49 identified on the maps from high-altitude photographs, compared to 71 points identified as urban and built-up land in the field. Much of the difference from field data is due to the larger ground mapping unit at 1:250 000.

There was no statistically significant difference between using high-altitude photographs or Landsat imagery for Level I land use and land cover mapping at 1:250 000 scale in non-urban areas. Landsat imagery could provide a reliable Level I land use and land cover map in the non-urban areas. Where urban land uses are mixed with agricultural land or forest land, complementary use of Landsat multispectral imagery and high-altitude photographs would provide the best classification accuracy.

REFERENCES CITED

Anderson, J. R., Hardy, E. E., and Roach, J. T., 1972, A land-use classification system for use with remote sensor data: U.S. Geol. Survey Circ. 671, 16 p.

Anderson, J. R., Hardy, E. E., Roach, J. T., and Witmer, R. E., 1976, A land use and land cover classification system for use with remote sensor data: U.S. Geol. Survey Prof. Paper 964, 28 p.

Berry, B. J. L., and Baker, A. M., 1968, Geographic sampling, *in* Berry, Brian J. L., and Marble, Duane F., eds., Spatial analysis—a reader in statistical geography: Englewood Cliffs, N. J., Prentice Hall, p. 91–100.

Fitzpatrick, K. A., 1975, Cost, accuracy and consistency comparison of land use maps made from high-altitude aircraft photography and ERTS imagery: Natl. Aeronautics and Space Admin., Goddard Space Flight Center, Type III final rept. for ERTS–1 investigation SR–125, v. 7, p. 61.

Natrella, M. G., 1963, Experimental Statistics: National Bureau of Standards Handbook 91, p. 2–12.

U.S. Bureau of the Census, 1972, 1970 Census of population: U.S. Dept. of Commerce Pub., v. 1 and 2.

Yuill, R. S., 1970, Technical notes on the measurement of census tracts and land-use areas, *in* Simpson, R. B., Production of a high-altitude land-use map and data base for Boston: Dartmouth College, Phase I Final Tech. Dept., p. 26–36, prepared for U.S. Geol. Survey under Contract No. 14–08–0001–12640.

Jour. Research U.S. Geol. Survey
Vol. 6, No. 1, Jan.–Feb. 1978, p. 41–50

HYPOTHESIS: MANY EARTHQUAKES IN THE CENTRAL AND SOUTHEASTERN UNITED STATES ARE CAUSALLY RELATED TO MAFIC INTRUSIVE BODIES

By F. A. McKEOWN, Denver, Colo.

Abstract.—Assessment of earthquake hazards in the United States is based largely upon knowledge acquired in the seismically active parts of the western United States. Earthquakes in the central and southeastern United States are seismologically and geologically very anomalous, however, compared with those in the western United States. For example, shallow earthquakes of magnitude 7+ in the western United States in general have tectonic surface faulting associated with them. No tectonic surface faulting, however, has been found to be associated with the New Madrid, Mo., earthquakes of 1811 and 1812, several of which had estimated magnitudes of 7+. The lack of surface faulting is, in part, responsible for the fact that the New Madrid earthquakes have not been related with certainty to any particular geologic structural element, which makes assessment of the seismic hazards associated with possible similar future earthquakes very difficult. Geologic and seismologic data from the central and southeastern United States, however, suggest a spatial correlation between mafic intrusive rocks and seismic activity. An additional supportive correlation is that the trend of many dikes coincides with the trend of nodal planes in many fault-plane solutions. These correlations differ greatly from the direct correlation of earthquakes with faults in the western United States. Consideration of different concepts of earthquake sources in the central and southeastern United States seems necessary. The preferred concept is that local high-stress concentrations, which may result in earthquakes, occur at or close to the contact of mafic intrusives and their felsic host rocks. Ancient rift zones may have been the primary control of the location of the mafic intrusives. Implications of a causal relation between mafic intrusives and seismicity are that more useful seismotectonic maps may be possible and that the source dimensions of the earthquakes would be small. Because of low attenuation, however, effects of earthquakes in the central and southeastern United States, even if relatively small because of smaller source dimensions, must be considered hazardous.

Assessment of earthquake hazards in the United States is based largely upon knowledge acquired in the seismically active part of the western United States, particularly California and Nevada. The seismic activity in these States is locally very high; more large- and moderate-sized earthquakes have occurred in them than in any other part of the United States, and tectonic surface ruptures related to historic (0–≈200 years before present) and Holocene (0–≈10 000 years B.P.) earthquakes are common. In addition, the active plate boundary, represented by the San Andreas fault system, and the thin crust (about 20 kilometers) make at least part of the western United States very unlike other seismically active parts of the United States.

In contrast, the seismically active central and southeastern parts of the United States have almost none of the above characteristics. Seismicity is low; large- to moderate-sized earthquakes occurred only in 1811, 1812, and 1886; no evidence of tectonic surface ruptures related to historic or Holocene earthquakes has been found; curently, active plate boundaries of any kind are unknown, and the crust is of normal (about 40 km) thickness. Furthermore, attenuation of seismic waves generated by earthquakes in the central and southeastern United States is very low compared to the attenuation of seismic waves generated in the western United States. Low attenuation accounts for the great distances at which earthquakes are felt in the central and eastern United States (Nuttli, 1973; Evernden, 1975).

The lack of evidence of tectonic surface rupturing expected from shallow magnitude 7+ earthquakes (as estimated by Nuttli, 1973) in the central and southeastern United States is an enigma particularly important to earthquake hazard assessment. This lack of surface rupturing has seriously hindered relating current and past seismicity to any particular geologic structural element or elements. Without establishing such relationships, little progress can be made in assessing seismic hazards associated with possible future large earthquakes.

Although studies of the New Madrid and Charleston earthquakes were neglected for many years, new studies by several organizations have been started because of a greatly increased public and Government awareness of the hazards that would be associated with a large earthquake in these areas today. More important is the question of whether similar earthquakes can occur far beyond the epicentral areas of earlier earthquakes. Prior to the recent studies, Heyl and others (1966, p. B6) related the earthquakes in the central United States to the New Madrid fault zone, which they had defined in 1961, and to the Sainte Genevieve fault zone. Earlier, Woollard (1958, p. 1144) recognized that the seismicity seemed related to the New Madrid fault zone, then unnamed, and believed it to be a part of a major structural feature

extending into the Saint Lawrence Valley. Other investigators have postulated different explanations for the earthquakes. McGinnis (1963) suggested that the earthquakes were related to water load in the Mississippi River. Sterns and Wilson (1972) suggested that the earthquakes were related to the superposition of the embayment syncline on the underlying Pascola arch. More recently, Ervin and McGinnis (1975) suggested that the current seismicity is caused by continued isostatic adjustment in part of a late Precambrian rift that was reactivated in late Mesozoic time.

The anomalous character of seismic areas in the central and southeastern United States compared to those in the western United States suggests that some of the earthquake source zones in the two regions may be different. The hypothesis suggested in this paper is that the locations of the earthquakes are controlled by the presence of mafic intrusive rock that causes local stress concentrations. Ancillary to this hypothesis is the suggestion, also made by others, that ancient rifts control the distribution of the mafic intrusives.

CURRENT GEOLOGIC STUDIES IN THE CENTRAL UNITED STATES

Inasmuch as the area (fig. 1) in which seismic activity occurs in the central United States is so large, current field geologic studies have had to be limited to select problems within this area. Several reported faults in Quaternary and Tertiary sediments and sedimentary rocks have been investigated and explored, sand blows have been mapped, and a search for young faults by geologic reconnaissance is continuing. Geomorphic analysis of select areas to identify recent deformation is under way. Tentative results and conclusions of these studies are that all reported offsets of upper Quaternary sediments, such as loess, are the result of landsliding or that they are steep sedimentary contacts. A few strong lineations in the flood plain of the Mississippi River may be the surficial expression of faults, but other explanations are also reasonable. Several scarps, also in the flood plain, bear geomorphic similarity to fault scarps but are very likely of erosional origin, as inferred by R. T. Saucier (oral commun., 1975). No evidence of strong motion, such as sand blows or disturbed sediments, has yet been found much beyond the sand-blow area originally described by Fuller (1912).

Lack of evidence of tectonic surface rupturing, related to either the 1811–12 series of earthquakes or earlier eathquakes, does not seem to be the result of incomplete investigations. That surface rupturing did not occur is supported by the permanence of the scarps in the flood plain that range in height from about 2 to 6 meters. The scarps in the flood plain of the Mississippi River west of New Madrid have Indian sites and mounds on their edges that are more than 700 years old. The ground around the sites shows no evidence of aggradation or erosion. Other evidence that change has been little in the flood-plain levels is the close correlation between types of soils as shown on soil maps and the relict braided stream channels and bars as seen on aerial photographs. Furthermore, interpretation of the history of the meander belts of the Mississippi River indicates that the present belt, along the east side of the flood plain and east of the scarps, was first established about 6000 years ago (Saucier, 1974, p. 2) It seems likely, therefore, that if fault scarps more than about 2 m high had ever existed in the same area during the past few thousand years, they too should be preserved.

Several interpretations of the distribution of sand blows (fig. 1) as related to epicenters of the 1811–12 series of shocks can be made. One interpretation is that the sand-blow area crudely defines a buried fault zone in which the shocks originated. The epicentral line of Fuller (1912, pl. 1) and of a "centrum" for the shocks is virtually the same interpretation. Another interpretation suggested here is that the distribution of sand blows is anomalous with respect to the approximate epicenters of the two largest shocks as inferred by Nuttli (1973, p. 231–233). Easily liquifiable sediments are widespread in the central Mississippi Valley. Sand blows or other liquefaction effects could, therefore, be expected to be distributed fairly symmetrically around the epicentral areas of the large shocks. The outstanding examples of the lack of symmetry may be shown for the December 16, 1811, and February 7, 1812, shocks. If the December 16 shock was located near the southern end of Lake Saint Francis (this area is approximately at Marked Tree on fig. 1), the area of sand blows is very asymmetric with respect to the earthquake source. Similarly, the February 7 shock is assumed to have been near New Madrid (fig. 1), but the area of abundant sand blows is south of there. It is possible that the epicenters inferred by Nuttli (1973) for these two shocks are in error. His data and reasoning, however, are convincing to me. Explanations for the lack of symmetry, such as differences in thickness of the liquifiable sediments have been investigated, but they failed to explain the anomaly and are too detailed and complex to discuss in this paper.

CORRELATION OF SEISMIC ACTIVITY WITH MAFIC INTRUSIVES

Although no correlation of proved faults with current seismicity or past earthquakes has been found, efforts to find relationships among geologic and seismologic data have not all been futile. The best correlation

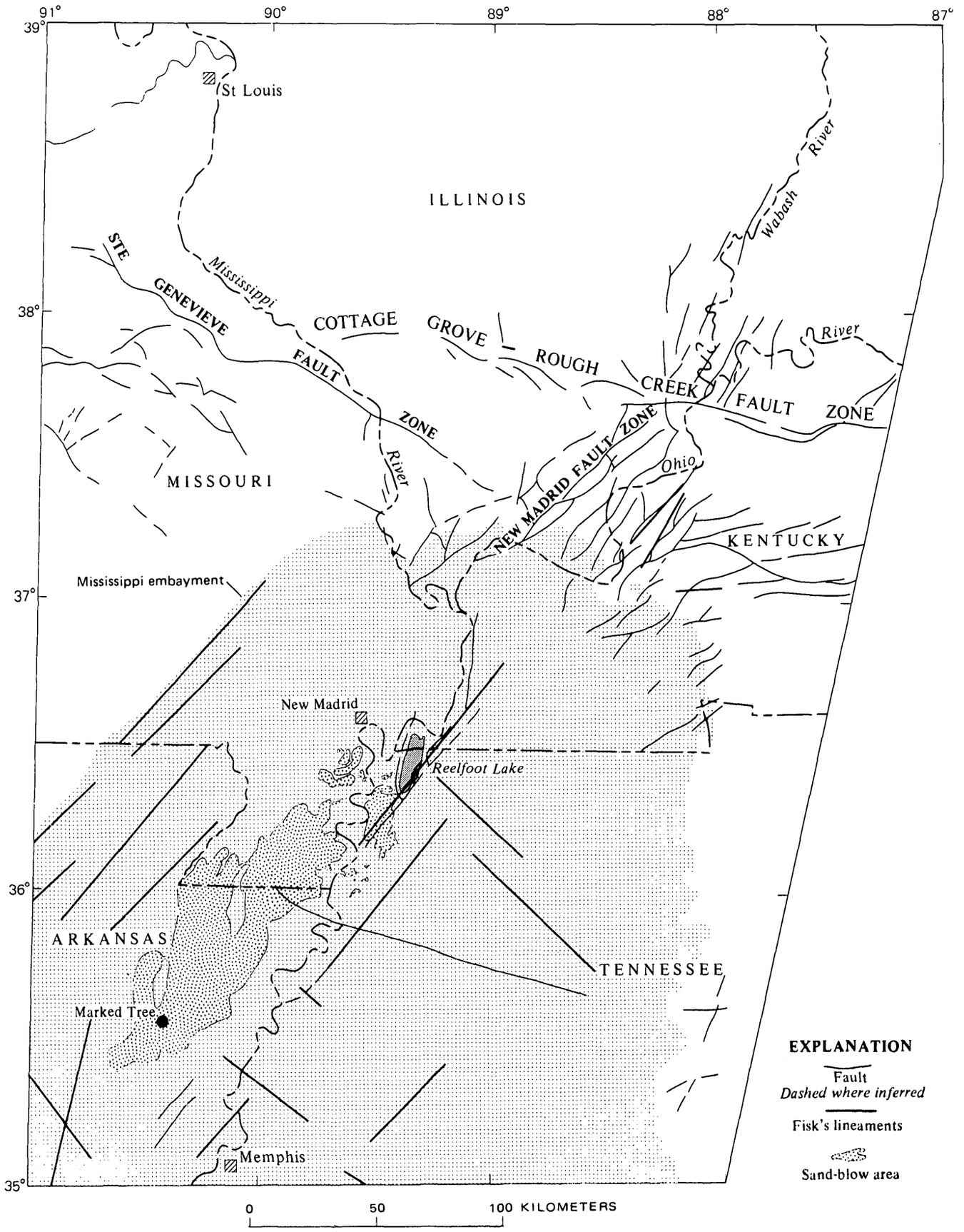

FIGURE 1.—Generalized fault map of seismically active part of the central United States including meizoseismal area of 1811–12 earthquakes represented by sand-blow area mapped by John Watson. Lineaments are from Fisk (1944), but many others can be recognized on different scales of photography.

observed to date is that of the distribution and trend of mafic intrusive rocks with seismicity. This correlation was also noted by Stearns and Wilson (1972, p. 2, 9A–37), but they did not develop their ideas.

Figure 2 shows the distribution of known mafic intrusive rocks superimposed on the contoured seismicity information from Hadley and Devine (1974). A gross correlation of seismicity and the distribution of mafic intrusives is evident in this figure. The validity of the representation of mafic rocks shown in figure 2 can be questioned. However, superposition of positive gravity anomalies suggests that the distribution shown in figure 2 is representative. Inherent in this suggestion is the assumption that positive gravity anomalies indicate buried mafic rocks. Local confirmation of this assumption has been made in the Charleston area where a drill hole penetrated basalt (Gottfried and others, 1976) and magnetic anomalies coincide with the gravity anomalies (Popenoe and others, 1976). Large gravity and magnetic anomalies are also west of New Madrid, and four drill holes have pentrated mafic rocks near Reelfoot Lake, Tenn.

In addition to these gross correlations of the distribution of seismicity to that of mafic rocks, the strike of nodal planes in both the central and the southeastern United States are subparallel to the strike of mafic dikes and some faults in these areas. Thirty-eight fault-plane solutions are given by Street, Hermann, and Nuttli (1974) for earthquakes in the central United States. These authors report that errors in the strike of the nodal planes in the solutions may be as much as 10° to 20°, which should be considered when using the strikes of the nodal planes. Rosettes of the strike of the nodal planes of 35 of the solutions for the earthquakes in the Wabash River area, the Saint Francis Mountains, and the Mississippi embayment are shown in figure 3. The nodal planes were grouped into these three areas because the structural framework and history of each one may be different. As only three solutions (six nodal planes) are available for the Wabash River area, the trends may not be meaningful. The north and northeast trends are, however, subparallel to the faults in the area. Two of the three trends of nodal planes from the fault plane solutions of earthquakes in the Saint Francis Mountains are subparallel to northwest- and northeast-striking faults. The north-trending nodal planes, however, are not correlative to a north-trending set of faults according to available maps but do correlate with the trends of mafic dikes. Nodal planes from the 24 solutions for earthquakes in the Mississippi embayment have a strong preferred orientation to the north. The few known faults in the embayment and nearly all inferred faults trend northeast and northwest. As in the Saint Francis Mountain area, north-trending faults are absent or are possibly undetected.

The nodal plane data shown for three areas in figure 3 are summarized in one rosette in figure 4. Also shown in figure 4 are the strikes of 211 Precambrian mafic dikes in the Saint Francis Mountain area (Gibbons, 1972) and the strikes of all faults on available maps of the area shown in figure 3 as well as other faults. A strong correlation between nodal plane trends and the strike of the mafic dikes is evident.

Two fault-plane solutions for earthquakes in the southeastern United States have nodal planes that strike northwest subparallel to diabase dikes exposed in the Appalachian Piedmont. Bollinger, Langer, and Harding (1976) interpret a northwest-trending reverse fault as the most likely to have caused the November 30, 1973, earthquake near Knoxville, Tenn. Tarr and Carver (1976) report that a fault-plane solution for the November 22, 1974, earthquake near Charleston, S. C., has both nodal planes striking N 42° W. Mafic rocks are not exposed in either of these areas, although mafic rocks are known to underline the Charleston area. It is probable, however, that the northwest structural grain of basement rocks exposed in the Piedmont, as indicated by the dikes, is also present under the Coastal Plain and under the thrusted and folded Appalachian Mountains near Knoxville.

CONCEPTS OF EARTHQUAKE SOURCES RELATED TO MAFIC ROCKS

All concepts of earthquake sources require consideration of geologic discontinuities, such as faults or contacts on which the earthquakes may occur, and the state of stress on the discontinuities. This section is a discussion of concepts of the relationship of earthquakes to possible discontinuities associated with mafic intrusives in the central and southeastern United States. Discussion of meager evidence of Quaternary deformation, which is indicative of active stresses, is beyond the scope of this paper.

One concept is that some, if not all, earthquakes occur on fractures in sets whose trend is parallel to the trend of the mafic dikes. A correlation among dike trends, dike distribution, and seismicity could then be expected.

Another concept is that the earthquakes occur at or close to the contact of mafic intrusives and their felsic host rocks. The correlation of the trends of dikes with nodal plane trends suggests a relation to either the dikes or the associated fracture sets, but the spatial correlation of earthquakes to mafic rocks themselves suggests that this rock type is in some way related to the earthquakes. If either this or the preceding concept is valid, the source dimensions of earthquakes explained by the concepts would probably be small, that is, less than about 10 km long. This estimate of length is based upon the observed length of mafic

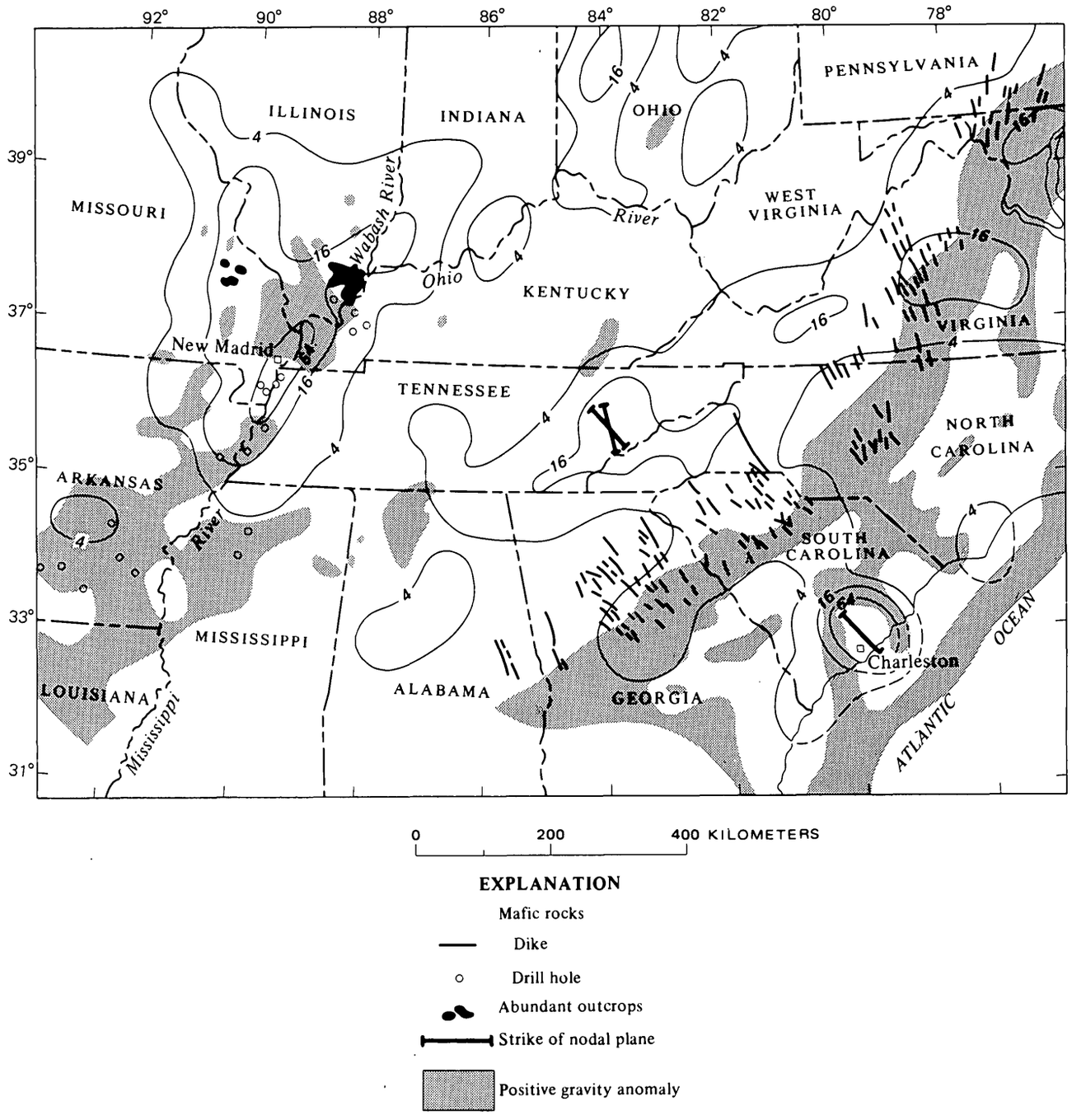

FIGURE 2.—Distribution of mafic rocks from Kidwell (1951), King and Beikman (1974), and A. V. Heyl (written commun., 1974). Contours from Hadley and Devine (1974) represent the number of earthquakes for 10 000 km². Strikes of nodal planes for the November 30, 1973, earthquake in eastern Tennessee, and the November 22, 1974, earthquake near Charleston, S.C., are also shown. Positive gravity anomalies from Woollard and Joesting (1964).

dikes. The dikes may, however, be part of major, structural features, such as those described below.

To be of optimum use, both concepts, assuming one or both are valid, requires knowledge of the occurrence and distribution of mafic intrusive rocks. Consideration of this requirement suggests that earthquakes in the central and southeastern, and possibly the northeastern, United States are related to ancient rift zones. The possible association of earthquakes with ancient rifts has been discussed in several ways by several investigators (Ervin and McGinnis, 1975; Kumarapeli and Saull, 1966; Sykes and others 1974). The rift association arises from the apparent correlation of seismicity with mafic rocks and the well-known association of mafic rocks, particularly mafic alkalic rocks, with known rifts (Willis, 1936; Holmes, 1965; Burke and Dewey, 1973). If, for example, the upper part of the Mississippi embayment, the Saint Lawrence Valley, and the Cottage Grove–Rough Creek fault zone are the loci of ancient rifts as proposed by Kumarapeli

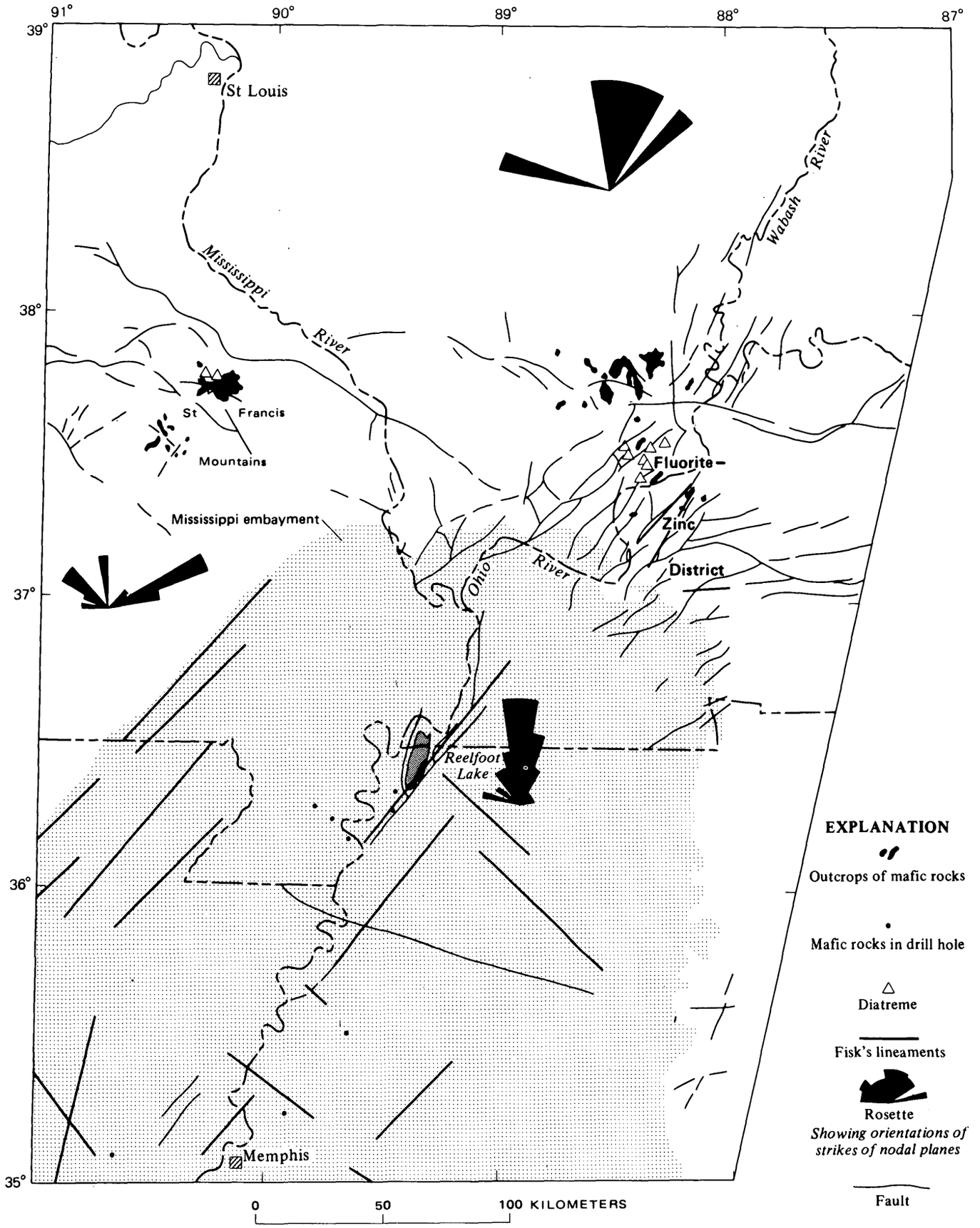

FIGURE 3.—Generalized fault map. Strikes of nodal planes are from Street, Herrman, and Nuttli (1974) and mafic intrusives are from Kidwell (1951) and A. V. Heyl (written commun., 1974).

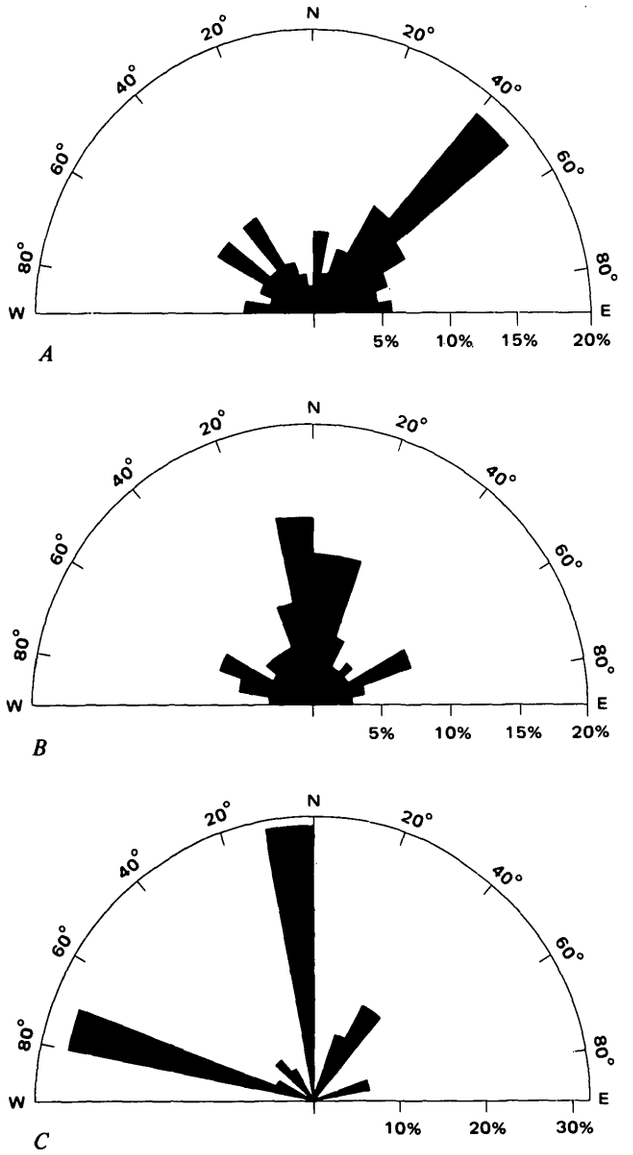

FIGURE 4.—Comparison of strikes of faults, nodal planes, and mafic dikes in the central Mississippi Valley region. *A*, Strikes of 538 faults. *B*, Strikes of nodal planes from 38 focal mechanism solutions (Street and others, 1974). *C*, Strikes of 211 vertical Precambrian dikes (Gibbons, 1972) in the Saint Francis Mountains, Mo.

and Saull (1966), then the structural and petrologic characteristics of rifts may explain trends of seismicity.

The major structural elements of rifts are the bounding faults, which may be long and continuous or may be a series of en echelon discontinuous faults. These types of faults are well documented in the East Africa rifts. Structural elements are also tranverse to the axes of rifts (Barberi and others, 1974; Garson and Krs, 1976; Willis, 1936). Furthermore, alkalic basalts are commonly associated with the transverse structures and are in contrast to the tholeiitic basalts that are commonly associated with the axial structural features (Baker and others 1972, p. 18; Barberi and others, 1974). The northwest-trending mafic alkalic dikes in the fluorite-zinc district of southern Illinois and western Kentucky may be evidence of transverse structures in a northeast-trending rift which may be equivalent to the New Madrid fault zone of Heyl and Brock (1961). The north-trending Precambrian diabase dikes in the Saint Francis Mountains may be evidence for en echelon structures bounding the west side of the rift. Mafic alkalic rocks of Devonian age occur in diatremes in the Saint Francis Mountains, however. These age differences and the Pennsylvanian and Permian ages for the mafic rocks in the fluorite-zinc district (Zartman and others, 1967) are reasons to ask whether the diabase dikes of Precambrian age and the mafic alkalic rocks of early Paleozoic age are all parts of the same rift that was reactivated at different times or whether they are parts of different rifts. The east-wing trending Sainte Genevieve and Cottage Grove–Rough Creek fault zone may also represent an ancient rift zone. The northwest-trending mafic dikes in the fluorite-zinc district are nearly as suggestive of this interpretation as they are of the northeast-trending rift. An east-west rift zone is, of course, an interpretation much like that of Heyl (1972) who proposed the 38th parallel lineament as a major deep-seated wrench-fault zone extending from northeastern Virginia to south-central Missouri.

The diabase dikes in the eastern United States are thought to be related to the rifting (separation) of the African Continent from the North American Continent (Dalrymple and others, 1975, p. 408; Dietz and Holden, 1970, p. 4946). This kind of rifting differs from intraplate rifting in that it has larger dimensions. Both types, however, have lower crust or possibly mantle rocks associated with them. So, regardless of the exact nature of the rift zones, the association of mafic rocks of some kind with rift zones seems ubiquitous. The gross distribution of mafic rocks may be indicative of possible buried or partially exposed rift zones, but additional geologic data and interpretation are needed to delineate the zones more precisely. If such delineation is successful and the apparent correlation of seismicity to mafic rocks is causal, then more useful seismotectonic maps could be made than those made solely from geologic structure exposed at the surface. Much more information and study are obviously necessary to confirm or negate this concept and to apply it to assessing seismic hazards in the central and eastern United States.

MAFIC INTRUSIVE BODIES AS STRESS CONCENTRATORS

The concept that earthquakes occur at or close to the contact of mafic intrusives and their felsic host rocks, which is based upon empirical data, can be supported by a physical explanation. The argument that follows is similar to the "stress amplification

mechanism" concept of Long (1976) and the concept suggested by M. F. Kane (written commun., 1976) that involves stress concentrations around mafic plutons.

As dikes and other intrusive bodies are in effect solid inclusions, their effect on stress concentrations may be estimated from theory. Fractures, on the other hand, do not have stress concentrations around them unless rupturing starts along them or the elastic moduli of the juxtaposed rocks differ.

The stress concentration around or in an inclusion is a function of the ratio of Young's modulus of the inclusion to the host, the shape of the inclusion, and the applied stresses. Figures 5 and 6 (modified from Oudenhoven and others 1972) show several examples of changes in stress concentrations as a function of the three variables for ovaloidal inclusions. Inasmuch as the number of combinations of these variables for a dike or other intrusive rock in the earth is extremely large, only gross generalities can be considered. Dikes or sills are the two intrusive forms with approximately plane surfaces which are like fault surfaces. The width to height ratios for such forms are much less than the smallest used by Oudenhoven, Baback, and Blake (1972); and stress concentrations would be greater than the examples given by these authors. The ratio of Young's modulus for mafic inclusions in a felsic host rock would be in the range of 2 to 5; the ratio of the applied maximum and minimum stresses in the Earth would be in the range of 1 to 5. These assumed ranges of values would result in stress concentrations at point B (fig. 5) in the range of 1 to more than 1.7. Using similar values for a point at B' within the inclusion, the stress concentration ranges from 1 to more than 2.3 (fig. 6).

An example of what part of a source zone for earthquakes in the central United States may look like is shown in figure 7. This figure of a roadcut shows

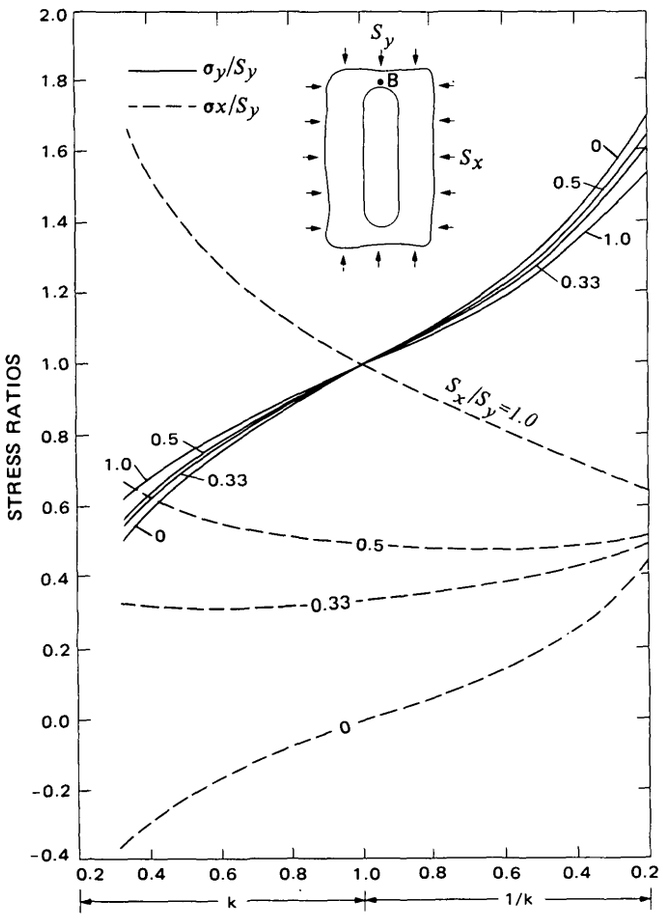

FIGURE 5.—Stress ratios, $\sigma x/S_y$ or $\sigma y/S_y$ at B for an ovaloidal inclusion with width to height ratio of 0.25, applied stress ratios (S_x/S_y) ranging from 0 to 1.0, and Young's modulus ratios (k) of inclusion to host ranging from 0.2 to 5. In the x and y directions, x and y are normal stresses. From Oudenhoven, Babcock, and Blake (1972).

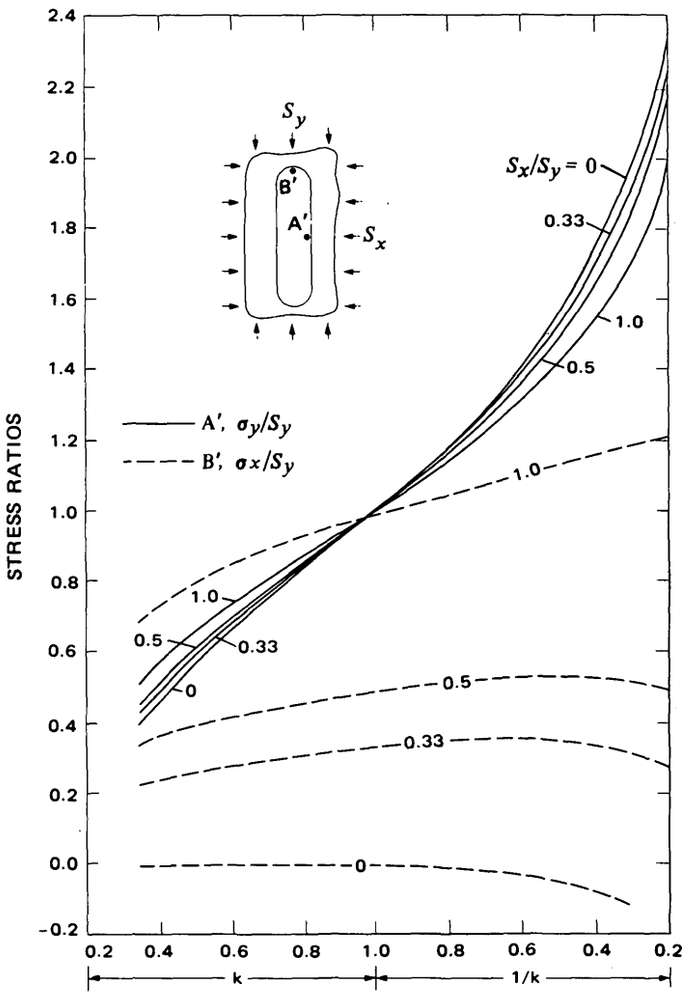

FIGURE 6.—Stress ratios, $\sigma y/S_y$ at A' or $\sigma x/S_y$ at B' for an ovaloidal inclusion with width to height ratio of 0.25, applied stress ratio (S_x/S_y) ranging from 0 to 1.0 and Young's modulus ratios (k) of inclusion to host ranging from 0.2 to 5. In the x and y directions, x and y are normal stresses. From Oudenhoven, Babcock, and Blake (1972).

shearing in and adjacent to several fine-grained diabase dikes. Not all dikes exposed at other places in the same roadcut are sheared nor is it expected that all dikes would be sheared. It should be noted that, although the dikes are parallel to the abundant fractures in the felsite host rocks and may, therefore, be contemporaneous with or later than the development of the fractures, shearing within the dikes indicates that structural deformation continued or recurred after emplacement of the dikes. Fracturing and injection of the dikes into fractures is indicative of a low horizontal stress. The change to shearing along the dikes suggests a change in the state of stress since injection.

IMPLICATIONS

Assessment of seismic hazards in the central and southeastern United States is difficult because seismicity is low and geologic structures to which the seismicity may be related have not been identified unequivocally. To help assess seismic hazards, the common practice has been to try to delimit seismotectonic provinces. The provinces, however, are delimited on the basis of geologic structures mapped at the surface of the Earth. This can be extremely misleading if the earthquake sources are at depths of more than a few kilometers and if the structures mapped at the surface may only extend to 1 or 2 km, as in the Appalachian Mountains and the Coastal Plain.

If mafic intrusives are causally related to earthquakes, establishing their distribution may provide a more rational basis for delineation of seismotectonic provinces than that now used. The size, geometry, and orientation of the intrusives should also be used to outline the provinces, if possible. Careful interpretation of magnetic and gravity data and of the known distribution of mafic intrusives presumably would be the first considerations toward delimiting the provinces. Additional analyses utilizing petrologic data and plate tectonic concepts may help to refine the province boundaries and to establish more detailed geologic characteristics of each province.

The diversity of focal mechanisms reported by Street, Herrmann, and Nuttli (1974) may be the result of a causal relation of the earthquakes to mafic intrusives. The intrusives would be expected to have diverse structural attitudes and shapes, as shown, for example, in figure 7. Local changes in the direction and the level of stress would be expected to be associated with such a complex system of geologic discontinuities. Focal mechanisms of earthquakes on them would, therefore, be diverse.

Another implication of a casual relation between mafic intrusives, such as dikes or sills, and earthquakes is that the source dimensions of the earthquakes are likely to be small, that is, less than about 10 km long. This is in agreement with Evernden's (1975) estimates of source dimensions of earthquakes of the eastern United States which are based upon a study of earthquake intensities. Because of low attenuation, however, high intensities may occur over

FIGURE 7.—Sheared north-trending mafic (diabase) dikes in felsite about 5.6 km west of Fredericktown, Mo.

large areas, and, consequently, earthquakes in the eastern United States must be considered hazardous even though they may be of smaller magnitude than those in the western United States.

REFERENCES CITED

Baker, B. H., Mohr, P. A., and Williams, L. A. J., 1972, Geology of the eastern rift system of Africa: Geol. Soc. America Spec. Paper 136, 67 p.

Barberi, F., Bonatti, E., Marinelli, G., and Varet, J., 1974, Transverse tectonics during the split of a continent—Data from the Afar Rift: Tectonophysics, v. 23, no. 1–2, p. 17–29.

Bollinger, G. A., Langer, C. J., and Harding, S. T., 1976, The Eastern Tennessee earthquake sequence of October through December 1974: Seismol. Soc. America Bull., v. 66, p. 525–547.

Burke, Kevin, and Dewey, J. F., 1973, Plume-generated triple junctions—Key indicators in applying plate tectonics to old rocks: Jour. Geology, v. 81, no. 4, p. 406–433.

Dalrymple, G. B., Gromme, C. S., and White, R. W., 1975, Potassium-argon age and paleomagnetism of diabase dikes in Liberia—Initiation of central Atlantic rifting: Geol. Soc. America Bull., v. 86, p. 399–411.

Dietz, R. S., and Holden, J. C., 1970, Reconstruction of Pangea—breakup and dispersion of continents, Permian to present: Jour. Geophys. Research, v. 75, p. 4939–4956.

Ervin, C. P., and McGinnis, L. D., 1975, Reelfoot Rift—reactivated precursor to the Mississippi embayment: Geol. Soc. America Bull., v. 86, p. 1287–1295.

Evernden, J. F., 1975, Seismic intensities, "SIZE," of earthquakes and related parameters: Seismol. Soc. America Bull., v. 65, p. 1287–1313.

Fisk, H. N., 1944, Geological investigation of the alluvial valley of the lower Mississippi River: U.S. Army Corps of Engineers, Mississippi River Comm., Vicksburg, Miss., 78 p.

Fuller, M. L., 1912, The New Madrid earthquake: U.S. Geol. Survey Bull. 494, 119 p.

Garson, M. S., and Krs, Miroslav, 1976, Geophysical and geological evidence of the relationship of Red Sea transverse tectonics to ancient fractures: Geol. Soc. America Bull., v. 87, no. 2, p. 169–181.

Gibbons, J. F., III, 1972, Tectonics of the eastern Ozarks area, southeastern Missouri: Syracuse Univ., Ph. D. thesis.

Gottfried, David, Annell, C. S., Higgins, Brenda, and Schwarz, L. J., 1976, Geochemistry of subsurface basalt near Charleston, South Carolina: Geol. Soc. America Abs. with Programs, v. 8, no. 2, p. 183–184.

Hadley, J. B., and Devine, J. F., 1974, Seismotectonic map of the eastern United States: U.S. Geol. Survey Misc. Field Studies Map MF–620, 3 sheets.

Heyl, A. V., 1972, The 38th parallel lineament and its relationship to ore deposits: Econ. Geology, v. 67, no. 7, p. 879–894.

Heyl, A. V., and Brock, M. R., 1961, Structural framework of the Illinois-Kentucky mining district and its relation to mineral deposits, *in* Short papers in the geologic and hydrologic sciences: U.S. Geol. Survey Prof. Paper 424–D, p. D3–D6.

Heyl, A. V., Brock, M. R., Jolly, J. L., and Wells, C. E., 1966, Regional structure of the Southeast Missouri and Illinois-Kentucky mineral districts: U.S. Geol. Survey Bull. 1202–B, p. B1–B20.

Holmes, Arthur, 1965, Principles of physical geology (revised ed.): New York, Ronald Press Co., 1288 p.

Kidwell, A. L., 1951, Mesozoic igneous activity in the northern Gulf Coastal Plain: Gulf Coast Assoc. Geol. Socs., Ann. Mtg., 1st, New Orleans, La., Trans., p. 182–199.

King, P. B., and Beikman, H. M., 1974, Geologic map of the United States: U.S. Geol. Survey, scale 1:2 500 000, 3 sheets [1975].

Kumarapeli, P. S., and Saull, V. A., 1966, The St. Lawrence Valley system—A North American equivalent of the East African rift system: Canadian Jour. Earth Sci., v. 3, p. 639–658.

Long, L. T., 1976, The "stress amplification" mechanism for intraplate earthquakes applied to the southeast United States: Geol. Soc. America Abs. with Programs, v. 8, no. 2, p. 221.

McGinnis, L. D., 1963, Earthquakes and crustal movement as related to water load in the Mississippi Valley region: Illinois State Geol. Survey Circ. 344, 20 p.

Nuttli, O. W., 1973. The Mississippi Valley earthquakes of 1811 and 1812—Intensities, ground motion, and magnitudes: Seismol. Soc. America Bull., v. 63, no. 1, p. 227–240.

Oudenhoven M. S. Babcock, C. O., and Blake, Wilson, 1972, A method for the prediction of stresses in an isotropic inclusion or orebody of irregular shape: U.S. Bur. Mines Rept. Inv. 7645, 36 p.

Popenoe, Peter, Phillips, J. D., and Higgins, Brenda, 1976, Lithology and structure of the basement in the Charleston, South Carolina area from interpretation of gravity and magnetic data: Geol. Soc. America Abs. with Programs, v. 8, no. 2, p. 248.

Saucier, R. T., 1974, Quaternary geology of the lower Mississippi Valley: Arkansas Archeol. Survey, Pub. on Archeology, Research Ser. 6, 26 p.

Stearns, R. G., and Wilson, C. W., Jr., 1972, Relationships of earthquakes and geology in West Tennessee and adjacent areas: Nashville, Tenn., Vanderbilt Univ., Rept. for TVA, 344 p.

Street, R. L., Herrmann, R. B., and Nuttli, O. W., 1974, Earthquake mechanics in the Central United States: Science, v. 184, no. 4143, p. 1285–1287.

Sykes, L. R., Fletcher, J. P., and Sbar, M. L., 1974, Seismic zones and mid-Mesozoic tectonic features in eastern North America [abs.]: EOS (Am. Geophys. Union Trans.), v. 55, no. 4, p. 447.

Tarr, A. C., and Carver, D. L., 1976, Recent seismicity in the source area of the 1886 Charleston, South Carolina earthquake: Geol. Soc. America Abs. with Programs, v. 8, no. 2, p. 284–285.

Willis, Bailey, 1936, East African plateaus and rift valleys: Carnegie Inst. Washington Pub. 470, 358 p.

Wollard, G. P., 1958, Areas of tectonic activity in the United States as indicated by earthquake epicenters: Am. Geophys. Union Trans., v. 39, no. 6, p. 1135–1150.

Woollard, G. P., and Joesting, H. R., 1964, The Bouguer gravity anomaly map of the United States: U.S. Geol. Survey, scale 1:2 500 000.

Zartman, R. E., Brock, M. R., Heyl, A. V., Thomas, H. H., 1967, K-Ar and Rb-Sr ages of some alkalic intrusive rocks from the central and eastern U.S.: Am. Jour. Sci., v. 265, no. 10, p. 848–870.

Jour. Research U.S. Geol. Survey
Vol. 6, No. 1, Jan.–Feb. 1978, p. 51–58

PORPHYRY COPPER EXPLORATION MODEL FOR NORTHERN SONORA, MEXICO

By GARY L. RAINES, Denver, Colo.

Abstract.—The regional tectonic pattern of the porphyry copper province of northern Sonora, Mexico, is similar to, but more complex than, the Colorado mineral belt. Four northeast-trending shear zones, spaced at 30- to 50-kilometer intervals from Hermosillo, Mexico, north to Nogales, Mexico, are interpreted from analysis of lineament data from Landsat–1 images. From comparison with other areas, these zones are believed to have Precambrian ancestry. North-northwest-trending lineaments, which commonly occur along range fronts, are interpreted to be the principal basin and range faults. North-south- and west-northwest-trending lineaments are believed to be related to lesser faults and fractures. Areas of hydrothermal alteration have been mapped on a regional scale by use of digital image-processing techniques. These altered areas occur on the flanks of the northeast-trending shear zones, generally near intersections with north-northwest-trending lineaments. This tectonic framework with associated alteration is similar to patterns in the Colorado Plateau, the porphyry copper province of Arizona, and central Mexico and is supported by relationships found in limited local mapping. The pattern of northeast-trending shear zones and north-northwest-trending faults in northern Sonora closely resembles the tectonic framework of the Colorado mineral belt. The younger sedimentary and volcanic cover, however, has not been eroded in Sonora as it has been in the Colorado mineral belt. This comparison with the Colorado mineral belt suggests that mineral deposits are most likely to be found in altered areas where a northeast-trending shear zone is intersected by north-northwest-trending faults. Seven areas with these characteristics have been defined in Sonora and are being evaluated by means of regional geophysical and geochemical data.

Major porphyry copper deposits in Sonora, Mexico (fig. 1), have been known for many years, but exploration efforts in recent years have had limited success. The major problem affecting continued exploration is that the area is extensively covered by Cenozoic volcanic rocks and pediment gravels, both of which mask deposits. Landsat–1 data provide a regional view of both the tectonic elements and the alterations of the region. Features that may be very subtle on the ground are easily observable from Landsat–1, and these subtle features, when used with existing geologic data, have provided a proposed regional tectonic model for the localization of porphyry copper mineralization in Sonora, Mexico.

Northern Sonora is tectonically very similar to the Colorado mineral belt as described by Tweto and Sims (1963). Before mineralization in northern Sonora, a system of four northeast-trending shear or fracture zones, probably of Precambrian ancestry, were intersected by the north-northwest trending faults. These as in the Colorado mineral belt, provided the basement plumbing system that controlled mineralization. The most favorable locations to find mineral deposits are areas of hydrothermal alteration where the northeast-trending shear zones are well developed and are intersected by the north-northwest trending faults. These shear zones and faults were open during Laramide mineralization and some continued to be active even after subsequent emplacement of volcanic cover; therefore, aspects of these structures are observable at the surface of the volcanic rocks, although the mineral deposits may be hidden beneath those rocks. This proposed model was derived by analogy with the Colorado mineral belt from two types of analysis of Landsat–1 data: lineament analysis and regional mapping of alteration. The lineament analysis and supporting literature provided information on the spatial distribution of fractures, faults, and shear zones. The mapping of alteration, done by the digital image-processing techniques described by Rowan and others (1974), provided information on the spatial association of lineament concentrations and alteration. For a comprehensive application, however, these remote-sensing techniques should be integrated with other regional geological techniques; remote sensing is simply one of the tools. The work reported here is one aspect of a large program; regional geophysical and geochemical data will also be available to evaluate the targets identified by these remote-sensing techniques. By this

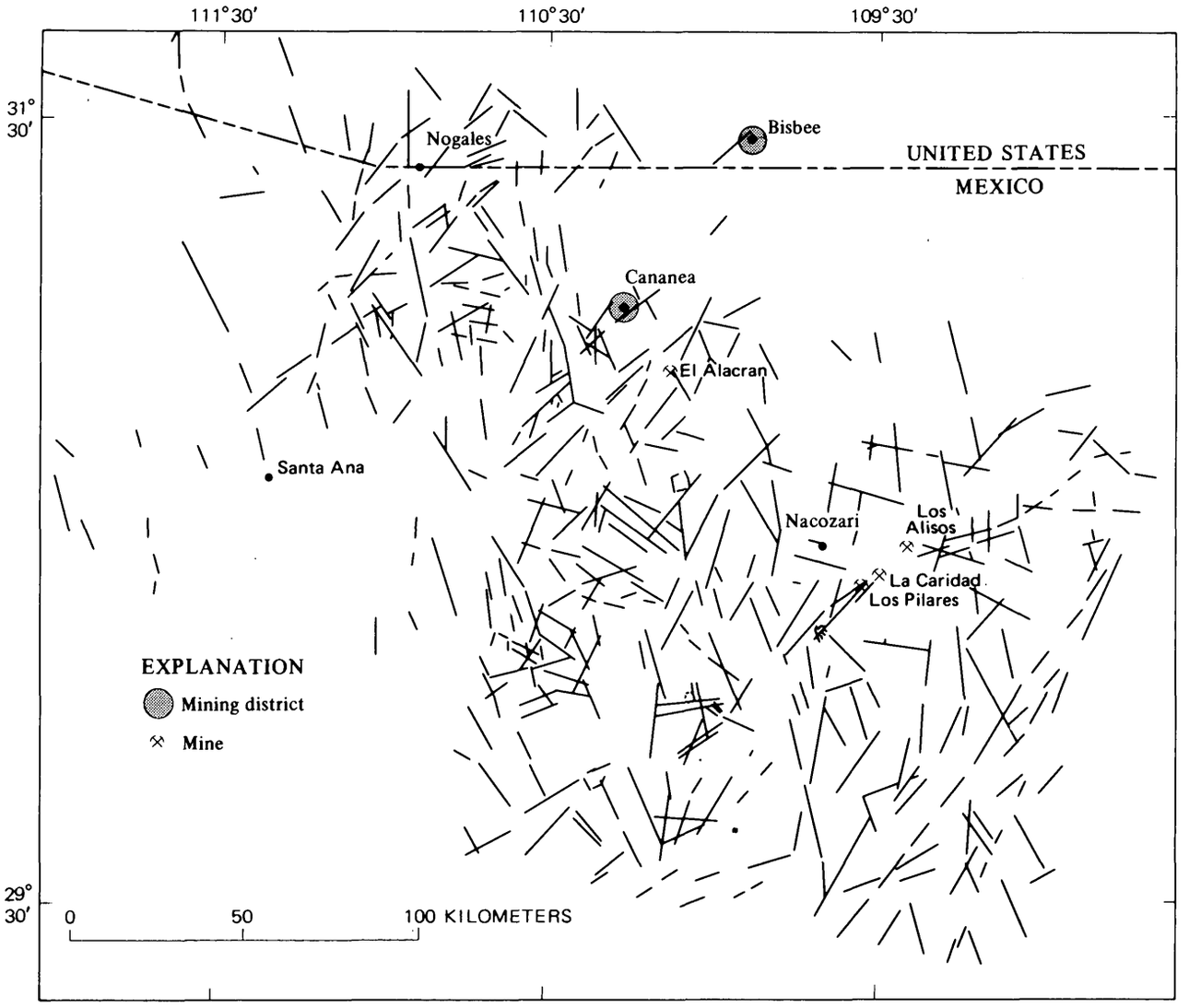

FIGURE 1.—Location and lineament map of the study area, northern Sonora, Mexico. The map is the digitized version of the original map; consequently, all lineaments have been approximated with straight line segments for the purpose of analysis.

integrated team approach, in which the information derived from remote-sensing techniques is available early in the program, the geophysical and geochemical activities can be designed with additional geologic information.

Acknowledgments.—I would like to thank my colleagues on this project for useful discussion and especially D. L. Sawatsky for the use of his programs and for many useful discussions concerning the analysis of lineaments.

This work was performed as part of a cooperative program between the U.S. Geological Survey and the Government of Mexico and was funded by the Government of Mexico, the U.S. Geological Survey, and the U.S. National Science Foundation.

ANALYSIS OF LANDSAT-1 DATA

The lineament map was derived from a standard photogeologic interpretation of Landsat–1 images. Only the band 5 transparency (600- to 700-nanometer spectral band), which is available from the EROS Data Center, was used because, from past experience, this band has been found to contain most of the structural information for semiarid environments. The lineaments were observed primarily in mountainous areas and not in valley fill as near Bisbee, Ariz. This map, of course, is very subjective, although care was taken to follow the lineament-mapping concepts as discussed by O'Leary, Friedman, and Pohn (1976). Statistical analysis procedures developed by D. L.

Sawatzky (Knepper, 1974, p. 129–132) were then used to define statistically significant trends.

Sawatzky's procedure assumes that the number of observations in any one direction is independent of the number of observations in any other direction and that each possible direction is equally as likely as any other. Therefore, if the total number of observations and the expected number of observations are known, then the probability of making a particular number of observations in any direction can be calculated by use of the binomial probability theory. Thus, a statistically significant direction is one having a number of observations that are statistically improbable in a random situation. This statistical analysis is performed on smoothed strike frequencies of the azimuths and on the azimuths weighted by the length of the lineaments. The smoothing was a 3° running average for this study. This procedure has the advantage that it is repeatable, well defined, and, if the significance value is selected beforehand, objective.

By use of this procedure and a 90-percent significance value, the following statistically significant trends were selected: west-northwest (N. 84°–70° W.), north-northwest (N. 39°–4°W.), and northeast (N. 20° – 57° E.). If an 80-percent significance value had been selected instead, a north-south direction also would have been identified. Figure 2 shows the histograms of these data. The north-northwest and northeast trends are very broad and may be composed of several geologically significant subgroups of trends. These subgroups, however, cannot be statistically separated at a 90-percent significance value.

Areas of complex intersections of these statistically defined trends are identified by contouring the spatial concentrations of lineaments of each statistically significant trend. The measure of concentration is the total length of lineaments within a grid cell of preselected size in data units, normalized to relative frequency, per unit area of the grid (D. L. Sawatzky, oral commun., 1976). Inspection of contour maps of the statistically identified trends (fig. 3) shows the concentration of the northeast trend (fig. 3*B*) as divided into four obvious zones, the north-northwest trend (fig. 3*C*) is more diffuse, and the west-northwest trend (fig. 3*D*) consists of a few lineaments that are longer than average. As described in the section "Significance of Pattern," the north-northwest and northeast trends are considered to be important controls of mineralization; and so the areas of complex intersections of these two trends were selected. A complex intersection is here defined as an area outlined by the upper quartile of concentration of the trends under consideration. Then, to simplify the presentation of the concentration of the north-northwest and northeast trends, these trends were contoured together, and the upper quartile of concentration on this map, where it outlines the areas selected on the basis of the individual trend and contour maps, was used as a map of areas of complex intersections. This procedure was used because a high concentration on the map of the north-northwest and northeast trends contoured to-

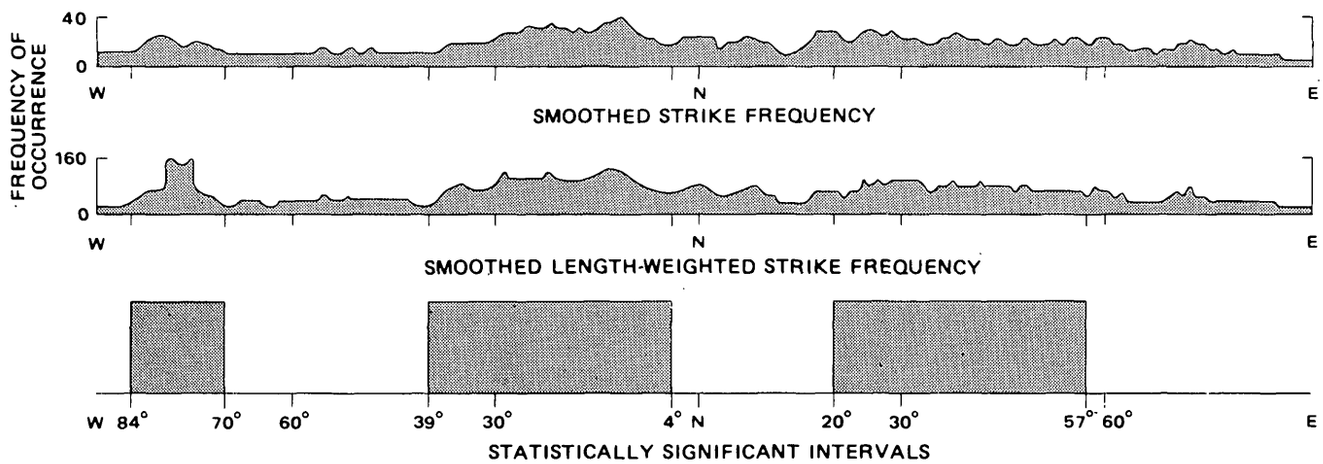

FIGURE 2.—Strike-frequency histograms and selected statistically significant intervals of the lineament map. The smoothed strike-frequency and length-weighted strike-frequency histograms have been smoothed by a 3° running average for analysis purposes. The number of observations in the smoothed strike-frequency histogram, 980, is the total number of lines observed. The number of observations in the length-weighted histogram, 1814, was derived by weighting each lineament by its length measured to the nearest hundredth of an inch on a map at a scale of 1:1 000 000. The statistically significant intervals is a box diagram of which intervals were selected at a 90-percent significance value and has no vertical scale.

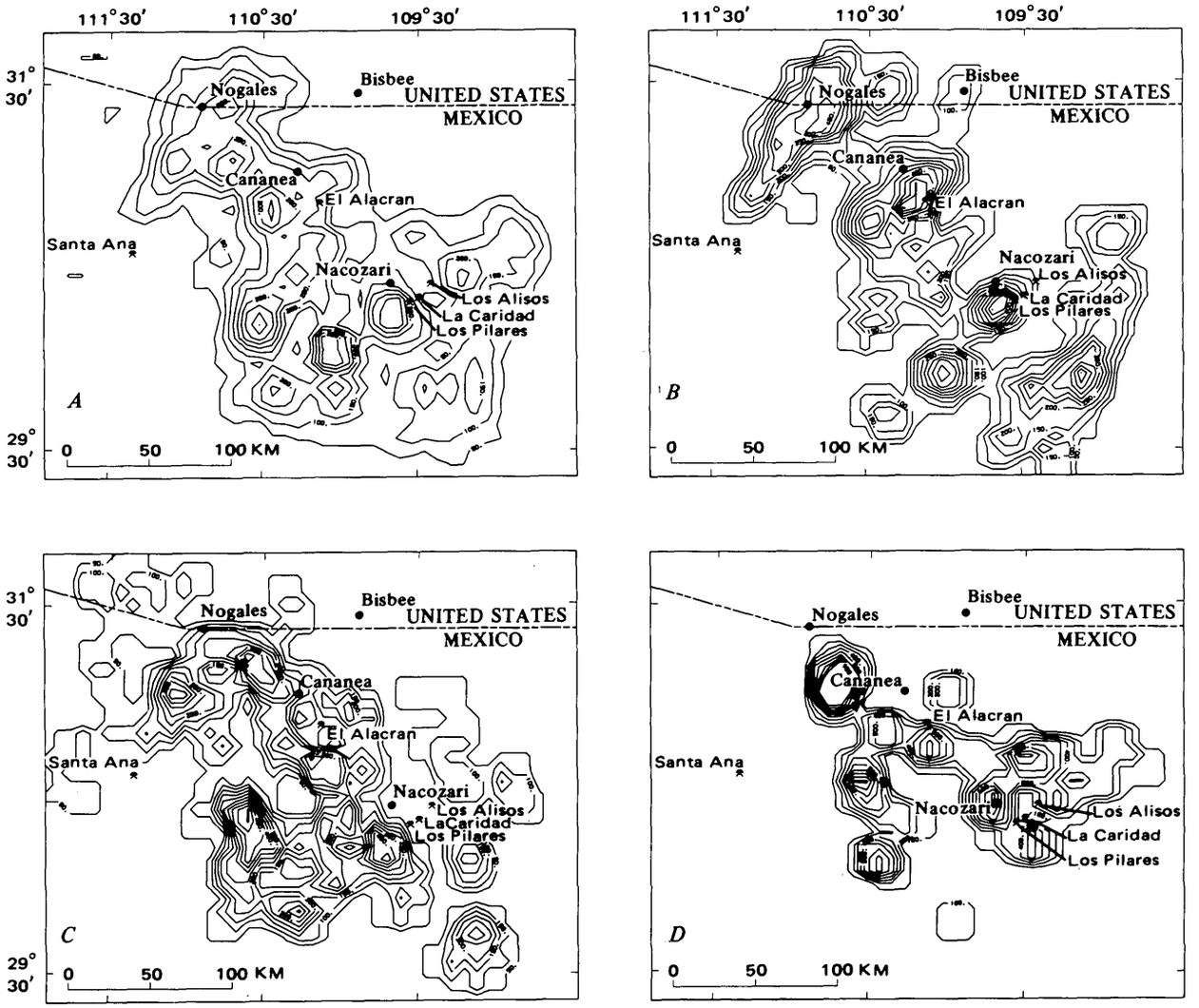

FIGURE 3.—Maps of lineament concentrations. Units of contour are in normalized lengths of lineaments per 0.3-in (0.08-cm) unit cell times 1000. *A*, All lineaments. *B*, Northeast trend. *C*, North-northwest trend. *D*, West-northwest trend.

gether could result from a high on the north-northwest map or on the northeast map or on both. Only those areas where both the north-northwest and the northeast concentrations are high are of interest. The selected areas are shown in figure 4.

Figure 4 also shows the location of areas of hydrothermal alteration. These areas were defined by means of the image-processing procedures as used by Rowan and others (1974) at Goldfield, Nev., and have not all been field checked. These altered areas are predominantly on the flanks of the northeast zones, suggesting a genetic relationship of the alteration to the northeast trend. Also note that the only known porphyry copper deposits, Cananea, Los Pilares, and La Caridad, are located on these northeast zones and that Bisbee, Ariz., is on the projection of the northeast zone through Cananea.

SIGNIFICANCE OF PATTERN

The pattern of lineaments and alteration, which is described above, is spatially related to known mineralization at Cananea, La Caridad, and Los Pilares; elements of this pattern, the north-northwest and the northeast trends, actively influenced mineralization. These trends were primarily channels along which the mineralizing fluids intruded the rocks (R. Avala, Chief Geologist at Cananea, oral commun., 1975; Ramirez Rubalcaba and others, 1973; Tenney, 1935). With this pattern a model can be developed that defines specific mineral-target areas.

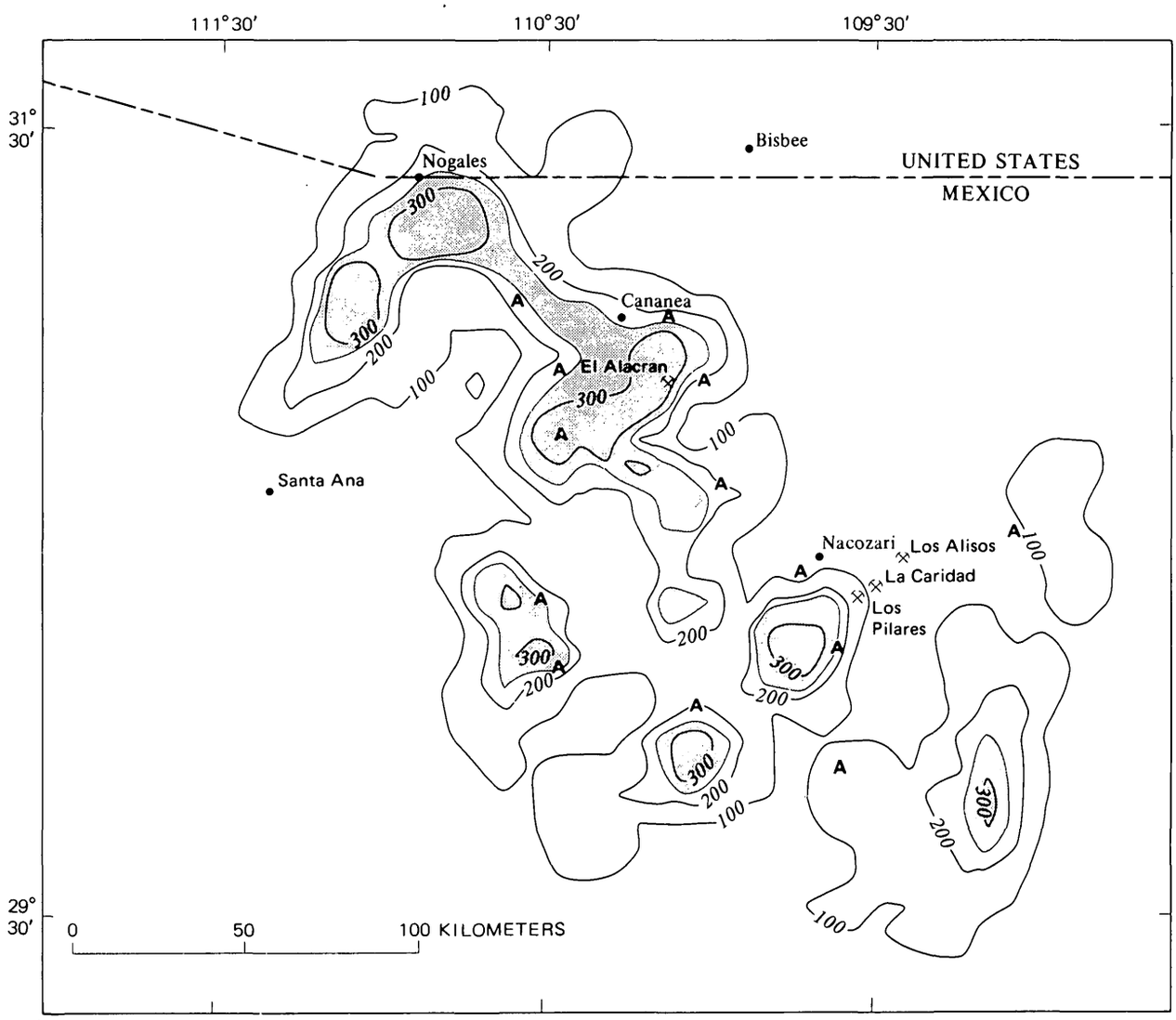

FIGURE 4.—Alteration and complex intersections of the northeast and north-northwest trends. The large A's mark altered areas. The shaded areas are the selected areas of complex intersection. These areas are the quartile of concentration above 250.

Regional patterns

The pattern of trends of linear features and the association with alteration and mineralization as described in this report is not unique. On the Colorado Plateau, Davis (1972a,b) defined a similar pattern in the distribution of the monoclines and described this pattern as being the shallow crustal expression of Precambrian basement fracture zones. These zones trend N. 20° W., N. 55° E., and N. 55° E. The N. 20° W. trend is an element of the north-northwest trend in Sonora, and the N. 20° E. and N. 55° E. trends are elements of the northeast trend in Sonora. Davis reported that there fracture zones are spaced approximately 45 km part. In Sonora, the northeast zones are spaced 30–50 km apart (fig. 3). Similarly, Shoemaker, Squires, and Abrams (1974) described a set of parallel northeast-trending fault systems on the Colorado Plateau, each of which could be traced for more than 100 km. These systems are spaced at approximately 50 km and are observable on Landsat-1 images. They have a Precambrian origin with continued activity to the present and have controlled the emplacement of many bodies of igneous rock. Thus, the pattern on the Colorado Plateau is similar to that in northern Sonora, Mexico; the pattern on the Colorado Plateau is believed to have Precambrian ancestry, and the fractures and faults associated with it are believed to have been active during the Laramide orogeny.

A similar pattern of fractures and faults exist in the copper province of southern Arizona. Rehrig and

Heidrick (1976), Anderson (1966), Schmitt (1966), and Wilson (1962) all make a strong case for the significance of northwest and northeast trends in controlling Laramide mineralization in Arizona. The north-south and east-west trends are given various degrees of significance. Rehrig and Heidrick (1976) studied the trends of Laramide and later Tertiary dikes, veins, and elongate stocks. For the Laramide, they found the major trend was east-northeast ±20° with a minor west-northwest trend. Anderson (1966) and Schmitt (1966) both attributed the northeast trends to Laramide structures that developed under the influence of Precambrian structures and believed the northeast trends to be regionally significant. Similarly, they believed the northwest trends to be regionally significant; these trends have more varied origins, although they are associated with northwest-trending Laramide and Tertiary faults. Specifically, Peterson (1962) concluded that mineralization in the Globe-Miami district of southern Arizona is controlled by a 10-km wide northeast-trending belt that originated in the Late Cretaceous or early Tertiary, but probably reflects a Precambrian zone of weakness. In other Arizona deposits, the regional control and the significance of Precambrian control is not so well understood. Noble (1970) also supported northeast trends in his study of the metallogenic provinces of western North America. The porphyry copper province of southern Arizona is shown as an elongate northeast-trending tract that is truncated on the southwest by a northwest-trending line.

Sonoran patterns

From limited detailed geologic mapping that has been done in northern Sonora, aspects of this same pattern can be documented. The new metallogenic map of Sonora (G. A. Salas, written commun., 1976), as contoured in figure 5, shows northeast trends of density of mineral occurrences that correlate with the northeast lineament zones. For the area in the Sierra Madre southeast of Hermosillo, King (1939) has shown that most of the major north-northwest trending ranges are fault bounded. Most of this deformation apparently occurred during and since the Late Cretaceous. Similarly, at Los Pilares mine, the major structural control is a northwest-trending fault zone that is augmented by east-west fractures (Tenney, 1935). Imlay (1939) and Taliaferro (1933) found a well-developed zone of west-northwest trending faults and dikes from the international border to 30 km south of the border. This west-northwest trend is believed to be related to the northern end of the Mexican geosyncline (Imlay, 1939) or parallel to the Texas lineament zone. Similarly, at Cananea, the north-northwest and west-northwest trends are well developed (R. Avala, Chief Geologist at Cananea, oral commun., 1975), and the northeast trend also is observed.

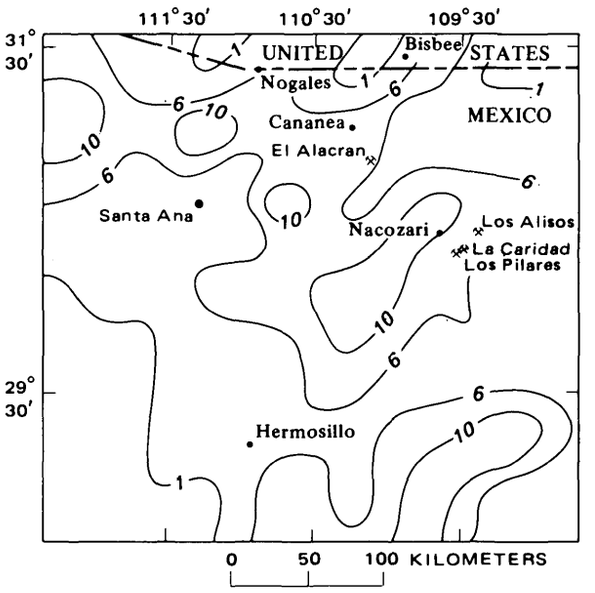

FIGURE 5.—Concentration of mines and prospects, Sonora, Mexico. The unit of measure is the number of mines per 30′ area and was contoured at intervals of 1, 6, and 10 mines and prospects per unit area. No weighting for the size of the mines was used. Original data from the metallogenic map of Sonora, Mexico (G. A. Salas, written commun., 1976).

In detailed studies by Ramirez Rubalcaba and others (1973) at El Alacran and Los Alisos, northwest and northeast trending faults and fractures were observed. The hydrothermal alteration in both of these areas occurs in association with faults of northwest and northeast trends. At El Alacran, an induced-polarization survey was conducted which shows a dominance of northeast-trending structures.

From these referenced reports in which the Cretaceous and younger sedimentary and volcanic rocks are described, the north-northwest and west-northwest trends seem to be well documented. The north-northwest trends are related to block faulting and commonly occur on the flanks of the ranges. The west-northwest trends have been related to faults and dikes. In areas of mineral prospects, the northeast trend is observed in detailed studies and is related to faults and fractures.

The northeast trend is apparently not obvious to field mappers, except where the field mapping involves Precambrian rocks. Salas (1968) studied the Precambrian rocks near Santa Ana, Sonora, and detected the following:

1. The lineations in Precambrian rocks trend on the average northeast (N. 25°–45° E.).
2. The faults trend north-south, northeast, and northwest.
3. The fractures and joints trend predominantly northeast with a complementary, less well developed set trending northwest.

Salas (1968) also showed that the northeast trend is well developed in the Cenozoic extrusive rocks and the Tertiary sedimentary rocks, and the northwest and northeast trends are both well developed in the intrusive rocks. Furthermore, the northeast trend controls the development of smaller streams and arroyos; even a trellis pattern was observed to have these trends (Salas, 1968).

Salas (1968) further reported the occurrence of Precambrian cataclasites, mylonites, and phyllonites. These rocks are related to major fault zones and, on the basis of field relationships, were determined to be of Precambrian age. The Precambrian age is supported by the radiometric dating of related rocks in this part of Sonora. Ages of 1.7, 1.4, and 1.1 billion years have been documented by Anderson and Silver (1970).

In central Mexico, a northeast trend also has been observed in Landsat–1 images and has been checked in a few places by G. P. Salas (written commun., 1975). He reported north-northwest, northwest, and northeast trends and stated that complex intersections of northwest and northeast trends are important controls of mineralization in Mexico. This conclusion is similar to the conclusion that Mayo (1958) and Schmitt (1966) derived for Arizona.

Three statistically significant trends of lineaments are observed in the Landsat–1 images of northern Sonora. These trends are west-northwest, north-northwest and northeast. The west-northwest and north-northwest trends seem to be well documented as related to major faults, the west-northwest trend as related to faults and dikes, and the north-northwest trend as related to block faulting. The northeast trend is less well understood, but it apparently is a trend of joints and faults. These fractures may be related to Precambrian fault zones or shear zones that were reactivated during the Laramide orogenic activity in Sonora. This pattern and the ages of activity are consistent with the relationships observed in southern Arizona, the Colorado Plateau, Mexico, and the Colorado mineral belt.

PROPOSED MODEL AND TARGETS

The pattern of fractures and faults of the model is very much like that in the Colorado mineral belt. I propose that this comparison with the Colorado mineral belt is valid and that exploration targets can be developed as a result of this comparison. The mineralized areas in the Colorado mineral belt, and, therefore, the exploration targets in Sonora have the following characteristics that can be interpreted from Landsat–1 data:

1. Complex intersection of the north-northwest-trending faults with the northeast-trending fracture zones.
2. Association of intersections with hydrothermal alteration.

These characteristics were derived by Tweto and Sims (1963) for the Colorado mineral belt, and they fit the observations derived from Landsat–1 images of Sonora, Mexico. The type of analysis presented here for Sonora was used by S. M. Nicolais (Knepper, 1974, p. 155–168) to define areas of known economic mineralization along the Colorado mineral belt.

Areas with both characteristics are shown in figure 4. These target areas are being evaluated further on the basis of regional geophysical and regional geochemical data to test the validity of the selection and to further define target areas. After this further evaluation, those areas that still appear promising will be investigated by more detailed techniques.

REFERENCES CITED

Anderson, C. A., 1966, Areal geology of the Southwest, *in* Titley, S. R., and Hicks, C. L., Geology of the porphyry copper deposits, southwestern North America: Tucson, Arizona Univ. Press, p. 3–16.

Anderson, T. H., and Silver, L. T., 1970, Reconnaissance survey of Precambrian rocks, northwestern Sonora, Mexico: Geol. Soc. America Abs. with Programs, v. 2, no. 7, p. 484.

Davis, G. H., 1975a, Regional fracture system of the Colorado Plateau as expressed by the monoclinal-fold pattern: Geol. Soc. America Abs. with Programs, v. 7, no. 7, p. 1046.

——— 1975b, Tectonic analysis of folds in the Colorado Plateau of Arizona: U.S. Dept. Commerce, Natl. Tech. Inf. Service Rept. N76–10611, 75 p.

Imlay, R. W., 1939, Paleogeographic studies in northeastern Sonora [Mexico]: Geol. Soc. America Bull., v. 50, no. 11, p. 1723–1744.

King, R. E., 1939, Geological reconnaissance in northern Sierra Madre Occidental of Mexico: Geol. Soc. America Bull., v. 50, no. 11, p. 1625–1722.

Knepper, D. H., 1974, Geologic and mineral and water resources investigation in western Colorado using ERTS–1 data—final report: Colorado School of Mines Remote Sensing Rept. 75–1, 212 p.

Mayo, E. B., 1958, Lineament tectonics and some ore districts of the Southwest: Am. Inst. Mining Metall. and Petroleum Eng. Trans., v. 10, no. 11, p. 1169–1175.

Noble, J. A., 1970, Metal provinces of the western United States: Geol. Soc. America Bull., v. 81, no. 6, p. 1607–1624.

O'Leary, D. W., Friedman, J. D., and Pohn, H. A., 1976, Lineament, linear, lineation—some proposed new standards for old terms: Geol. Soc. America Bull., v. 87, no. 10, p. 1463–1469.

Peterson, N. P., 1962, Geology and ore deposits of the Globe-Miami district, Arizona: U.S. Geol. Survey Prof. Paper 342, 151 p.

Ramirez Rubalcaba, Jose, Osoria, Amador, de la Campa, Genaro, Alarcon L., Ubaldo, Aguilera, Eduardo, Velasco Hernandez, Juan, and Lopez Avila, Javier 1973, Investigaciones geologico-mineras sobre cobre en los prospectos de "Los Alisos," "La Caridad," "El Alacran"—reconocimiento geologico y geofisico regional en el distrito de Nacozari, en el estado de Sonora [Geological-mineral investigations concerning copper in the prospects of "Los Alisos," "La Caridad," "El Alacran"—regional geological and geophysical reconnaissance in the Nacozari district, in the state of Sonora, Mexico]: Mexico, Consejo de Recursos Naturales no Renovables Bol. 79, 97 p.

Rehrig, W. A., and Heidrick, T. L., 1976, Regional tectonic stress during Laramide and Late Tertiary intrusive periods, Basin and Range Province, Arizona: Arizona Geol. Soc. (Tectonic Digest), p. 205–228.

Rowan, L. C., Wetlaufer, P. H., Goetz, A. F. H., Billingsley, F. C., and Steward, J. H., 1974, Discrimination of rock types and detection of hydrothermally altered areas in south-central Nevada by the use of computer-enhanced ERTS images: U.S. Geol. Survey Prof. Paper 883, 35 p. [1975].

Salas, G. A., 1968, Areal geology and petrology of the igneous rocks of the Santa Ana region, northwest Sonora: Soc. Geol. Mexicana Bol., v. 31, no. 1, p. 11–64 [1970].

Schmitt, H. A., 1966, The porphyry copper deposits in their regional setting, *in* Titley, S. R., and Hicks, C. L., eds., Geology of the porphyry copper deposits, southwestern North America: Tucson, Arizona Univ. Press, p. 17–34.

Shoemaker, E. M., Squires, R. L., and Abrams, M. J., 1974, The Bright Angel and Mesa Butte fault systems of northern Arizona, *in* Karlstrom, T. M. V., Swann, G. A., and Eastwood, R. L., eds., Geology of northern Arizona, with notes on archaeology and paleoclimate, pt. 1, Regional studies: Geol. Soc. America Rocky Mtn. Section meeting, Flagstaff, Ariz., 1974, p. 355–391.

Taliaferro, N. L., 1933, An occurrence of Upper Cretaceous sediments in northern Sonora, Mexico: Jour. Geology, v. 41, no. 1, p. 12–37.

Tenney, J. B., 1935, The Pilares mine, Los Pilares de Nacozari, Sonora, Mexico, *in* Copper resources of the world: Internat. Geol. Congress, 16th, Washington, D.C., p. 419–424.

Tweto, Ogden, and Sims, P. K., 1963, Precambrian ancestry of the Colorado mineral belt: Geol. Soc. America Bull., v. 74, no. 8, p. 991–1014.

Wilson, E. D., 1962, A resume of the geology of Arizona: Arizona Bur. Mines Bull. 171, 140 p.

Jour. Research U.S. Geol. Survey
Vol. 6, No. 1, Jan.–Feb. 1978, p. 59–72

PORPHYRY-TYPE METALLIZATION AND ALTERATION AT LA FLORIDA DE NACOZARI, SONORA, MEXICO

By TED G. THEODORE and MIGUEL PRIEGO DE WIT [1]
Menlo Park, Calif.; Mexico 7, D. F.

Abstract.—Pervasive secondary biotite-rich mineral assemblages, characteristic of potassic alteration found in the cores of most commercial porphyry copper systems, are associated spatially with a conspicuous color and a geochemical anomaly at La Florida de Nacozari, Sonora. These composite biotite-magnetite assemblages, with or without actinolite, quartz, rutile, sphene, chalcopyrite, and pyrite assemblages, are primarily the result of early dispersed biotitic (EDB) alteration of andesite. The bulk of the near-surface copper in the area, however, was introduced later by veins that cut the EDB-altered andesite. These late veins are distinguished by a quartz-calcite-chlorite±laumontite±chalcopyrite assemblage, and the chalcopyrite in these veins may reflect upward remobilization of deep EDB copper by fluids associated with the emplacement of nearby coarse-grained granite. Fluid-inclusion relations in the late veins suggest that their fluids were nonboiling and relatively dilute.

At least 25 porphyry copper deposits occur along a 300-kilometer linear belt that extends from Sacaton, Ariz. to La Caridad, Sonora. This structural belt, recognized for many years (Mayo, 1958; Schmitt, 1959; Lowell, 1974; and many others), trends about N. 35° W. (fig. 1) and is partly coinicident with late Mesozoic and early Tertiary granitic plutons, whose exposed parts are elongated in a similar direction. This linear belt containing porphyry copper deposits may also reflect a northwest-striking zone of structural weakness in the Precambrian basement that was reactivated during Mesozoic and Tertiary time and provided conduits for ascending magmas and fluids (Drewes, 1976). North of the international border the belt, as outlined by rocks judged to be the most favorable hosts for major copper deposits, pinches and swells broadly (U.S. Geological Survey, 1973, 1974); in Mexico the belt, as now known, seems to be more narrowly defined by a discontinuous set of conspicuous color anomalies. These color anomalies, formed primarily by the oxidation of disseminated iron sulfides, are especially conspicuous in Sonora between the two commercial porphyry copper deposits at Cananea and La Caridad and at Cananea itself. Outcrops at some of these color anomalies contain visible chalcopyrite and molybdenite in addition to secondary copper minerals. One of these color anomalies occurs in an area of 10 square kilometers in the vicinity of the La Florida mine, an inactive gold-silver mine about 3 km west-northwest of the town of Nacozari and about 15 km northwest of the prophyry copper deposits at La Caridad (fig. 2). The area is in the Basin and Range province of Sonora and straddles, in an east-west direction, the en echelon junction between two north-trending ranges, the Sierra Copercuin and the Sierra Cobriza. The intense reddish color of many outcrops in the vicnity of the old workings at the La Florida mine generated renewed interest in the area in the 1960's, when a resource evaluation of Sonora was jointly undertaken by the United Nations and the Mexican Government (United Nations, 1969). This evaluation eventually culminated in an extensive drilling program by industry and the Government (Amaya, 1971; Vazquez and Islas, 1971) that outlined some low-grade hypogene copper metallization around La Florida.

In 1972 a Scientific and Technical Cooperative Agreement was signed by the Secretaries of State of Mexico and the United States, and in 1974 a cooperative project between the U.S. Geological Survey and Consejo de Recurso Minerales was initiated. The prime focus of the project is to evaluate various geochemical exploration techniques in the Sonoran desert environment. The metallized rocks at La Florida were selected for some of the initial geophysical, geochemical, and geologic investigations in order to provide information on a known mineralized area to compare with other regional studies being conducted as part of the project. As members of this investigation, the authors spent 3 weeks mapping the geology and alteration of about 30 km² at La Florida; these field studies were supplemented by standard petrologic and X-ray exam-

[1] Consejo de Recursos Minerales, Mexico 7, D.F.

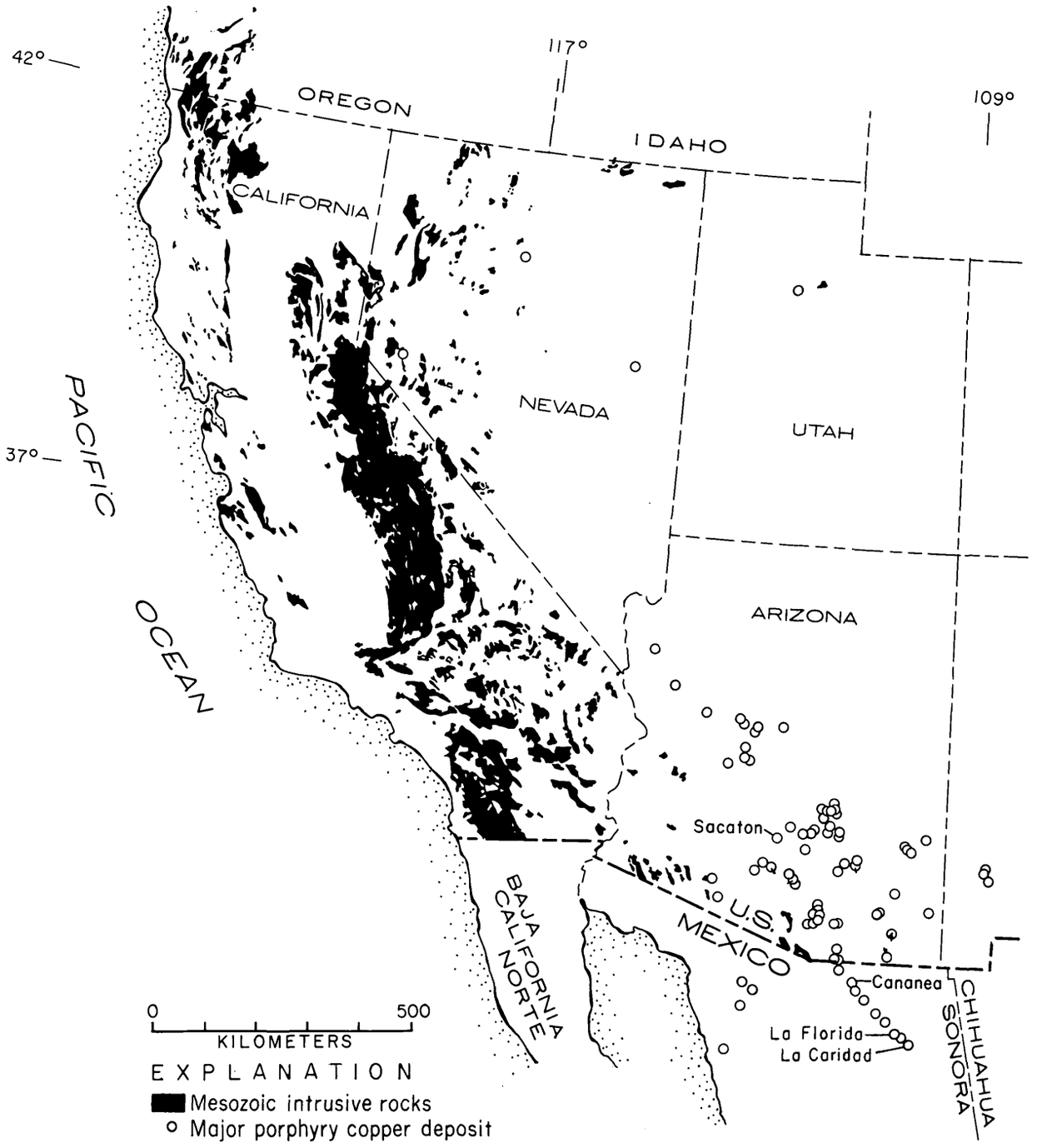

FIGURE 1.—Location of Jurassic and Late Cretaceous and (or) early Tertiary porphyry deposits in southwestern United States and northwestern Mexico, and Mesozoic intrusive rocks in southwestern United States. From Lowell (1974) and Jerome and Cook (1967).

ination of about 125 rock samples of outcrop and drill core. This report describes the geology, classic porphyry-type alteration assemblages (Creasey, 1966; Meyer and Hemley, 1967; Lowell and Guilbert, 1970), and exploration possibilities of the La Florida area.

Acknowledgments.—Our study of the La Florida area was facilitated greatly by the excellent logistic support provided us by other members of the joint U.S.-Mexican team. Fruitful discussions were held in the field and office with Dr. José Luis Lee M., project coleader who first introduced us to the geology and geochemistry of the La Florida area. In the field, we were assisted by Ing. Luis Caire, Ing. Juan Morin, Ing. Arturo Gómez, and Ing. Antonio Ortiz. The staff

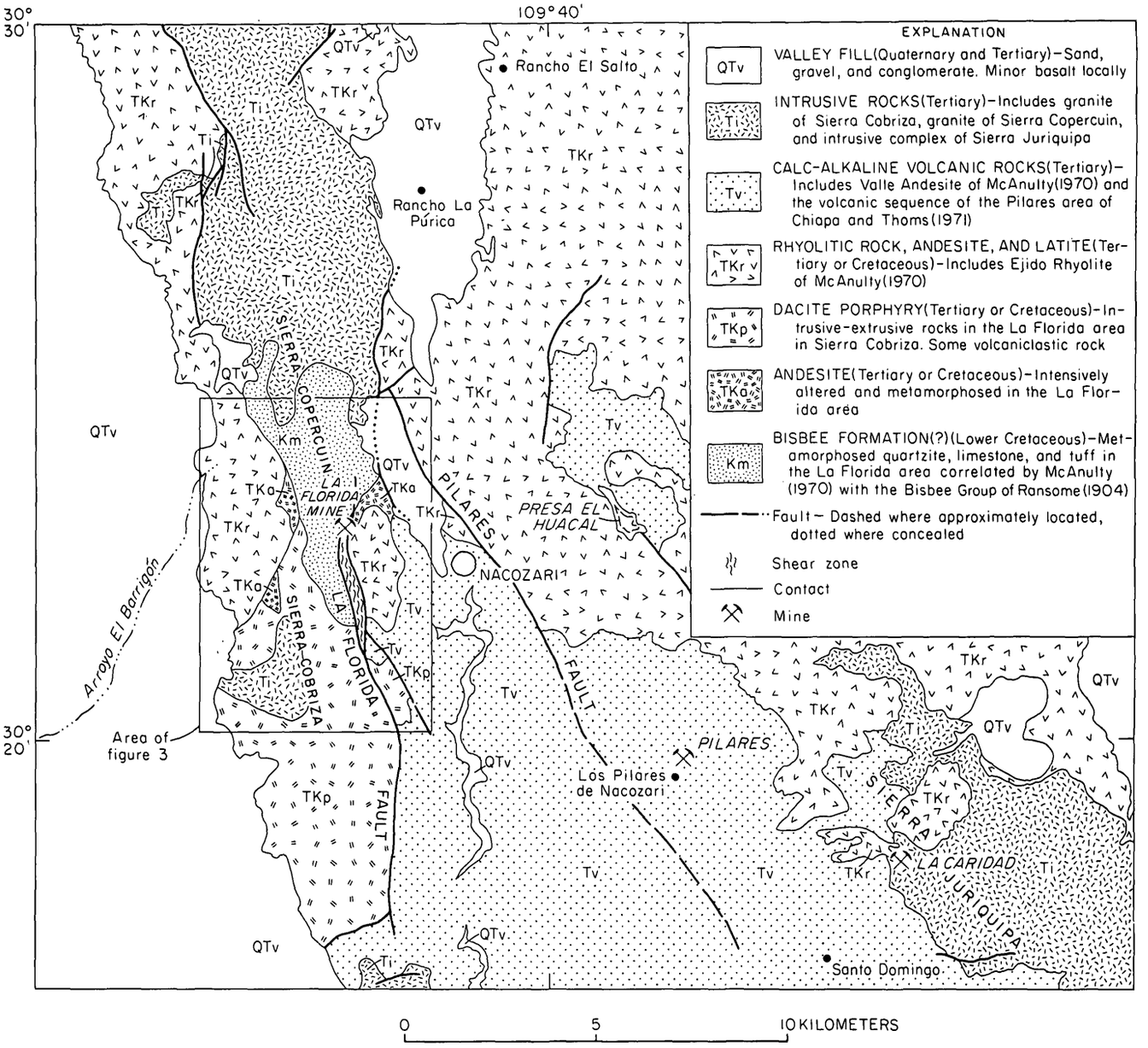

FIGURE 2.—Geologic map of Nacozari-La Caridad region, Sonora. Modified from Consejo de Recursos Naturales No Renovables (1967), McAnulty (1970), and Chiapa and Thoms (1971).

of the Nogales office of the Consejo de Recursos Minerales graciously laid out many hundred of meters of drill core for us to inspect. Field expenses in Mexico for one of us (T. G. Theodore) were paid partly by National Science Foundation Grant AG525 to the U.S. Geological Survey.

GENERAL GEOLOGY

The La Florida area is lithologically and structurally complex (fig. 3). Table 1 summarizes the stratigraphic units exposed in the La Florida area. Regional stratigraphic assignments of the rocks at La Florida, however, necessarily must be tentative until in-depth studies of the stratigraphy and structure of the region are completed. The block of rocks making up the topographically high core of the area consists of steeply dipping, tightly folded, and metamorphosed Early Cretaceous quartzite, limestone, conglomerate, and tuff, and Cretaceous or Tertiary andesite, all of which have been partly intruded by Cretaceous or Tertiary dacite porphyry. The age of the metasedimentary rocks is not established firmly. Four previous reconnaissance geologic studies in the Sierra Copercuin

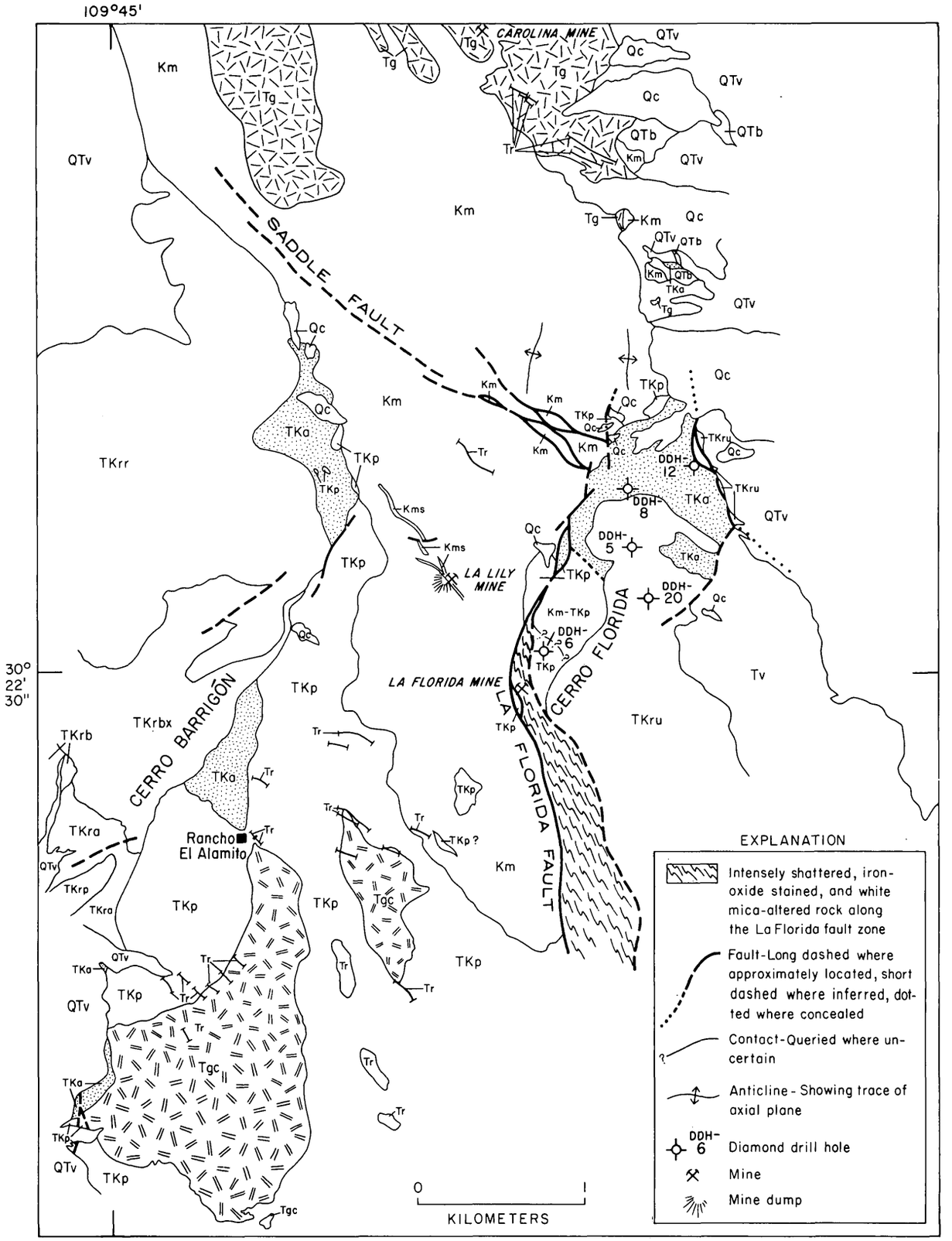

FIGURE 3.—Geologic map of the La Florida area, Sonora, Mexico. Geology by M. Priego de Wit and T. G. Theodore, unpub. data, 1974; in part modified from Vazquez and Islas (1970).

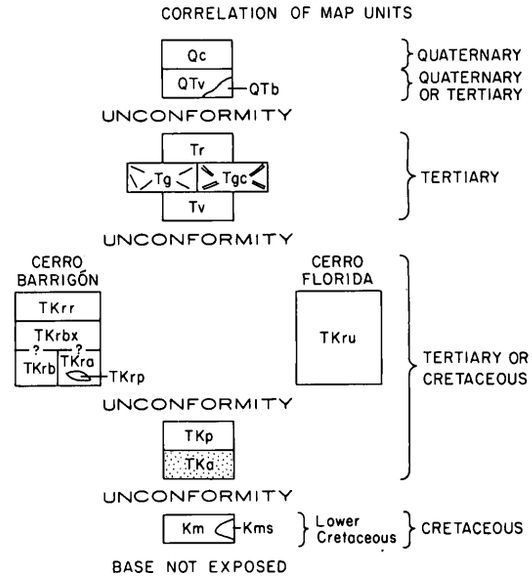

DESCRIPTION OF MAP UNITS

Qc	COLLUVIAL DEPOSITS - Locally well-stained by iron oxide
QTv	VALLEY FILL - Sand, gravel, and conglomerate. Shallow dips
QTb	Basalt
Tr	RHYOLITE DIKES AND PLUGS
Tg	GRANITE OF SIERRA COPERCUIN
Tgc	GRANITE OF SIERRA COBRIZA
Tv	VALLE ANDESITE OF McANULTY (1970)
	REPRESO MEMBER OF EJIDO RHYOLITE OF McANULTY (1970). Includes:
TKrr	Rhyolite tuff
TKrbx	Volcanic breccia
TKrb	Black andesite
TKra	Andesite tuff
TKrp	Dacite porphyry - Locally interbedded
TKru	Represo Member, undivided, of Cerro Florida
TKp	DACITE PORPHYRY - Plugs, sills, and flows
TKa	ANDESITE - Pervasively altered and mineralized
Km	QUARTZITE, LIMESTONE, CONGLOMERATE, AND TUFF - Metamorphosed. Questionably correlated by McAnulty (1970) with the Lower Cretaceous Bisbee Group of Ransome (1904) in southeastern Arizona
Kms	Skarn - Converted from limestone as at the La Lily mine

suggested that the age of the limestone and marble-bearing metasedimentary rocks there is either unknown (Wade and Wandke, 1920; Consejo de Recursos Naturales No Renovables, 1967) or Paleozoic (Imlay, 1939; Fries, 1962). McAnulty's study (1970), based on lithologic and stratigraphic similarities of these sedimentary rocks to the Lower Cretaceous Bisbee Group of southeastern Arizona (Ransome, 1904), suggested that the sequence of metasedimentary rocks exposed in the Sierra Copercuin may be Early Cretaceous. In this report, we accept McAnulty's (1970) correlation of these rocks with the Bisbee (fig. 3); we have not, however, subdivided the metasedimentary rocks, other than to show some skarn, because of the limited extent of our mapping. In the area studied, gray-green andesite of Cretaceous or Tertiary age crops out mainly in three areas on both the east and the west flanks of the range. The three main outcrops are irregularly shaped areas that range in area from 0.25 to 0.75 km^2 and have a subdued topography with gentle slopes, except for several deeply incised arroyos. Several deep drill holes, whose locations are not shown in figure 3, were collared in andesite and bottomed in metaquartzite (Vazquez and Islas, 1970), suggesting to us that the andesite was deposited unconformably as a volcanic flow on the metasedimentary sequence. The andesite is intensely hydrothermally altered, and it hosts the bulk of the known copper metallization in the area. Porphyries, mostly dacitic in composition, make up a silicic lava complex consisting of near-surface intrusions, flows, and sills that are partly intrusive into the andesite and the metasedimentary rocks. These variably altered porphyries compose part of the Lily Formation of McAnulty (1970). Previously formed structural discontinuities, including faults and unconformities, localized emplacement of the intrusive porhyries. Some outcrops of the porphyries include abundant fragments of the metasedimentary wallrock.

Cretaceous or Tertiary volcanic rocks, assigned by McAnulty (1970) to the Represo Member at the base of his Ejido Rhyolite, rest with a slight angular unconformity on the sequence of rocks described above. Where it crops out on the flanks of the range, the Ejido Rhyolite dips shallowly outward from the core of the range. Near the La Florida mine in Cerro Florida, the Represo Member is undivided and comprises air-fall or rhyolitic ash-flow tuff, minor amounts of intercalated porphyritic andesite flows, and sandy beds of volcaniclastic debris. A diamond drill hole (DDH–20, fig. 3), collared in uncompacted rhyolitic crystal-lithic tuff in the Represo Member, penetrated about 102 meters of the member before passing into dacite porphyry (Vazquez and Islas, 1970). Locally the Represo Member is intensely hydrothermally altered; it is bleached, silicified, and flooded with white mica-pyrite-quartz-carbonate ± potassium feldspar mineral assemblages. West of Rancho El Alamito

TABLE 1.—*Stratigraphic units exposed in the La Florida area, near Nacozari, Sonora*

Formation	Age	Thickness (meters)	Lithology
Valley fill	Quaternary or Tertiary	30	Sand, gravel and conglomerate; includes minor basalt
Valle Andesite of McAnulty (1970)	Tertiary	200	Andesite, partly altered
Represo Member of the Ejido Rhyolite of McAnulty (1970)	Tertiary or Cretaceous	60-300	Rhyolitic tuff, volcanic breccia, andesite, andesitic tuff
Andesite	Tertiary or Cretaceous	90-170	Andesite, metallized
Quartzite, limestone, conglomerate, and tuff	Early Cretaceous	500+	Metamorphosed

near Cerro Barrigón (fig. 3), the base of the Represo Member is not exposed. Here we divided the member into five units. A basal andesitic tuff is interbedded with a dacite porphyry and a distinctive black andesite. These units appear to be overlain unconformably by volcanic breccia that contains remarkable concentrations of secondary pyrite and epidote. The uppermost unit of the Represo Member here is a rhyolite tuff that is also locally altered and pyritized.

A small lobe of the widespread Tertiary Valle Andesite of McAnulty (1970) extends from southeast of Nacozari into the east-central part of the study area. The Valle Andesite here crops out in an area of about 1 km^2 and rests stratigraphically on the undivided Represo Member. The Valle Andesite is the basal formation of the regionally extensive suite of calc-alkaline volcanic rocks that surrounds the nearby loci of major copper metallization at Pilares and La Caridad (Chiapa and Thoms, 1971). Chiapa and Thoms refer to the Valle Andesite as the "andesites of the area west of Pilares." In the La Florida area, only a small part of the Valle Andesite is altered. Where exposed, the altered rock contains mostly assemblages of quartz, chlorite, epidote, pyrite, and chalcopyrite. It is important to note that this formation is the youngest volcanic unit exposed in the area that contains copper metallization. Locally, near the base of the Valle Andesite, there are some dacite and rhyodacite flows (not shown in fig. 3); they contain a microcrystalline groundmass of alined plagioclase microlites and also some wispy flow bands of devitrified glass that in very small domains show a well-developed eutaxitic texture.

Several coarse-grained Tertiary granite plutons and many small rhyolite dikes crop out at La Florida (fig. 3). (We categorize the coarse-grained rocks using the modal classification of Streckeisen and others 1973). On the north, the granite of Sierra Copercuin intrudes the Cretaceous metasedimentary rock. Near the south edge of the area of figure 3, two small plutons of the granite of the Sierra Cobriza crop out in an area of about 2 km^2 and intrude the Cretaceous or Tertiary dacite porphyry. McAnulty (1970) combined the granite of the Sierra Copercuin and the granite of the Sierra Cobriza into a single map unit, his Carolina stock. Although these two granites of ours are probably about the same age and have the same overall chemical composition, we nonetheless differentiate between them because the granite of the Sierra Cobriza seems to be more intensely altered by secondary fluids than the granite of Sierra Copercuin. Textures of both units are generally hypidiomorphic-granular; however, a porphyritic facies is present locally. This facies exhibits some droplike intergrowths of quartz and alkali feldspar similar to those from copper-bearing porphyries elsewhere in the Basin and Range province. The porphyritic facies grades into the hypidiomorphic one. The most common type of secondary alteration in the granite of the Sierra Cobriza is white mica, quartz, and pyrite along fractures and joints that cut the unit. This sericitic alteration is not notably pervasive through the unit. Many narrow rhyolite dikes occur throughout the La Florida area; most of them have a northwest-southeast strike parallel to the swarm of rhyolite dikes north of the Carolina mine (fig. 3) mapped by McAnulty (1970). Most of these dikes are also hydrothermally altered by a quartz-white mica-pyrite assemblage.

Some unaltered and unmetallized basalt flows crop out near the northeast corner of the area; these rocks underlie and are partly interbedded with the uncon-

solidated Tertiary or Quaternary gravel that fills the valley east of La Florida.

Several faults in the La Florida area are important premetallization structures that localized fluids associated with some of the alteration assemblages. One of these, the La Florida fault (fig. 3), is probably the major structural feature in the area mapped. The La Florida fault is a north-south-striking east-dipping normal fault that includes a zone of shattered and iron-oxide-stained rock as much as 0.3 km wide along its trace near the southern part of the area. The now inactive and inaccessible workings of the La Florida mine penetrated copper- and precious-metal-bearing veins along the fault. The width of shattered clayey rock and numerous individual fault strands along this fault zone further suggest a history of repeated movement, perhaps continuing long after circulation of metal-bearing fluids ceased. On the basis of the present position of the base of the Represo Member east of the La Florida fault zone, cumulative vertical separations across the fault zone measure at least 200 m in the general area of the La Florida mine. The amount of offset apparently decreases from south to north. In the general area of the Cretaceous or Tertiary andesite just northeast of the La Florida mine, the zone seems to have stepped en echelon toward the east across the andesite (fig. 3). Here major displacements along the fault zone probably border the andesite on the east, and the fault zone changes its strike to about N. 30° W., which locally parallels the trace of the Pilares fault (fig. 2). Along the La Florida fault, the tuff of the Represo Member is altered intensely to white-mica and pyrite assemblages. McAnulty's (1970) map of the area north of the Carolina mine (fig. 3) shows a continuation of the La Florida fault zone that brings granite of the Sierra Copercuin against several members of the Ejido Rhyolite and against the valley-fill gravel. North of the Carolina mine the La Florida fault resumes its overall north-south strike.

METALLIZATION AND ALTERATION

The bulk of the copper metallization outlined by drilling centers on the andesite that crops out in a 0.75-km² area northeast of the La Florida mine (fig. 3). The andesite, locally at least 170 m thick, is probably a flow; it may reflect some of the earliest volcanism in this province during Late Cretaceous or early Tertiary time. Exposures of the andesite commonly contain supergene copper minerals, mostly chrysocolla and malachite. Vazquez and Islas (1971) documented a bedrock geochemical anomaly from this area northeast of the La Florida mine. Copper concentrations range from 530 to 3500 parts per million. At depth below the oxide zone, copper typically is dispersed through the andesite in concentrations that range from a few tenths of a percent to almost 2 percent by weight. Analyses given in Vazquez and Islas (1970) show the distribution of copper and molybdenum in drill hole DDH–5 (fig. 4), which was collared 0.25 km south of the main exposure of the andesite (fig. 3). About 150 m of dacite porphyry, which is intrusive into andesite and which we judge to have accompanied the early stage alteration of the andesite, was penetrated by drill hole DDH–5 (fig. 4). Copper concentrations in the porphyry range from 50 to 1900 ppm (Vazquez and Islas, 1970). In this hole, the andesite was found at depths from 212 m below ground surface to the bottom of the hole at 385 m below ground surface. Copper as chalcopyrite is the dominant metal introduced into the andesite. Vazquez and Islas (1970) stated that gold was not detected in any samples of the andesite at a lower limit of detection of 0.1 ppm, silver occurs at concentrations of 5–13 ppm, molybdenum at concentrations of 20–150 ppm, and zinc at concentrations of 65–230 ppm. There are some notable concentrations of zinc in the hole in rocks assigned to the Represo Member. Zinc was found at concentrations up to 7000 ppm near the top of the hole in a few 3-m intercepts of highly altered andesite belonging to the undivided Represo Member.

The introduction of hypogene copper into the andesite at La Florida reflects metallization during two stages of hydrothermal alteration. An early dispersed replacement stage was first, wherein chalcopyrite was introduced penecontemporaneously with a strong flooding of the andesite by high concentrations of very fine grained secondary biotite. This early dispersed biotitic (EDB) stage was followed by a quartz-calcite-chlorite stockwork vein stage containing significant concentrations of additional chalcopyrite and the zeolite, laumontite ($CaO \cdot Al_2O_3 \cdot 4SiO_2 \cdot 4H_2O$). The bulk of the copper was introduced into the andesite during this event. Representative textural relations result from these two major postmagmatic events (fig. 5 and 6). Quartz-white mica-pyrite alteration at La Florida has affected rocks as young as the granite of the Sierra Cobriza and the rhyolite dikes. Textural relations among these various alteration types suggest that quartz-white mica-pyrite alteration occurred penecontemporaneously with the quartz-calcite-chlorite stockwork veins.

In our study at La Florida, we have been able to determine the relative age of copper metallization but not the radiometric age. Most likely, however, the age of metallization is Late Cretaceous or early Tertiary.

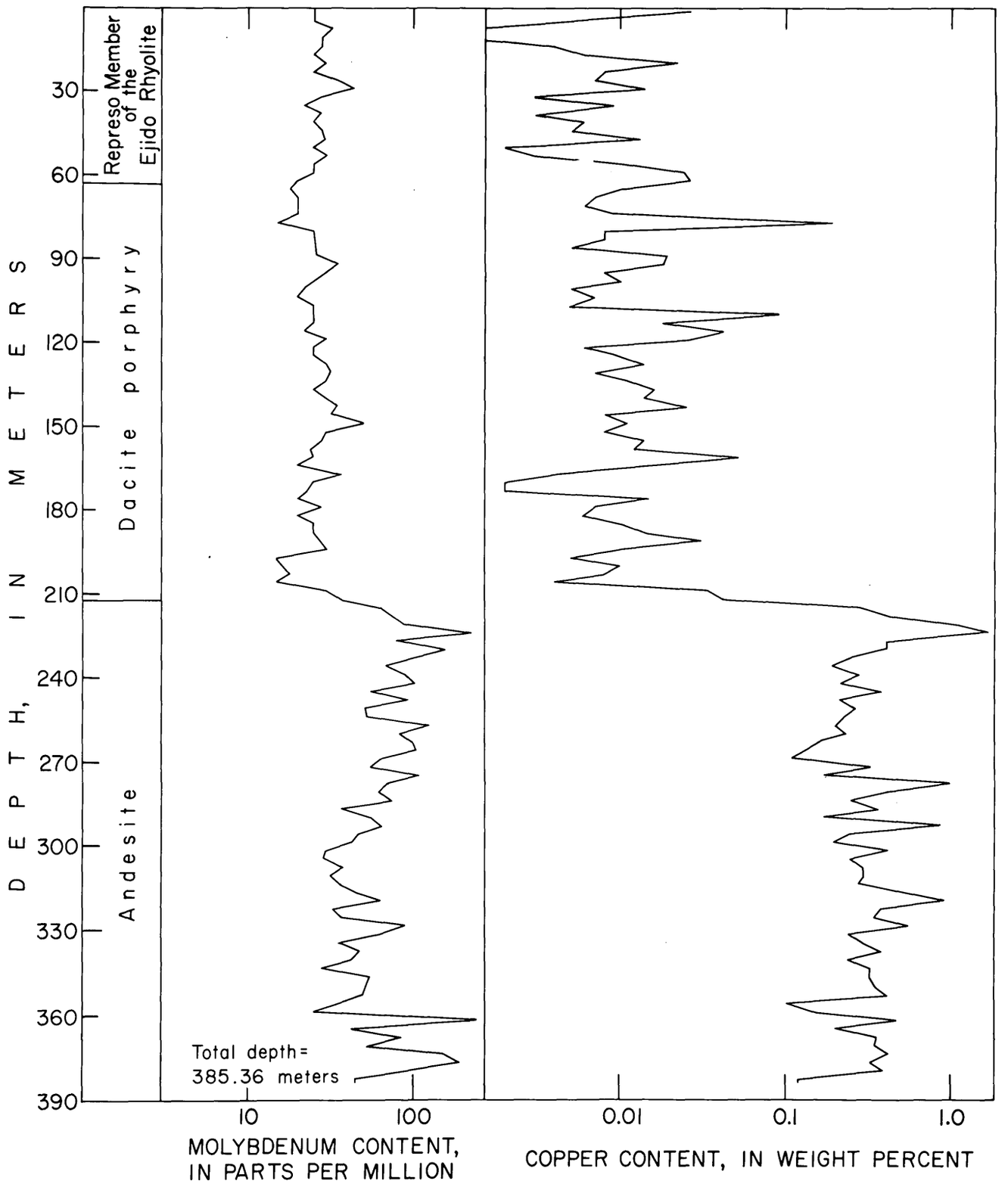

FIGURE 4.—Lithology and distributions of copper and molybdenum in core samples from drill hole DDH–5. Prepared from analyses given in Vazquez and Islas (1970).

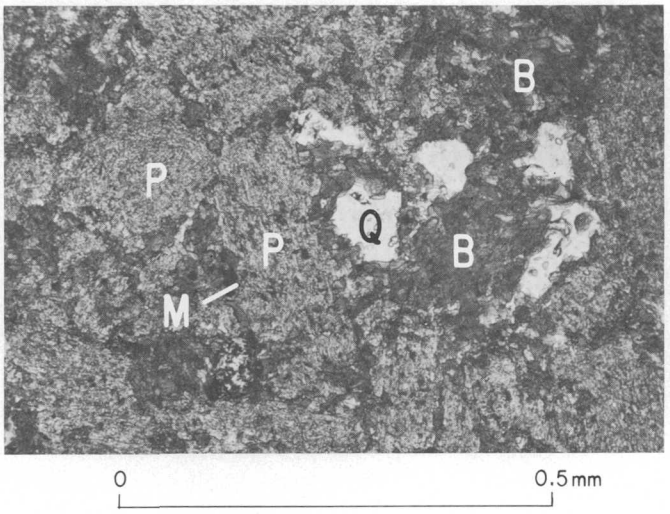

FIGURE 5.—Photomicrograph showing textural relations of early dispersed biotitic alteration of andesite at La Florida. Sample from drill hole DDH–5, 293 m below ground surface. B, biotite; P, plagioclase; M, magnetite; Q, quartz. Plane-polarized light.

The epigenetic introduction of copper (as chalcopyrite) into the andesite probably reflects circulation through the andesite of fluids associated with the emplacement of the dacite porphyry. McAnulty (1970) recognized the importance of this porphyry (his quartz-feldspar porphyry stock and dike unit) in the genesis of this porphyry copper system; however, he ascribed the bulk of the copper metallization to a small porphyry body that crops out near the La Florida mine. We believe that the entire porphyry complex must be considered as potential source for the fluids; our reasons for this are detailed below. A few absolute ages of intrusion and metallization are available from some other nearby areas for comparison. Damon (1968) reported an age of 54 ± 1.6 million years for metallization at the Guadalupe mine, near La Caridad; this is based on a determination of the age of pegmatitic biotite using the potassium-argon method. Livingston (1973) found that at La Caridad a suite of hydrothermally altered premetallization intrusive rocks yielded $54.0 \pm 1.6 - 48.9 \pm 1.9$ m.y. by the potassium-argon method. P. E. Damon (oral commun., 1976) also found that biotite from a quartz monzodiorite sampled near Batamote (about 16 km northwest of La Florida) has a 55.4 ± 1.2 m.y. age. All of these absolute ages fall into either the Paleocene or the Eocene Epoch.

EARLY DISPERSED BIOTITIC ALTERATION

The EDB alteration is the most penetrative type of alteration present in metallized andesite and is mentioned briefly by Salas and Hollister (1972). Greenish-brown biotite, the dominant indicator mineral of this alteration stage, is ubiquitous in the andesite. This secondary biotite is undoubtedly rich in magnesium, and, at La Florida, rarely occurs in veins that cut the igneous fabric of the andesite. Instead, this biotite, in places accompanied by secondary magnetite and other minerals, pervades the andesite and locally composes as much as 60 percent of it. The secondary biotite replaces plagioclase laths along their margins and penetrates plagioclase crystals along cleavage and twin planes but mostly occurs in the groundmass of the

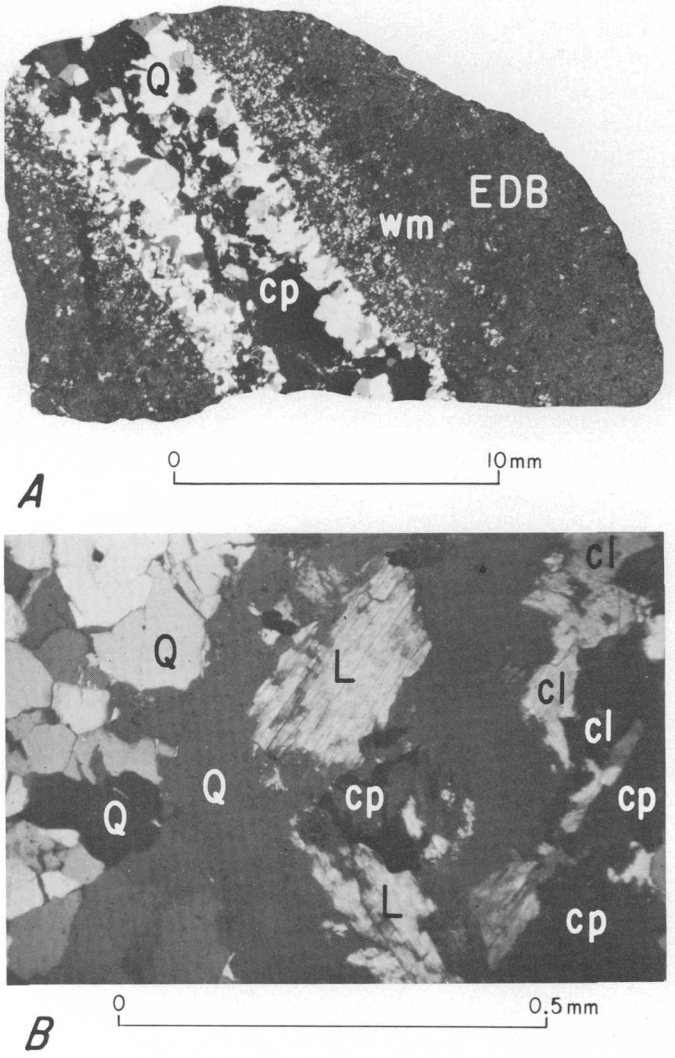

FIGURE 6.—Photomicrographs showing textural relations of early dispersed biotitic alteration. *A*, EDB-altered andesite cut by late-stage stockwork vein, containing abundant quartz (Q) and chalcopyrite (cp), mantled by a quartz- and white-mica-bearing alteration envelope (wm). *B*, Quartz (Q), chlorite (cl), laumontite (L), and chalcopyrite (cp) in the vein. Sample from drill hole DDH–5, 293 m below ground surface. Partially crossed nicols.

rocks. Because few veins are associated with this stage of alteration, we suggest that the flooding by secondary biotite was a relatively passive event and that the andesite was not yielding by brittle failure during EDB alteration. Much of the plagioclase interjacent to the biotite appears unaltered under the microscope; phenocrystic laths have a composition in the range An_{55-70} and 0.1- to 0.2-millimeter-long microlites are roughly An_{40} in composition. Plagioclase zoning is normal and in places very pronounced. Typically, interstices between poorly oriented plagioclase crystals are filled by dense mats of very fine grained secondary biotite that include equant granules of magnetite. Some specific mineral assemblages of the EDB alteration observed are:

a. biotite-apatite-quartz-rutile-magnetite;
b. biotite-chalcopyrite-pyrite-magnetite;
c. biotite-actinolite-magetite-quartz-chalcopyrite-epidote;
d. biotite-sphene-magnetite; and
e. biotite-white mica-magnetite-pyrite.

In addition, secondary amphibole present in these rocks is pale blue green under the microscope and presumably is a variety of actinolite that is intermediate in composition between the end members tremolite and ferrotremolite (Deer and others, 1963). Where this actinolite is abundant in the andesite, some clouding of plagioclase has also occurred as a result of the presence of minute secondary minerals. Some clots of intergrown actinolite and secondary biotite seem to have replaced primary hornblende and primary biotite, which occur locally in minor amounts as relicts in the andesite. In outcrops of andesite, the disseminated chalcopyrite has been altered by supergene fluids to malachite and (or) chrysocolla.

Our petrographic and field observations suggest that the intensity of the EDB alteration varies laterally and vertically through the andesite. In the general area of drill hole DDH–8, near the west edge of one major body of andesite (fig. 3), the andesite seems to be replaced to a greater extent by actinolite-bearing EDB assemblages than it is in andesite penetrated by DDH-12, which is near the easternmost part of the body. We found no actinolite in the four samples of andesite we examined from 243 m of this unit penetrated by drill hole DDH–12. The variability of EDB alteration with depth is reflected in the andesite penetrated by drill hole DDH–5. In this hole, the six samples of andesite examined, ranging from 229 m to almost the very bottom of the hole at 385 m below the collar, show a progressive increase in the intensity of EDB alteration with depth. The most intensely altered rock is the deepest sample, which shows plagioclase laths that are now diffuse shadows of their former crystal outlines because they have been heavily permeated by EDB alteration minerals. In this hole, however, actinolite is not found in the rocks that contain the highest concentration of EDB minerals. Instead, actinolite seems to be confined to some domains of the andesite originally rich in primary amphibole.

We want to stress the fact that rocks containing EDB alteration are not notably enriched in copper at the levels of the porphyry system penetrated by the drill holes. Nevertheless, as we described above, there are minor amounts of sulfide (chalcopyrite and pyrite) dispersed through and intergrown with EDB assemblages containing abundant secondary magnetite. Early-stage chalcopyrite appears to be evenly distributed through rocks of the biotite and biotite-actinolite assemblages, in contrast to that reported by Carson and Jambor (1974) in some porphyry prospects in British Columbia and by Lanier, Folsom, and Cone (1975) in the Bingham, Utah, porphyry deposit. Our failure to recognize such a relation may reflect a low contrast in copper concentrations between these two EDB assemblage types, a difference in concentration that was overwhelmed by the subsequent deposition of additional copper in stockwork veining during the succeeding quartz-calcite-chlorite vein stage. Some chalcopyrite and pyrite are found locally intergrown with and temporally part of the most intense EDB alteration; however, the overall copper content is still not very high. We examined samples from drill hole DDH–5 between depths of 381 and about 385 m. These samples show some of the strongest EDB alteration found; however, copper concentrations do not exceed 0.12 percent.

Minerals diagnostic of EDB alteration were found in only two other rock units at La Florida: the metasedimentary rocks and the dacite porphyry. Alteration of quartz-rich metasedimentary sequences commonly yielded a biotite hornfels (quartz-biotite-white mica-tourmaline ± garnet ± epidote ± magnetite ± sulfide composite assemblages); some metasedimentary rocks near the granite of the Sierra Cobriza were metamorphosed to a hornblende hornfels; alteration of carbonate-rich beds at the La Lily mine (fig. 3) yielded garnet-pyroxene skarn (Nasser Nasser, 1968) or epidote skarn probably derived from a garnet skarn. Although not very abundant, there nonetheless is some secondary biotite and potassium feldspar in the dacite porphyry dispersed locally through the groundmass of the dacite porphyry on the Sierra Cobriza, at least 4 km south of the major body of metallized

andesite. The restriction of EDB alteration assemblages to the older rock units in the area (the metasedimentary, dacite porphyry, and andesite units) suggests that all rocks younger than these, including the Represo Member, the Valle Andesite, and the granites of the Sierra Cobriza and the Sierra Copercuin, were not present prior to the EDB alteration stage.

QUARTZ-CALCITE-CHLORITE ALTERATION

A mineral assemblage including quartz, calcite, and chlorite is common to most of the late hypogene stage veins that cut EDB-altered andesite. These calcic veins range in width from 0.5 to 10.0 mm, and their minerals, which became stable as the porphyry system evolved, are the ones primarily associated with the bulk of the copper anomaly determined in the exposures of the andesite. Some specific mineral assemblages in these veins are as follows:

a. chlorite-calcite-quartz-epidote-pyrite-sphalerite;
b. quartz-pyrite-chalcopyrite-chlorite;
c. calcite-quartz-chlorite-chalcopyrite-magnetite;
d. calcite-laumontite;
e. laumontite-quartz-chalcopyrite-pyrite-magnetite-sphene (trace)-calcite (trace);
f. quartz-calcite-chlorite-sphene-pyrite-chalcopyrite-sphalerite(?, trace)-white mica (trace);
g. quartz-calcite;
h. quartz-calcite-laumontite-chalcopyrite;
i. quartz-chlorite-calcite-chalcopyrite; and
j. molybdenite-quartz-calcite-epidote-albite.

Wallrock alteration adjacent to these veins forms narrow envelopes variably penetrative into the surrounding EDB-altered groundmass. Many of the envelopes measure several millimeters across, and they may consist of (1) alteration of EDB biotite to white mica and (or) chlorite, (2) crystallization of sphene, (3) alteration of some plagioclase to white mica and possibly kaolinite, and (4) introduction of quartz. Samples from some localities indicate that the bulk of the EDB biotite has been altered to chlorite and that epidote has crystallized as irregular small clots replacing the cores of plagioclase crystals. Alteration assemblages that include chlorite, calcite, and quartz are found at La Florida in rocks as young as the Valle Andesite. Some outcrops of volcanic breccia belonging to the Represo Member, northwest of Rancho El Alamito (fig. 3), include widespread and abundant concentrations of epidote and pyrite that probably formed penecontemporaneously with the quartz-calcite-chlorite veins.

The dacite porphyry initially contained more potassium and less iron and magnesium than did the andesite; consequently, alteration of the dacite porphyry by fluids associated with the quartz-calcite-chlorite stage of alteration seems to have yielded mineral assemblages similar to those in the stockwork veins and their envelopes but including some white mica (sericite?) and kaolinite. White mica and kaolinite are especially well developed in the sill of dacite porphyry penetrated by drill hole DDH–5, where sanidine phenocrysts have been replaced partially by intergrown kaolinite, chlorite, calcite, and pyrite, and some plagioclase phenocrysts (about An_{35}) have been almost completely replaced by white mica. A representative assemblage, composited from our petrographic studies of the dacite porphyry, would be quartz, chlorite, calcite, white mica (sericite?), and epidote, with or without kaolinite, pyrite, magnetite, chalcopyrite, apatite, and sphalerite(?). The andesite is strongly altered to this assemblage for a distance of at least 3 m from the porphyry-andesite contact. In spite of this strong alteration, some relict EDB biotite can still be recognized in the andesite near this contact.

Fluid inclusions in the late-stage veins are not well developed; they are generally very sparse and extremely small (<5 microns). In a few larger veins, the fluid inclusions are correspondingly larger. These inclusions are a two-phase (liquid-plus-vapor) type at room temperature. Most inclusions contain more or less uniform proportions of liquid and vapor. The vapor bubble makes up about 10–20 percent of the volume of a typical inclusion, and, if tests were made with a heating stage, they would most likely fill with liquid at relatively low temperatures (less than 250° C). This low temperature is inferred from observations and extensive tests on similar inclusions from other mineral deposits. We did not see any halide-bearing or gas-rich inclusions in samples collected from any of these veins; consequently, we believe that the fluids associated with the late veins at La Florida were not boiling during their emplacement (see Nash, 1976). A few small inclusions that contain daughter minerals were noted in some secondary quartz-actinolite intergrowths formed during the EDB stage of alteration; however, these daughter minerals are so small that they could not be identified, even at magnifications of 1000×. Their morphology suggests that the daughter minerals may be anhydrite, which occurs in many other porphyry systems. Some quartz phenocrysts in dacite porphyry intensely altered to white mica, sampled in drill hole DDH–6 near the La Florida mine (fig. 3), contain the gas-rich liquid-plus-vapor type of inclusion.

QUARTZ-WHITE MICA-PYRITE ALTERATION

Quartz-white mica-pyrite alteration at La Florida has affected rocks as young as the granites of the Sierra Cobriza and the Sierra Copercuin and the rhyolite dikes (fig. 3). This type of alteration is not pervasive in the granite of the Sierra Cobriza but is instead confined mostly to structures. Outcrops of this granite commonly show concentrations of quartz, white mica, and pyrite along fractures and joints, a relation indicating that some fluids associated with this alteration circulated through the granite after it had solidified to the point where it could sustain brittle fracture. In those localities where this alteration is pervasive, quartz, white mica, and pyrite are associated with some chlorite, epidote, and very minor amounts of tourmaline. The general paucity of tourmaline at La Florida contrasts with the nearby La Caridad deposit, where tourmaline is abundant in rosettes over the central part of the ore body (Saegart and others, 1974). At La Florida, quartz-white mica-pyrite alteration is best developed, both in terms of volume of rock affected and in amount of alteration minerals crystallized, in the Represo Member east of the La Florida mine and along the La Florida fault zone.

PROPOSED MODEL FOR THE LA FLORIDA PORPHYRY COPPER SYSTEM

Our geologic study suggests a multistage extrusive and intrusive history at La Florida combined with a related series of hypogene alteration events to compose a porphyry-type system (fig. 7). The bulk of the metallization is found in an andesite host rock, which is altered intensely by superposed or telescoped (Titley, 1975) types of alteration. Both of these distinct types of alteration occurred contemporaneously with the introduction of chalcopyrite and very minor amounts of molybdenite. Early EDB or potassic alteration was followed by late stockwork fracturing and veining. Most of the copper was introduced during this stockwork veining into the levels of the porphyry system tested to date by drilling. The mineral assemblages of the stockwork veins are similar to propylitic alteration assemblages in many other porphyry deposits. At La Florida, the bulk of the EDB alteration is associated temporally and genetically, but not necessarily spatially, with emplacement of intrusions belonging to an extensive complex of dacite porphyry. Although dacite porphyry crops out in several small exposures near the largest exposures of metallized andesite, the main mass of the dacite porphyry is exposed about 2 km to the southwest, where it makes up more of the Sierra Cobriza (fig. 3). The dacite porphyry also contains some secondary biotite there at some localities, but the biotite is not as pervasive as that in andesite. Textures of the dacite porphyry are in places similar to intrusive rocks intimately associated with porphyry copper mineralization elsewhere in the Basin and Range province. Rock textures in the dacite porphyry complex also emphasize the subvolcanic environment of the porphyry system at La Florida. We further suggest that the evolution of the porphyry system at La Florida was interrupted by uplift and erosion some time after the EDB stage of alteration and that the volcanic and volcaniclastic rocks of the Represo Member, and probably the Valle Andesite, were deposited after uplift and erosion. The intrusive and alteration history of the area appears to have culminated during emplacement of the granites of the Sierra Cobriza and the Sierra Copercuin (fig. 7). Widespread but only locally pervasive quartz-white mica-pyrite alteration seems to be associated genetically with the granite of the Sierra Cobriza. The chalcopyrite-bearing quartz-calcite-chlorite stockwork veins in the andesite may have formed preferentially in the andesite from the same fluids that yielded the quartz-white mica assemblages in the Represo and the granite. We believe that the quartz-calcite-chalcopyrite vein

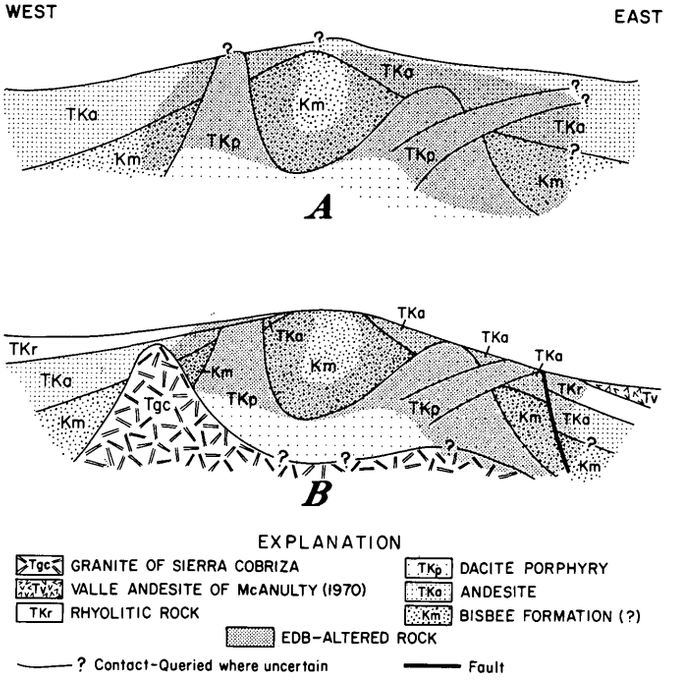

FIGURE 7.—Schematic cross section showing sequential development of porphyry copper system at La Florida. *A*, Emplacement of dacite porphyry penecontemporaneously with EDB alteration in premineral andesite. *B*, Subsequent emplacement of granite of Sierra Cobriza associated with extensive quartz-white mica-pyrite alteration of the Represo Member and other units, and probably with quartz-calcite-chlorite stockwork veining in andesite.

stage in the andesite and the other temporally related alteration phenomena do not reflect retrograde collapse at the end of the EDB event. These alteration types are best explained by a separate and discrete circulation of fluids subsequent to EDB alteration. The fluids probably were channeled by the La Florida fault zone and were temporally related to the granite of the Sierra Cobriza, which acted as a heat source driving their circulation.

Physical conditions during alteration and metallization at La Florida can be deduced from the geologic environment of the porphyry system and by referring the observed mineral assemblages to experimentally determined stabilities. A probable maximum cover of about 2 km (equivalent to about 53,000 kilopascals lithostatic pressure and 20,000 kPa hydrostatic pressure) can be reconstructed over the La Florida area during the late-vein stage of alteration (see McAnulty, 1970; Chiapa and Thoms, 1971). The widespread brecciation at La Caridad suggested to Saegart, Sell, and Kilpatrick (1974) that the associated metallization and alteration occurred there at a depth less than about 1 km. La Caridad is situated near the top of the Late Cretaceous or early Tertiary volcanic pile, whereas La Florida is near the base. Nevertheless, the geologic history of the La Florida area suggests that exposed parts of the porphyry system developed at very shallow depths. Laumontite, a major constituent of many of the quartz-calcite-chlorite-bearing veins associated with most of the chalcopyrite in the metallized andesite and La Florida, has a fairly restricted thermal stability. Experimental studies show that laumontite is stable to temperatures no greater than about 225°C at fluid pressures of approximately 50,000 kPa, under conditions such that aqueous fluid pressure is equal to total pressure and that minor elements are absent from the system (Liou, 1971a, b; Winkler, 1974, fig. 15–1). When aqueous fluid pressures are not equal to total pressure—a reasonable assumption for the veins at La Florida because of carbon dioxide in the system and the very shallow geologic environment—then the maximum stable temperature of laumontite would be significantly less than 225°C at 50,000 kPa total pressure. Thus, the late-vein stage of copper metallization at La Florida seemingly occurred at remarkably low temperatures for a porphyry copper system. In addition, the abundant magnetite and laumontite suggest an alkaline environment during the late-vein stage (see Barnes and Czamanske, 1967). Temperatures during the EDB stage of alteration, however, must have been much higher than during the vein stage. In light of the extensive thermometry available for many potassic zones in other porphyry copper systems (Roedder, 1971; Nash and Theodore, 1971; Moore and Nash, 1974), we suggest that the EDB alteration at La Florida most likely formed somewhere in the range between 400° and 600°C.

SUGGESTIONS FOR EXPLORATORY PROGRAMS

The two interesting features in the La Florida area from the viewpoint of porphyry copper exploration are the late-stage veins that yield much of the copper anomaly at the surface and the EDB alteration that is present in all the metallized andesite and some of the dacite porphyry. The extent of the EDB alteration is especially significant if one considers that some chalcopyrite was introduced during this alteration stage. The late-stage veins could reflect the propylitic fringes of a deeply buried, post-EDB porphyry system. Conceivably the late veins at La Florida, which contain chalcopyrite, might also reflect a low-temperature partial remobilization of copper from a deep, possibly commercial, source in EDB rock. Remobilization of copper by late fluids circulating through a deposit may be fairly common in most porphyry systems (Sheppard and others, 1971). At La Florida, then, one needs to determine if there is an economic deposit of chalcopyrite genetically associated with EDB altered rock or with a porphyry system emplaced subsequent to the EDB alteration. Comparisons of the widths of the alteration envelopes about the late-stage veins, the chalcopyrite abundances in the veins themselves, and the copper concentrations in the wallrocks adjacent to the veins suggest that the vein chalcopyrite was not derived locally. It therefore must have come from a copper source at depth that may or may not be economic. A well-conceived deep-drilling program that builds upon the drilling already completed could provide information at depth to evaluate the entire area thoroughly. The possibility remains, however, that the EDB alteration at La Florida may be the root zone of a porphyry system (Durning, 1976) that has had its commercial parts eroded. Finally, our recognition of secondary potassic assemblages in the dacite porphyry complex on the Sierra Cobriza, at least 4 km south of the main body of metallized andesite, suggests that this complex and its gravel-covered margins must be considered carefully in all future exploration programs.

REFERENCES CITED

Amaya, R., 1971, Petrografia del cuerpo intrusivo mineralizado en el area Florida-Barrigon, municipio de Nacozari, Sonora: Mineria y Metalurgia, Mem. 9, p. 73–77.

Barnes, H. L., and Czamanske, G. K., 1967, Solubilities and transport of ore minerals, *in* Barnes, H. L., ed., Geochemistry of hydrothermal ore deposits: New York, Holt, Rinehart, and Winston, p. 334–381.

Carson, D. J. T., and Jambor, J. L., 1974, Mineralogy, zonal relationships and economic significance of hydrothermal alteration at porphyry copper deposits, Babine Lake area, British Columbia: Canadian Mining and Metall. Bull., p. 1–24.

Chiapa, A., and Thoms, J. A., 1971, Bosquejo geologico del distrito minero de Nacozari, *in* Libreto guia de excursiones: Mineria y Metalurgia, Mem. 9, p. 1–11.

Consejo de Recursos Naturales No Renovables, 1967, Mapa geologico de la parte septentrional del estado de Sonora: Mexico Consejo Recursos Nat. No Renovables, zona 9, scale 1:100 000.

Creasey, S. C., 1966, Hydrothermal alteration, *in* Titley, S. R., and Hicks, C. L., eds., Geology of the porphyry copper deposits, southwestern North America: Tucson, Ariz., Arizona Univ. Press, p. 51–85.

Damon, P. E., 1968, Correlation and chronology of ore deposits and volcanic rocks: U.S. Atomic Energy Comm. Ann. Prog. Rept. No. C00–689–100, p. 42–48.

Deer, W. A., Howie, R. A., and Zussman, J., 1963, Rock-forming minerals, V. 2: London, Longmans, Green, and Co., 379 p.

Drewes, Harald, 1976, Tectonic setting of the porphyry copper deposits of southeastern Arizona and some adjacent areas: Arizona Geol. Soc. and Arizona Univ., Tucson, Porphyry Copper Symposium, Prog. and Abs., p. 9–10.

Durning, W. P., 1976, The root zone characteristics of porphyry copper systems as identified at the Little Hill mines area, Pinal County, Arizona: Arizona Geol. Soc. and Arizona Univ., Tucson, Porphyry Copper Symposium, Prog. and Abs., p. 8–9.

Fries, Carl, Jr., 1962, Resena de la geologia del estado de Sonora, con enfasis en el Paleozoico: Asoc. Mexicana Geologos Petroleros Bol., v. 50, no. 11–12, p. 257–274.

Imlay, R. W., 1939, Paleogeographic studies in northeastern Sonora: Geol. Soc. America Bull., v. 50, p. 1723–1744.

Jerome, S. E., and Cook, D. R., 1967, Relation of some metal mining districts in the Western United States to regional tectonic environments and igneous activity: Nevada Bur. Mines Bull. 69, 35 p.

Lanier, George, Folsom, R. B., and Cone, S., 1975, Alteration of equigranular quartz monzonite, Bingham mining district, Utah, *in* Bray, R. E., and Wilson, J. C., eds., Guidebook to the Bingham mining district: Soc. Econ. Geologists, p. 73–97.

Liou, J. G., 1971a, Synthesis and stability relations of prehnite, $Ca_2Al_2Si_3O_{10}(OH)_2$: Am. Mineralogist, v. 56, p. 507–531.

——— 1971b, Stilbite-laumontite equilibrium: Contr. Mineralogy and Petrology, v. 31, p. 171–177.

Livingston, D. E., 1973, A plate tectonic hypothesis for the genesis of porphyry copper deposits of the southern Basin and Range province: Earth Planetary Sci. Letters, v. 20, p. 171–179.

Lowell, J. D., 1974, Regional characteristics of porphyry copper deposits of the southwest: Econ. Geology, v. 69, no. 5, p. 601–617.

Lowell, J. D., and Guilbert, J. M., 1970, Lateral and vertical alteration-mineralization zoning in porphyry ore deposits: Econ. Geology, v. 65, p. 373–408.

Mayo, E. B., 1958, Lineament tectonics and some ore districts of the southwest: Mining Eng., v. 11, p. 1169–1175.

McAnulty, W. N., Jr., 1970, Geology of the northern Nacozari district, Sonora, Mexico: Albuquerque, New Mexico Univ., Ph. D. thesis, 103 p.

Meyer, Charles, and Hemley, J. J., 1967, Wallrock alteration, *in* Barnes, H. L., ed., Geochemistry of hydrothermal ore deposits: New York, Holt, Rinehart, and Winston, p. 166–235.

Moore, W. J., and Nash, J. T., 1974, Alteration and fluid-inclusion studies of the porphyry copper ore body at Bingham, Utah: Econ. Geology, v. 69, p. 631–645.

Nash, J. T., 1976, Fluid inclusions as a guide to porphyry copper deposits: U.S. Geol. Survey Open-File Rept. 76–482, 16 p.

Nash, J. T., and Theodore, T. G., 1971, Ore fluids in the porphyry copper deposit at Copper Canyon, Nevada: Econ. Geology, v. 66, p. 385–399.

Nasser Nasser, Abraham, 1968, Estudio geologico de la Mina Nueva Lily, Nacozari de Garcia, Sonora: Mexico Univ. Nac. Autonoma Inst. Prof. thesis, 66 p.

Ransome, F. L., 1904, The geology and ore deposits of the Bisbee quadrangle, Arizona: U.S. Geol. Survey Prof. Paper 21, 168 p.

Roedder, Edwin, 1971, Fluid-inclusion studies on the porphyry-type ore deposits at Bingham, Utah, Butte, Montana, and Climax, Colorado: Econ. Geology, v. 66, no. 1, p. 98–120.

Saegart, W. E., Sell, J. D., and Kilpatrick, B. E., 1974, Geology and mineralization of La Caridad porphyry copper deposit, Sonora, Mexico: Econ. Geology, v. 69, no. 7, p. 1060–1077.

Salas, Guillermo, and Hollister, V. F., 1972, Alteration minerals as ore guides in the porphyry copper province of northern Sonora, Mexico: Internat: Geol. Cong., 24th, Montreal, Proc., sec. 4, p. 261–265.

Schmitt, H. A., 1959, The copper province of the southwest: Mining Eng., v. 11, no. 6, p. 597–600.

Sheppard, S. M. F., Nielsen, R. L., and Taylor, H. P., Jr., 1971, Hydrogen and oxygen isotope ratios in minerals from porphyry copper deposits: Econ. Geology, v. 66, no. 1, p. 515–542.

Streckeisen, A. L., and others, 1973, Plutonic rocks; Classification and nomenclature recommended by the IUGS Subcommission on the Systematics of Igneous Rocks: Geotimes, v. 18, no. 10, p. 26–30.

Titley, S. R., 1975, Characteristics of some telescoped alteration patterns in southwestern Pacific porphyry copper deposits [abs.]: Mining Eng., v. 27, no. 12, p. 71.

United Nations, 1969, Survey of metallic mineral deposits in Mexico: United Nations, Devel. Programme Rept. DP/SF/UN/19–Mexico, New York, 72 p.

U.S. Geological Survey, 1973, Map showing potential for copper deposits in the eastern three-quarters of the Nogales 2° quadrangle, Tucson area, Arizona: U.S. Geol. Survey Misc. Inv. Map I–844–G, scale 1:250 000.

——— 1974, Preliminary map showing potential for copper deposits in the east half of the Tucson 2° quadrangle, Arizona: U.S. Geol. Survey Open-File Map 74–143, scale 1:250 000.

Vazquez, A., and Islas, J., 1970, Informe actualizado de las investigaciones efectuadas en el prospecto "Florida-Barrigon" municipio de Nacozari, Sonora: Mexico Consejo Recursos Nat. No Renovables, admin. report, 117 p.

——— 1971, Exploracion geologico-minera del prospecto curifero La Florida-Barrigon, municipio de Nacozari, Sonora: Mineria Metalurgia, Mem. 9, p. 295–301.

Wade, R. W., and Wandke, Alfred, 1920, Geology and mining methods at Pilares mine: Am. Inst. Mining Metall. Engineers Trans., v. 63, p. 382–395.

Winkler, H. G. F., 1974, Petrogenesis of metamorphic rocks: New York, Springer-Verlag, 320 p.

Jour. Research U.S. Geol. Survey
Vol. 6, No. 1, Jan.–Feb. 1978, p. 73–80

METAMORPHIC FORSTERITE AND DIOPSIDE FROM THE ULTRAMAFIC COMPLEX AT THE TUOLUMNE RIVER, CALIFORNIA

By BENJAMIN A. MORGAN, Reston, Va.

Abstract.—Metamorphic forsterite (Fo=98) and diopside (Wo:En:Fs=48.5:49.5:2.0) have been formed from serpentinite within intensely sheared zones in the large ultramafic complex at the Tuolumne River near Sonora, Calif. Bladelike grains of forsterite are elongate, parallel to *c*, and have prominent idiomorphic faces developed in (010). Metamorphic diopside occurs as small grains, free of inclusions, in rocks containing forsterite. The formation of forsterite and forsterite +diopside in serpentinite probably took place by the following reactions:

antigorite+magnesite→2 forsterite+fluid
3 antigorite+calcite→4 forsterite+diopside+fluid

Iron derived from the primary olivine and chromite has been oxidized almost entirely to magnetite and may be treated as an indifferent or accessory component. Stratigraphic reconstruction indicates that the total load pressures probably did not exceed 3 kilobars. At these pressures, the reaction should take place between 400° and 500°C with a fluid composition ranging from nearly pure H_2O to less than 5 mole percent CO_2. The restriction of forsterite and forsterite+diopside to shear zones may be attributed to the presence of carbonate in the rock prior to metamorphism and to the dilution of a CO_2-bearing fluid phase by water coming from outside the area of the reaction.

Study of the metamorphism of ultramafic rocks has been given considerable impetus as a result of theoretical and experimental studies by Greenwood (1967) and Johannes (1969) and of extensive field investigations by Bernard Evans and Volkmar Trommsdorff (for example, Trommsdorff and Evans, 1972, 1974; Evans and Trommsdorff, 1970, 1974). Trommsdorff and Evans (1974) reported that metamorphic olivine in alpine-type serpentinite is formed by the reaction.

antigorite + brucite→olivine + fluid. (1)

The reaction takes place at about the biotite zone of regional metamorphism in pelitic rocks. This paper describes metamorphic reactions that generate nearly pure forsterite and diopside in serpentinite by reaction of antigorite with carbonate rocks. These reactions take place within intensely sheared zones of the large serpentinized dunite and harzburgite complex, herein called the ultramafic complex at the Tuolumne River, in the western Sierra Nevada near Sonora in Tuolumne County, Calif. (fig. 1).

The western Sierra Nevada between Mariposa and Sonora consists of thick sequences of rocks ranging in age from late Paleozoic at the edge of the Sierra Nevada batholith in the east to Jurassic near the margin of the Great Central Valley of California to the west. These sequences all dip steeply to the east, and the contacts between Jurassic and Paleozoic units are marked by extensive fault systems that can be traced for more than 300 km (Clark, 1960). The Melones and Bear Mountains faults are the principal faults within the region shown in figure 1. These faults are actually wide zones along which Paleozoic and Mesozoic rocks are chaotically mixed to form a melange (Duffield and Sharp, 1975; Eric and others, 1955; Saleeby, 1975; Schweikert and Cowan, 1975). Large ultramafic bodies are exposed within and near these fault systems. The ultramafic rocks are found with gabbro, diorite, and volcanic rocks in an association suggesting an ophiolitic assemblage (Morgan, 1973; Saleeby, 1974), although the volcanic rocks are more likely products of an island-arc complex rather than an oceanic-ridge environment.

A large ultramafic complex of partially serpentinized harzburgite, dunite, wehrlite, and clinopyroxenite is exposed at the Tuolumne River near Sonora along the Bear Mountains fault zone. Morgan (1973) interpreted it as a basement on which a thick sequence of andesitic pillow breccias and flows, the Peñon Blanco Volcanics (Clark, 1964), was deposited. The breccias and flows were metamorphosed to the greenschist facies in the lower part of the section immediately overlying the ultramafic basement. Mineral assemblages include epidote-chlorite-albite-calcite-sphene. Higher in the section, these rocks grade gradually into a pumpellyite facies; mineral assemblages include pumpellyite-stilpnomelane-chlorite-albite-calcite-sphene and rare prehnite. Metamorphic actinolite

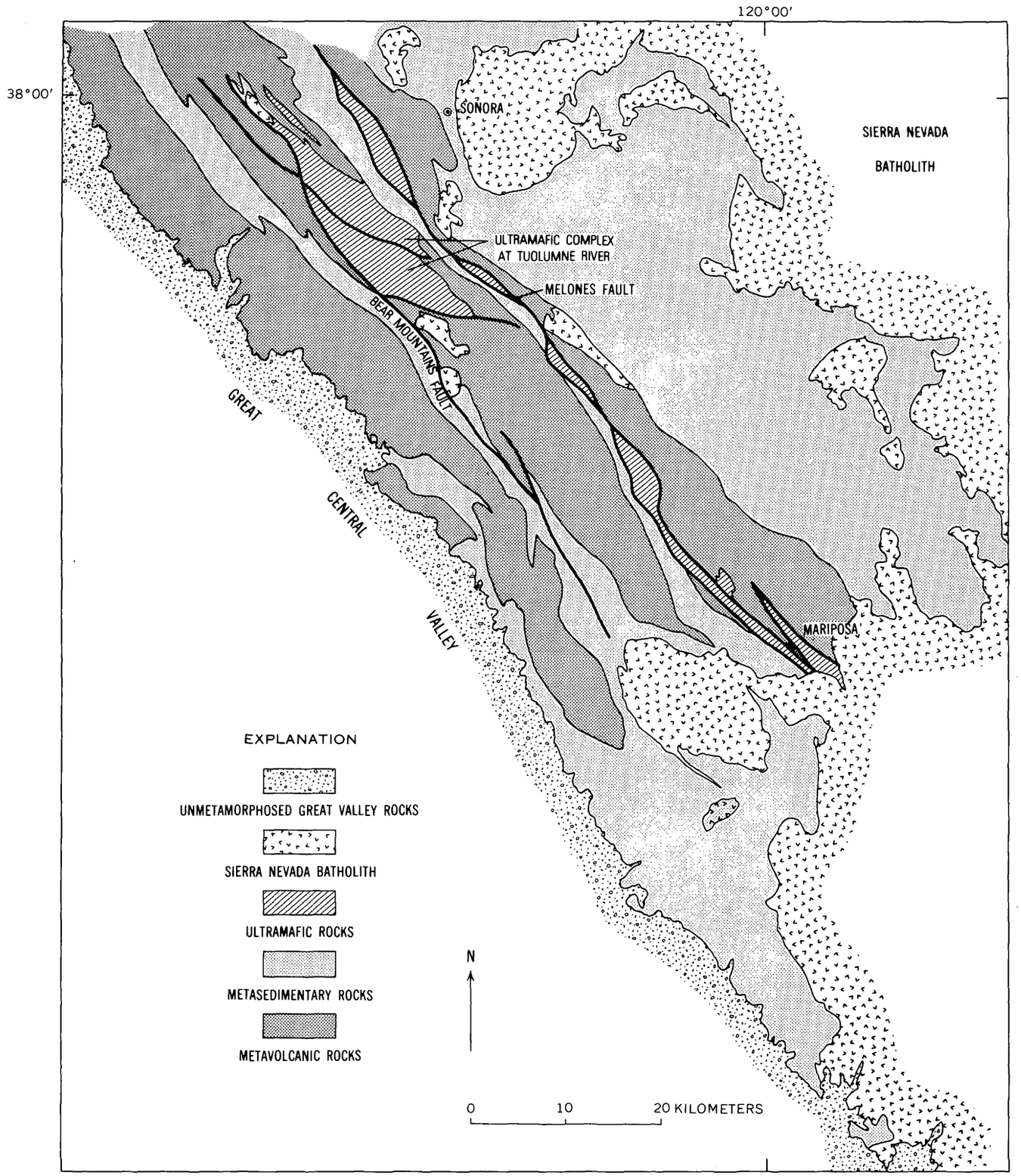

FIGURE 1.—Generalized geologic map of the western Sierra Nevada between Sonora and Mariposa, Calif., showing the location of the ultramafic complex at the Tuolumne River.

is not found anywhere in the section, although relict hornblende and augite are common.

The ultramafic complex can be divided into two structural blocks. One block consists dominantly of harzburgite and minor dunite, wehrlite, and clinopyroxenite, all of which are partly altered to serpentinite containing chrysotile, lizardite, and minor carbonate and magnetite. The second block consists dominantly of dunite and minor harzburgite, partly altered to serpentinite containing antigorite, carbonate, and magnetite. The degree of serpentinization in both blocks is variable, ranging from about 10 to 100 percent. Forsterite and diopside formed in the second block within serpentinized dunite near the Bear Mountains fault zone; however, these minerals are not present in all serpentinites but are restricted to highly sheared units containing antigorite-carbonate-magnetite and relict chromite.

Acknowledgment.—The author is grateful for helpful comments and review by B. W. Evans, University of Washington.

PETROGRAPHY AND MINERALOGY

Table 1 gives results of whole-rock chemical analyses of two unsheared serpentinized dunite sample that contain relict olivine (samples 1037 and 1041). Electron-microprobe analyses of relict olivine and chromite as well as magnetite and antigorite from these samples are included. Electron-microprobe analyses of forsterite, diopside, magnetite, and antigorite as well as relict chromite from two sheared dunites are also given in table 1 (samples 1042 and 1052).

Whole-rock chemical analyses of the two typical dunites containing no forsterite or diopside (samples 1037 and 1041, table 1) show that both samples contain normative orthopyroxene. However, no relict orthopyroxene or clinopyroxene was observed, and there is no textural evidence to suggest their former presence. Some loss of Mg may have taken place during serpentinization. The relict primary minerals in these serpentinized dunites are olivine and chromite. Olivine grains (1–2 mm) are altered around margins and across fractures and are broken into a mosaic of subgrains, usually having a largest dimension of about 0.1 mm (see fig. 2*A*). Microprobe analyses of relict olivine from these rocks (table 1) show an average forsterite content of 92 mole percent, typical of alpine-type dunites that have a range of about Fo_{90}–Fo_{92}. The relict olivine grains are charged with fine crystals (less than 0.05 mm diameter) of brown spinel; qualitative analyses of the spinel by microprobe show that the spinel is high in Cr and Al. The spinel is randomly distributed in some olivine grains and forms long irregular trains of small crystals in others. Larger grains (0.5–1 mm diameter) of high-Cr chromite are scattered through the sample; no ferrichromite was detected from microprobe analyses. Partial serpentinization has altered olivine to antigorite (with minor lizardite), magnetite, and carbonate. Partial analyses of carbonates for Ca, Mg, and Fe with the electron microprobe show that, in almost all samples, the carbonate mineral is magnesite; only a few samples contained calcite. Brucite was not observed. Serpentine minerals (with magnetite and carbonate) typically may make up 50 to 80 percent by volume of the dunite. Fine-grained (0.1 mm long) blades of antigorite and small equant grains (0.1 mm diameter) of magnetite partly replace olivine. In addition, larger (1–2 mm long) blades of antigorite form rosettes that cut across the fine-grained antigorite and relict olivine (see fig. 2*A*).

In the highly sheared zones nearer the Bear Mountains fault zone, large (2–4 mm long) antigorite grains make up most of the serpentinite and obliterate much of the fine-grained serpentine as well as the relict olivine; the result is a coarse-grained antigorite schist with minor magnetite, carbonate, and relict chromite. Samples containing forsterite and (or) diopside (1042 and 1052, table 1) contain much coarse-grained antigorite and are lighter in color than those containing relict primary olivine. The assemblages consist of antigorite-magnetite-forsterite-magnesite and, more rarely, antigorite-magnetite-forsterite-diopside-calcite. In addition, a minor amount of disseminated relict chromite is present. Relict olivine and forsterite do not occur in the same samples. Forsterite has distinctive blades that are elongate in the "*c*" crystallograhpic direction and has pronounced idiomorphic faces developed on (010). The forsterite grains are clear and relatively free of inclusions, unlike the relict olivines previously described. Chemically, forsterite is quite distinct from the relict olivine in that the forsterite content is very high: 97.5 mole percent for sample 1042 and 98.0 for sample 1052. Diopside was identified in only a few samples and coexisted with forsterite in all. Diopside usually occurs as very fine grains (0.1 mm diameter), virtually free of inclusions, in rocks containing calcite rather than magnesite. Microprobe chemical analyses given in table 1 show that the diopside is a nearly pure "end member" (Ca:Mg:Fe= 48.5:49.5:2.0). This composition contrasts strongly with that of clinopyroxene in wehrlite from elsewhere in the ultramafic complex; the clinopyroxene contains a substantial tschermak's component and is less calcic.

Two metamorphic reactions can be proposed on the basis of the petrographic descriptions and field rela-

TABLE 1.—*Chemical analyses of rocks and minerals*

[Analyses of dunite are rapid rock analyses, U.S. Geological Survey laboratories. All mineral analyses are by ARL EMX-SM electron microprobe. Natural olivine, pyroxene, chromite, and magnetite from the collections of the U.S. Geological Survey and the U.S. National Museum were used for standards. The computer program for the reduction of electron-probe data was written by Hadidiacos, Finger, and Boyd (1971). Iron is treated as FeO for all minerals except chromite and magnetite, which have been calculated for both FeO and Fe_2O_3 assuming ideal stoichiometry. N.d., not detectable; Tr., trace]

Sample	Dunite		Sample	Olivine				Chromite		Magnetite		Diopside	Antigorite		
	1037	1041		1037	1041	1042	1052	1041	1052	1041	1052	1042	1041	1042	1052
Chemical analyses			**Chemical analyses**												
SiO_2	36.3	36.3	SiO_2	40.7	41.1	41.6	42.7	----	0.1	0.2	0.2	54.8	43.0	40.7	42.1
Al_2O_3	.30	.30	Al_2O_3	N.d.	N.d.	N.d.	N.d.	3.7	12.4	N.d.	.1	.2	.3	1.5	----
Cr_2O_3	.25	.35	Cr_2O_3	N.d.	N.d.	N.d.	N.d.	62.5	52.4	.5	N.d.	.1	N.d.	.3	----
Fe_2O_3	3.4	3.6	Fe_2O_3	----	----	----	----	4.4	5.6	69.7	69.5	----	----	----	----
FeO	3.1	3.5	FeO	7.4	7.7	2.8	1.4	23.5	19.4	29.2	27.9	1.3	2.0	1.6	.8
NiO	.55	.54	NiO	----	----	----	----	----	----	----	----	----	----	----	----
MnO	.08	.11	MnO	.1	.2	.3	.2	.7	.4	Tr.	Tr.	Tr.	Tr.	.1	----
MgO	43.6	43.8	MgO	50.9	50.9	54.4	55.7	5.6	9.2	1.4	2.0	18.2	40.5	40.1	41.8
CaO	.13	.06	CaO	Tr.	Tr.	Tr.	N.d.	Tr.	Tr.	Tr.	N.d.	24.8	Tr.	Tr.	----
Na_2O	.19	.19	Na_2O	N.d.	N.d.	N.d.	N.d.	N.d.	N.d.	N.d.	N.d.	.1	N.d.	N.d.	----
K_2O	.06	.06	K_2O	----	----	----	----	----	----	----	----	----	----	----	----
H_2O+	12.0	11.6	H_2O+	----	----	----	----	----	----	----	----	----	----	----	----
H_2O-	.50	.49	H_2O-	----	----	----	----	----	----	----	----	----	----	----	----
TiO_2	.04	.03	TiO_2	N.d.	N.d.	N.d.	N.d.	N.d.	0.1	N.d.	N.d.	N.d.	N.d.	N.d.	----
P_2O_5	N.d.	N.d.	P_2O_5	----	----	----	----	----	----	----	----	----	----	----	----
CO_2	.18	.38	CO_2	----	----	----	----	----	----	----	----	----	----	----	----
Total	101	101	Total	99.1	99.9	99.1	100.0	100.4	99.6	99.9	99.7	99.5	85.8	84.3	84.7
Normative reduction			**Atomic proportions**												
or	0.3	0.3													
ab	1.0	1.0													
opx	7.4	6.2													
ol	88.3	89.6													
mt	2.4	2.5													
cc	0.3	0.1													
il	.1	Tr.													
cm	.2	.3													
				Four oxygens								Six oxygens	Seven oxygens		
			Si	1.00	1.00	1.00	1.01	-----	Tr.	0.01	0.01	1.99	2.03	1.96	2.00
			Ti	Nil	Nil	Nil	Nil	Nil	0.01	Nil	Nil	Nil	Nil	Nil	-----
			Al^{iv}	Nil	Nil	Nil	Nil	-----	-----	-----	-----	.01	-----	.04	-----
			Al^{vi}	Nil	Nil	Nil	Nil	0.15	.48	Nil	Tr.	-----	.02	.04	-----
			Cr	Nil	Nil	Nil	Nil	1.73	1.37	.02	Nil	Tr.	Nil	.01	-----
			Fe^3	-----	-----	-----	-----	.12	.14	1.98	1.99	-----	-----	-----	-----
			Fe^2	.15	.16	.06	.03	.69	.54	.92	.89	.04	.08	.06	.03
			Mn	Nil	Nil	.01	.01	.02	.01	Tr.	Tr.	Tr.	Tr.	.01	-----
			Mg	1.86	1.84	1.95	1.96	.29	.45	.08	.11	.99	2.85	2.87	2.96
			Ca	Tr.	Tr.	Tr.	Nil	Tr.	Tr.	Tr.	Nil	.97	Tr.	Tr.	-----
			Na	Nil	Nil	Nil	Nil	------	-----	-----	-----	.01	Nil	Nil	-----

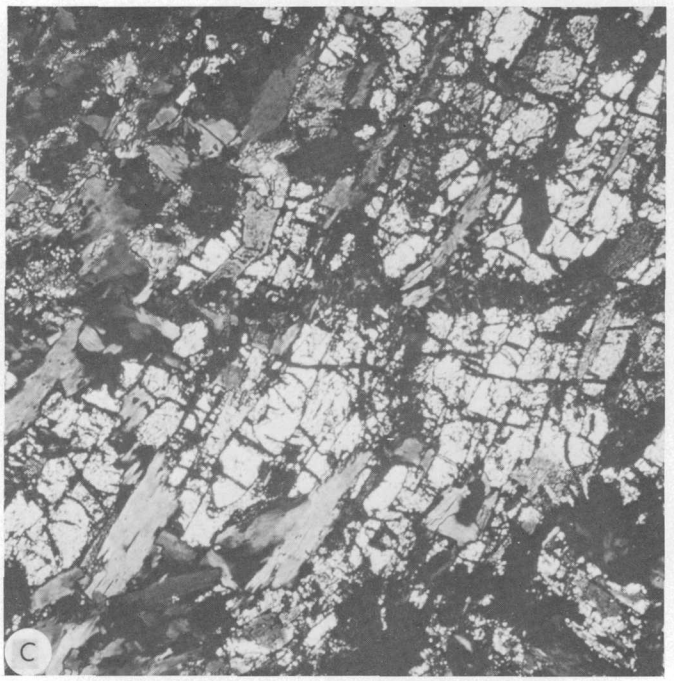

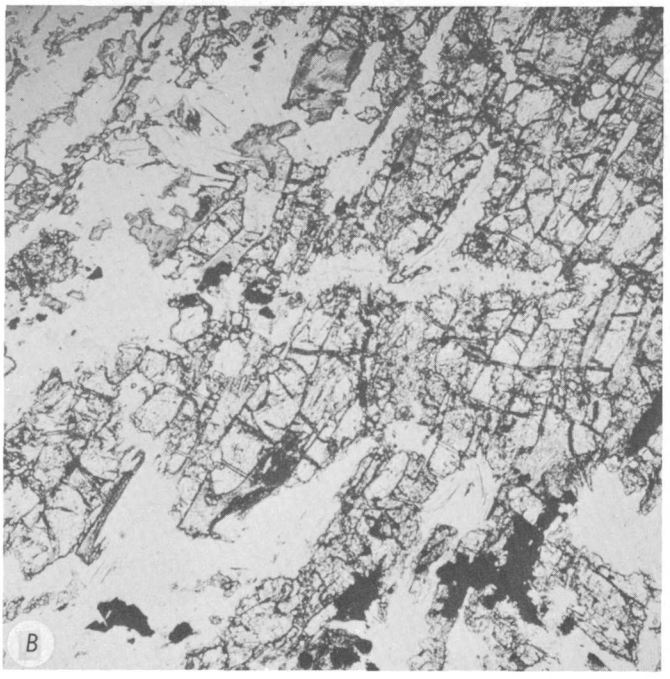

FIGURE 2.—*Photomicrographs of dunite (field of view is 2.2 mm). A*, Sample 1041; partly serpentinized dunite in plane-polarized light; clear crystals in high relief are relict olivine set in a mesh-textured mosaic of fine-grained serpentine minerals, principally antigorite; large bladed mineral is later antigorite; opaque minerals are relict chromite. *B*, Sample 1052; serpentinite with magnesite and forsterite in plane-polarized light; clear bladed mineral in high relief is forsterite; clouded mineral is magnesite, and opaque mineral is relict chromite; Antigorite grains are clear and have low relief. *C*, Sample 1052; same as *B*, but with cross-polarized light.

tions just described and from the data in table 1:

$$\underset{\text{antigorite}}{Mg_3Si_2O_5(OH)_4} + \underset{\text{magnesite}}{MgCO_3} \rightarrow 2\,\underset{\text{forsterite}}{Mg_2SiO_4} + \underset{\text{fluid}}{CO_2} + 2H_2O \quad (2)$$

$$3\,\underset{\text{antigorite}}{Mg_3Si_2O_5(OH)_4} + \underset{\text{calcite}}{CaCO_3} \rightarrow 4\,\underset{\text{forsterite}}{Mg_2SiO_4} + \underset{\text{diopside}}{CaMgSi_2O_6} + 6\,\underset{\text{fluid}}{H_2O} + CO_2 \quad (3)$$

As written, reaction 2 has four components and four phases and 3 has five components and five phases, so that the reactions are divariant as written; without constraints on temperature, pressure, or fluid composition, the reactants and products should be stable over a limited range of temperature and pressure. Magnetite and relict chromite are present in rocks containing relict olivine as well as in those containing forsterite (table 1). Compositions of both sets of spinels are similar. Chromite in both rocks has high Cr and moderate Al; reduction to atomic proportions and recalculation of ferric iron indicate only minor amounts of magnetite in the chromite. Magnetite in both rocks is nearly pure $(MgO \cdot FeO)Fe_2O_3$ with about 10 mole percent $MgO \cdot Fe_2O_3$. Neither the relict chromite nor the magnetite produced during serpentinization of primary olivine participated in reaction 2 and 3. Presumably, the generation of forsterite and diopside took place at a relatively high and constant oxygen fugacity so that no reduction of iron took place. Iron can be

treated as an indifferent or accessory component because it is present in silicates in small amounts and because magnetite was not involved in the reactions. Reactions 2 and 3 represent nearly, but not quite, closed-system conditions (except for the ultimate loss of fluids) in the systems $MgO\text{-}SiO_2\text{-}H_2O\text{-}CO_2$ and $CaO\text{-}MgO\text{-}SiO_2\text{-}H_2O\text{-}CO_2$, respectively. Small amounts of aluminum present in antigorite are not accounted for in the reaction products. Likewise, forsterite contains more manganese than the antigorite analyses show; manganese may have been obtained from carbonate. Diopside more easily accommodated aluminum into its structure as well as chromium, but the source of sodium is not known. However, these differences are very small, and reactions 2 and 3 should closely model the mineral transformations that took place.

DISCUSSION

Estimates of load pressure for the metamorphism of the ultramafic rocks may be calculated from stratigraphic considerations, but such estimates are very tentative. From mapping data, the Tuolumne River ultramafic complex appears to be 4–5.5 km thick. The overlying Peñon Blanco Volcanics and Mariposa Formation have maximum thicknesses of 450 and 1500 meters, respectively, (Clark, 1964). Such a stratigraphic succession could result in a maximum pressure of about 3 kilobars. The absence of kyanite, glaucophane schist, and eclogite, the presence of andalusite, sillimanite and cordierite-bearing assemblages in higher grade-pelitic rocks, and the apparent regional progression from prehnite-pumpellyite to greenschist to amphibolite facies of metamorphism all suggest that extreme pressures during regional metamorphism in the western Sierra Nevada were never attained.

Consideration of the metamorphism of both the surrounding sedimentary and volcanic rocks as well as the ubiquitous presence of serpentine in the ultramafic rocks of the region suggests that temperatures of metamorphism were never much in excess of 500°C and may, in fact, have been much less.

A model for the formation of forsterite in shear zones can be made from temperature-fluid composition diagrams for a given total pressure; such a diagram is figure 3*A*, modified from figure 2 of Johannes (1969), which shows isobaric equilibrium curves at 2 kbar in the system $MgO\text{-}SiO_2\text{-}H_2O\text{-}CO_2$. The fluid is assumed to consist only of CO_2 and H_2O; only that part of the system that has a low CO_2 content is shown. Johannes reported only chrysotile in his runs; in a later investigation (Johannes, 1975), he reported that the thermal decomposition of antigorite is approximately 50°C higher than that of chrysotile at about 4 kbar. Hence, all the equilibria shown in figure 3*A* may be mestastable relative to equilibria involving antigorite.

In figure 3*A*, chrysotile and brucite react at about 375°C to form forsterite + fluid. However, very small amounts of CO_2 convert brucite to magnesite and greatly increase the thermal stability of chrysotile + magnesite relative to chrysotile + brucite as the mole fraction of CO_2 in the fluid is increased. For 2 kbar, the limiting condition for all assemblages containing chrysotile within the system is approximately 500°C and only 0.05 mole fraction of CO_2; at higher temperatures, serpentine reacts to form forsterite + talc, an assemblage not found in the study area. The isobaric invariant points that define the limits of reaction 2 are labeled FMST and MOST. The variation of these points with change of fluid pressure and temperature are shown in figure 3*B*. The reaction that produces forsterite from serpentine and magnesite is limited by temperatures that range from 350°C to about 500°C within the pressure range of 1–4 kbars.

As stated previously, forsterite and diopside are not widely distributed in the ultramafic complex but are restricted to shear zones containing abundant magnesite (or calcite in diopside-bearing rocks). Metamorphic reaction 1 is not applicable to these rocks because of the absence of brucite from the lower grade serpentinites. However, the bulk composition of the serpentinite prior to metamorphism did exert a strong control on the presence of olivine and pyroxene of metamorphic origin, inasmuch as the presence of a premetamorphic carbonate was a prerequisite for the reaction to take place. In the unsheared rocks, serpentine minerals are stable, suggesting that these rocks were in contact or in equilibrium with a large, H_2O-rich reservoir containing less than 0.05 mole fraction of CO_2. However, shearing of carbonate-bearing serpentinites may have resulted in a heavy influx of H_2O-rich fluid from outside the area of the immediate reaction, so that the mole fraction of CO_2 became much lower, perhaps approaching 0.01. In these shear zones, the metamorphic fluid, dilute in CO_2, would permit reactions 2 and 3 to take place well below the 500°C temperature necessary to generate forsterite by the thermal decomposition of serpentine.

REFERENCES CITED

Clark, L. D., 1960, Foothills fault system, western Sierra Nevada, California: Geol. Soc. America Bull., v. 71, no. 4, p. 483–496.

——— 1964, Stratigraphy and structure of part of the western Sierra Nevada metamorphic belt. California: U.S. Geol. Survey Prof. Paper 410, 70 p.

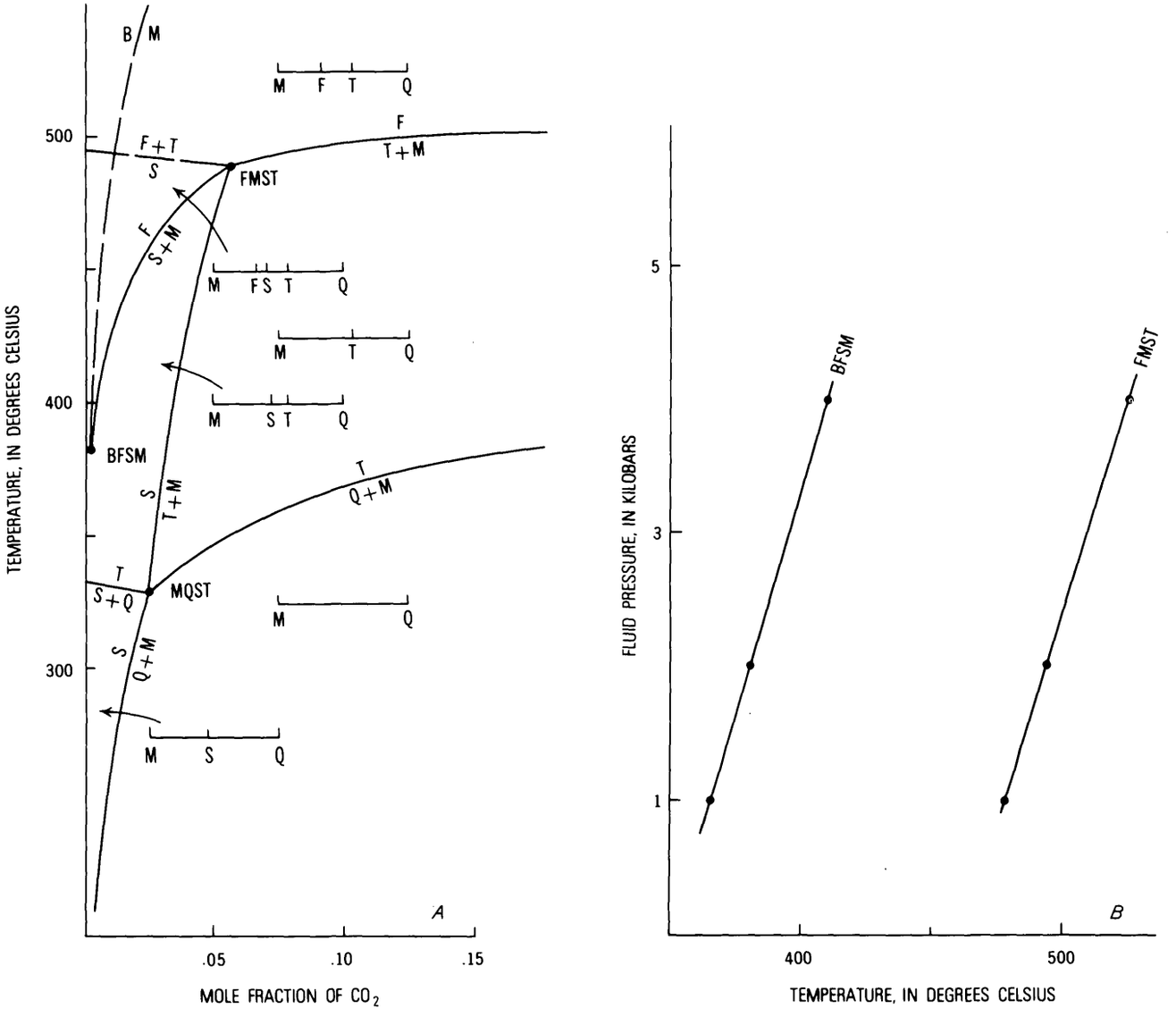

FIGURE 3.—Abbreviations are B, brucite; F, forsterite; M, magnesite; Q, quartz; T, talc; S, serpentine. *A*, Isobaric temperature-CO_2 plots of equilibria in system MgO-SiO_2-H_2O-CO_2 for 2 kbar (modified from Johannes, 1969, fig. 2, p. 1090). Isobaric invariant points are labeled FMST, BFSM, and MOST. Bar diagrams show assemblages permitted in each divarient field. *B*, Equilibrium conditions of isobaric invariant points BFSM and FMST which bracket reaction 2, serpentine+magnesite→forsterite+fluid (data modified from Johannes, 1969).

Duffield, W. A., and Sharp, R. V., 1975, Geology of the Sierra foothills melange and adjacent areas. Amador County, California: U.S. Geol. Survey Prof. Paper 827, 30 p.

Eric, J. H., Stromquist, A. A., and Swinney, C. M., 1955, Geology and mineral deposits of the Angels Camp and Sonora quadrangles, Calaveras and Tuolumne Counties, California: California Div. Mines Spec. Rept. 41, 55 p.

Evans, B. W., and Trommsdorff, V., 1970, Regional metamorphism of ultramafic rocks in the Central Alps: Parageneses in the system CaO-MgO-SiO_2-H_2O: Schweiz. Mineralog. u. Petrog. Mitt., v. 50, p. 481–492.

——— 1974, Stability of enstatite+talc and CO_2-metasomatism of metaperidotite, Val d'Efra, Lepontine Alps: Am. Jour. Sci., v. 274, no. 3, p. 274–296.

Greenwood, H. J., 1967, Mineral equilibria in the system MgO-SiO_2-H_2O-CO_2, *in* Researches in geochemistry, v. 2, Abelson, P. H., ed.: New York, John Wiley and Sons, p. 542–567.

Hadidiacos, C. G., Finger, L. W., and Boyd, F. R., 1971, Computer reduction of electron probe data: Carnegie Inst. Washington Year Book, no. 69, p. 294.

Johannes, W., 1969, An experimental investigation of the system MgO-SiO_2-H_2O-CO_2: Am. Jour. Sci., v. 267, no. 9, p. 1083–1104.

——— 1975, Zur Synthese und thermischen Stabilitat von Antigorit: Fortschr. Mineralogie, v. 53, p. 36.

Morgan, B. A., 1973 Tuolumne River ophiolite, western Sierra Nevada, California [abs.]: Geol. Soc. America Abs. with Programs, v. 5, no. 1, p. 83.

Saleeby, Jason, 1974, Preliminary report on the mafic-ultramafic belt of the southwestern Sierra Nevada foothills, California [abs.]: Geol. Soc. America Abs. with Programs, v. 6, no. 3, p. 247.

——— 1975, Serpentinite melange belt—southwestern Sierra Nevada foothills, California: Geol. Soc. America Abs. with Programs, v. 7, no. 3, p. 367.

Schweikert, R. A., and Cowan, D. S., 1975, Early Mesozoic tectonic evolution of the western Sierra Nevada, California: Geol. Soc. America Bull., v. 86, no. 10, p. 1329–1336.

Trommsdorff, Volkmar, and Evans, B. W., 1972, Progressive metamorphism of antigorite schist in the Bergell tonalite aureole (Italy): Am. Jour. Sci., v. 272, no. 5, p. 423–437.

——— 1974, Alpine metamorphism of peridotitic rocks: Schweiz. Mineralog. u. Petrog. Mitt., v. 54, p. 333–352.

Jour. Research U.S. Geol. Survey
Vol. 6, No. 1, Jan.–Feb. 1978, p. 81–94

PETROLOGY OF THE PRECAMBRIAN INTRUSIVE CENTER AT LAKE GEORGE, SOUTHERN FRONT RANGE, COLORADO

By R. A. WOBUS,[1] and R. S. ANDERSON,[2]
Williamstown, Mass., Palo Alto, Calif.

Abstract.—The intrusive center at Lake George, at the western margin of the Pikes Peak batholith (1030 m.y.) of central Colorado, contains rocks of both the potassic and sodic differentiation trends recognized in the batholith. Finer grained variants of the Pikes Peak Granite initially formed a texturally zoned stock 8 kilometers in diameter that cut the dominant coarse-grained granite of the batholith. This granite stock (potassic trend) was later intruded by partial ring dikes of quartz syenite to fayalite granite and by a central stock of quartz syenite to syenomonzonite (sodic trend). Xenoliths of alkali gabbro, diorite porphyry, and granodiorite are included within rocks of both differentiation trends. All major rock types of the intrusive center are thought to be derivatives of alkali basaltic magma from the mantle, modified by fractional crystallization and reaction melting of crustal rocks. The geometry of the intrusive center was controlled by ring-dike/cauldron-subsidence mechanisms.

The intrusive center at Lake George is located at the western edge of the Pikes Peak batholith in the Front Range of central Colorado (fig. 1). The roughly elliptical complex, approximately 6½×8 kilometers in diameter, is centered 3.2 km northeast of the town of Lake George; it lies on the boundary between the Hackett Mountain and Lake George 7½-minute quadrangles. Arcuate ridges of the complex (fig. 2) rise several hundred meters above a widespread erosion surface of probable late Eocene age (Scott, 1975). Crystal Peak, elevation 2910 meters, is the highest point of the outermost of these ridges and is named for the exceptional smoky quartz, topaz, and amazonite (green microcline) crystals collected from pegmatites in the area since about 1865.

Granite of the Pikes Peak batholith has been dated at 1030 million years (Barker and others, 1976) and is the product of the youngest of three major Precambrian plutonic events recognized in the southern Front Range (Wobus, 1969). Just west of the batholith are granitic rocks representative of the Silver Plume (about 1450 m.y.) and Boulder Creek (about 1700 m.y.) intrusive episodes. These earlier plutonic events are associated with periods of tectonic activity, but the later Pikes Peak event apparently occurred during a time of crustal quiescence (Hutchinson and Hedge, 1967).

Within or adjacent to the Pikes Peak batholith, and temporally as well as spatially related to it, are seven small intrusive centers composed, at least in part, of alkalic rocks (Wobus, 1976). Six of these centers, including the complex at Lake George, are thought to lie along two northwest-trending linears drawn parallel to one of the dominant fault trends of the southern Front Range (fig. 1). The northern linear passes through the syenite of Sugarloaf Mountain, the quartz syenite of West Creek (Barker and others, 1975), and a small syenite stock west of the Air Force Academy in the Rampart Range. The complex at Lake George lies along the southern linear, between an elliptical gabbro-monzonite stock cut by the Redskin Granite southeast of Tarryall (Hawley, 1969) and the Mount Rosa Granite (Barker and others, 1975; Gross and Heinrich, 1965). The syenite pluton at Spring Creek near Cripple Creek (Sage, 1966) is aberrant. Table 1 summarizes the important characteristics of each intrusive center, including the principal rock types and the most recent interpretation of the order of intrusion at each locality.

The rocks of the complex at Lake George are of two compositional varieties: (1) fine- to medium-grained granites, thought to be late textural variants of the Pikes Peak Granite and (2) ring dikes of fayalite granite to quartz syenite and a centrally located syenomonzonite stock, all of which are younger than the granitic rocks and are products of a more sodic differentiation trend. Small bodies of alkali gabbro, diorite porphyry, and granodiorite occur as xenoliths within both the granite and syenite.

[1] Dept. of Geology, Williams College, Williamstown, Mass., and U.S. Geological Survey, Denver Colo.
[2] Dept. of Geology, Stanford University, Palo Alto, Calif.

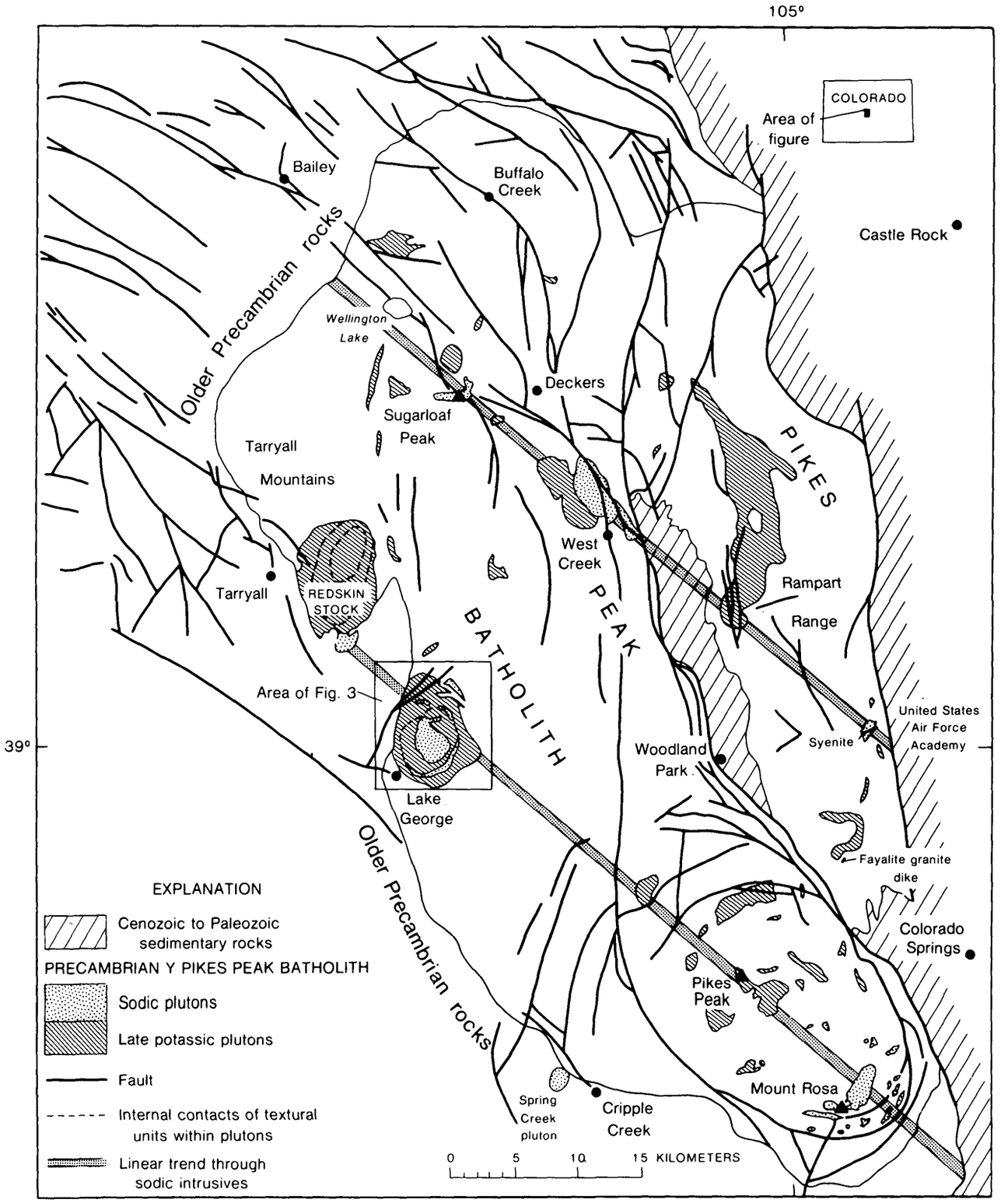

FIGURE 1.—Geologic index map of the Pikes Peak batholith showing locations of sodic and late potassic plutons and linear trends through sodic intrusive centers. From Bryant and Wobus (1975) and Scott and others (1976).

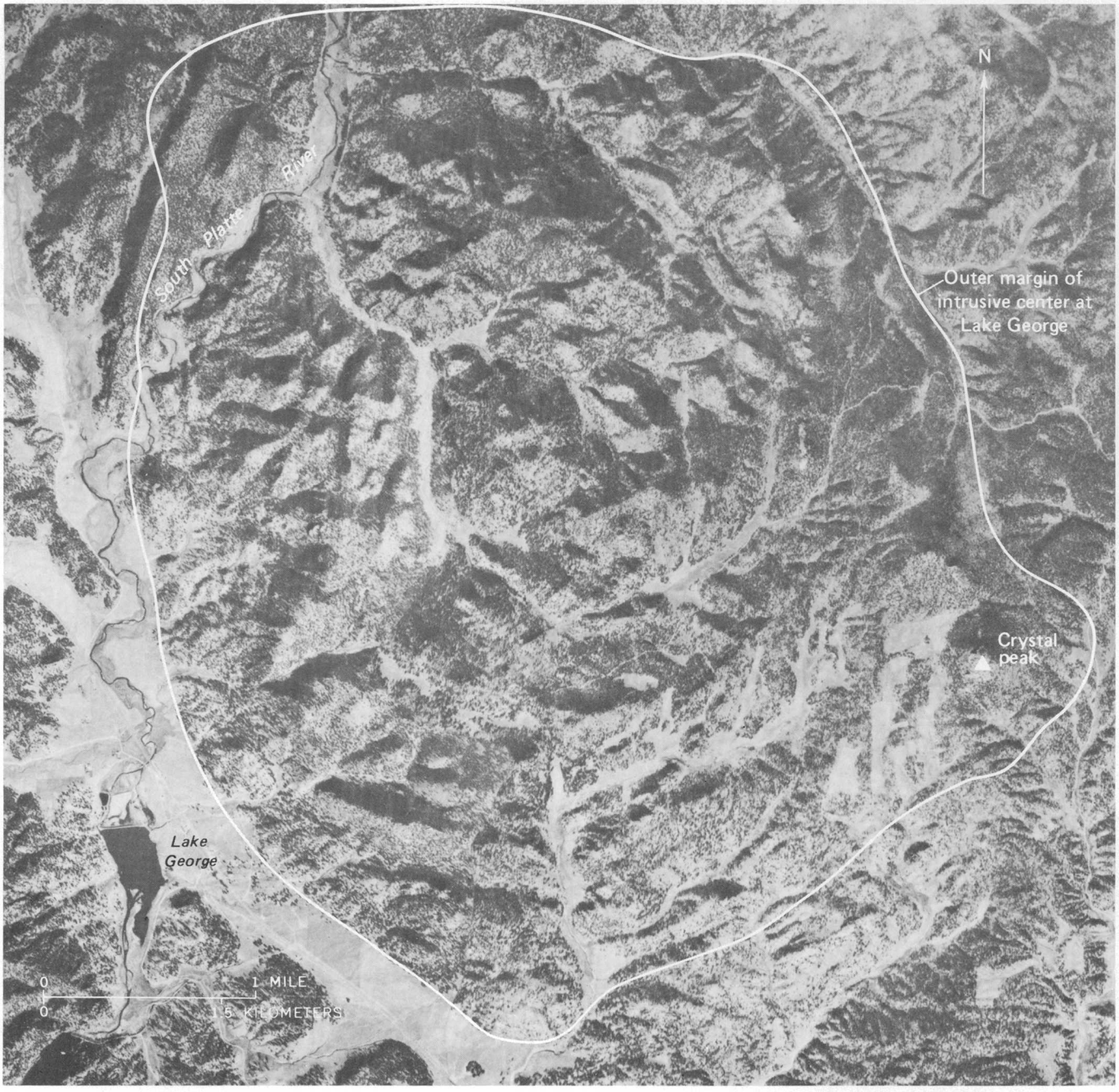

FIGURE 2.—Aerial photograph of the area of the intrusive center at Lake George, showing circular topographic expression of rock types composing the center.

The intrusive center at Lake George was first studied on a reconnaissance basis by R. M. Hutchinson in 1963–64. Stewart (1964) concentrated on the petrology and structure of the syenomonzonite stock and alluded to the possible control of the intrusion by ring-dike/cauldron-subsidence mechanisms. The area around the stock was mapped on a 7½-minute base by Wobus during the summers of 1971 and 1972 as part of the program of the U.S. Geological Survey to prepare geological maps of the Pueblo and Denver 1°×2° quadrangles. Ten chemical analyses of several rock types are reported; these analyses, performed by the U.S. Geological Survey, have been supplemented by X-ray fluorescence analyses of 10 additional samples of the syenite made by Anderson at Williams College using a Norelco vacuum spectrograph and Survey igneous rock standards. A wet chemical technique (Jeffery, 1970, p. 267–70) was used for ferrous

TABLE 1.—*Alkalic intrusive centers of the Pikes Peak batholith*

[Uppermost rock type, youngest at each locality. Vertical line, relative age uncertain]

Locality	Major rock types and relative ages	Dimensions	Structural relations and geometry	Reference
Lake George----------	Quartz syenite to fayalite granite Quartz syenite to syenomonzonite Fine- and medium-grained granite Pikes Peak Granite Granodiorite Diorite porphyry Alkali gabbro	6 1/2 x 8 km	Stock and partial ring dikes of syenitic rocks and fayalite granite intrude texturally zoned granitic stock	This paper.
Mount Rosa----------	Mount Rosa Granite Windy Point Granite Tan (riebeckite-bearing) granite Granite of Almagre Mountain Pikes Peak Granite Fayalite granite Hornblende monzonite	Arc of fayalite granite approx. 8 km in diameter	Discontinuous arc of fayalite granite (roots of ring structure?) around Mount Rosa and other alkalic granites	Barker and others, 1975.
Tarryall----------	Redskin Granite (three textural varieties) Pikes Peak Granite Quartz monzonite Gabbro	1 1/2 x 2 1/2 km	Ring dike(?) of gabbro surrounds stock of quartz monzonite; both rock types are cut by the Redskin Granite	Hawley and Wobus, 1977.
Spring Creek (NW of Cripple Creek).	Gabbro Syenite Pikes Peak Granite	1 1/2 x 3 km	Ring dike of gabbro surrounds syenite stock	Sage, 1966.
West Creek----------	Syenite Fine-grained granite Pikes Peak Granite Granodiorite	7 x 8 km	Crudely elliptical syenite stock appears to cut pluton of fine-grained granite	Barker and others, 1975; Bryant and Wobus, 1975.
Rampart Range---------	Syenite Fine-grained granite (Windy Point Granite) Pikes Peak Granite	1 x 1 1/2 km	Irregular stock of syenite	Wobus, 1976.
Sugarloaf----------	Syenite Fine-grained granite Pikes Peak Granite	1 x 3 km	Elongate stock of syenite	Bryant and Wobus, 1975.

iron determination in the latter 10 samples. Petrographic work by both authors used thin sections prepared by the Survey.

AGE RELATIONS

On the basis of field relationships, the plutonic rocks of the intrusive center at Lake George (fig. 3) have been determined to be of three different age groups, all probably related to the Pikes Peak intrusive event. (1) Rocks of the oldest group—alkali gabbro, diorite porphyry, and granodiorite—occur only as inclusions; age relationships among these three rock types are not known. (2) Rocks of the intermediate age group appear to be textural variants of the Pikes Peak Granite: typical coarse-grained equigranular biotite granite, medium-grained equigranular to porphyritic granite, and fine-grained equigranular granite. The fine-grained granite is the youngest of these, occurring at the center of a small, texturally zoned, presyenite stock which has a rim of medium-grained granite. The same kind of textural zonation was found by Hawley and others (1966) in the Redskin Granite stock, another granitic pluton of late Pikes Peak age located at the edge of the batholith 13 km to the northwest of the Lake George locality. (3) The rocks of the youngest group are alkalic; they occur in partial ring dikes of quartz syenite to fayalite granite and a central stock of quartz syenite to syenomonzonite, all of which intrude the zoned granitic stock. No field evidence has been found that indicates the age of the fayalite granite relative to that of the syenites; the innermost ring dike contains both of these types, but no mappable contact is exposed between them. The K-Ar age of a single sample of syenite from the stock, reported by Hutchinson (1963), is 955 m.y.; a more recent Rb-Sr age (Barker and others, 1976) indicates that the alkali gabbro is 1030 m.y., or about the same age as the granite of the Pikes Peak batholith.

PETROLOGY

Alkali gabbro

Xenoliths of alkali gabbro, some of them hundreds of meters long, occur in the central syenomonzonite stock and in the fine-grained Pikes Peak Granite immediately surrounding the stock. Stewart (1964) interpreted these elongate gabbro bodies as late dikes, but the syenite shows a chilled margin in contact with the gabbro and the fine grained granite intrudes the gabbro at several localities.

The gabbro is dark gray to black and generally fine-grained, locally containing irregular clusters of biotite as much as 2 cm in diameter. In thin section it is xenomorphic granular and contains poorly twinned, zoned andesine (An_{45-50}) intergrown with olivine (Fa_{30-40}), clinopyroxene of the augite-ferroaugite

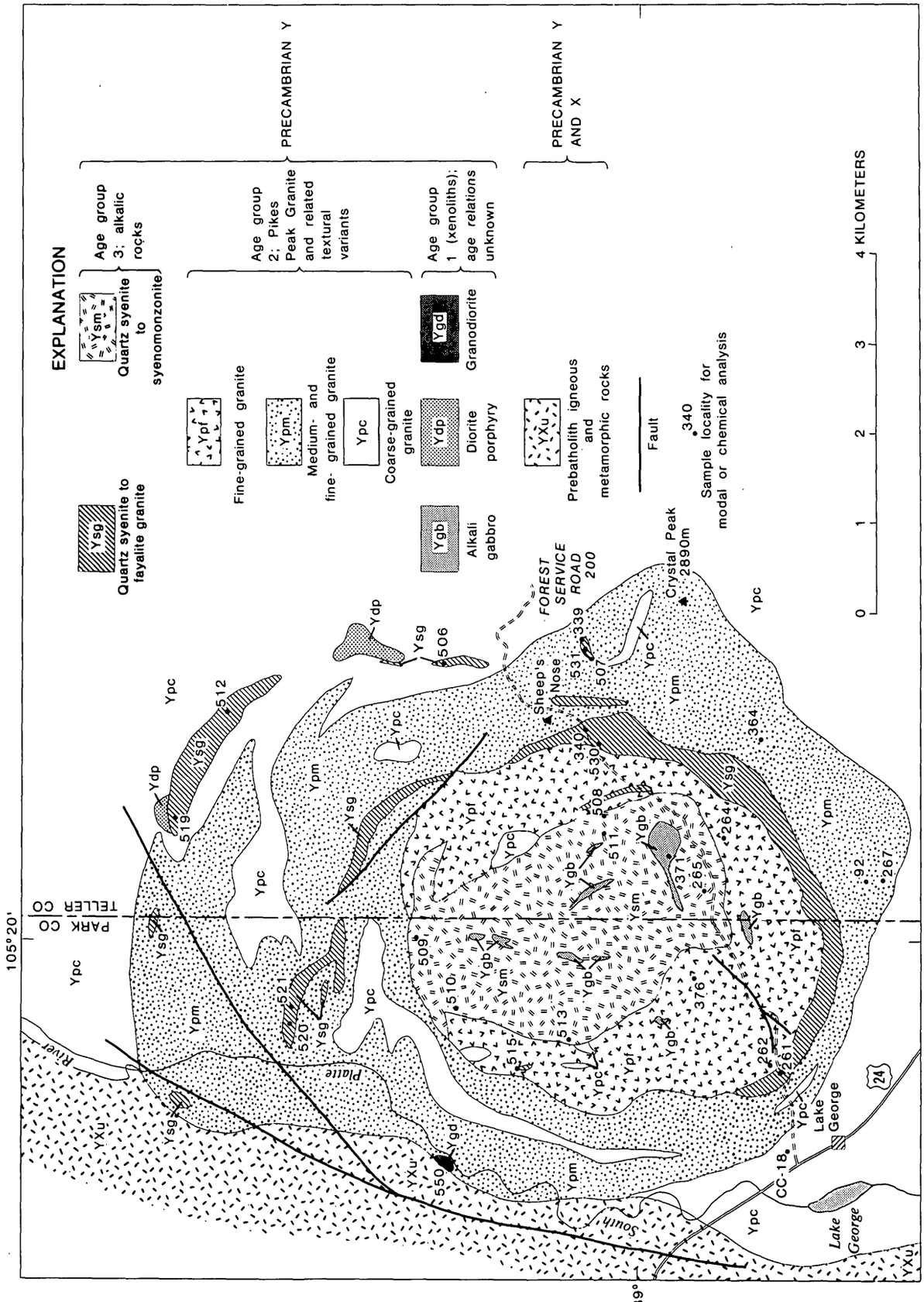

FIGURE 3.—Geologic map of the intrusive center at Lake George, showing sample locations.

TABLE 2.—*Point-counted modes of representative samples from the Lake George intrusive center*

[Tr., <0.5 percent; --, not observed]

	Older intrusive rocks							Younger intrusive rocks								
Rock name	Alkali gabbro	Granodiorite		Granitic rocks				Fayalite granite		Syenite						
Occurrence	Xenoliths			Texturally zoned granitic stock				Inner ring dike		Outer ring dike			Central stock		Chilled margin of stock		
Field number (see fig. 3)	[1]371	[1]550	92	[1]267	264	[1]364	376	[1]261	340	[1]339	512	520	[1]265	511	[1]508	[1]510	[1]513
Quartz	--	20	36	32	36	31	37	15	20	10	11	10	2	2	5	9	1
Plagioclase (albite-oligoclase unless otherwise noted)	68 (andesine)	46 (andesine)	13	17	23	11	13	2	9	28	9	7	17	11	28	8	11
Perthitic alkali feldspar	--	9	45	45	36	51	41	74	62	39	65	75	65	86	51	74	79
Biotite	13	17	6	4	5	6	7	Tr.	Tr.	5	--	1	Tr.	Tr.	1	.5	5
Amphibole:																	
ferrohastingsite	--	--	--	--	--	--	--	7	5	17	13	5	10	1	12	6	.5
hornblende	--	Tr.	--	--	--	--	--	--	--	--	--	--	--	--	--	--	--
Pyroxene:																	
hedenbergite	--	--	--	--	--	--	--	--	--	Tr.	--	--	2	--	--	--	--
augite	8	--	--	--	--	--	--	--	--	--	--	--	--	--	--	--	--
Olivine:																	
forsterite	5	--	--	--	--	--	--	--	--	--	--	--	--	--	--	--	--
fayalite (iddingsite)	--	--	--	--	--	--	--	Tr.	2	--	1	.5	1	--	--	--	2
Opaque	5	4	Tr.	2	Tr.	.5	1	2	1	1	1	.5	3	Tr.	3	2	.5
Zircon	Tr.	.5	Tr.	Tr.	Tr.	Tr.	Tr.	Tr.	Tr.	Tr.	Tr.	Tr.	Tr.	Tr.	Tr.	--	Tr.
Chevkinite	--	--	--	--	--	--	--	--	Tr.	--	--	--	--	--	Tr.	Tr.	Tr.
Apatite	1	.5	Tr.	--	--	--	--	--	--	Tr.	--	Tr.	Tr.	--	--	--	--
Fluorite	--	--	Tr.	Tr.	--	.5	Tr.	Tr.	1	Tr.	--	1	--	Tr.	Tr.	.5	1
Epidote	--	2	--	--	--	--	--	--	--	--	--	--	--	--	--	--	--
Muscovite	--	1	Tr.	--	--	--	1	--	--	--	--	--	Tr.	--	--	--	Tr.

[1]Chemically analyzed sample.

series ($2V = 30°–40°$), apatite, and opaque minerals (table 2, fig. 4). Biotite is secondary, enclosing olivine, pyroxene, and abundant accessory apatite (fig. 5).

Diorite porphyry

Diorite porphyry occurs only as badly weathered xenoliths in the Pikes Peak Granite. This rock type has white to light-gray plagioclase phenocrysts, 1–2 cm in diameter, in a very fine-grained, dark-gray groundmass. Small rounded clusters of dark minerals, usually 1–2 millimeters in diameter, are also distinguishable from the groundmass. In thin section, the largest grains are subhedral phenocrysts of faintly zoned andesine (about An_{40}) and glomeroporphyritic aggregates of biotite and hornblende with apatite and opaque minerals. Sieve texture is common in the biotite and hornblende aggregates. The groundmass consists of anhedral plagioclase, biotite, hornblende, apatite, and opaque minerals; quartz and alkali feldspar occur interstitially in a few samples. No chemical or modal analyses were made of these rocks because of the degree of alteration of the samples and the very fine grained nature of the groundmass.

Granodiorite

A single large xenolith of biotite granodiorite a few tens of meters on a side is exposed in a fresh roadcut along the South Platte River. The xenolith occurs in medium-grained granite just east of an intrusive breccia that defines the western margin of the complex at Lake George. The rock was sampled and analyzed because of its megascopic similarity to a larger granodiorite xenolith (0.8 km long) in fine-grained granite about 7 km north of Pikes Peak (Wobus and Scott, 1977). The Lake George rock is bluish-gray when fresh, medium grained, and faintly porphyritic. Modally (table 2, fig. 4) it consists of intermediate andesine, quartz, and biotite, with about 10 percent perthitic alkali feldspar.

Pikes Peak Granite and related textural variants

Coarse-grained Pikes Peak Granite is the dominant rock type of the western part of the Pikes Peak batholith in the vicinity of Lake George. Large xenoliths and septa of this granite also occur within the elliptical boundaries of the intrusive center. The coarse granite is massive, equigranular to seriate porphyritic, and pink when fresh; in its more common weathered state, it is pale orange red. Outcrops are typically rounded; the easily weathered granite disaggregates by biotite hydration and expansion to form very coarse grus, which is locally a few tens of meters thick (Blair, 1975). Mineralogically the granite is composed of perthitic alkali feldspar, quartz, oligoclase, and biotite and (or) hornblende. Fluorite, zircon, allanite, and opaque minerals are common accessories.

The medium-grained equigranular to porphyritic granite is a pink to buff biotite granite that intrudes coarse-grained Pikes Peak Granite. The more common

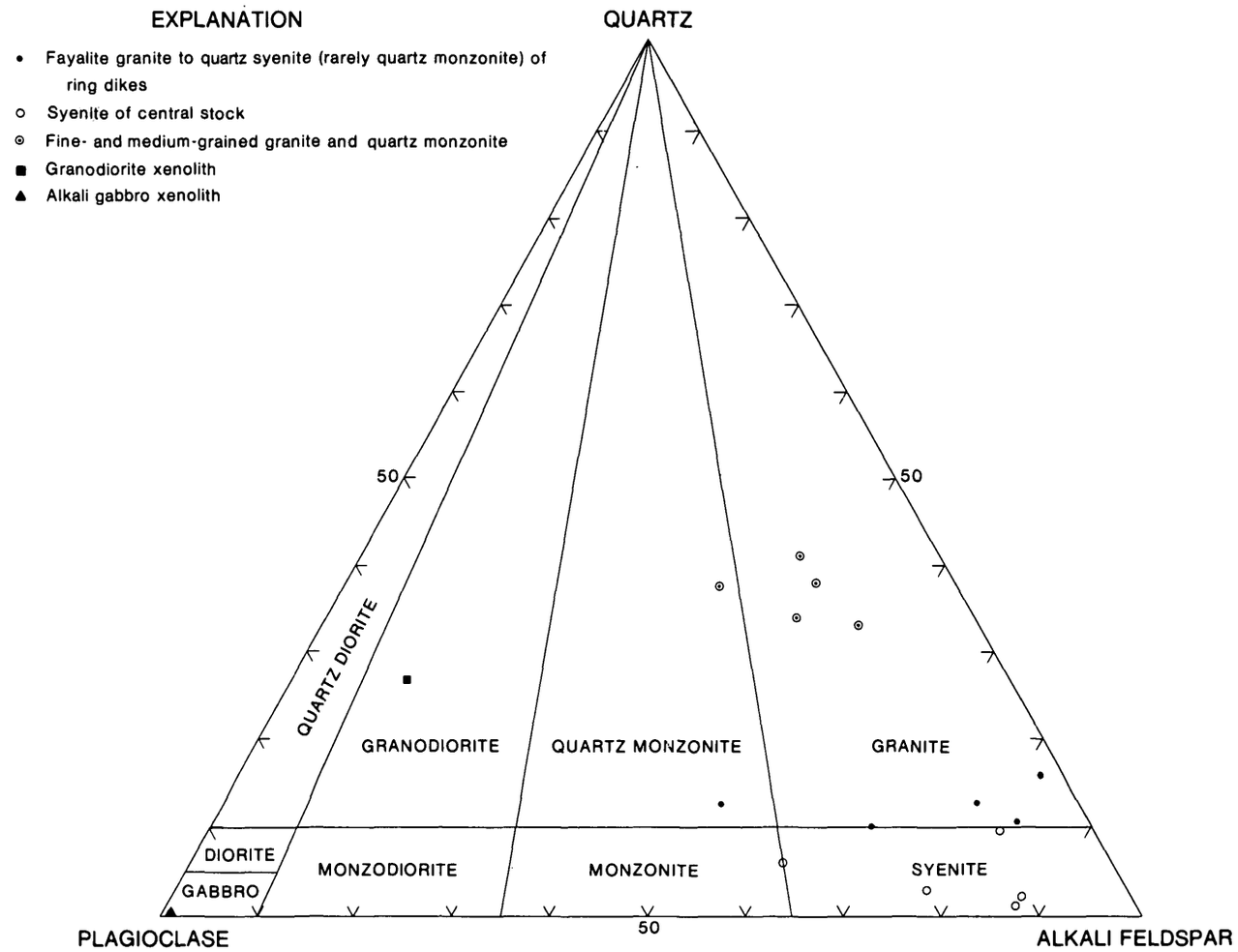

FIGURE 4.—Ternary diagram showing quartz-plagioclase-alkali feldspar plot of modes of representative samples from the Lake George intrusive center.

porphyritic variety contains subhedral phenocrysts of alkali feldspar and plagioclase, as well as rounded quartz grains and biotite clusters, in a fine-to medium-grained groundmass. Texturally and mineralogically this porphyritic variety of granite resembles the Windy Point Granite of the Pikes Peak massif (Finlay, 1916) and the Rampart Range (Wobus, 1976). As in those areas, the rock in the vicinity of Lake George is more resistant to weathering and erosion than is the coarse granite, and many of the topographically prominent ridges and hills of the complex at Lake George, including Crystal Peak, are underlain by this unit. In thin section, the medium-grained equigranular to porphyritic granite consists dominantly of perthitic microcline and quartz, with lesser amounts of oligoclase (An_{20-25}), biotite, and accessory zircon and opaque minerals.

Fine-grained equigranular granite (called aplogranite by Stewart, 1964) intrudes the coarse- and medium-grained varieties of Pikes Peak Granite and was itself intruded by the central syenomonzonite stock. This rock is pink when fresh; the contrast between the light-colored minerals and biotite produces a "salt-and-pepper" texture. Alteration colors range from dark red to orange and yellow. The most distinctive feature of this granite in thin section is the lack of perthitic feldspar textures. Instead, separate microcline and plagioclase (An_{25-30}) phases exist, along with quartz, biotite, and accessory minerals.

Quartz syenite to syenomonzonite of central stock

Quartz syenite to syenomonzonite forms the small central stock of the complex at Lake George. The stock is exposed in low, rounded outcrops; it has a medium- to coarse-grained equigranular core (sample 265, fig. 3) and a fine-grained chilled border (sample 513, fig. 3). An intrusive breccia occurs along its northern contact. The unweathered coarse syenite is

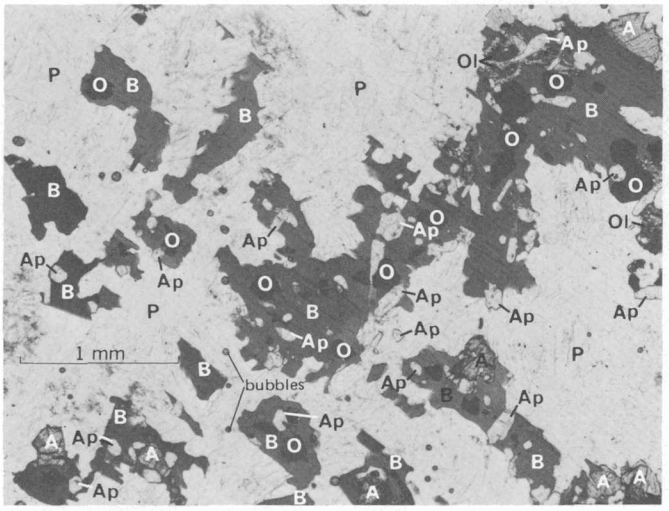

FIGURE 5.—Photomicrograph of gabbro, showing secondary anhedral biotite. B, biotite; P, plagioclase; A, augite; Ol, olivine; Ap, apatite; O, opaque iron and titanium oxides. Plane-polarized light, 20× magnification. Photomicrograph by Louise Hedricks.

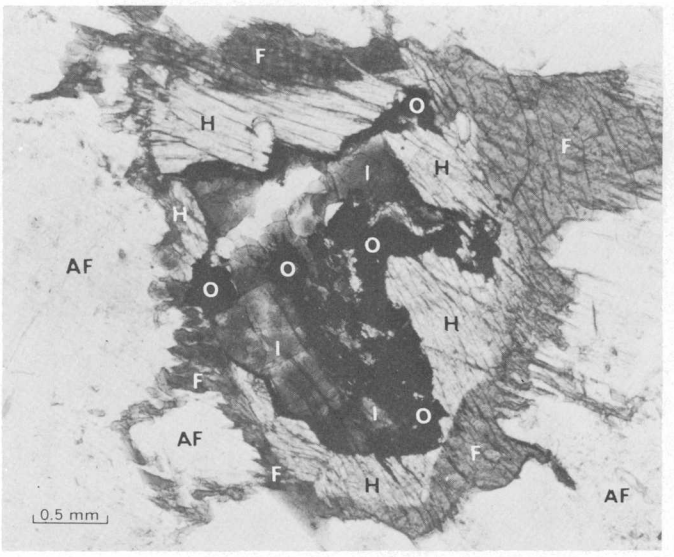

FIGURE 6.—Photomicrograph of medium-grained syenite from stock, showing reaction rim of hedenbergite and ferrohastingsite around altered fayalite (now iddingsite and opaques). I, iddingsite; H, hedenbergite; F, ferrohastingsite; O, opaque minerals; AF, perthitic alkali feldspar. Plane-polarized light, 100× magnification. Photomicrograph by Louise Hedricks.

dark green, but typical weathered outcrops are tan to buff. The fine-grained rock at the border of the stock is dark gray to grayish purple and locally contains inclusions of Pikes Peak Granite.

Petrographically the syenites consist primarily of perthitic alkali feldspar (table 2, fig. 4). The perthite textures vary from flame or braided to patch. A separate albite-oligoclase phase is present in all samples studied, though the amounts of this phase vary considerably. Quartz is anhedral interstitial and seems to be late; it also occurs in granophyric intergrowths with alkali feldspar. The mafic minerals are abundant and varied. Sodium-iron amphibole (ferrohastingsite) dominates, showing pleochroism from light yellow to dark blue-green, a negative optic sign, and an optic angle ($2V$) of less than 20°. Pyroxene (hedenbergite) is present in small amounts in several samples, as is fayalite, mostly altered to iddingsite. A reaction sequence among the dark minerals was found in several samples: fayalite is rimmed by pyroxene, and pyroxene, by amphibole (fig. 6). Secondary biotite is present but minor. Accessory minerals are apatite, fluorite, zircon, allanite, chevkinite, and opaque minerals.

Quartz syenite to fayalite granite of ring dikes

Fayalite-bearing granite has been recognized only in the ring dike southwest of the central syenomonzonite stock. The fayalite granite (sample 261, fig. 3) is tan to pink, is medium-grained equigranular, and has a distinctive fabric caused by interlocking tabular laths of alkali feldspar. This fabric apparently accounts for the superior resistance to erosion shown by the rock, which forms a pronounced ridge over the short distance it is exposed. The fabric of the feldspar and the presence of amphibole rather than biotite as the dominant dark mineral are the chief criteria in the field for distinguishing the fayalite granite from medium-grained Pikes Peak Granite. In thin section, the fayalite granite is composed principally of subhedral microcline perthite grains which are often Carlsbad twinned, anhedral quartz, and Na-Fe amphibole (ferrohastingsite). Minor biotite also occurs, along with albite-oligoclase, fayalite (mostly altered to iddingsite), and accessory fluorite, chevkinite, and opaque minerals.

Quartz syenite in the ring dikes (for example, samples 519, 530, and 531 in fig. 3) is medium-grained equigranular or fine-grained equigranular to slightly porphyritic. In hand specimen, its colors range from pale yellow to shades of red. It is mineralogically similar to quartz syenite of the central stock, although one sample (339) contains enough albite-oligoclase to be considered a quartz monzonite.

CHEMISTRY

Chemical work on samples from the Lake George intrusive center has concentrated on a comparison of the granitic (older) and alkalic (younger) rocks.

Single analyses are also reported for the alkali gabbro and granodiorite inclusions, but the samples of diorite porphyry were too highly altered to warrant chemical analysis. An earlier analysis of coarse-grained Pikes Peak Granite from near Lake George, reported by Barker and others (1975), is also included for comparison.

The chemical data are presented in table 3 and in Harker variation diagrams for the granitic and alkalic (syenites and fayalite granite) rock groups (fig. 7). An analysis of the xenolithic alkali gabbro is included on both Harker diagrams, because alkali gabbro is a possible precursor of either of the rock groups. Each

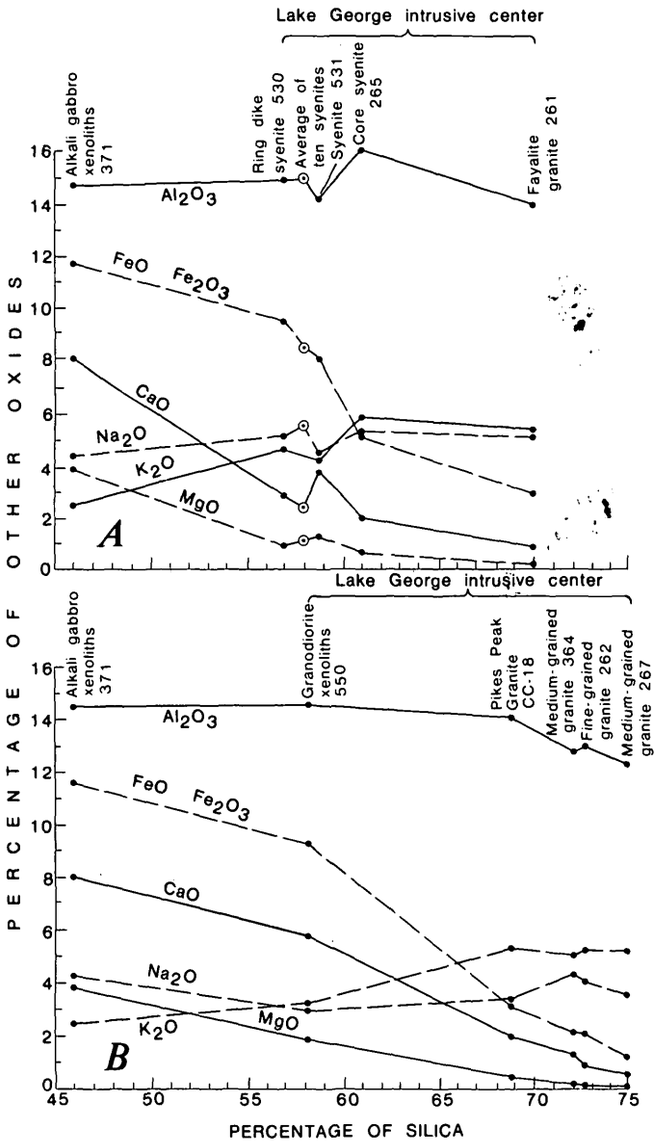

FIGURE 7.—Harker-type silica variation diagrams of (A) fayalite-bearing and (B) fayalite-free rocks of the Lake George intrusive center.

diagram illustrates a fairly regular decrease in total iron, MgO, and CaO and an increase in alkalies with increasing silica. The alkalies, particularly sodium, are notably higher in the fayalite-bearing rocks (syenite and fayalite granite), as is numerically apparent from the Na_2O/K_2O values in table 3. Although the number of analyses is small, the two Harker diagrams appear to define two separate differentiation trends, one more sodic than the other.

CIPW rock norms are also presented in table 3, and normative quartz-albite-orthoclase (Qz-Ab-Or) values are plotted on the ternary diagram in figure 8. The granitic and syenitic rocks occupy widely separated compositional fields on the diagram, with fayalite granite in between. In addition to being less siliceous, the syenites and fayalite granite also appear more sodic than the granitic rocks. The granitic rock compositions lie close to the experimentally determined ternary minima in the Qz-Ab-Or system for H_2O-saturated systems at moderate pressures, where $P_{H_2O} = P_{total}$ (Tuttle and Bowen, 1958; Luth and others, 1964).

The rocks of the Lake George intrusive center are compared in the Qz-Ab-Or diagram with rocks from small alkalic plutons of the Pikes Peak batholith and with granitic rocks from the batholith itself (Wobus, 1976; Barker and others, 1976; Barker and others, 1975). The syenites at Lake George are most similar chemically to the syenite of the Spring Creek pluton and to hornblende monzonite from north of Mount Rosa; considerable overlap also occurs with the compositional field of quartz syenite from West Creek. The single analysis of fayalite granite from Lake George contains less normative quartz than the fayalite granite in the Mount Rosa Granite, although the amounts of SiO_2 are comparable. Samples of the fine- and medium-grained granites from Lake George appear more sodic on the diagram than any of the fayalite-free granite analyses reported by Barker and others (1975); they are more similar chemically to the Redskin Granite (Hawley and others, 1966).

The analysis of the granodiorite inclusion from Lake George is compared, on a separate Qz-Ab-Or ternary diagram (fig. 9), with the other published analyses of granodiorite from the Pikes Peak batholith (Hawley and Wobus, 1977; Barker and others, 1975; Hutchinson, 1960). As indicated by the diagram, the granodiorite at Lake George is less potassic than granodiorite from the vicinity of Wellington Lake and Buffalo Creek in the northern part of the batholith; it is also lower in SiO_2 and higher in iron, CaO, and MgO.

TABLE 3.—*Chemical analyses and CIPW norms of representative*

[First ten analyses made in U.S. Geological Survey rock analysis laboratories in Denver; remaining ten

	USGS analyses									
	Older intrusive rocks									
Rock name	Alkali gabbro	Grano-diorite	Pikes Peak Granite of batholith	Granitic rocks			Fayalite granite	Syenite		
Occurrence	Xenoliths			Texturally zoned granitic stock			Inner ring dike		Outer ring dike	Central stock
Field number (see fig. 3)	[1]371	[3]550	[4]CC-18	[1]262	[1]267	[1]364	[1]261	[2]530	[2]531	[1]265
SiO_2	45.8	58.2	68.93	72.6	75.0	72.0	70.2	57.3	59.0	61.5
Al_2O_3	15.0	14.7	14.70	13.5	12.8	13.3	14.2	15.4	14.4	16.5
Fe_2O_3	2.1	5.8	1.90	1.2	.49	.86	1.8	2.2	1.4	1.1
FeO	9.8	3.9	1.44	1.1	.92	1.4	1.2	7.5	6.9	4.2
MgO	4.0	2.0	.36	.10	.04	.10	.07	.95	1.4	.60
CaO	8.3	5.3	2.18	.87	.68	1.5	.82	2.9	3.9	2.1
Na_2O	4.4	3.0	3.36	4.1	3.7	4.5	5.1	5.3	4.4	5.4
K_2O	2.5	3.2	5.64	5.4	5.4	5.1	5.4	4.6	4.2	5.9
H_2O^+	.59	.30	.33	.61	.43	.45	.56	1.0	.91	.67
H_2O^-	.09	.21	.07	.08	.03	.08	.03	.15	.05	.08
TiO_2	3.0	1.4	.52	.17	.06	.18	.22	1.1	1.5	.74
P_2O_5	3.9	1.1	.17	.05	.03	.02	.02	.28	.85	.17
MnO	.25	.13	.09	.09	.04	.06	.09	.42	.29	.22
CO_2	<.05	.01	.18	<.05	<.05	<.05	<.05	<.05	<.05	<.05
F	n.d.	.56	.16	n.d.	n.d.	n.d.	n.d.	n.d.	n.d.	n.d.
Total	100	99	100.03	100	100	100	100	99	99	99
Na_2O/K_2O	1.76	.94	.59	.76	.69	.88	.94	1.15	1.05	.92
CIPW norms:										
Quartz	--	18.7	24.0	26.2	31.1	23.7	18.7	--	6.4	1.2
Orthoclase	14.8	18.9	33.3	31.9	32.0	30.3	32.0	27.4	25.0	35.2
Albite	33.8	25.4	28.2	34.7	31.4	38.2	43.1	45.2	37.5	46.1
Anorthite	13.8	15.7	7.5	2.5	2.4	1.0	--	4.7	7.2	3.4
Corundum	--	.6	.4	--	--	--	--	--	--	--
Wollastonite	.8	--	n.d.	.6	.3	2.6	1.6	3.3	2.8	2.5
Diopside	1.6	--	n.d.	1.3	.7	3.7	1.4	6.9	5.7	5.2
Hypersthene	--	5.3	n.d.	.5	1.0	--	--	4.6	10.2	4.9
Olivine	15.5	--	--	--	--	--	--	3.9	--	--
Nepheline	1.9	--	--	--	--	--	--	--	--	--
Magnetite	3.0	8.4	2.8	1.7	.7	1.2	2.5	3.2	2.0	1.6
Ilmenite	5.7	2.7	1.0	.3	.1	.3	.4	2.1	2.9	1.4
Apatite	9.3	2.6	.4	.1	.1	.05	.05	.7	2.0	.4

[1]Analysis by U.S. Geological Survey; P. Elmore, G. Chloe, H. Smith, J. Glenn, J. Kelsey, analysts.
[2]Analysis by U.S. Geological Survey; P. Elmore, J. Glenn, H. Smith, J. Kelsey, analysts.
[3]Analysis by U.S. Geological Survey; Lowell Artis, analyst.

The gabbro inclusions in the complex at Lake George, containing 6.9 percent total alkalies, are clearly more alkalic than the average alkali basalt, containing 4.6 percent total alkalies (Manson, 1967). Recent work on minor elements and isotopes of this gabbro (Barker and others, 1976) has shown that it also contains two to three times the amount of rare-earth elements in typical alkali basalt, owing, in large part, to the concentration of cumulate apatite (P_2O_5 =3.9 percent) in the groundmass. The low initial $^{87}SR/^{86}Sr$ ratio of 0.7044 reported in this work indicates a mantle source for the gabbro, however.

INTERPRETATIONS AND CONCLUSIONS

The data from the intrusive rocks of the Lake George center seem to support the genetic model proposed by Barker and others (1975) of two separate differentiation trends for sodic and potassic rocks of the Pikes Peak batholith. According to the model, refined from the reaction theory of Bowen

samples from the Lake George intrusive center

partial analyses by x-ray fluorescence at Williams College. --, absent; n.d., not determined]

Williams College analyses										
Younger intrusive rocks										
Syenite										Average of preceding 10 syenite analyses
Inner ring dike	Outer ring dike					Chilled margin of stock				
[5]515	[5]339	[5]506	[5]507	[5]519	[5]521	[5]508	[5]509	[5]510	[5]513	
54.5	57.7	59.2	57.4	58.8	57.4	58.0	58.5	59.2	58.6	57.9
14.6	15.0	16.0	15.4	17.2	15.1	14.7	15.2	14.3	15.5	15.3
4.5	2.8	3.8	2.8	1.8	3.8	6.0	2.5	3.5	2.4	3.4
5.0	6.2	5.6	6.3	5.1	7.0	3.9	6.6	2.5	3.2	5.1
1.1	1.3	1.6	1.5	1.1	1.4	.8	1.1	.3	.4	1.1
2.2	2.8	3.1	3.0	2.6	3.3	1.6	2.2	1.2	1.3	2.3
5.7	5.0	5.6	5.6	5.2	6.5	5.5	6.2	4.9	5.4	5.6
5.0	4.6	4.7	4.5	4.4	4.5	5.7	4.6	5.3	5.9	4.9
n.d.	n.d.	n.d.	n.d.	n.d.	n.d.	n.d.	n.d.	n.d.	n.d.	n.d.
n.d.	n.d.	n.d.	n.d.	n.d.	n.d.	n.d.	n.d.	n.d.	n.d.	n.d.
n.d.	n.d.	n.d.	n.d.	n.d.	n.d.	n.d.	n.d.	n.d.	n.d.	n.d.
n.d.	n.d.	n.d.	n.d.	n.d.	n.d.	n.d.	n.d.	n.d.	n.d.	n.d.
n.d.	n.d.	n.d.	n.d.	n.d.	n.d.	n.d.	n.d.	n.d.	n.d.	n.d.
n.d.	n.d.	n.d.	n.d.	n.d.	n.d.	n.d.	n.d.	n.d.	n.d.	n.d.
n.d.	n.d.	n.d.	n.d.	n.d.	n.d.	n.d.	n.d.	n.d.	n.d.	n.d.
92.6	95.4	99.6	96.5	96.2	99.0	96.2	96.9	91.2	92.7	95.6
1.14	1.10	1.19	1.25	1.18	1.43	.98	1.36	.93	.91	1.14
--	1.4	--	--	1.9	--	1.1	--	8.1	1.1	n.d.
29.8	27.1	27.9	26.4	26.3	27.0	33.5	27.0	31.1	34.8	n.d.
39.4	42.6	47.3	47.0	44.4	38.0	44.0	49.1	41.3	45.5	n.d.
--	4.7	4.7	3.8	10.1	--	--	.1	1.4	.8	n.d.
--	--	--	--	--	--	--	--	--	--	n.d.
--	--	--	--	--	--	--	--	--	--	n.d.
9.0	8.6	8.9	9.5	2.7	13.9	6.4	9.5	3.6	4.9	n.d.
--	6.3	3.1	--	7.8	--	.7	--	.1	1.8	n.d.
3.1	--	1.8	7.4	--	6.6	--	8.0	--	--	n.d.
4.9	--	--	--	--	9.3	--	1.9	--	--	n.d.
5.8	4.0	5.5	4.1	2.7	4.0	7.5	3.7	5.1	3.5	n.d.
n.d.	n.d.	n.d.	n.d.	n.d.	n.d.	n.d.	n.d.	n.d.	n.d.	n.d.
n.d.	n.d.	n.d.	n.d.	n.d.	n.d.	n.d.	n.d.	n.d.	n.d.	n.d.

[4]Analysis by U.S. Geological Survey; E. S. Daniels, analyst (Barker and others, 1975).
[5]X-ray fluorescence analysis by R. S. Anderson at Williams College.

(1928), alkali olivine basalt magma from the mantle first reacts with and partially melts K_2O-depleted rocks of the lower to intermediate crust to produce relatively sodic magmas. The alkali gabbro of Lake George could be a very early product of this reaction-melting process, only slightly contaminated by reaction with crustal rocks. If these sodic magmas of Barker's model reached the upper crust without further reaction or contamination, they could crystallize directly to rocks of syenitic compostion or could differentiate to yield fayalite granite and (or) riebeckite granite. If, however, the ascending sodic magma reacted extensively with the older Precambrian wall and roof rocks (chiefly granodiorite to granite of Boulder Creek and Silver Plume ages) that constituted large portions of the middle crust beneath the Pikes Peak region 1 billion years ago, a more potassic liquid would have been produced. The major granitic rock types of the Pikes Peak batholith are thought to have

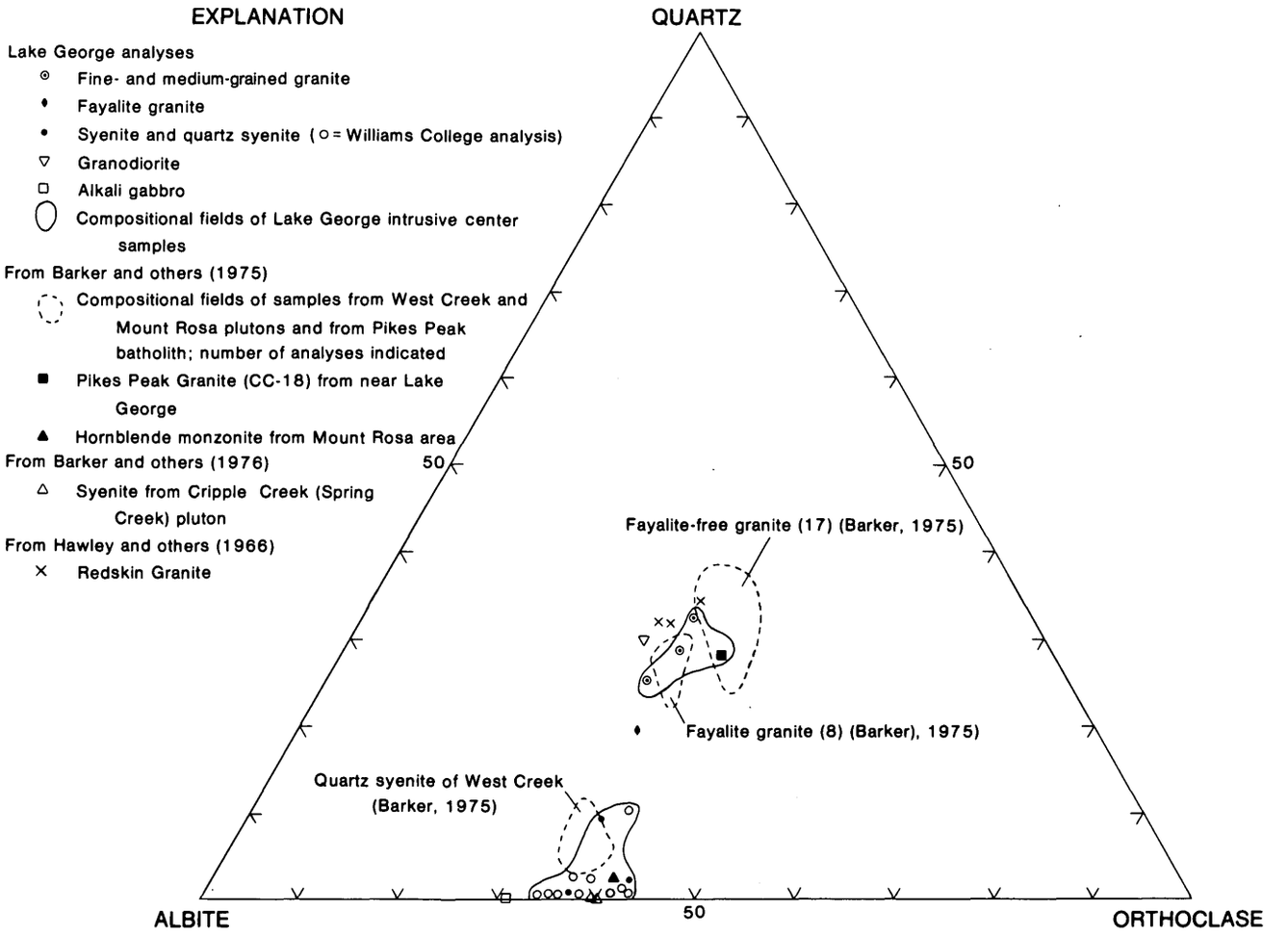

FIGURE 8.—Ternary diagram showing normative quartz-albite-orthoclase values for rocks of the Lake George intrusive center and other plutons of the Pikes Peak batholiths.

crystallized in the epizone from a potassic magma derived in this way. Minor textural variations among granites of the batholith resulted from different cooling rates in the several large intrusive centers that compose the batholith (Hutchinson, 1972). The granodiorite and diorite porphyry inclusions in the granite presumably represent intermediate stages of the reaction-melting process in which larger amounts of refractory minerals are preserved.

Field relations in the Lake George area show that the dominant coarse-grained Pikes Peak Granite of the western part of the batholith had already crystallized when it was intruded by a late pulse of granitic magma, slightly enriched (by differentiation) in silica and alkalies. This magma cooled rapidly to produce a small, texturally zoned stock at the edge of the batholith. The nearby Redskin stock, of similar size and composition, was also emplaced after the crystal-

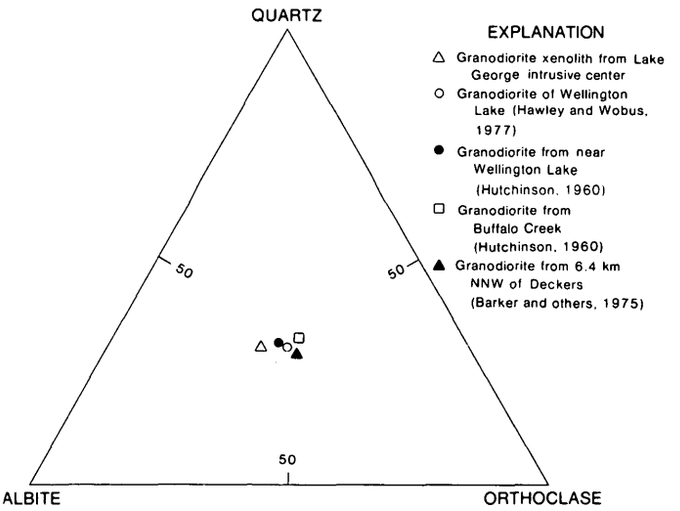

FIGURE 9.—Ternary diagram showing normative quartz-albite-orthoclase values of chemically analyzed granodiorites of the Pikes Peak batholith.

lization of the Pikes Peak Granite (Hawley and others, 1966).

After crystallization of the small granitic pluton of Lake George, ring fracture and possible cauldron subsidence of the central part of the pluton occurred during the emplacement of uncontaminated syenitic magma, which must have risen rapidly through fractures from the lower crust. Chilling of the syenite magma at the margin of the central stock produced a fine-grained border zone, while differentiation of the magma in the inner ring dike yielded fayalite granite in one part of the dike.

Alkalic ring complexes are typically shallow crustal (epizonal) features, as has been observed by many authors (for example, Sorensen, 1974); associated lavas may be preserved in the down-faulted interiors of such complexes. Whether the Lake George or other intrusive centers related to the Pikes Peak batholith ever yielded volcanic deposits is purely speculative, but the shallow level of emplacement of these small plutons and of the batholith itself is indicated by both structural and mineralogical features. Ring dikes, chilled margins, and the miarolitic cavities of the Pikes Peak Granite and its associated plutons are indicators of shallow (epizonal) emplacement (Buddington, 1959), and the chemical and mineralogical data of Barker and others (1975) suggest that crystallization of the Pikes Peak batholith and the alkalic complex at Mount Rosa occurred at pressures of about 1.5 kilobars or at 5 km depth. The Lake George intrusives, having a better developed ring structure, may indicate an even shallower level of emplacement than the alkalic rocks at Mount Rosa.

Alkalic plutons characteristically occur in anorogenic regions; indeed, reaction melting of the type envisioned by Baker and others (1975) could not have occurred under conditions of tectonic activity. Such plutons are, however, often associated with regional fracture systems, especially rifts, and may be localized by them (Chapman, 1968). These fractures presumably have served as the conduits that allowed syenitic magma from the lower crust to reach epizonal levels rapidly, without further reaction with rocks of the intermediate crust. As noted earlier, six of the seven alkalic intrusive centers of the Pikes Peak batholith, including the Lake George center, appear to be alined along northwest-trending linears (fig. 1) that parallel major Precambrian fault systems of the southern Front Range (Wobus, 1976; Bryant and Wobus, 1975). The three intrusive centers along the southern linear—Tarryall, Lake George, and Mount Rosa, as well as the Spring Creek syenite pluton further to the south—have crudely to well-developed ring structures, while those to the north do not, perhaps indicating that erosion has exposed deeper levels of the batholith toward the north.

REFERENCES CITED

Barker, Fred, Millard, H. T., Jr., Hedge, C. E., and O'Neil, J. R., 1976, Pikes Peak batholith—Geochemistry of some minor elements and isotopes, and implications for magma genesis, *in* Epis, R. C., and Weimer, R. J., eds., Studies in Colorado Field Geology: Colorado School Mines Prof. Contr. 8, p. 44–56.

Barker, Fred, Wones, D. R., Sharp, W. N., and Desborough, G. A., 1975, The Pikes Peak batholith, Colorado Front Range, and a model for the origin of the gabbro-anorthosite-syenite-potassic granite suite: Precambrian Research, v. 2, p. 97–160.

Blair, R. W., Jr., 1975, Weathering and geomorphology of the Pikes Peak Granite in the southern Rampart Range, El Paso County, Colorado: Colorado School Mines Ph. D. thesis, 115 p.

Bowen, N. L., 1928, The evolution of the igneous rocks: Princeton, N. J., Princeton Univ. Press, 334 p.

Bryant, Bruce, and Wobus, R. A., compilers, 1975, Preliminary geologic map of the southwestern quarter of the Denver 1°×2° quadrangle, Colorado: U.S. Geol. Survey Open-File Rept. 75–340.

Buddington, A. F., 1959, Granite emplacement with special reference to North America: Geol. Soc. America Bull., v. 70, no. 6, p. 671–747.

Chapman, C. A., 1968, Intersecting belts of post-tectonic "alkaline" intrusions in New England: Illinois Acad. Sci. Trans., v. 61, no. 1, p. 46–52.

Finlay, G. I., 1916, Description of the Colorado Springs quadrangle [Colorado]: U.S. Geol. Survey Geol. Atlas, Folio 203.

Gross, E. B., and Heinrich, E. W., 1965, Petrology and mineralogy of the Mount Rosa area, El Paso and Teller Counties, Colorado—pt. 1, The granites: Am. Mineralogist, v. 50, no. 9, p. 1273–1295.

Hawley, C. C., 1969, Geology and beryllium deposits of the Lake George (or Badger Flats) beryllium area. Park, and Jefferson Counties, Colorado: U.S. Geol. Survey Prof. Paper 608–A, 44 p.

Hawley, C. C., Huffman, Claude, Jr., Hamilton, J. C., and Rader, L. F., Jr., 1966, Geologic and geochemical features of the Redskin Granite and associated rocks, Lake George beryllium area, Colorado: U.S. Geol. Survey Prof. Paper 550–C, p. C138–C147.

Hawley, C. C., and Wobus, R. A., 1977, General geology and petrology of the Precambrian crystalline rocks, Park and Jefferson Counties, Colorado: U.S. Geol. Survey Prof. Paper 608–B, 77 p.

Hutchinson, R. M., 1960, Structure and petrology of the north end of Pikes Peak batholith, Colorado, *in* Weimer, R. J., and Haun, J. D., eds., Guide to the geology of Colorado: Denver, Colo., Rocky Mtn. Assoc. Geologists, p. 170–180.

———1963, Time span and field-time relations of Pikes Peak batholith and its wall rocks, Colorado: Geol. Soc. America Abs. for 1963, Rocky Mtn. Sec. Mtg., p. 277.

———1972, Pikes Peak batholith and Precambrian basement rocks of the central Colorado Front Range—Their 700-million-year history [abs.]: 24th Internat. Geol. Cong., Proc., Sec. 1, Program No. 24, p. 201–212.

Hutchinson, R. M., and Hedge, C. E., 1967, Precambrian basement rocks of the central Colorado Front Range and its 700-million-year history: Geol. Soc. America, Rocky Mtn. Sec., Guidebook for Field Trip No. 1, 51 p.

Jeffrey, P. G., 1970, Chemical methods of rock analysis: Oxford, Pergamon Press, 509 p.

Luth, W. C., Jahns, R. H., and Tuttle, O. F., 1964, The granite system at pressures of 4 to 10 kilobars: Jour. Geophys. Research, v. 69, no. 4, p. 759–773.

Manson, Vincent, 1967, Geochemistry of basaltic rocks—Major elements, *in* Hess, H. H., and Poldervaart, A., eds., Basalts —The Poldervaart treatise on rocks of basaltic composition: New York and London, Interscience Publishers, v. 1, p. 215–269.

Sage, R. P., 1966, Geology and mineralogy of the Cripple Creek syenite stock, Teller County, Colorado: Colorado School Mines M.S. thesis, 236 p.

Scott, G. R., 1975, Cenozoic surfaces and deposits in the southern Rocky Mountains, *in* Curtis, B. F., ed., Cenozoic history of the southern Rocky Mountains: Geol. Soc. America Mem. 144, p. 227–248.

Scott, G. R., Taylor, R. B., Epis, R. C., and Wobus, R. A., 1976, Geologic map of the Pueblo 1°×2° quadrangle, south-central Colorado: U.S. Geol. Survey Map MF–775.

Sorensen, Henning, 1974, Introduction—Regional distribution and tectonic relations, in Sorensen, Henning, ed., The alkaline rocks: New York, Wiley-Interscience, p. 145–148.

Stewart, D. D., 1964, Geology and petrology of the Lake George syenite stock, Park and Teller Counties, Colorado: Colorado School Mines M. S. thesis, 115 p.

Tuttle, O. F., and Bowen, N. L., 1958, Origin of granite in the light of experimental studies in the system $NaAlSi_3O_8$ —$KAlSi_3O_8$—SiO_2—H_2O: Geol. Soc. America Mem. 74, 153 p.

Wobus, R. A., 1969, Granitic rocks of the Florissant quadrangle, southern Front Range, Colorado: Geol. Soc. America Abs. with Programs 1969, pt. 5, p. 90.

———1976, New data on potassic and sodic plutons of the Pikes Peak batholith, central Colorado, *in* Epis, R. C., and Weimer, R. J., eds., Studies in Colorado Field Geology: Colorado School Mines Prof. Contr. 8, p. 57–67.

Wobus, R. A., and Scott, G. R., 1977, Reconnaissance geologic map of the Woodland Park 7½-minute quadrangle, Teller County, Colorado: U.S. Geol. Survey Misc. Field Studies Map MF–842.

Jour. Research U.S. Geol. Survey
Vol. 6, No. 1, Jan.–Feb. 1978, p. 95–106

IGNEOUS AND METAMORPHIC PETROLOGY OF THE SOUTHWESTERN DANA MOUNTAINS, LASSITER COAST, ANTARCTIC PENINSULA

By WALTER R. VENNUM,[1] Rohnert Park, Calif.

Abstract.—The southwestern Dana Mountains of the southern Antarctic Peninsula are underlain by the western part of a composite concentrically zoned Upper Cretaceous batholith consisting largely of granodiorite. The granodiorite (felsic phase) was intrusive into older heterogeneous gabbro-diorite (mafic phase) which makes up the margin of the batholith. Flat-lying pegmatite bodies and abundant inclusions, roof pendants, and septa of metasedimentary rocks and gabbro-diorite suggest that the granodiorite lies near the roof of the batholith. Petrography, chemistry, field relations, and radiometric age dates indicate that the batholith is part of the Andean intrusive suite, a suite of calc-alkaline plutonic rocks that crops out extensively throughout the Antarctic Peninsula and Chilean and Patagonian Andes. Textural features, mineralogy, and chemical data indicate that both phases of the batholith in the southwestern Dana Mountains have been contaminated by assimilation of the Latady Formation, an Upper Jurassic sequence of shale, siltstone, and sandstone that underlies large parts of the southern Antarctic Peninsula. Composition of the granodiorite also has been modified by assimilation of lesser amounts of the gabbro-diorite phase. Such contaminated plutonic rocks occur in several places in the northern Antarctic Peninsula; the batholith in the southwestern Dana Mountains represents the southernmost exposures of contaminated igneous rocks known from the Antarctic Peninsula. Hornblende andesite dikes cut both the mafic and felsic phases of the batholith. Chemical data imply that the dikes represent small amounts of mafic material remobilized by intrusion of the granodiorite.

During the austral summers of 1969–70, 1970–71, and 1972–73, U.S. Geological Survey personnel mapped in reconnaissance approximately 30 000 square kilometers of the Lassiter Coast and southern Black Coast near the southeastern base of the Antarctic Peninsula (fig. 1). During the final field season, relatively detailed studies were made in the southwestern Dana Mountains (fig. 2) because contact relations between two phases of the concentrically zoned Werner batholith and between the batholith and its pelitic metasedimentary country rocks are unusually well exposed there. Flat-lying pegmatite bodies and abundant inclusions, roof pendants, and septa of the metasedimentary rocks and older mafic phase as long as several hundred meters indicate that the felsic plutonic rocks lie near the roof of the batholith. Field relations and the presence of garnet crystals randomly distributed throughout both phases of the batholith suggest contamination of the plutonic rocks of the southwestern Dana Mountains by pelitic sedimentary rocks.

This report discusses the petrography, geochemistry, and igneous history of the plutonic rocks of the southwestern Dana Mountains that were given detailed study. This report also briefly describes the contact-metamorphic effects produced in the sedimentary country rocks and the evidence that the igneous phases were contaminated by significant assimilation of sedimentary country rocks and older igneous rocks.

The modal classification of the igneous rocks discussed in this paper follows Bateman (1961, fig. 2). Optical properties of hornblende and biotite were estimated by conventional flat-stage techniques. Plagioclase compositions were determined using the extinction-curve method of Tobi (1963). Modes were determined by counting 600 points on standard-size stained thin sections using the methods of Van der Plas and Tobi (1965).

Acknowledgments.—This study was financed by National Science Foundation grant AG–187. Logistical support was provided by the U.S. Antarctic Research Program of the National Science Foundation and U.S. Navy Squadron VXE–6. I thank the other five members of the field party: S. J. Boyer, E. N. Kamenev, K. S. Kellogg, P. D. Rowley, and R. B. Waitt, Jr.; all were with the U.S. Geological Survey except Kamenev who is a member of the Research Institute of the Geology of the Arctic, Leningrad, USSR. This report draws heavily on their field notes and observations. R. V. Davis, a student at California State College, Sonoma, made the modal analyses of the analyzed

[1] Work done when author was employed by the U.S. Geological Survey, Menlo Park, Calif. Present address is Department of Geology, California State College, Sonoma, Rohnert Park, CA 94928.

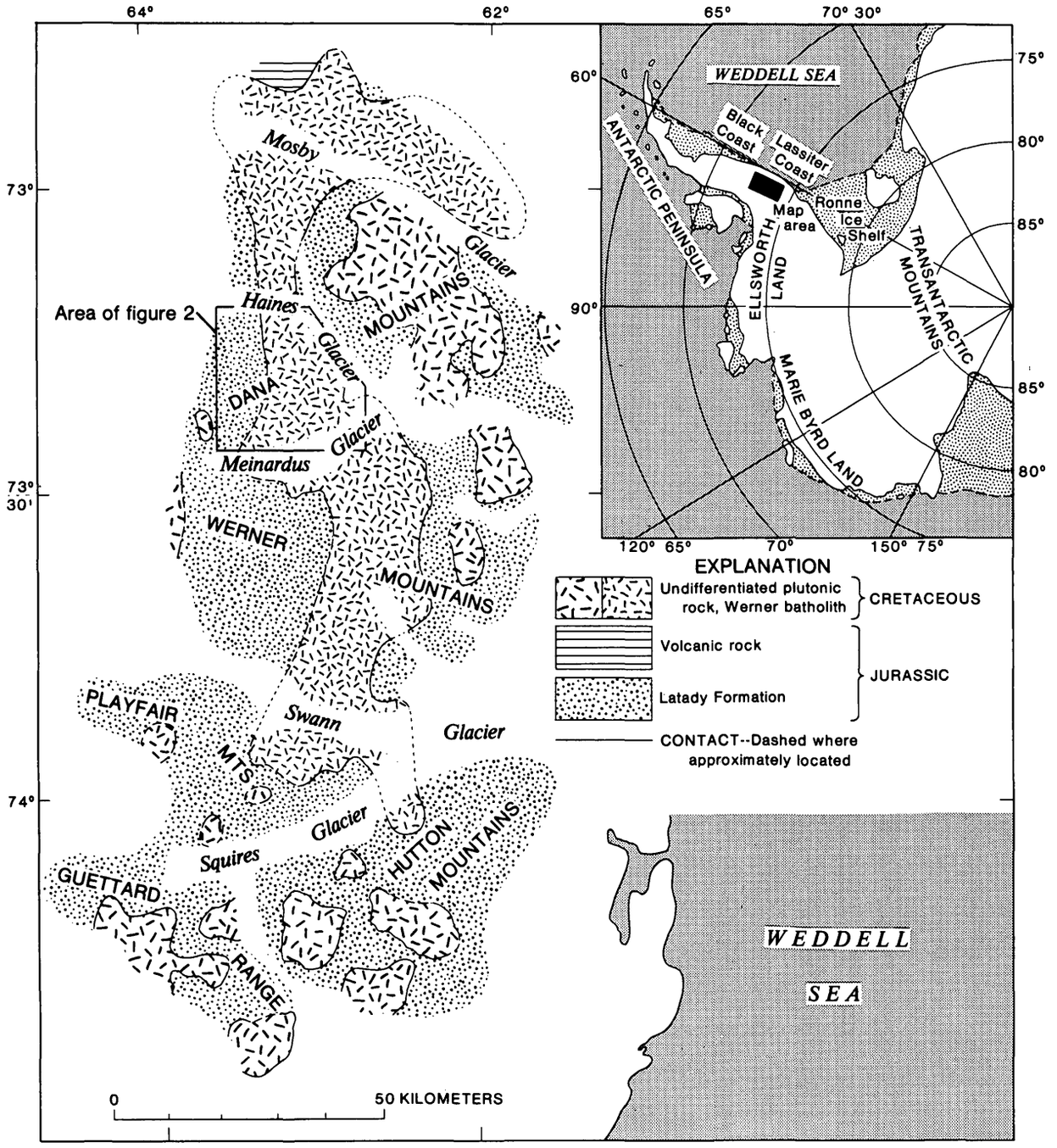

FIGURE 1.—Preliminary geologic map of the southern Black Coast and northern Lassiter Coast, Antarctic Peninsula, showing distribution of the Werner batholith. Compiled by P. D. Rowley (unpub. data, 1976). Area of figure 2 is outlined.

rocks. I am grateful to my wife Barbara for her help with the manuscript and for her indulgence in my long absence from home during the austral summer of 1972–1973. P. D. Rowley, H. J. Prostka, A. B. Ford, and M. A. Kuntz reviewed the manuscript.

GEOLOGIC SETTING

Williams, Schmidt, Plummer, and Brown (1972), Williams and Rowley (1971), and Rowley (1973) summarized the geology of the entire Lassiter Coast and southern Black Coast. The Latady Formation, a sequence of intensely folded black and gray shale, siltstone, and minor sandstone, is the oldest and most widespread unit on the Lassiter Coast. It contains abundant volcaniclastic material (Williams and Rowley, 1972). Locally abundant invertebrate fossils indicate a Late Jurassic age (R. W. Imlay and E. G. Kauffman, written commun., 1976) for the formation.

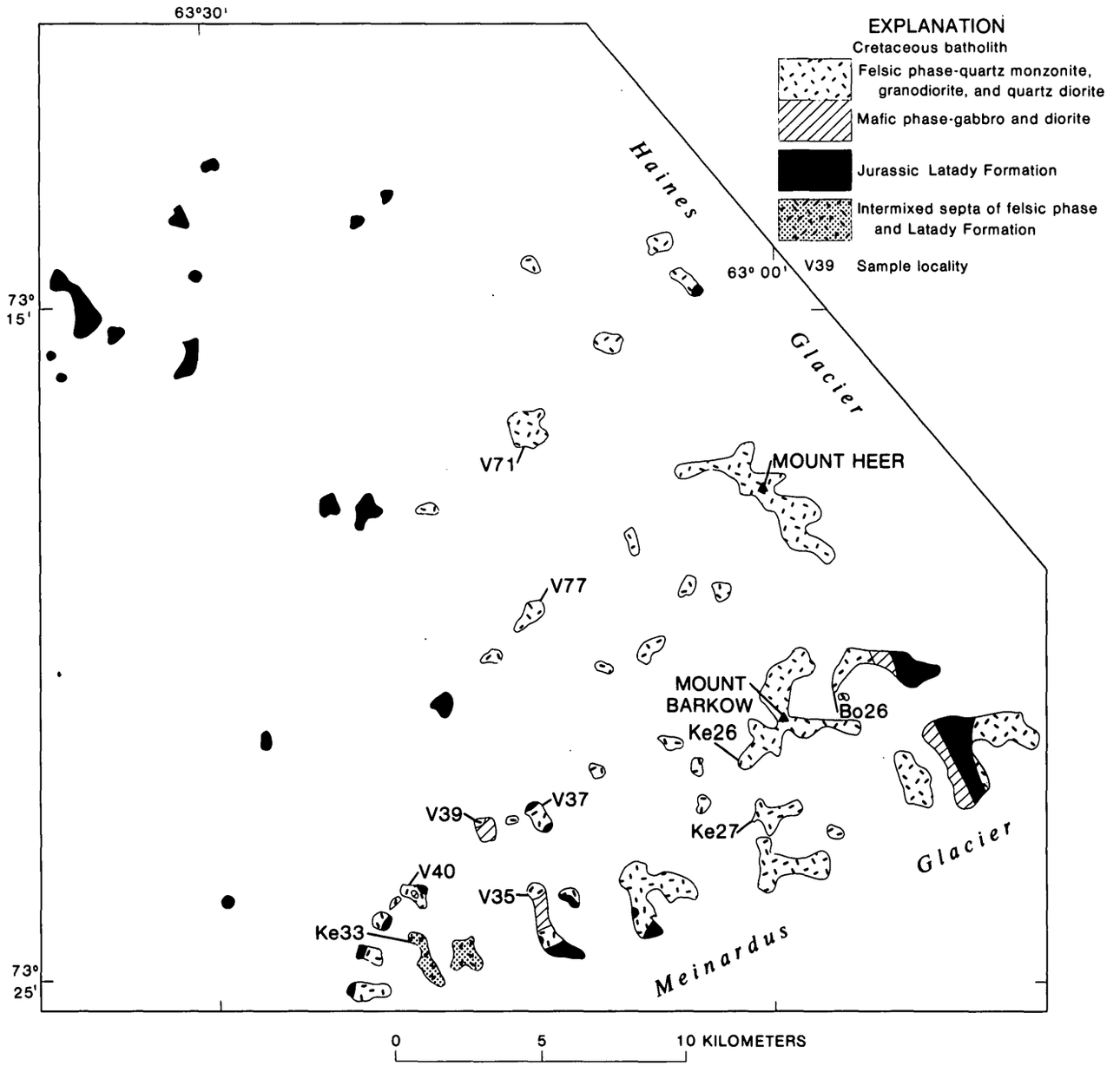

FIGURE 2.—Preliminary geologic map of the southwestern Dana Mountains, Lassiter Coast, Antarctic Peninsula. Outlines show nunataks, which are surrounded by snow and ice. Mapped by P. D. Rowley, W. R. Vennum, K. S. Kellogg, S. J. Boyer, R. B. Waitt, Jr. and E. N. Kamenev.

The Latady is overlain and intertongued by silicic ash-flow tuff, andesitic to dacitic lava flows, and air-fall tuff (Williams and others, 1972) that are considered to be Late Jurassic on the basis of intertonguing relations with the Latady and of age relations of similar volcanic rocks exposed elsewhere on the Antarctic Peninsula (Adie, 1972; Dalziel and Elliot, 1973).

The Latady Formation and overlying Upper Jurassic volcanic rocks were intruded and contact metamorphosed by more than 50 stocks and batholiths, which are largely quartz monzonite, granodiorite, and quartz diorite, but range in composition from gabbro to granite. Field relations, petrography, and chemistry (Rowley and Williams, 1974) indicate that the plutonic rocks are correlative with the Andean intrusive suite, a suite of calc-alkaline plutonic rocks exposed extensively throughout the Antarctic Peninsula and Chilean and Patagonian Andes Mountains (Adie, 1955). Dikes of prophyritic to even-grained andesite or dacite cut the plutonic and sedimentary rocks. K-Ar ages (Mehnert and others, 1975; Rowley and others, 1975;

Rowley and others, 1976) of 16 samples from eleven plutons and one dike are Late Cretaceous. Scattered local copper and molybdenum mineralization, with similarities to the porphyry type, was a late-stage product of the igneous activity (Rowley and others, 1975; Rowley and others, 1977).

The largest pluton in the Lassiter Coast is the Werner batholith (fig. 1) which is named herein for extensive exposures of this body in the Werner Mountains. This batholith averages about 20 kilometers in width and extends for nearly 150 km southward from the southern Black Coast to the central Lassiter Coast. Most of this concentrically zoned batholith consists of quartz diorite and granodiorite that intrudes a thin marginal phase (generally less than 2 km wide) of heterogeneous gabbro and diorite (P. D. Rowley, unpub. data, 1976). The southwestern Dana Mountains lie at the western edge of the central part of the Werner batholith. Five K-Ar dates that range from 98.2 to 114.4 m.y. (million years) have been obtained from the Werner batholith (Rowley and others, 1976). The main felsic phase is about 100 m.y. old and the mafic phase probably is about 114 m.y. old.

INTRUSIVE ROCKS OF THE SOUTHWESTERN DANA MOUNTAINS

Most igneous rocks in the southwestern Dana Mountains are light-colored biotite granodiorite and biotite-quartz diorite. These rocks represent a single felsic phase of the Werner batholith and intruded an older heterogeneous mafic phase of gabbro and diorite along the western margin of the Werner batholith (fig. 2). The mafic phase is cut by hornblende diorite pegmatite dikes; tourmaline-garnet-muscovite pegmatite dikes and garnet-muscovite aplite dikes intruded the felsic phase of the batholith. Hornblende-rich andesite dikes intruded both plutonic phases and, in at least one location (V77), cut the aplite dikes. Modes of chemically analyzed samples from the southwestern Dana Mountains are plotted in figure 3 and listed in table 1.

TABLE 1.—*Modes (volume percent) of chemically analyzed samples from the southwestern Dana Mountains*

[Tr., trace, less than 0.1 percent; dash leaders, not detected.]

Sample	V39f	V39c	V77c	V35a	V35e	Bo26a	V39g	V71	Ke26d
Plagioclase	64.5	51.4	24.1	48.2	57.2	45.3	56.1	44.2	31.7
Quartz	5.4	6.2	6.1	13.6	27.0	27.7	26.8	26.1	26.0
K-feldspar	1.5	3.1	4.2	8.2	5.1	15.9	7.1	16.3	41.5
Felsic groundmass	----	----	15.7	----	----	----	----	----	----
Biotite	11.6	Tr.	----	21.1	8.9	6.1	9.5	8.2	Tr.
Hornblende	15.0	32.2	33.8	5.7	.3	2.0	.1	1.1	----
Chlorite	.8	.3	8.1	2.8	.4	.9	.1	.3	----
Sericite	.2	.6	.2	.2	.1	.2	----	1.2	.8
Opaques	.4	1.3	2.7	Tr.	----	----	.2	Tr.	----
Sphene	----	1.7	2.0	.1	Tr.	.2	----	Tr.	----
Apatite	----	1.9	Tr.	Tr.	.1	.6	Tr.	.1	Tr.
Epidote	.6	1.0	3.1	.1	.6	1.1	.1	1.9	----
Zircon	----	.3	Tr.	----	.3	Tr.	Tr.	.6	Tr.
Calcite	----	Tr.	Tr.	----	----	----	----	----	----
Allanite	----	----	----	----	----	Tr.	----	Tr.	----
Garnet	Tr.	----	----	Tr.	----	----	Tr.	----	Tr.
Rutile	Tr.	----	----	----	----	----	----	----	----

SAMPLE DESCRIPTIONS

V39f. Diorite, 73°23' S., 63°15' W.
V39c. Diorite, 73°23' S., 63°15' W.
V77c. Hornblende andesite dike, 73°20' S., 63°12' W.
V35a. Quartz diorite inclusion in felsic phase, 73°24' S., 63°13' W.
V35e. Quartz diorite, 73°24' S., 63°13' W.
Bo26a. Granodiorite, 73°21' S., 63°02' W.
V39g. Quartz diorite, 73°23' S., 63°15' W.
V71. Granodiorite, 73°17' S., 63°13' W.
Ke26d. Aplite dike, 73°22' S., 62°59' W.

Plutonic Rocks

Mafic phase

Dark gray to black mafic plutonic rock that ranges in composition from quartz-bearing hornblende gabbro to calcic biotite-hornblende diorite crops out on three nunataks about 10–14 km southwest of Mount Barkow, on one nunatak 2 km northeast of Mount Barkow and on one nunatak about 5 km east of Mount Barkow (fig. 2). Biotite and hornblende K-Ar ages from sample V39f are 101 and 114 m.y., respectively (Rowley and others, 1976). Rocks of this phase are hypidiomorphic, range from fine ($\leq$1 millimeter) to medium (1–5 mm) grained, and in many places have a spotted or speckled appearance due to the presence of large (5–6 mm) anhedral to subhedral plagioclase crystals and rare clear glassy quartz grains. Hornblende is the principal mafic mineral, but the hornblende-biotite ratio is highly variable (table 1). Biotite in some rocks occurs as poikiloblastic crystals or

TABLE 2.—*Petrographic characteristics of the mafic phase, Werner batholith, southwestern Dana Mountains*

Mineral	Description
Plagioclase	Subhedral tablets, normally zoned (An_{75}-An_{35}) having saussuritized cores, calcic cores sharply demarcated from much more sodic rims. Rare patchy extinction and oscillatory zoning.
Amphibole	Absorption and pleochroism weak, colorless, pale olive green; $2V_\alpha$=85-90°, Z^c=17°, σ=0.016. Poikilitic plates or prisms (3-5 mm) having ragged terminations. Inclusions of biotite arranged in linear fashion. Several grains in each section show marginal alteration to chlorite (σ=0.001, faint green pleochroism) and lesser amounts of calcite, epidote, and sphene.
Biotite	Absorption and pleochroism strong, α colorless to straw yellow, γ reddish-brown; $2V_\alpha$=2-5°; slight marginal alteration to chlorite (isotropic, colorless) and epidote.
Quartz	Highly fractured crystals or mosaics of several grains. Strong undulatory extinction. Interstitial.
Accessory minerals.	All thin sections contain potassium feldspar, apatite, sphene, opaque oxides, and pyrite. Hematite (50 percent of all thin sections) as 0.1-0.2-mm rims on opaques and as 0.1-0.2-mm euhedral grains. Garnets (2 sections) pale chocolate brown, anhedral, isotropic (Ke33i), feebly birefringent (0.002) anhedral-subhedral, irregular zonation from pale chocolate brown cores to colorless rims (V40c). Traces of calcite and chlorite (isotropic faint-yellow pleochroism). Rutile (V39f only).

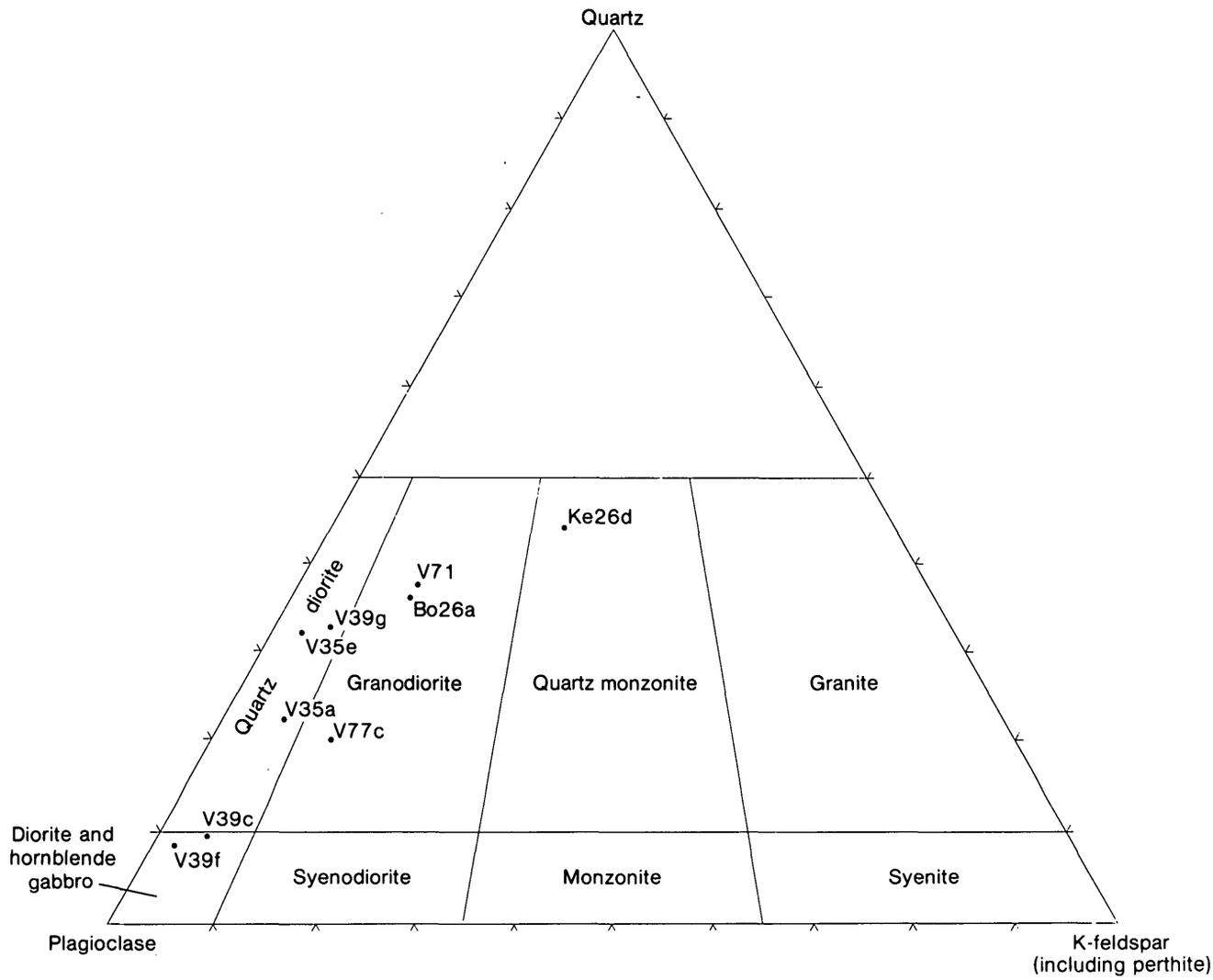

FIGURE 3.—Ternary diagram showing distribution of modal quartz, potassium feldspar, and plagioclase from chemically analyzed samples of igneous rocks from the southwestern Dana Mountains, Antarctic Peninsula. Classification is from Bateman (1961, fig. 2).

as clots of several crystals as long as 10 mm. Small reddish-brown garnet crystals occur in widely scattered outcrops. Small amounts of scolecite coat fracture surfaces in the mafic phase at outcrop V35a. Its mode of occurrence suggests it is a product of hydrothermal alteration (Vennum and Bentz, 1976). Modal analyses and petrographic characteristics of this phase are given in tables 1 (V39c, V39f) and 2, respectively.

Felsic phase

Most rock (90 percent) in the southwestern Dana Mountains is a light-gray medium- to coarse- (>5 mm) grained biotite granodiorite and quartz diorite that varies slightly in modal composition (V35e, Bo26a, V39g, V71, table 1). A K-Ar date of 105 m.y. (Rowley and others, 1976) was obtained from biotite (Ke33h). Hand samples are characterized by conspicuous crystals of smoky quartz (6–8 mm) and scattered indistinct poikilitic phenocrysts of white potassium feldspar that have a maximum length of 50–80 mm. Biotite is essentially the only ferromagnesian mineral present; hornblende occurs only as an accessory mineral. Small reddish-brown garnet crystals were found in scattered outcrops south and west of Mount Barkow.

The felsic phase cannot be divided into separate mappable units in the field, but microscopic petrography reveals significant variation in the degree of deuteric alteration, biotite to hornblende ratio, plagioclase composition, biotite optical properties, and accessory-mineral content. Mafic minerals, especially biotite, commonly occur in clots and usually are poikilitic or sieve textured. Plagioclase grains commonly have

moderately zoned calcic cores that are sharply demarcated from a weakly zoned or nonzoned albitic rim that is not in optical continuity with the core; plagioclase commonly shows extreme oscillatory zoning and patchy extinction. Accessory minerals are generally abundant. Samples from Mount Heer and the group of nunataks to the west and north (fig. 2) are characterized by extensive deuteric alteration and abundant myrmekite, whereas those nunataks adjacent to Mount Barkow are characterized by relatively fresh rock. Modal analyses and petrographic characteristics of this phase of the batholith are given in table 1 and 3, respectively.

Inclusions

Inclusions found within the felsic phase are very similar in both megascopic and microscopic (table 1, V35a) characteristics to samples of the mafic phase. They range from 50 mm to 5 m in diameter and compose from 0 to 2 percent of all outcrops examined. None show megascopic evidence of disaggregation and their contacts with the host granodiorite are sharp. Most rock is fresh, and alteration is confined to the sharply demarcated calcic cores of saussuritized plagioclase and to chloritized margins of biotite flakes. Optical properties of hornblende and biotite are identical to those in the mafic phase. Hornblende occurs in large poikilitic plates and prisms enclosing biotite. Plagioclase, however, shows much better crystal form in the inclusions than in the mafic phase and is significantly less calcic (An_{55}). Quartz is interstitial but in some rocks occurs in long tentaclelike grains that have reacted with the margins of other minerals. Rare isotropic subhedral to euhedral chocolate-brown garnet crystals occur in some thin sections. Accessory minerals include epidote, apatite, zircon, and sphene.

Dike Rocks

Hornblende diorite pegmatite

The mafic phase is veined by dikes and pods of hornblende diorite pegmatite as long as 25 m. This rock is characterized by black, randomly oriented poikilitic prisms of hornblende as long as 70 mm set in a matrix

TABLE 3.—*Petrographic characteristics of the felsic phase, Werner batholith, southwestern Dana Mountains*

Mineral	Description, Mount Heer area	Description, Mount Barkow area
Plagioclase--	Euhedral-subhedral tablets, minor oscillatory zoning, extensively saussuritized, albite twins common, normally zoned from An_{45} to An_{25}. Myrmekite abundant.	Euhedral-subhedral tablets, major oscillatory zoning (An_{50}-An_{15}), saussuritization minor. Albite and Carlsbad twins common. Several grains in each thin section have strongly oscillatorily zoned calcic cores sharply separated from a weakly zoned or nonzoned more sodic rim. Myrmekite absent.
Biotite------	Strongly pleochroic, α pale yellow, γ dark olive brown; $2V_{\alpha}$=10-15°. Strongly altered to chlorite (green pleochroism) and lesser epidote and sphene.	Strongly pleochroic, α colorless, γ deep red brown. $2V_{\alpha}$=0-5°. Grain margins altered to chlorite (colorless) and traces of epidote and muscovite.
Hornblende---	Subhedral-euhedral prisms. Moderately pleochroic, α pale yellow green, γ green. $2V_{\alpha}$=70°, $Z \wedge c$=18°, σ=0.021. Simply twinned. Minor alteration to epidote. Mantles biotite (Ke27a only).	Absent.
Quartz-------	Highly fractured interstitial grains or as mosaics of several interlocking grains. Strong undulatory extinction.	Similar to Mount Heer area.
Potassium---- feldspar.	Phenocrysts poikilitic (inclusions of plagioclase and biotite) and microperthitic. Groundmass grains show grid twinning.	Similar to Mount Heer area.
Accessory---- minerals.	All thin sections contain apatite (euhedral-subhedral needles), zircon (euhedral inclusions in biotite), epidote (granular, deuteric), sphene. Half of all thin sections contain opaque oxides and pyrite, hematite rims (0.1-0.2 mm) on pyrite and rarely on biotite. Allanite (10 percent of all thin sections) weakly pleochroic in shades of brown, locally rimmed by epidote. Garnets anhedral, colorless, birefringent (0.001-0.002), associated with biotite.	Similar to Mount Heer area. Garnets similar to Mount Heer area, but larger and more numerous. Monazite (Ke33h only).

of plagioclase. Most dikes are stained by orange iron oxide minerals.

The mineralogy and textural features of the pegmatite are similar to those of the mafic phase, suggesting that the dikes are late-stage magmatic differentiates. Hornblende is more strongly pleochroic (α moderate yellow green, γ pale blue green) than in the parent rock but has comparable optical data (table 2). The amphibole prisms are very highly poikilitic, and in many places the inclusions in the amphibole are so numerous that it is hard to determine the outline of the host grain. Almost all inclusions are composed of biotite, most of which occurs as thin plates alined parallel to the long axis of the amphibole prisms.

Pegmatite and aplite

Pegmatite and aplite dikes from 20 mm to 2 m thick intruded the felsic phase. Many dikes appear to fill primary joints. Some thick dikes are composite and grade from a pegmatite border into an aplite core. Garnet and muscovite occur in one-half of the aplite dikes (Ke26d, table 1) examined in the field, and these minerals plus tourmaline and small amounts of biotite occur in approximately one-third of the pegmatite dikes. Clusters of black tourmaline prisms as long as 100 mm occur in a flat-lying pegmatite dike at outcrop V37f.

Potassium feldspar is microperthitic. Plagioclase is unzoned and has an average composition of An_{15}. Twinning is largely on the albite law, but a few grains show combined Carlsbad-albite lamellae. Garnet crystals are colorless in thin section, but some larger grains show incipient alteration to a pale-yellow to reddish-brown chlorite(?) along fractures. Tourmaline is strongly dichroic, from almost colorless to yellow green. On the margins of some larger grains, the yellow-green color grades outward to indigo blue. Trace amounts of euhedral apatite needles are scattered throughout the groundmass.

Hornblende andesite

Dark-gray to dark-gray-green hornblende andesite dikes from 0.5 m to 3 m wide intruded the plutonic rocks of the southwestern Dana Mountains. In hand samples, they show either a porphyritic texture in which acicular needles of hornblende (3 mm) are embedded in a groundmass of smaller hornblende and plagioclase grains, or they are aphanitic. A modal analysis of one specimen is given in table 1 (V77c). Xenocrysts of quartz occur in about one-third of the samples. Most dikes appear to fill primary joints.

Phenocrysts of hornblende typically occur as weakly pleochroic (α pale yellow, γ yellow green) prisms and needles having the following optical properties: $2V_\alpha = 90°$, $Z \wedge c = 17°$, and $\sigma = 0.020$. Many prisms are simply twinned and some show very slight zonation.

Groundmass plagioclase is generally so highly saussuritized that determination of its composition is impossible. In one sample (Ke33j), this mineral occurs in large fresh grains (An_{35}). Reddish-brown biotite is found in one-third of the thin sections as ragged shreds in the groundmass or as thin rims on hornblende.

In addition to plagioclase, hornblende, and biotite, the groundmass contains minor amounts of potassium feldspar, quartz, calcite, epidote (strong yellow pleochroism), sphene, pyrite, opaque oxides, muscovite, apatite, zircon, hematite, and pale-yellow to green isotropic chlorite. Scattered highly resorbed quartz xenocrysts are rimmed with calcite in one-third of the thin sections examined.

Geochemistry

Major-element oxide analyses, trace-element abundances, and CIPW norms for two samples of the mafic phase, four of the felsic phase, one hornblende andesite dike, one aplite dike, and one mafic inclusion are presented in table 4. Examination of a silica variation diagram (fig. 4) reveals trends similar to those found in plutonic rocks throughout the Lassiter Coast (Rowley and Williams, 1974), the northern Antarctic Peninsula (Adie, 1955, 1964), and nearby eastern Ellsworth Land (Laudon, 1972): as SiO_2 increases, CaO, MgO, and total iron oxides decrease while K_2O and Na_2O increase. Alumina, however, shows a large amount of variance. The two analyses from the mafic phase (V39f, V39c) are almost identical in SiO_2 percentages (51.1 versus 51.9 percent respectively), but their Al_2O_3 contents differ by 6.7 percent. The sample having the higher Al_2O_3 content (V39f) contains 13 percent more modal plagioclase, 11 percent more biotite, 15 percent less hornblende, and 4.8 percent less MgO. The four analyses of the felsic phase (V35e, Bo26a, V39g, V71) vary from 68.5 to 73.0 percent SiO_2 and from 15 to 19 percent Al_2O_3, but the amount of Al_2O_3 does not vary consistently with the SiO_2 percentage. The felsic samples that are high in Al_2O_3 average 10–12 percent more modal plagioclase and 10 percent less potassium feldspar than the other samples. Three of the four felsic rocks and the analyzed aplite (Ke26d) are corundum normative, a feature which is uncommon in analyses of rocks of the Andean intrusive suite from both the northern (Adie, 1955,

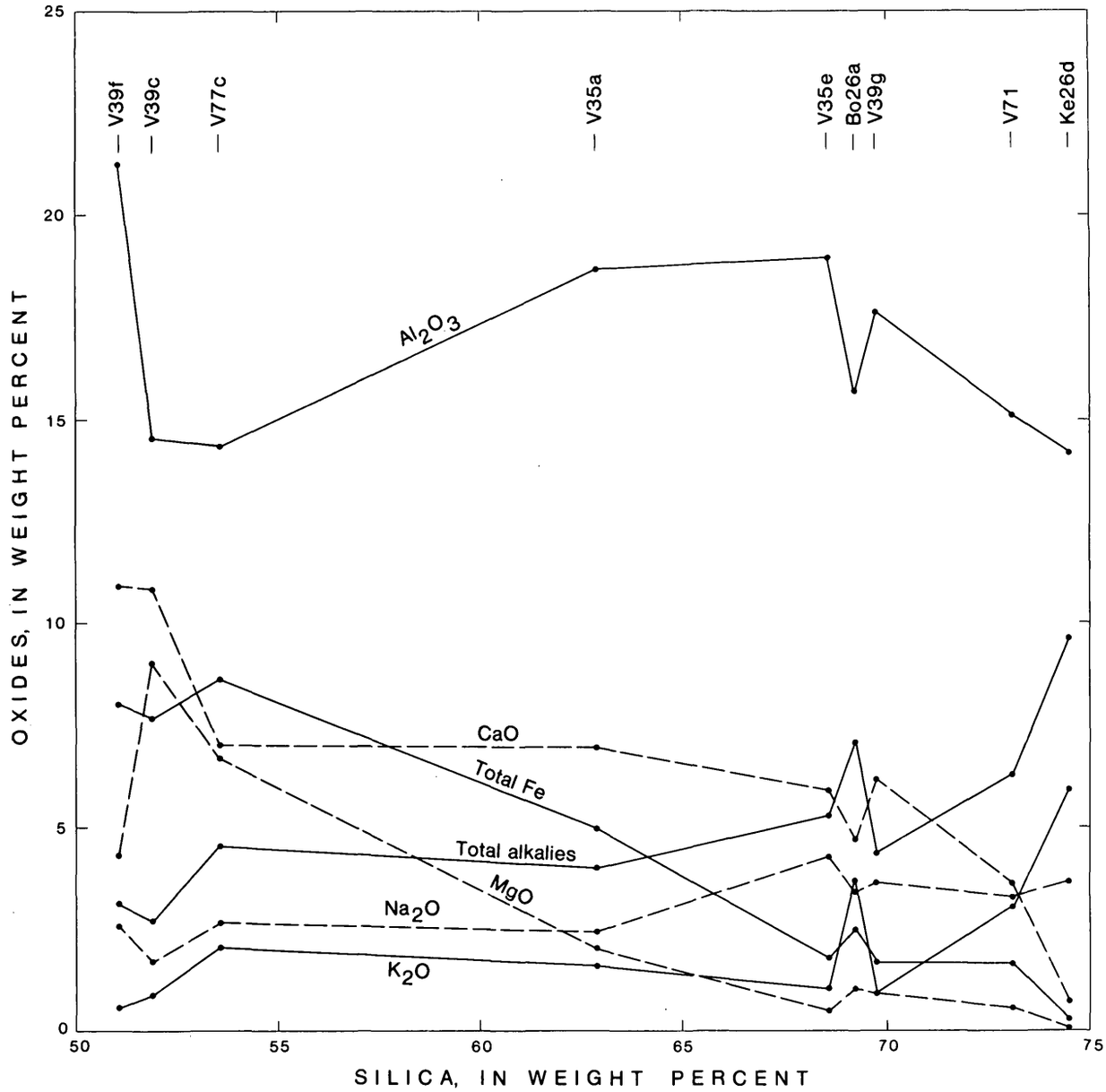

FIGURE 4.—Harker silica variation diagram for samples of igneous rocks of the southwestern Dana Mountains, Antarctic Peninsula.

1964) and southern (P. D. Rowley, written commun., 1976) Antarctic Peninsula.

When the above analyses are plotted on an alkali-magnesium-iron ternary diagram (fig. 5), they show a typical calc-alkaline differentiation trend having strong late-stage alkali enrichment. The alkali-lime index of approximately 69 (fig. 4) is much higher than the average (61) for the Lassiter Coast (Rowley and Williams, 1974); this reflects the relatively high CaO content of the felsic rocks in the southwestern Dana Mountains. This relationship is more graphically depicted in ternary plots of normative Ab–An–Or (fig. 6) and K_2O–Na_2O–CaO percentages (fig. 7), both of which indicate that CaO is depleted by differentiation only in the analyzed aplite (Ke26d).

Beryllium is the only trace element whose concentration remains relatively constant. Cobalt, copper, nickel, titanium, vanadium, and zinc decrease while barium, lead, yttrium, and zirconium increase as SiO_2 increases. Manganese and scandium are high and zirconium is low in two of the analyzed felsic samples (Bo26a and V71) relative to rocks having similar SiO_2 percentages. Chromium and nickel are also anomalously high in sample Bo26a and relatively low

TABLE 4.—*Chemical and normative data of selected fresh rocks from the southwestern Dana Mountains*

[Rapid rock chemical analyses of samples V39f, V35a, V35e, Bo26a, V39g, and V71 by Hezekiah Smith; samples V39c, V77c, and Ke26d by Paul Elmore. Methods used are described in U.S. Geological Survey Bulletin 1144 and are supplemented by atomic absorption. Six-step semiquantitative spectrographic analyses of samples V39f, V35a, V35e, Bo26a, V39g, and V71 by Joseph L. Harris; samples V39c, V77c, and Ke26d by Janet D. Fletcher. See table 1 for sample locations and descriptions. Leaders (--), below detection level; dash (-), not present.]

Sample	V39f	V39c	V77c	V35a	V35e	Bo26a	V39g	V71	Ke26d
Chemical analyses in weight percent									
SiO_2	51.1	51.9	53.6	62.8	68.5	69.2	69.7	73.0	74.4
Al_2O_3	21.2	14.5	14.3	18.6	19.0	15.7	17.6	15.1	14.2
Fe_2O_3	3.2	1.0	3.2	.8	.4	.7	.3	.4	.1
FeO	4.6	6.7	5.5	4.2	1.2	1.8	1.3	1.2	.1
MgO	4.3	9.1	6.7	2.0	.5	1.1	.8	.5	.06
CaO	10.8	10.7	7.0	7.0	5.9	4.6	6.2	3.7	.7
Na_2O	2.5	1.7	2.5	2.4	4.2	3.4	3.5	3.2	3.6
K_2O	.6	.9	2.1	1.6	1.0	3.7	.8	3.1	6.0
H_2O^+	.9	1.4	2.0	1.0	.5	.5	.7	.8	.5
H_2O^-	.2	.1	.1	.05	.1	.2	.1	.1	.1
TiO_2	.5	.4	.9	.3	.2	.2	.2	.1	.06
P_2O_5	.2	.2	.3	.2	.02	.2	.2	.1	.06
MnO	.1	.2	.2	.1	0	.05	0	.01	.02
CO_2	.02	.2	.6	.1	.03	.1	.04	.05	.01
Total--	100.22	99.00	99.00	101.15	101.55	101.45	101.44	101.36	99.91
Semiquantitative spectrographic analyses in parts per million									
Ba	165	165	375	365	330	515	345	650	5
Be	--	--	1	1	1	2	--	2	1
Ce	--	--	85	--	--	70	--	40	--
Co	30	40	35	10	5	5	5	5	--
Cr	20	215	190	1	10	35	5	5	2
Cu	20	35	40	2	--	--	25	5	--
Dy	3	--	6	4	--	7	--	--	--
Eu	--	--	--	--	1.5	1.0	--	1.1	--
Ga	9	2	9	7	10	9	7	8	11
Gd	--	--	4	--	--	--	--	--	--
Ho	--	--	--	--	--	2	--	2	--
La	--	--	20	--	--	27	--	20	--
Mo	5	2	2	3	--	1	--	--	--
Nb	--	--	2	--	--	5	--	--	6
Nd	--	--	40	--	--	--	--	--	--
Ni	20	80	50	1	2	15	5	5	1
Pb	5	2	9	5	7	20	5	20	80
Pr	--	--	5	4	--	6	--	6	--
Sc	40	27	24	14	3	13	1	11	1
Sn	--	--	--	--	--	6	--	--	--
Sr	610	340	630	510	630	450	660	330	3
V	220	130	230	90	20	30	30	20	2
Y	9	7	19	19	--	30	--	17	7
Yb	1	1	2	3	1	4	1	3	1
Zn	70	80	85	60	20	30	25	20	--
Zr	20	30	120	65	165	75	145	75	15
CIPW norms in weight percent									
Q	4.506	2.640	7.328	22.303	25.888	24.079	31.154	33.064	29.234
C	-	-	-	.963	.393	-	.273	.178	.770
Or	3.540	5.546	12.525	9.337	5.824	21.552	4.774	18.077	35.523
Ab	21.123	14.516	21.351	20.055	35.024	28.359	29.181	26.719	30.520
An	44.785	29.452	21.795	32.187	28.530	16.412	28.706	16.963	2.775
Di Wo	3.123	8.960	3.084	-	-	1.682	-	-	-
Di En	1.975	5.636	2.071	-	-	.867	-	-	-
Di Fs	.951	2.770	.781	-	-	.778	-	-	-
Hy En	8.178	17.234	14.770	4.919	1.203	1.833	1.963	1.303	.150
Hy Fs	4.200	8.470	5.572	6.666	1.602	1.644	1.750	1.736	.076
Mt	4.633	1.463	4.683	1.145	.572	1.000	.429	.572	.145
Il	.910	.824	1.802	.638	.281	.412	.412	.150	.114
Ap	.402	.430	.693	.538	.047	.514	.490	.304	.142
Cc	.045	.528	1.423	.225	.067	.224	.090	.112	.023
Total--	98.911	98.468	97.878	98.976	99.429	99.361	99.222	99.178	99.472
Salic--	73.953	52.153	62.999	84.845	95.659	90.401	94.089	95.001	98.822
Femic--	24.958	46.315	34.879	14.131	3.771	8.960	5.133	4.177	.650

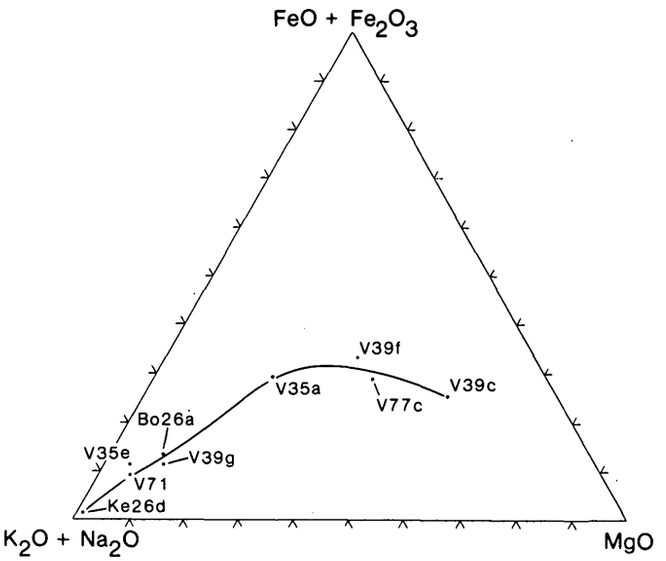

FIGURE 5.—Ternary diagram showing distribution and trend line of total alkalies, magnesium, and iron expressed as oxides in igneous rocks of the southwestern Dana Mountains, Antarctic Peninsula.

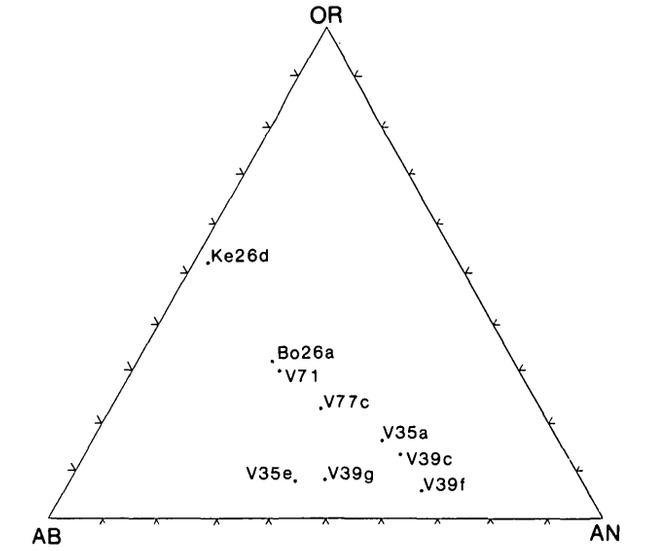

FIGURE 6.—Ternary diagram showing distribution of normative albite, anorthite, and orthoclase in igneous rocks of the southwestern Dana Mountains, Antarctic Peninsula.

in one of the diorite samples (V39f). This reflects the relative abundance of MgO and total iron oxides in samples Bo26a and V39f but not in sample V71. Both barium and lead are relatively low in sample V39g, a quartz diorite having a relatively low K_2O content.

Adie (1955) noted that cobalt is in excess of nickel in rocks of the Andean intrusive suite, a reversal of the situation that exists in most calc-alkaline rocks. This relationship also holds for the plutonic rocks of the southwestern Dana Mountains.

The analyzed aplite dike (Ke26d) contains four times as much lead as any other sample, but in general the dike has a very low trace-element content and is almost depleted in many of these elements. This relationship is typical of many aplitic rocks and can

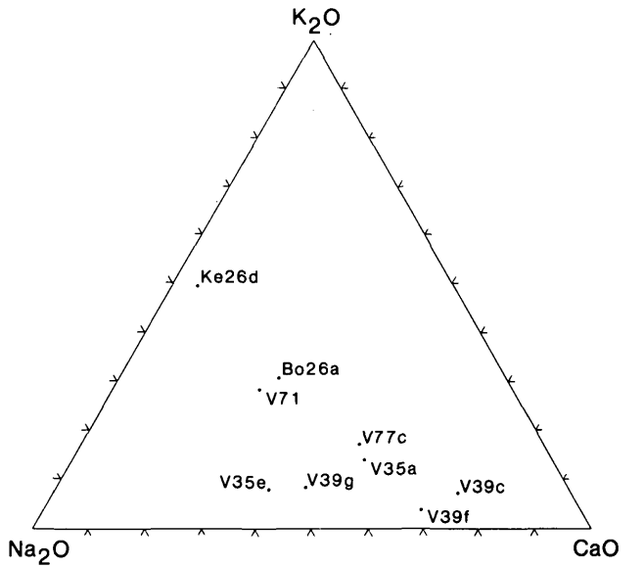

FIGURE 7.—Ternary diagram showing distribution of Na_2O, CaO, and K_2O in igneous rocks of the southwestern Dana Mountains, Antarctic Peninsula.

readily be explained as resulting from the using up of most trace elements during the early stages of crystallization and the concentration of only those elements having large ionic radii in the residual liquids (Nockolds and Mitchell, 1948).

CONTACT-METAMORPHIC ROCKS

The contact-metamorphic effects produced in the Upper Jurassic Latady Formation by intrusion of the Werner batholith are similar to those described by Plummer (1974) from contact aureoles of the southern Lassiter Coast. Thin sections of all contact-metamorphosed rocks examined are of fine-grained quartz sandstone containing various amounts of argillaceous material. Quartz makes up 50–90 percent of all samples. Groundmass minerals include oligoclase, reddish-brown biotite, muscovite, graphite, and relict zircon. Many hand samples are spotted with euhedral to anhedral andalusite and (or) biotite porphyroblasts. Spongy indistinct porphyroblasts of cordierite and pale-brown euhedral garnet crystals have been recognized in thin section but are smaller and less common than the andalusite and biotite. Some andalusite crystals have been almost completely retrograded to sericite while others show sericitization along only their margins or are enclosed by thin rims of graphite. All biotite porphyroblasts have been partly retrograded to muscovite, but cordierite and garnet are unaltered. Although tourmaline and metamorphic hornblende are present in other contact aureoles along the Lassiter Coast (Plummer, 1974), they do not appear in the contact metamorphic rocks of the southwestern Dana Mountains. The metamorphic mineral assemblages discussed in this report are indicative of hornblende hornfels facies (Turner, 1968).

CONTAMINATION OF PLUTONIC ROCKS

British geologists (Goldring, 1962; Hooper, 1962; Elliott, 1965, 1966; Curtis, 1966; Dewar, 1970; West, 1974) have reported hybrid (that is, contaminated) plutonic rocks from parts of the northern Antarctic Peninsula and offshore islands. These workers postulated that contamination was due to assimilation of argillaceous sedimentary rocks or mafic plutonic rocks. These hybrid rocks are similar to those studied elsewhere (Joplin, 1959; Lee and Van Loenen, 1971; Prostka, 1973). In the southern Lassiter Coast, Rowley, Williams, and Schmidt (1977) documented minor assimilation of parts of stoped blocks of granodiorite (105 m.y. old) by younger quartz monzonite (95 m.y. old) in the Copper Nunataks area. Most plutonic rocks in other parts of the Lassiter Coast and southern Black Coast, however, show no evidence of contamination.

Extremely irregular contacts of plutonic rock with the Latady Formation and the presence of abundant xenoliths and stoped blocks of the Latady Formation as long as several hundred meters suggest that contamination by assimilation of country rock was more widespread in the southwestern Dana Mountains than elsewhere along the Lassiter Coast and southern Black Coast. Xenoliths and stoped blocks appear in some places to be digested by the plutonic material. Other petrologic and geochemical characteristics discussed above, including the variable compositions shown by the limited chemical analyses, may be explained by contamination. Thus, both the mafic and felsic phases have been modified by assimilation.

The presence of garnet in the plutonic rocks also is suggestive of contamination. Green (1976) showed experimentally that garnet was a residual phase in granitic liquids derived from pelitic compositions at pressures greater than 7 kilobars. With the exception of garnet crystals in an aplite dike which are considered phenocrysts, the plutonic garnet crystals of the southwestern Dana Mountains are not igneous phenocrysts, but most likely resulted from contamination by pelitic sediments; the garnet crystals occur only in plutonic rocks of the southwestern Dana Mountains and are absent in rocks of similar composition elsewhere within the concentrically zoned Werner batholith (Vennum and Meyer, 1977). Garnet crystals are randomly distributed within that part of the batholith in which they do occur.

Xenoliths of the mafic phase are abundant in the felsic phase along contacts between these two intrusive units, but the borders between the xenoliths and the host rock are generally sharp and the xenoliths do not show megascopic evidence of disaggregation. However, the one chemically analyzed xenolith is intermediate in composition between the mafic and felsic phases. Similar relations between xenoliths and contaminated host rocks were reported by Curtis (1966) from the Graham Coast 800 km north of the southwestern Dana Mountains and suggest that local assimilation of stoped blocks and inclusions of the mafic phase also have modified the composition of the felsic phase.

ORIGIN OF THE HORNBLENDE ANDESITE DIKES

Joplin (1959) called attention to the presence of satellitic mafic bodies of hybrid or contaminated origin along the margins of felsic batholiths and noted the common presence of carbonate-bearing hornblende-rich dikes cutting the felsic rocks. She further suggested that the hornblende-rich rocks originated either through a reaction between mafic rocks and a volatile-rich felsic magma resulting in little change in chemical composition of the mafic material or that they represent gas-charged residual liquids trapped in the mafic rocks.

The residual-liquid model cannot be ruled out as an origin of the hornblende andesite dikes in the southwestern Dana Mountains, but chemical evidence more strongly supports the reaction hypothesis. Compared to the more felsic rocks, the mafic phase has a much lower content of barium, lead, zirconium, and rare earth elements. These elements occur in approximately equal amounts in the analyzed felsic rocks, the andesite dike, and the inclusion of the mafic phase. The dike also has a slightly higher content of SiO_2, Na_2O, K_2O, FeO, and Fe_2O_3 than the analyzed mafic-phase rocks. Resorbed quartz xenocrysts suggest that the dikes have been contaminated, and the chemical features described above suggest that they originated through remobilization of mafic rocks during intrusion of the granodiorite; the SiO_2, Na_2O, K_2O, barium, lead, zirconium, and rare earths were added from the felsic magma.

CONCLUSIONS

The plutonic rocks of the southwestern Dana Mountains are the products of a complex history of igneous events. The oldest known igneous rock, the mafic phase, which has a minimum radiometric age of about 114 m.y., intruded the Latady Formation. These rocks were later (105 m.y.) intruded by the main felsic phase of the composite concentrically zoned Werner batholith. These plutonic events produced contact-metamorphic rocks of hornfels facies. Refolding of the Latady Formation along intrusive contacts indicates that the batholith was forcefully emplaced. Field relations indicate that the plutonic rocks lie near the roof of the batholith. Presence of numerous xenoliths and stoped blocks, some apparently resorbed, and other field data, microscope observations, and limited chemical analyses suggest that the older mafic phase was contaminated by assimilation of the Latady Formation and that the younger felsic phase was contaminated by assimilation of the Latady Formation and, to a lesser extent, by assimilation of the mafic phase. The amount of assimilation appears to be significantly higher than that observed elsewhere in the Lassiter Coast and southern Black Coast.

Hornblende diorite pegmatite dikes intruded the mafic phase; felsic pegmatite and aplite dikes intruded the felsic phase. Hornblende andesite dikes intruded both phases of the batholith and crosscut the aplite dikes in at least one location (V77). The hornblende andesite dikes probably formed by intrusion of mafic plutonic rock that was remelted during emplacement of the younger felsic phase.

REFERENCES CITED

Adie, R. J., 1955, The petrology of Graham Land; II, The Andean granite-gabbro intrusive suite: Falkland Islands Dependencies Survey Sci. Rept., 12, 39 p.

——— 1964, The geochemistry of Graham Land, *in* R. J. Adie, ed., Antarctic geology: Internat. Symposium on Antarctic Geology, 1st, Capetown 1963, Proc., p. 541–547.

——— 1972, Evolution of volcanism in the Antarctic Peninsula, *in* Adie, R. J., ed., Antarctic geology and geophysics: Internat. Union Geol. Sci. Symposium on Antarctic Geology and Solid Earth Geophysics, Oslo 1970, ser. B, no. 1, p. 137–141.

Bateman, P. C., 1961, Granitic formations in the east-central Sierra Nevada near Bishop, California: Geol. Soc. America Bull., v. 72, no. 10, p. 1521–1537.

Curtis, R., 1966, The petrology of the Graham coast, Graham Land: British Antarctic Survey Sci. Rept. 50, 51 p.

Dalziel, I. W. D., and Elliot, D. H., 1973, The Scotia Arc and Antarctic margin, *in* Nairn, A. E. M., and Stehli, F. G., eds., The ocean basins and margins, v. 1: New York, Plenum Press, p. 171–246.

Dewar, G. J., 1970, The geology of Adelaide Island: British Antarctic Survey Sci. Rept., 57, 66 p.

Elliot, D. H., 1965, Geology of the north-west Trinity Peninsula, Graham Island: British Antarctic Survey Bull. 7, p. 1–24.

——— 1966, Geology of the Nordenskjöld Coast and a comparison with the north-west Trinity Peninsula, Graham Land: British Antarctic Survey Bull. 10, p. 1–43.

Goldring, D. C., 1962, The geology of the Loubet Coast, Graham Land: Falkland Islands Dependencies Survey Sci. Rept. 36, 50 p.

Green, T. H., 1976, Experimental generation of cordierite or garnet-bearing granitic liquids from a pelitic composition: Geology, v. 4, no. 2, p. 85–88.

Hooper, P. R., 1962, The petrology of Anvers island and adjacent islands: Falkland Island Dependencies Survey Sci. Rept. 34, 69 p.

Joplin, G. A., 1959, On the origin and occurrence of basic bodies associated with discordant bathyliths: Geol. Mag., v. 96, no. 5, p. 361–373.

Laudon, T. S., 1972, Stratigraphy of eastern Ellsworth Land, *in* Adie, R. J., ed., Antarctic geology and geophysics: Internat. Union Geol. Sci. Symposium in Antarctic Geology and Solid Earth Geophysics, Oslo 1970, ser. B, no. 1, p. 215–223.

Lee, D. E., and Van Loenen, R. E., 1971, Hybrid granitoid rocks of the southern Snake Range, Nevada: U.S. Geol. Survey Prof. Paper 668, 48 p.

Mehnert, H. H., Rowley, P. D., and Schmidt, D. L., 1975, K-Ar ages of plutonic rocks in the Lassiter Coast area, Antarctica: U.S. Geol. Survey Jour. Research, v. 3, no. 2, p. 233–236.

Nockolds, S. R., and Mitchell, R. L., 1948, The geochemistry of some Caledonian plutonic rocks—a study in the relationship between the major and trace elements of igneous rocks and their minerals: Royal Soc. Edinburgh Trans., v. 61, pt. 2, no. 20, p. 533–575.

Plummer, C. C., 1974, Contact metamorphism of the Latady Formation, southern Lassiter Coast, Antarctic Peninsula: Antarctic Jour. U.S., v. 9, no. 3, p. 82–83.

Prostka, H. J., 1973, Hybrid origin of the Absarokite-Shoshonite-Banakite series. Absaroka volcanic field, Wyoming: Geol. Soc. America Bull., v. 84, no. 2, p. 697–702.

Rowley, P. D., 1973, Geologic observations of the northern Lassiter Coast and southern Black Coast: Antarctic Jour. U.S., v. 8, no. 4, p. 154–155.

Rowley, P. D., Farrar, Edward, and McBride, S. L., 1976, Preliminary interpretation of potassium-argon ages of plutons in the northern Lassiter Coast and southern Black Coast, Antarctica: Antarctic Jour. U.S. v. 11, no. 4, p. 257–258.

Rowley, P. D., and Williams, P. L., 1974, Plutonic rocks of the Lassiter Coast: Antarctic Jour. U.S., v. 9, no. 5, p. 225–226.

Rowley, P. D., Williams, P. L., Schmidt, D. L., Reynolds, R. L., Ford, A. B, Clark, A. H. Farrar, Edward, and McBride, S. L., 1975. Copper mineralization along the Lassiter Coast of the Antarctic Peninsula: Econ. Geol., v. 70, no. 5, p. 982–987.

Rowley, P. D., Williams, P. L., and Schmidt, D. L., 1977, Geology of an Upper Cretaceous copper deposit in the Andean Province, Lassiter Coast, Antarctic Peninsula: U.S. Geol. Survey Prof. Paper 984, 36 p.

Tobi, A. C., 1963, Plagioclase determination with the aid of the extinction angles in sections normal to (010)—a critical comparison of current albite-Carlsbad charts: Am. Jour. Sci., v. 261, no. 2, p. 157–181.

Turner, F. J., 1968, Metamorphic petrology—mineralogical and field aspects: New York, McGraw-Hill Book Co., 403 p.

Van der Plas, L., and Tobi, A. C., 1965, A chart for judging the reliability of point counting results: Am. Jour. Sci., v. 263, no. 1, p. 87–90.

Vennum, W. R., and Meyer, C. E., 1977, Plutonic garnets from the Werner batholith, Lassiter Coast, Antarctic Peninsula: American Mineralogist. (In press.)

Vennum, W. R., and Bentz, J. L., 1976, An unusual occurrence of scolecite from the Antarctic Peninsula: Antarctic Jour. U.S., v. 11, no. 4, p. 258–259.

West, S. B., 1974, The geology of the Danco Coast, Graham Land: British Antarctic Survey Sci. Rept. 84, 58 p.

Williams, P. L., and Rowley, P. D., 1971, Geologic studies of the Lassiter Coast: Antarctic Jour. U.S., v. 6, no. 4, p. 120.

——— 1972, Composition of Jurassic sandstones, Lassiter Coast: Antarctic Jour. U.S., v. 7, no. 5, p. 145–146.

Williams, P. L., Schmidt, D. L., Plummer, C. C. and Brown, L. E., 1972, Geology of the Lassiter Coast area, Antarctic Peninsula; a preliminary report, *in* Adie, R. J., ed., Antarctic geology and geophysics: Internat. Union Geol. Sci. Symposium on Antarctic Geology and Solid Earth Geophysics, Oslo, 1970, ser. B, no. 1, p. 143–148.

Jour. Research U.S. Geol. Survey
Vol. 6, No. 1, Jan.–Feb. 1978, p. 107–114

IMPLICATIONS OF THE PETROCHEMISTRY OF PALLADIUM AT IRON CANYON, LANDER COUNTY, NEVADA

By NORMAN J PAGE, TED G. THEODORE, PAUL E. VENUTI; and
ROBERT R. CARLSON; Menlo Park, Calif.; Denver, Colo.

Abstract.—Approximately one-half of the 270 samples from the Iron Canyon area, Nevada, analyzed for platinum-group metals, contain measurable amounts of palladium in the 0.001- to 0.02-part per million range with an average of 0.0034 ppm. The rocks include lower Paleozoic sedimentary and volcanic rocks, Tertiary granitic porphyries, and breccia, all of which exhibit various degrees of hydrothermal alteration. Fault-related iron oxides and vein quartz are also present. The area lies astride the outermost fringes of the zone of dispersed alteration visible in outcrops around the middle Tertiary porphyry-copper system at Copper Canyon, Nevada. At Iron Canyon, the palladium concentrations greater than 0.003 ppm seem to be spatially related to the Butte fault zone, a north-striking fault system active during the time of porphyry-type mineralization. Palladium contents vary directly with those of mercury, arsenic, strontium, silver, lanthanum, and boron, as well as with lead, gold, and copper in obviously metallized rocks. This relation probably reflects the mobility of palladium during porphyry-type mineralization. However, our study failed to document conclusively the overall introduction of palladium during mineralization. Among the likely sources of palladium are the lower Paleozoic volcanic rocks or fluids equilibrated with magma(s) associated with the middle Tertiary porphyries.

Lode deposits containing most of the significant concentrations of platinum-group metals are usually associated with basic or ultrabasic rocks. The metals occur as magmatic disseminations or closely related secondary concentrations therefrom (Mertie, 1969). However, several recent studies (Stumpfl, 1972; Keays and Kirkland, 1972; Mihálik and others, 1974) have emphasized that platinum-group metals also occur in an epigenetic, hydrothermal environment. Indeed, in the United States, some platinum-group metals long ago were recognized as occurring in epigenetic environments associated with both Precambrian basic and Phanerozoic granitic intrusions. These environments include those associated with Cretaceous and Tertiary porphyry copper deposits (Eilers, 1913; Smith, 1976), quartz-sulfide veins (Knopf, 1915; Hewett, 1931), and sulfide veins in Precambrian hornblende gabbro (Lovering, 1929). This report describes the implications of low, but nonetheless detectable, concentrations of platinum-group metals in a middle Tertiary porphyry copper environment in the Battle Mountain mining district, Nevada.

PREVIOUS GEOLOGIC AND GEOCHEMICAL STUDIES

Trace amounts of palladium and platinum were previously found in rock and mineral materials in the southern part of the Battle Mountain mining district (fig. 1). Some of the palladium detected there is strongly associated with gold in both placer and lode deposits. Samples of placer gold obtained from the Iron Canyon area (Theodore and Roberts, 1971) and from the Natomas placer (Theodore and Blake, 1975) at the mouth of Copper Canyon contain 2–100 ppm (parts per million) palladium. The gold in the Natomas placer was probably derived from lode deposits in the general area of the Copper Canyon porphyry copper deposits (Roberts and Arnold, 1965). Custom spectrographic analyses by A. L. Sutton, Jr. (Theodore and Blake, 1975, p. B50) of lode gold from one of the porphyry deposits detected palladium in one of 15 samples of lode gold analyzed. One gold flake contained 10 ppm palladium, 36 000 ppm silver, and 30 ppm molybdenum. Followup geochemical studies of sulfides from the porphyry deposits established that trace amounts of palladium also occur in concentrates of chalcopyrite, pyrrhotite, and pyrite. These concentrates were tested for palladium, platinum, and rhodium; 4 of the 42 samples contain detectable palladium in the 0.004- to 0.020-ppm range (L. B. Riley, written commun., 1971). Three of these four samples also contain more than 15 ppm gold, and it was inferred accordingly that palladium and gold were petrogenetically related and that they were probably introduced into the rocks penecontemporaneously during the hy-

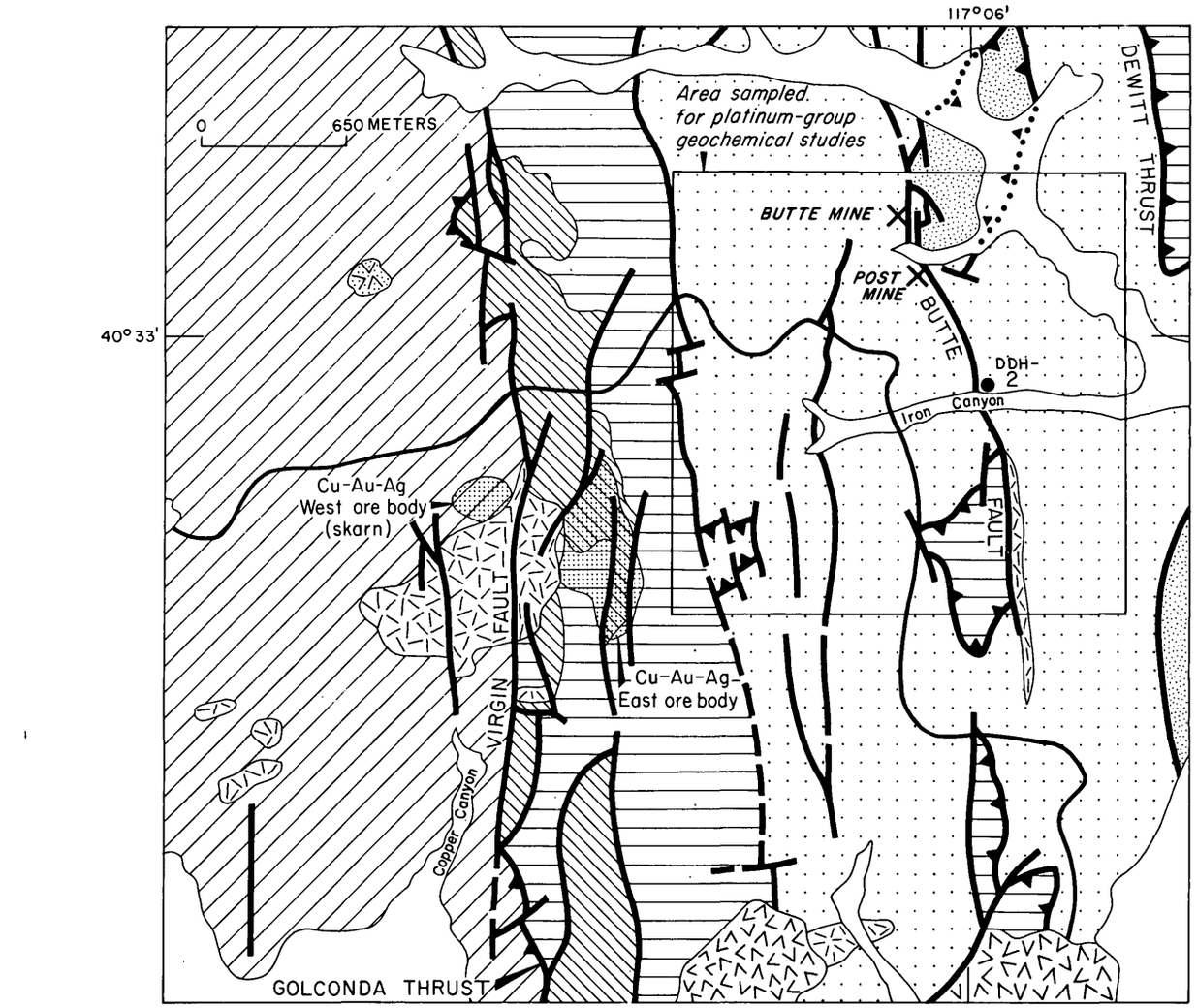

FIGURE 1.—Geologic sketch map of southern part of Battle Mountain mining district, Lander County, Nev. Modified from Roberts (1964).

pogene circulation of relatively dilute late-stage fluids (Nash and Theodore, 1971; Theodore and Blake, 1975). Additional geochemical studies (Theodore and others, 1976) reported the geochemical distribution of palladium, silver, mercury, gold, boron, and lanthanum in analyses of 102 sedimentary rocks, 73 greenstones (altered andesite and (or) basalt), 25 porphyry dike rocks, 64 fault breccias, iron oxides, or quartz vein rocks, and 6 soil samples collected from the Iron Canyon area, Nevada (fig. 1). Tabulated results of analyses for 33 elements from the same samples have also been published (Carlson and others, 1976).

Notwithstanding these previous geochemical studies, many questions remained concerning the geochemistry of platinum-group metals in a porphyry copper system—for example, the possibility that the palladium at Copper Canyon might be indigenous to the rocks in which it occurs and that its geochemical associations simply were modified as the porphyry system evolved. We had not established conclusively the overall introduction of platinum-group metals into the deposit. This paper attempts to resolve some of these ambiguities by focusing on the association of platinum-group metals with other elements in a small area at Iron Canyon near the periphery of the Copper Canyon porphyry system.

GEOLOGIC BACKGROUND

The Iron Canyon area (fig. 1) is underlain almost entirely by Cambrian and Ordovician rocks that moved eastward in the upper plate of the Roberts Mountains thrust during the middle Paleozoic (Roberts, 1964). The master sole of this plate is not exposed in the area but must underlie it at a depth greater than 1400 m (Theodore and Roberts, 1971). Another middle Paleozoic structure, the DeWitt thrust, which is an imbricate structure related to the Roberts Mountains thrust, crops out at Iron Canyon and forms the contact between arkosic sandstone and shale of the Upper Cambrian Harmony Formation and chert, shale, argillite, and greenstone of the Lower or Middle Cambrian Scott Canyon Formation. Locally the original thrust relations between Scott Canyon and Harmony are disturbed by north-striking normal faults of Tertiary age. These Tertiary normal faults are steeply dipping, and some Tertiary granitic porphyry has been emplaced along them. Biotite from a porphyritic dike penetrated by drill hole DDH–2 between 871.1 and 876.9 m below ground surface yielded a 37.5 ± 0.8-m.y. age by the K-Ar method (Theodore and others, 1973), the same radiometric age as the metallization in the Copper Canyon deposit. A small thrust plate of quartzite of the Ordovician Valmy Formation crops out near the Butte and Post mines in the north-central part of the area. Disseminated iron sulfides occur in outcrops exposed throughout the southwestern quarter of the Iron Canyon area. The distribution of these sulfides defines the outermost fringes of disseminated metallization related to the Copper Canyon porphyry system (Theodore and Roberts, 1971; Theodore and Blake, 1975). The precious-metal veins of the Butte and Post mines are localized along the Butte fault zone and compose part of the gold-silver halo that mantles the Copper Canyon deposit (Roberts and Arnold, 1965).

ANALYTICAL TECHNIQUES FOR PLATINUM AND PALLADIUM

The samples were analyzed for platinum and palladium using the fire-assay emission spectrography techniques of Cooley, Curry, and Carlson (1976). Their fire-assay flux for standards was used on sample sizes up to 15 grams. To compensate for the oxidizing power of the samples, 0.1–0.6 g additional graphite powder was added to the fluxes, producing lead buttons in the 20- to 35-g range; less than 20 g of lead results in poor noble-metal retrieval during fusion, whereas more than 35 g of lead results in losses during the extended cupellation. The lower detection limits varied with refinements in technique and with the sample size analyzed. Fifty-four samples were analyzed using palladium detection limits of 0.001 ppm, 204 at 0.002 ppm, and 12 at 0.003 ppm or above (platinum detection limits were approximately twice those of palladium). Seven samples with palladium values in the 0.001- to 0.010-ppm range were analyzed four to seven times each. A plot of the resulting relative standard deviations (RSx) versus mean sample palladium values produced a mean RSx increasing exponentially from 15 percent at 0.010 ppm to approximately 27 percent at 0.003 ppm, and 45 percent at 0.001 ppm (fig. 2). The RSx of the fire-assay emission spectrography method, exclusive of geologic samples, is 11 percent for palladium.

DISTRIBUTION OF PALLADIUM BY ROCK TYPE

Palladium was detected in 137 of the 270 samples analyzed; the average of these 137 samples was 0.0034 ppm, and the highest concentration was 0.02 ppm (Theodore and others, 1976). In order to study the distribution of palladium by rock type, the analyzed samples were grouped into four classes as follows: (class 1) sedimentary rocks that include chert, shale, and argillite of the Scott Canyon Formation, arkose and quartzite of the Harmony Formation, and quartzite of the Valmy Formation; (class 2) greenstones of

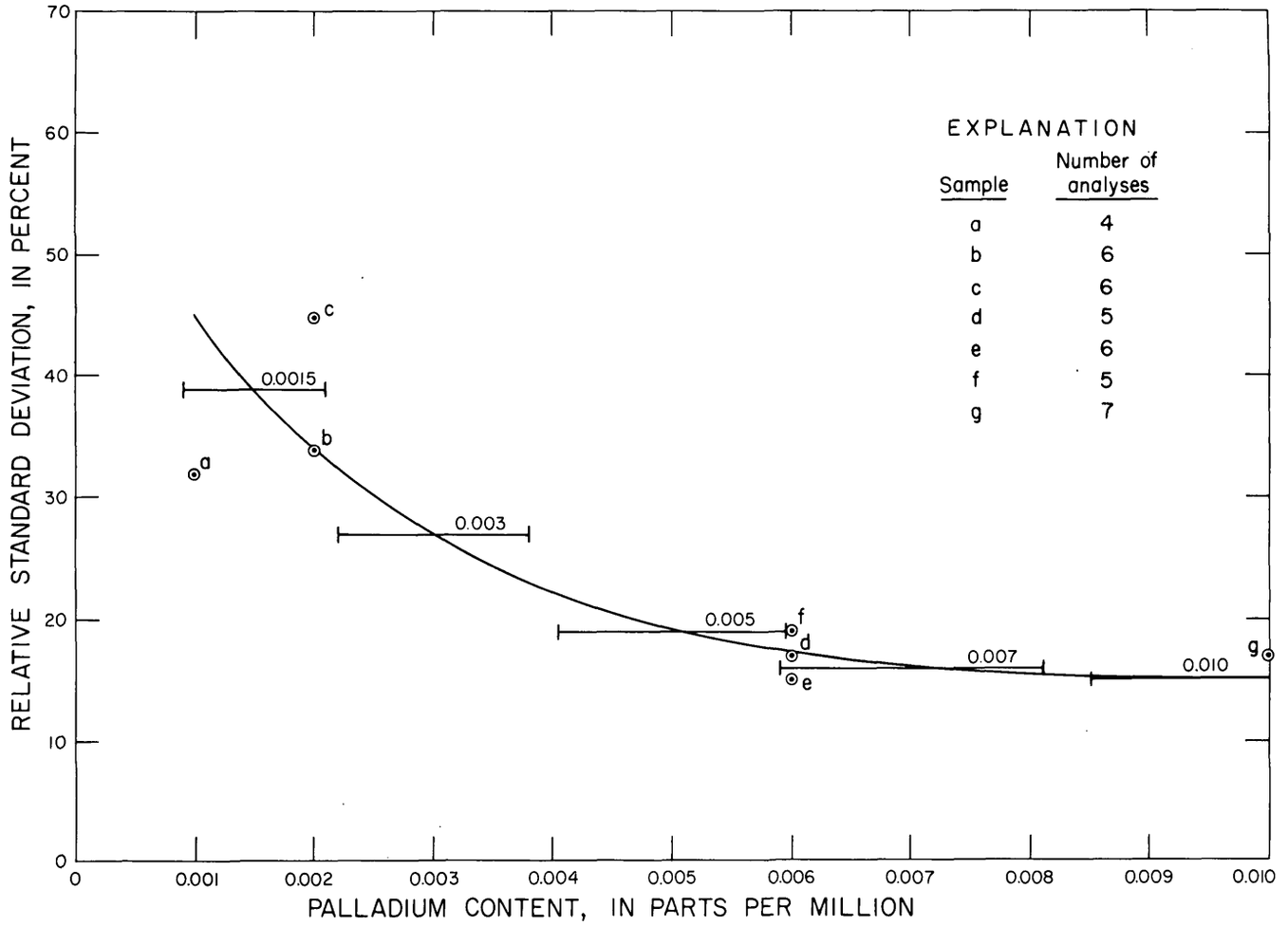

FIGURE 2.—Relative standard deviation versus mean concentration of palladium for seven rock samples collected from Iron Canyon area and analyzed from four to seven times each.

the Scott Canyon Formation; (class 3) granitic porphyry; and (class 4) fault breccia, iron oxides, and vein quartz. Table 1 shows the number of analytical determinations, the means, and the ranges for each of these four classes of rock. All four classes of rocks generally contain similar measurable concentrations of palladium that fall somewhere in the 0.001- to 0.02-ppm range and contain 0.003- to 0.004-ppm means for the unqualified determinations. About 72 percent of the samples of granitic porphyry contain measurable amounts of palladium (greater than 0.001 ppm), and about 32 percent of the rocks grouped into the fault breccia, iron oxides, and vein quartz class contain measurable amounts of palladium. Histograms prepared from these data show no significant differences in the distributions of palladium among the four classes. The concentrations of palladium in the rocks seemingly compose near-background distributions for the various rock types. Nonetheless, palladium concentrations greater than 0.003 ppm in all rock types at Iron Canyon seem to be related closely to the Butte fault zone, which must have been active in the Tertiary during porphyry-type mineralization there (Theodore and others, 1976). This relation, however, is difficult to reconcile with the apparently uniform distribution in the <0.001- to 0.02-ppm range of palladium by rock type.

Because many concentrations of palladium in obviously unaltered and unmetallized lower Paleozoic chert are about the same as intensely altered and heavily metallized rocks (including the sedimentary rocks, the Tertiary porphyries, and the veins), it is not possible to document an overall introduction of palladium concomitant with the development of this porphyry copper system during the Tertiary. Our failure to establish conclusively whether or not the palladium was introduced results mostly from two factors: (1) the palladium concentrations with which we

TABLE 1.—*Summary of analytical determinations for palladium from the Iron Canyon area*

Class	Rock type	Total number of Pd determinations	Number of unqualified Pd determinations	Range (ppm) of unqualified Pd determinations		Mean (ppm) of unqualified Pd determinations
				Maximum	Minimum	
1	Sedimentary	100	56	0.01	0.001	0.003
2	Greenstone	73	39	.02	.001	.004
3	Granitic porphyry	25	18	.007	.002	.003
4	Fault breccia, iron oxide, and vein quartz	64	21	.02	.001	.003

are dealing are near the detection limit, where analytical discrimination must necessarily become less precise and (2) there was no accompanying petrographic examination of the type and strength of the alteration and mineralization in each of the 270 samples. Thin-section studies would have provided us with the data to refine and supplement our classification of the rocks.

Some platinum-group element analyses of individual rocks from Iron Canyon are within the overall ranges reported recently from some mafic complexes. As a comparison, platinum-group element analyses from an alpine-type ultramafic complex at Burro Mountain, Calif., average 0.0128 ppm platinum, 0.0037 ppm palladium, and <0.005 ppm rhodium (Loney and others, 1971). Dunite, harzburgite, and similar rocks from Red Mountain and New Idria, Calif., and Twin Sisters and Cypress Island, Wash., average <0.01 ppm platinum, <0.004 ppm palladium, and <0.005 ppm rhodium (Page, 1969). Ten chromitites analyzed from the Medford-Coos Bay 2° quadrangles, Oregon, contain an average of 0.15 ppm platinum, 0.0075 palladium, and 0.0254 ppm rhodium (Page and others, 1975). However, it should be noted that even the highest concentrations of palladium detected at Iron Canyon (0.02 ppm) are low compared to the average platinum-group contents of the Merensky Reef (8.6 ppm), the Great Dyke (3.4–5.1 ppm), and Sudbury (0.86 ppm) reported by Allen (1960) and chromitites from the Stillwater Complex, Mont., reported by Page, Riley, and Haffty (1969).

ELEMENT ASSOCIATIONS OF PALLADIUM

Theodore, Venuti, Page, and Carlson (1976) determined the strengths of association by Spearman rank correlation for the total sample population (270) from the Iron Canyon area and found statistically significant positive correlations of palladium with 14 elements (Ag, Hg, B, La, Cr, Pt, Cu, As, Fe, Sn, Au, Pb, Mo, and Sr). The strength of the direct variations of palladium concentrations with silver concentrations was determined in 81 samples of all rock types (fig. 3). One conclusion of that study was that palladium possibly was remobilized during the porphyry-type mineralization at Iron Canyon. Examination by rock type of the strengths of association between elements using the same techniques and restrictions as outlined previously (Theodore and others, 1976), strongly supports their conclusions (table 2). The presence of many of these elements (Hg, Fe, As, Ag, Au, Pb, and Cu) must reflect the fringe aspects of porphyry-type mineralization in this part of the mining district. The analyzed samples were grouped into four classes for the correlation studies. Three of these classes are the same as before (compare tables 1 and 2); the fourth group includes classes 3 and 4 (the porphyries and the fault rocks), because the porphyries by themselves make up a sample group of only 25—a relatively small population sample upon which to base meaningful correlation studies. The data in table 2 indicate that there are many more elements strongly associated with palladium in the fault breccia group (class 4), and presumably in the porphyries also, than in either the

TABLE 2.—*Correlation coefficients of palladium with various elements by rock types at Iron Canyon*

[----, not statistically significant at confidence levels greater than 95.0 percent; ( ), degrees of freedom at 99.75 percent confidence levels; [ ], degrees of freedom at 95.0–99.5 percent confidence levels]

Element	Sedimentary rock (Class 1)	Greenstone (Class 2)	Fault breccias, iron oxide, and vein quartz (Class 4)	Porphyries, fault breccia, iron oxide, and vein quartz[1] (Classes 3 and 4)	All rocks (Classes 1+2+3+4)
Hg	0.36 [36]	----	0.41 [40]	0.43 (46)	0.37 (119)
Fe	----	----	.27 [41]	.26 [49]	.23 [135]
As	----	----	.40 [29]	.41 [35]	.36 [57]
Ag	.29 [31]	----	.53 (36)	.55 (44)	.46 (80)
Au	----	----	.36 [30]	.34 [35]	.33 [52]
Pb	----	----	.30 [40]	.32 [47]	.23 [99]
Cu	.29 [41]	----	----	.28 [49]	.26 (133)
Mo	----	----	----	----	.26 [60]
Sn	----	----	----	----	.34 [35]
B	----	----	.65 (31)	----	.42 (87)
V	.34 [42]	----	----		----
Cr	.38 [42]	0.33 [32]	.35 [41]	.27 [49]	.29 (135)
Sr	----	----	.48 (31)	.32 [38]	.28 [87]
Ba	----	.35 [32]	----	----	----
La	----	----	.74 [8]	.63 [10]	.48 (44)
Y	----	----	.30 [37]	----	----
Sc	----	----	.28 [34]	----	----

[1]Spearman rank-correlation coefficients were not calculated for the porphyries alone (class 3 rocks of table 1) because of the relatively small number (25) of these rocks analyzed for platinum-group metals.

sedimentary rocks or the greenstones. Although palladium has a low to moderate positive, statistically significant correlation with five elements (Hg, V, Cr, Cu, and Ag) in the sedimentary rocks and a similar correlation with chromium and barium in the greenstones, the strong association of palladium with five elements (Hg, As, Sr, Ag, and La,), as well as with lead, gold, and copper in the metallized porphyries and fissure fillings, must reflect the mobility of palladium during mineralization.

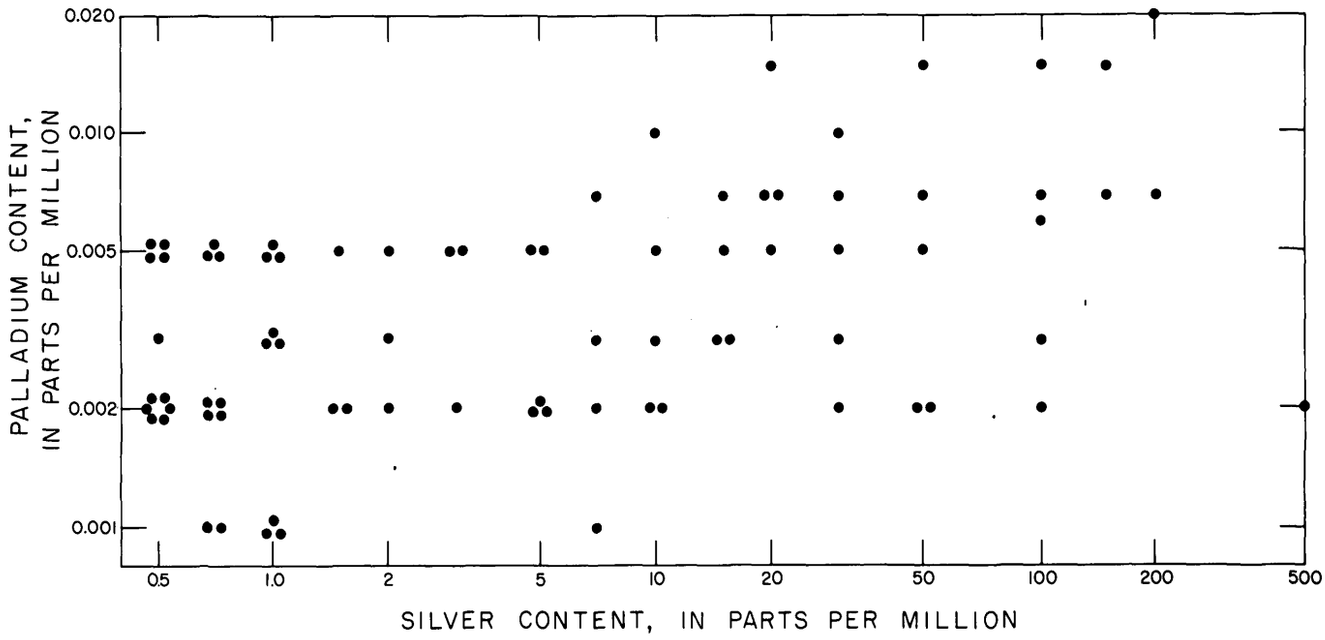

FIGURE 3.—Variability of palladium versus silver concentrations in 81 rock samples from Iron Canyon area containing determinable concentrations of each metal.

CONCLUSIONS

This study of a small area at the fringe of a Tertiary porphyry copper system provides additional documentation, primarily by statistical examination of whole-rock analyses for palladium, of the mobility of platinum-group metals in such a geologic environment. The source of the small amounts of palladium ($\leq$0.02 ppm) remains unresolved, however. Among the likely sources are either (1) the exposed lower Paleozoic greenstone bodies or (2) the fluids equilibrated with the magmas associated with the porphyries that were emplaced during the middle Tertiary. If the greenstones provided the bulk of the palladium found during this study, then the palladium leached from them must eventually have been deposited preferentially, along with other metals, near the Butte fault zone, possibly during a multicycle-mixing event there. Although the concentrations of platinum-group metals at Iron Canyon have no economic potential by themselves, platinum-group metals should not be overlooked as byproducts from mining operations in any hydrothermal environment.

REFERENCES CITED

Allen, C. C., 1960, The platinum metals: Canada Mineral Resources Div., Dept. Mines and Tech. Surveys Mineral Rept. 3, 68 p.

Carlson, R. R., Venuti, P. E., Page, N. J, and Theodore, T. G., 1976, Descriptions and chemical analyses of 270 rocks and soils analyzed for platinum-group metals from the Iron Canyon area, Lander County, Nevada: U.S. Geol. Survey Open-File Rept. 76–524, 32 p.

Cooley, E. F., Curry, K. J., and Carlson, R. R., 1976, Analysis of the platinum-group metals and gold by fire-assay emission spectrography: Appl. Spectroscopy, v. 30, no. 1, p. 52–56.

Eilers, A., 1913, Rare metals in blister copper: Am. Inst. Mining Eng. Trans., v. 47, p. 217–218.

Hewett, D. F., 1931, Geology and ore deposits of the Goodsprings quadrangle, Nevada: U.S. Geol. Survey Prof. Paper 162, 172 p.

Keays, R. R., and Kirkland, M. C., 1972, Hydrothermal mobilization of gold from copper-nickel sulfides and ore genesis at the Thomson River copper mine, Victoria, Australia: Econ. Geology, v. 67, no. 8, p. 1263–1275.

Knopf, Adolph, 1915, A gold-platinum-palladium lode in southern Nevada: U.S. Geol. Survey Bull. 620, p. 1–18.

Loney, R. A., Himmelberg, G. R., and Coleman, R. G., 1971, Structure and petrology of the alpine-type peridotite at Burro Mountain, California, U.S.A.: Jour. Petrology, v. 12, p. 245–309.

Lovering, T. S., 1929, The new world or Cooke City mining district, Park County, Montana: U.S. Geol. Survey Bull. 811, 87 p.

Mertie, J. B., Jr., 1969, Economic geology of the platinum metals: U.S. Geol. Survey Prof. Paper 630, 120 p.

Mihalik, P., Jacobsen, J. B. E., and Hiemstra, S. A., 1974, Platinum-group minerals from a hydrothermal environment: Econ. Geology, v. 69, no. 2, p. 257–262.

Nash, J. T., and Theodore, T. G, 1971, Ore fluids in the porphyry copper deposit at Copper Canyon, Nevada: Econ. Geology, v. 66, p. 385–399.

Page, N. J, 1969, Platinum content of ultramafic rocks, *in* U.S. Geol. Survey Heavy Metals Program progress report 1968—Topical studies: U.S. Geol. Survey Circ. 622, p. 5.

Page, N. J, Johnson, M. G., Haffty, Joseph, and Ramp, Len, 1975, Occurrence of platinum group metals in ultramafic rocks of the Medford-Coos Bay 2° quadrangles, southwestern Oregon: U.S. Geol. Survey Misc. Field Studies Map MF–694, scale 1:250 000.

Page, N. J, Riley, L. B., and Haffty, Joseph, 1969, Platinum, palladium, and rhodium analyses of ultramafic and mafic rocks from the Stillwater Complex, Montana: U.S. Geol. Survey Circ. 624, 12 p.

Roberts, R. J., 1964, Stratigraphy and structure of the Antler Peak quadrangle, Humboldt and Lander Counties, Nevada: U.S. Geol. Survey Prof. Paper 459–A, p. A1–A93.

Roberts, R. J., and Arnold, D. C., 1965, Ore deposits of the Antler Peak quadrangle, Humboldt and Lander Counties, Nevada: U.S. Geol. Survey Prof. Paper 459–B, p. B1–B94.

Smith, R. M., 1976, Mineral resources, Pt. 2 of Geology and mineral resources of White Pine County, Nevada: Nevada Bur. Mines and Geology Bull. 85, p. 36–105.

Stumpfl, E. F., 1972, Compositional variation in the hollingworthite-irarsite group: Neues Jahrb. Mineralogie Monatsh., no. 9, p. 406–415.

Theodore, T. G., and Blake, D. W., 1975, Geology and geochemistry of the Copper Canyon porphyry copper deposit and surrounding area, Lander County, Nevada: U.S. Geol. Survey Prof. Paper 798–B, p. B1–B86.

Theodore, T. G., and Roberts, R. J., 1971, Geochemistry and geology of deep drill holes at Iron Canyon, Lander County, Nevada, *with a section on* Geophysical logs of drill hole DDH–2 *by* Charles J. Zablocki: U.S. Geol. Survey Bull. 1318, 32 p.

Theodore, T. G., Silberman, M. L., and Blake, D. W., 1973, Geochemistry and K-Ar ages of plutonic rocks in the Battle Mountain mining district, Lander County, Nevada: U.S. Geol. Survey Prof. Paper 798–A, 24 p.

Theodore, T. G., Venuti, P. E., Page, N. J, and Carlson, R. R., 1976, Maps showing distribution of palladium and other elements in rocks at Iron Canyon, Lander County, Nevada: U.S. Geol. Survey Misc. Field Studies Map MF–790, 2 sheets.

Jour. Research U.S. Geol. Survey
Vol. 6, No. 1, Jan.–Feb. 1978, p. 115–131

GALIURO VOLCANICS, PINAL, GRAHAM, AND COCHISE COUNTIES, ARIZONA

By S. C. CREASEY and MEDORA H. KRIEGER, Menlo Park, Calif.

Abstract.— The Galiuro Volcanics occurs in the Galiuro, Winchester, and Little Dragoon Mountains, east and northeast of Tucson, Ariz. The sequence comprises lava flows and ash-flow tuffs ranging in composition from andesite to rhyolite. In general they can be subdivided into two parts separated by a major erosional unconformity. The lower part is predominantly lava flows ranging from andesite to rhyodacite but contains three ash-flow tuffs. The upper part is chiefly ash-flow tuff but also includes two areas of rhyolite-obsidian flows and domes and rhyolitic to andesitic flows. Conglomerate separates many if not all of the rock units in the upper part. The individual flows and tuffs are lenticular, and the stratigraphic relations are complex. Chemical variation diagrams suggest consanguinity among all the volcanic rocks, but the complex intercalation of rhyolite and andesite and of lava flows and ash-flow tuff indicates more than one magma chamber, different stages of differentiation in separate magma chambers, and several eruption centers. Chemical analyses indicate that the magmas were normal calc-alkaline. Eleven potassium-argon age determinations indicate that the Galiuro Volcanics accumulated from about 29 to 23 million years ago, which is in the middle of the mid-Tertiary volcanic and plutonic event in Arizona.

The Galiuro Volcanics occurs in the Galiuro, Winchester, and Little Dragoon Mountains, extending from a point about 64 kilometers east of Tucson northwestward for about 110 km (fig. 1). Most of the area underlain by the unit is shown on the geologic sketch map (fig. 2), but known or probable exposures of the formation crop out in and southeast of the gorge of the Gila River below San Carlos Lake (Creasey and others, 1961; Willden, 1964) and in the low pass between the Santa Teresa and Pinaleno (Graham) Mountains (fig. 1). Except in one small area (Krieger, 1968d), the Galiuro does not now extend southwest of the San Pedro valley, although it probably originally extended for some distance in that direction. Volcanic rocks of a similar age crop out in the Tucson (Damon and Bikerman, 1964), Santa Rita (Drewes, 1971a), and Patagonia Mountains (Simons, 1974; Drewes, 1971b), and slightly younger ash-flow tuffs and lavas occur west of Miami and between Miami and Ray (fig. 1) (Peterson, 1969; Creasey and others, 1975).

Plutonic rocks coeval with the Galiuro Volcanics crop out extensively in a northwest-trending zone defined by the Dragoon, Rincon, Santa Catalina, and Tortolita Mountains (fig. 1). No mid-Tertiary volcanic rocks occur within these ranges, only plutonic rocks. The contemporaneous volcanic rocks are confined to the flanking ranges to the southwest and northeast. Apparently this zone has been uplifted, and erosion since the mid-Tertiary has removed any preexisting mid-Teritary volcanic rocks and exposed the coeval plutonic rocks. These plutonic rocks do not extend southeast of Sulphur Spring Valley (fig. 1), and their extent to the northwest is not known to us.

The Galiuro Volcanics is gently deformed; dips uncommonly, if ever, exceed 20°. The rocks probably were tilted during the basin-and-range deformation of late Tertiary time. North of lat 32°45′, the Galiuro has been deformed into a broad, gentle downwarp, the axis of which trends east-west at the latitude of Aravaipa Creek. The elevation of the northern Galiuro Mountains probably is due to bounding normal faults on the northeast and southwest, although the faults are now largely covered by the basin fills of the San Pedro and Aravaipa valleys. South of lat 32°45′, the pile of Galiuro Volcanics forms a tilted fault block dipping gently to the east and southeast; only the western side of the mountains here is bounded by normal faults, which are well exposed around a butte near lat 32°42′, long 110°29′ (fig. 2). A parallel west-dipping normal fault extends for about 32 km through the center of the mountains (fig. 2). This fault has a vertical offset of 900–1200 meters and apparently was active during the accumulation of the Galiuro Volcanics.

PREVIOUS WORK

Early descriptions of the lithology and distribution of the Galiuro Vocanics are brief and generalized. As a part of the description of the wallrocks of a gold prospect in the central part of the Galiuro Mountains, Blake (1902) mentioned tuffs and lavas, and Darton

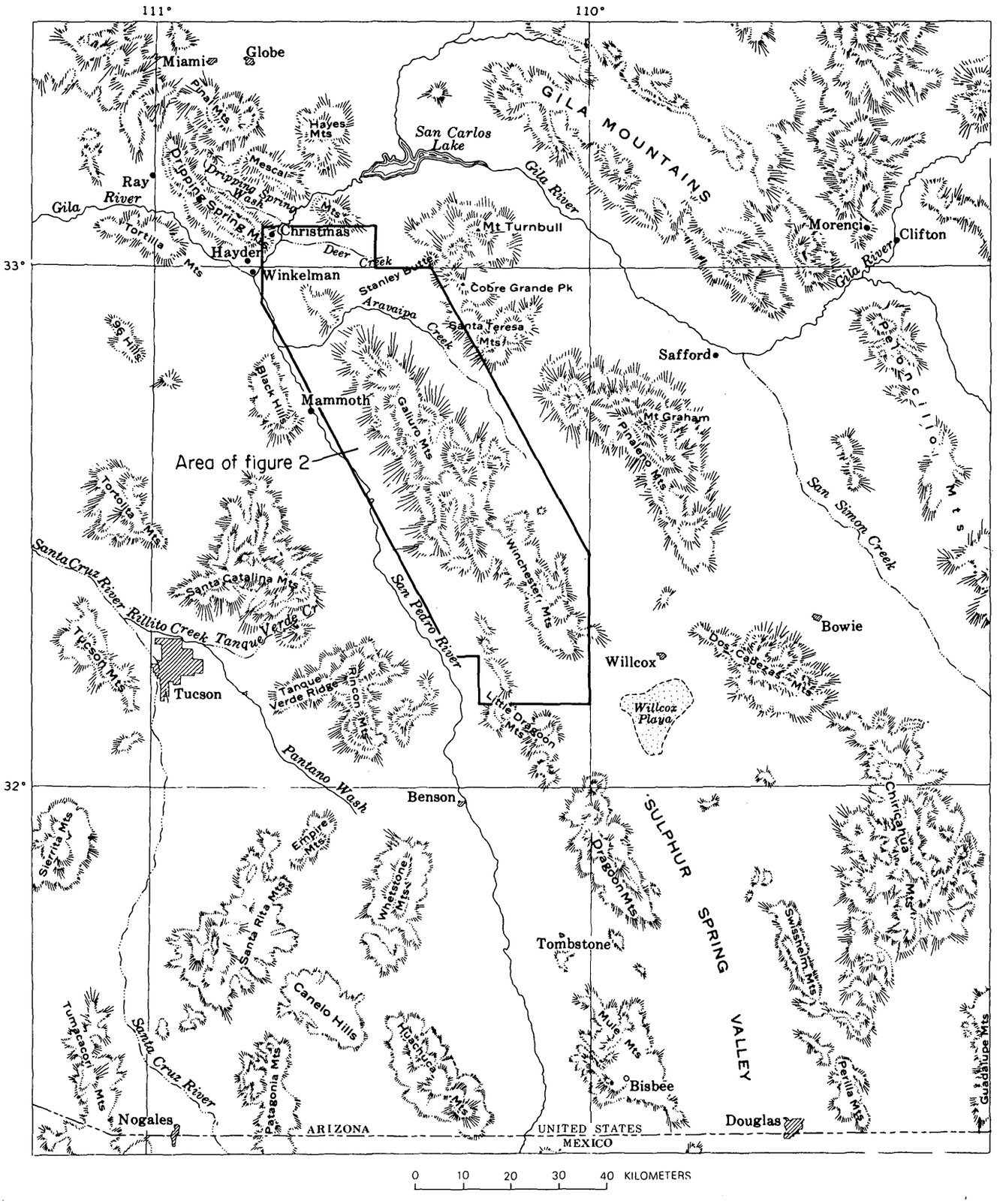

FIGURE 1.—Principal ranges and valleys in southeastern Arizona in relation to study area.

(1925), p. 273) described the Galiuro Mountains as "a great thickness of Tertiary volcanic rocks with some included beds of tuff, ash, and conglomerate." The first detailed descriptions of the Galiuro Volcanics were by Cooper and Silver (1964) and by Simons (1964). Although Blake referred to the rocks as the Galiuro Rhyolite, Cooper and Silver changed the name to Galiuro Volcanics because of the diverse lithology. Willden (1964) published a generalized geologic map of the northern end of the Galiuro Mountains, which contains a thin section of the volcanic rocks; however, he did not correlate those rocks with the Galiuro Volcanics. Kreiger (1968a,b,c,d) published detailed subdivisions of the volcanic rocks in the Holy Joe Peak quadrangle, and, while evaluating the mineral potential of the Galiuro Wilderness, S. C. Creasey (unpub. data) mapped in reconnaissance the central Galiuro Mountain, which contains the thickest section of the Galiuro Volcanics. With the completion of Creasey's mapping, the distribution and general character of the Galiuro Volcanics have been studied over an area from about lat 32°10′ to about 33°02′ (fig. 2). This paper summarizes what is now known of the general stratigraphy, lithology, chemical composition, and age of the formation.

Considering the complex stratigraphic relations of mappable units within the Galiuro Volcanics, agreement among those who have published maps of the rocks is remarkable. The only difference of major importance is between Simons (1964) and Krieger (1968a) on interpretation of the stratigraphic relation of andesite flows and rhyolite-obsidian near the boundary between the Klondyke and Brandenburg Mountain quadrangles. This difference is discussed below.

STRATIGRAPHY

A profound erosional unconformity separates the Galiuro Volcanics from the underlying rock. In the Little Dragoon Mountains, the volcanic rocks rest on a Tertiary conglomerate, Cretaceous sedimentary rocks, and Precambrian granite. In the middle of the Galiuro Mountains, the only exposure of the underlying rock is in a deep canyon at lat 32°32′, long 110°19′; it consists of the Precambrian Oracle Granite of Peterson (1938).

In the northern Galiuro Monutains, where the volcanic rocks thin, the underlying rocks are well exposed. They consist of Tertiary conglomerate; the Tertiary and (or) Cretaceous Copper Creek Granodiorite; the Cretaceous Glory Hole Volcanics; Paleozoic sedimentary rocks; and Precambrian diabase, Troy Quartzite, Apache Group, and Pinal Schist. Hence, the gently dipping Galiuro Volcanics are draped across rocks ranging in age from Precambrian to Tertiary.

Tertiary and Quaternary gravels and basalt overlie the Galiuro Volcanics, mostly south of lat 32°45′. In some places, the angular discordance with the overlying rocks is pronounced, and in others it is slight.

The Galiuro Volcanics accumulated throughout a period of about 6 million years, during which time volcanism was intermittent and uplift, tilting, and erosion were active. Conglomerates, which are an important but subordinate part of the formation, separate most, if not all, of the lithologic units, and erosional discordances between units are common. The most pronounced erosional unconformity, on which the topographic relief south of lat 32°50′ is estimated to be about 300 m, divides the Galiuro Volcanics into two parts, a lower part dominated by lava flows and an upper part by ash-flow tuffs (fig. 3). Stratigraphy of the upper part of the Galiuro Volcanics is complex owing to differences of lithology, to lenticularity of the intercalated units, and to erosion of one unit before burial of the next. In figure 2, north of lat 32°45′, the upper part is divided into six map units. From oldest to youngest they are the lower rhyolite-obsidian unit; the ash-flow tuff and andesite unit; the upper rhyolite-obsidian unit; the crystal, vitric, and lithic tuff unit; the Apsey Conglomerate Member; and the upper andesite unit (fig. 3).

Andesite-rhyodacite and ash-flow tuff unit

The andesite-rhyodacite and ash-flow tuff unit (fig. 2) includes andesite and latite and ash-flow tuff of S. C. Creasey (unpub. data); lower andesite, latite, and silicic volcanic rocks of Simons (1964); andesite of Little Table Mountain, latite, and porphyritic andesite of Krieger (1968b, c); and basalt and andesite and latite of Cooper and Silver (1964). These rocks are all listed and correlated in figure 3.

The andesite-rhyodacite and ash-flow tuff unit extends from about lat 32°15′ in the Little Dragoon Mountains to about 32°50′ where it is overlapped by the upper part. Although the thickness of the lower part differs from place to place, Krieger (1968b) indicated as much as 200 m of flows in the northern Galiuro Mountains, and Simons (1964) more than 275 m at lat 32°45′. The thickest section is in the central part of the Galiuro Mountains; Creasey estimates the thickness here as 750–900 m. Southward from there the thickness diminishes, and in the Little

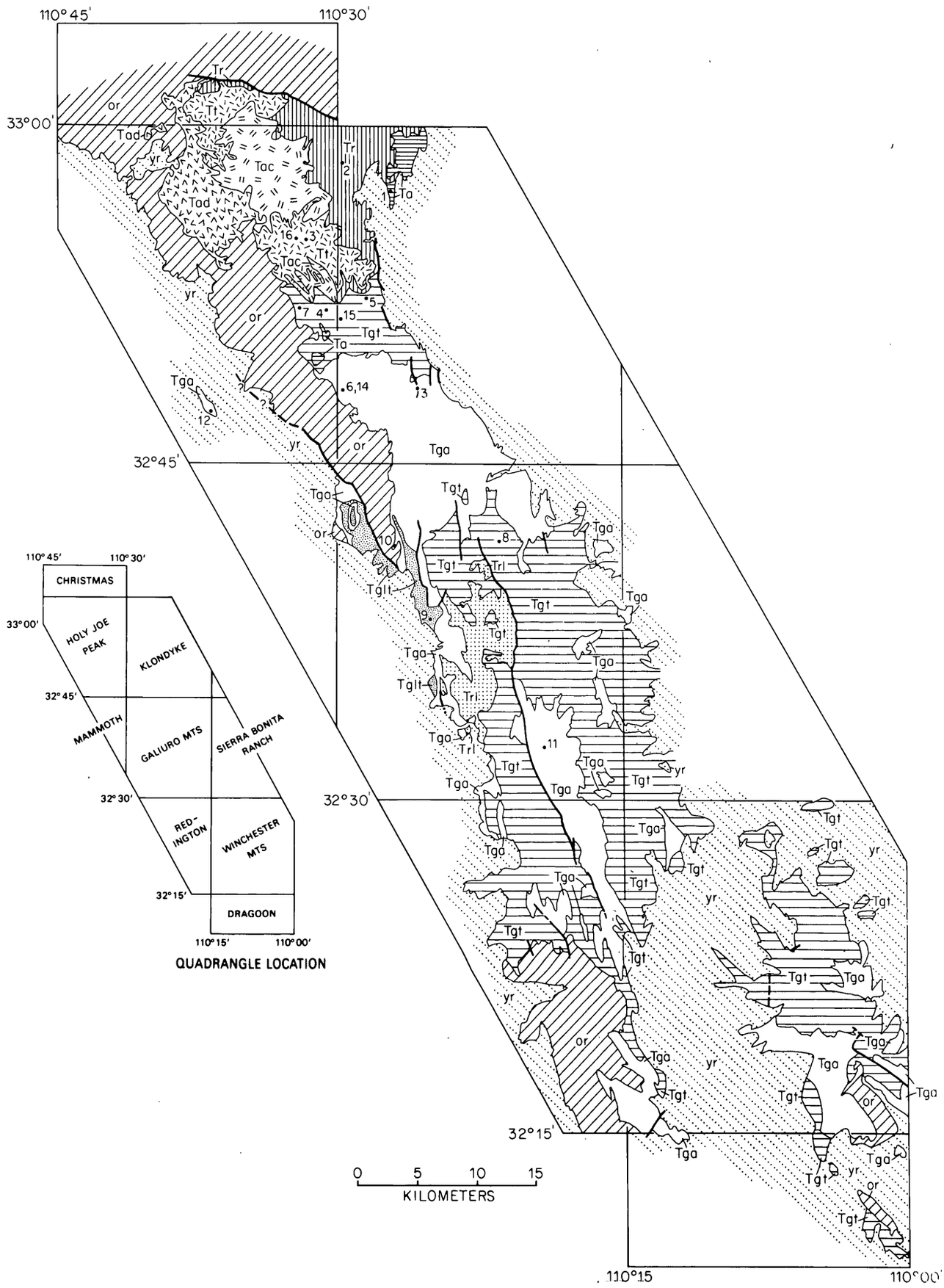
110°45'
110°30'
33°00'
32°45'
32°30'
32°15'
110°15'
110°00'
Tr
Tf
Tad
Tac
Ta
Tgt
Tga
Trl
Tgll
or
yr
0 5 10 15
KILOMETERS
CHRISTMAS
HOLY JOE PEAK
KLONDYKE
MAMMOTH
GALIURO MTS
SIERRA BONITA RANCH
RED-INGTON
WINCHESTER MTS
DRAGOON
QUADRANGLE LOCATION

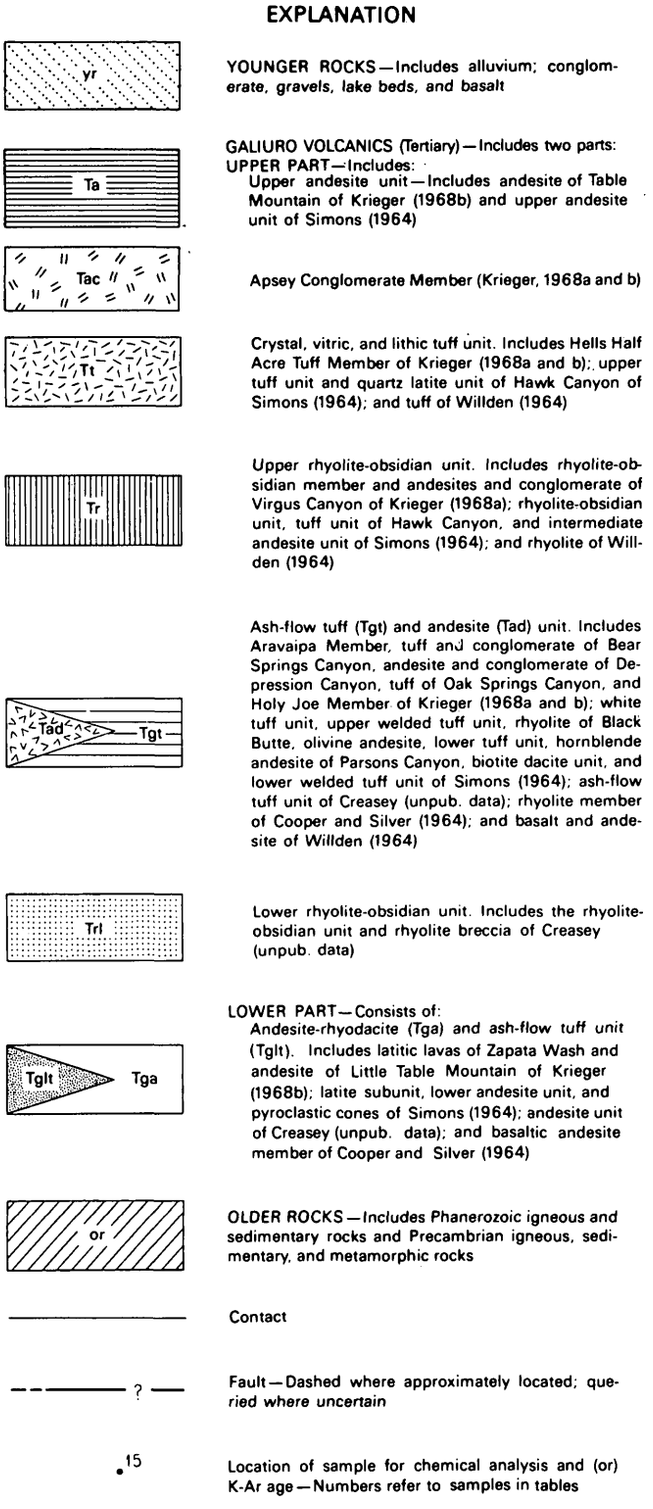

FIGURE 2.—Geologic sketch map showing general distribution and lithology of the Galiuro Volcanics.

Dragoon Mountains, it is only as much as 230 m (Cooper and Silver, 1964).

Within andesite-rhyodacite, Krieger (1968c) recognized both andesite and latite, but, because the two rocks are not in contact, she was not certain of their stratigraphic relation. Because both are overlain by a distinctive porphyritic andesite, locally called "turkey track" andesite, she suggested time equivalency. At the top of the unit, Simon (1964) also recognized locally the "turkey track" andesite, but he did not map it separately. He did, however, map separately a local latite and a local thin layer of heterogeneous silicic volcanic rocks at the top of the unit.

Creasey (unpub. data) recognized flows of different composition within the lower part, but he did not map them separately. In the field the flows were called latite, but chemical analyses have indicated that at least some are rhyodacite or rhyolite (table 1, No. 11)[1]. One thick (table 1, No. 9) and two thin ash-flow tuff units occur within the lower part between lat 32°25′ and 32°45′, but only the thick tuff (table 1, No. 9) is shown in figure 2. The tuff unit is lenticular. It starts at about lat 32°42½′ and thickens rapidly southward to as much as 580 m; its southern extent is unknown, owing to overlap by the younger gravel in the San Pedro valley.

Lower rhyolite-obsidian unit

The lower rhyolite-obsidian unit (fig. 2) includes a wedge of sedimentary rhyolite breccia lying along the eastern flank of the rhyolite-obsidian. The breccia accumulated against an active fault by erosion from topographically higher rhyolite-obsidian domes and flows.

The lower rhyolite-obsidian unit lies between lat 32°33′ and 32°41′ and occurs at the base of the upper part. It must have been a hill as high as 610 m resting on andesite and latitic flows at the time of eruption of the great sheets of ash-flow tuff, which eventually covered the lower rhyolite-obsidian unit. The lenticularity of the unit is indicated by a lateral-extent-to-thickness ratio of about 25:1.

Ash-flow tuff and andesite unit

Within the stratigraphic interval of the ash-flow tuff and andesite unit, Krieger (1968a,b) separated five map units in the Holy Joe Peak and Brandenburg Mountain quadrangles; Simons (1964), eight in the Klondyke quadrangle; Willden (1964) and Cooper and Silver (1964), two each in the Christmas and Dragoon quadrangles; and S. C. Creasey (unpub. data), one in the Galiuro Mountains quadrangle. These map units are listed in the explanation of figure 2 and are correlated in figure 3.

[1] Numbers refer to both chemical analyses and to the locations in figure 2.

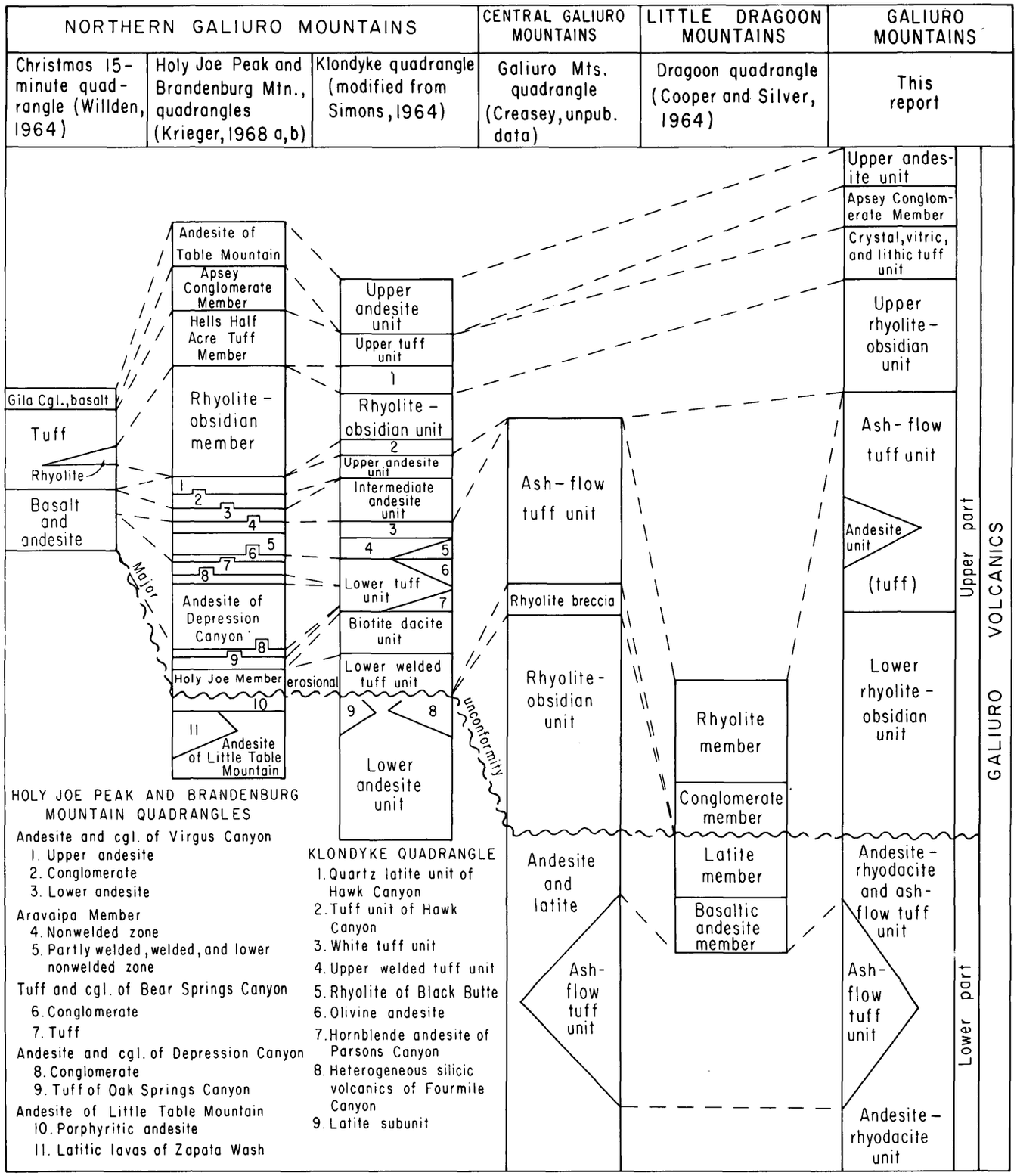

FIGURE 3.—Correlation chart showing relations of stratigraphic units in the Galiuro Volcanics within area of figure 2. Thicknesses of units are maximum in each quadrangle.

TABLE 1.—*Rock classification of analyzed samples of Galiuro Volcanics based on chemical and normative analyses*

Loc. on fig. 2	Laboratory no.	Rock unit of Krieger (1968) except nos. 9 and 10	Peterson (1961)	Rittmann (1952)	Irving and Barager (1971)	O'Connor (1965)
1	F2678	Andesite of Table Mountain	Andesite	Andesite	Andesite	N.A.[1]
2	F2779	Rhyolite-obsidian member	Rhyolite	Alkali rhyolite	Rhyolite	Rhyolite
3	M101317W	do	do	Rhyolite	do	Do.
4	159531	Aravaipa Member	do	do	do	Do.
5	F2680	do	do	do	do	Do.
6	G2965	Holy Joe Member	Quartz latite	Dark quartz latite	Dacite	Do.
7	159527	do	do	Rhyolite	Rhyolite	Do.
8	W182412	do	do	Quartz latite	do	Do.
9	W182414	Ash-flow tuff unit in andesite-rhyodacite unit	do	do	do	Do.
10	W182413	Dike	do	do	do	Do.
11	W182411	Andesite of Little Table Mountain	Rhyolite	Trachyte	do	Do.
12	M101316W	Latitic lavas of Zapata Wash	Rhyodacite	Rhyodacite	Dacite	Rhyodacite
13	F2681	Andesite of Little Table Mountain "turkey track"	do	Trachyandesite	Andesite	Rhyolite
14	F2682	Andesite of Little Table Mountain	Andesite	Olivine andesite	do	N.A.

[1] Contains less than 10 percent normative quartz; classification does not apply.

Ash-flow tuffs dominate this unit. They make up the Holy Joe and Aravaipa Members of Krieger (1968 a, b); the lower and upper welded tuffs and white tuff units of Simons (1964), the ash-flow tuff unit of Creasey (unpub. data), and the rhyolite (ash-flow tuff) and conglomerate members of Cooper and Silver (1964). North of lat 32°45′, the bulk of the ash-flow tuffs are in two sequences separated by andesite, dacite, rhyolite, conglomerate, tuff, and minor ash-flow tuff. In figure 2, all the rocks that separate the two sequences of ash-flow tuffs are shown as andesite, but the details of the stratigraphy are in figure 3 in the columnar sections for the Holy Joe Peak-Brandenburg Mountain and Klondyke quadrangles. Although not shown in either figure 2 or 3, at least five andesite flows occur in the Galiuro Mountains quadrangle within the ash-flow tuff unit.

Upper rhyolite-obsidian and andesite unit

The upper rhyolite-obsidian unit includes rhyolite-obsidian, the andesite and conglomerate of Virgus Canyon of Krieger (1968a, b), the intermediate andesite unit and tuff unit of Hawk Canyon of Simons (1964), and the tuff and rhyolite of Willden (1964) (fig. 2).

In that part of the southern end of the Christmas 15′ quadrangle covered by volcanic rocks, Willden mapped two small areas of rhyolite and the remainder as tuff and rhyolite undivided. The latter is interpreted to include rhyolite-obsidian, Hells Half Acre Tuff, and Apsey Conglomerate Members of Krieger (1968a, b, d); figure 2 shows Krieger's interpretation of the distribution of these members in the Christmas 15′ quadrangle.

The outcrop of the upper rhyolite-obsidian unit in figure 2 is restricted to the area between lat 32°55′ and 33°02′. Despite this lateral restriction, it is about 300 m thick. The exposed-lateral extent-to-thickness ratio is about 40:1, which differs somewhat from the 25:1 ratio for the lower rhyolite-obsidian unit.

Crystal, vitric, and lithic tuff; Apsey Conglomerate Member; and upper andesite unit

The three units overlying the upper rhyolite-obsidian unit of figure 2 are not composite except for the inclusion of a small area of latite flows with the upper tuff unit in the Klondyke quadrangle. The stratigraphic relations of the three units are shown in figure 3. Although agreement on the stratigraphy above the ash-flow tuff and andesite unit is generally good, Simons (1964) and Krieger (1968a) disagree on the position of the upper andesite unit. The differences between their interpretations of the stratigraphy are shown in figure 4. Krieger believes that the upper andesite unit north of Aravaipa Creek, which locally rests on the upper rhyolite-obsidian unit, is above Simons' upper tuff unit, whereas Simons believes it

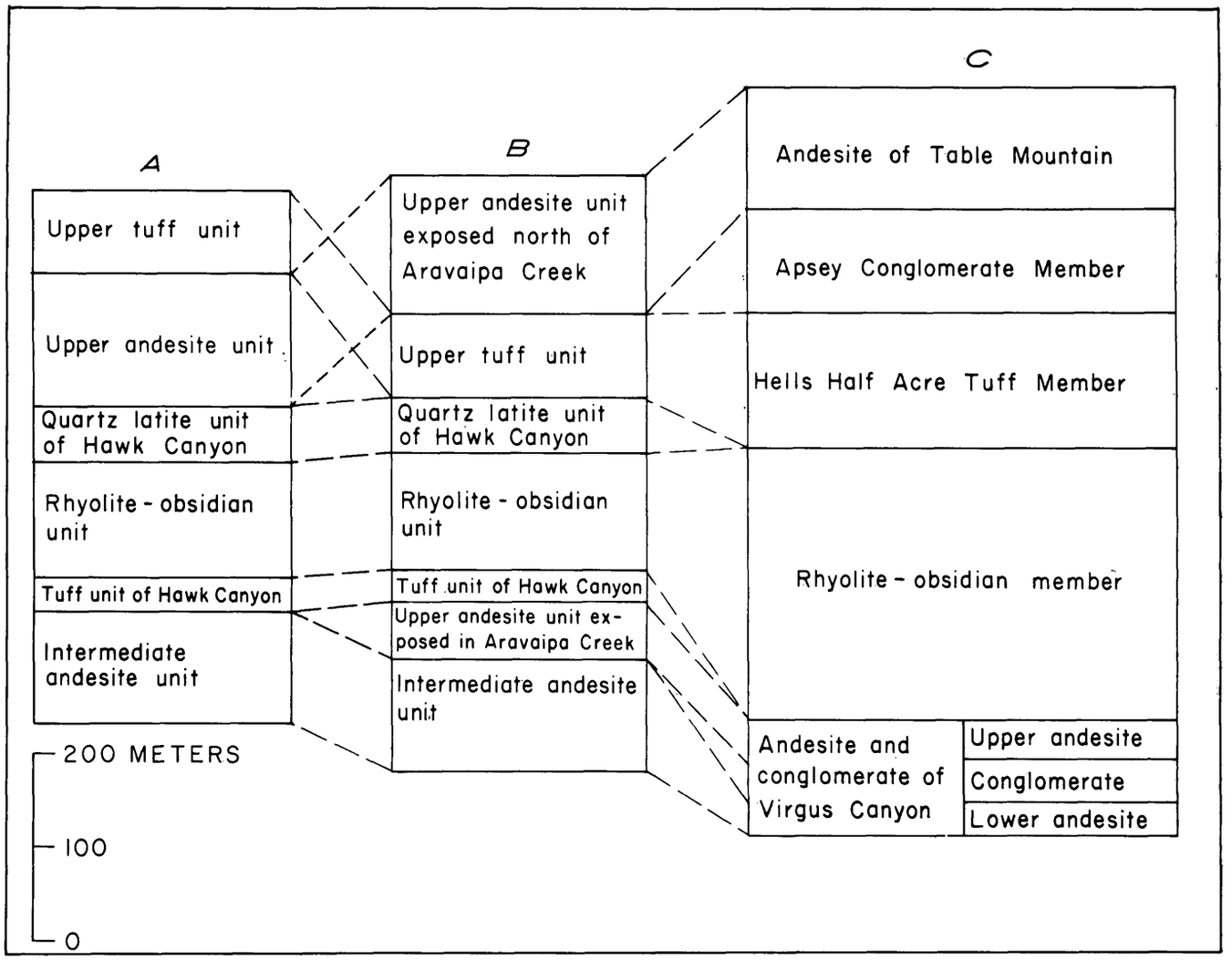

FIGURE 4.—Difference between Simons' and Krieger's interpretations of stratigraphic position of upper andesite unit. *A*, Simon's (1964) stratigraphy in Klondyke quadrangle. *B*, Krieger's reinterpretation of stratigraphy in Klondyke quadrangle. *C*, Krieger's (1968a, b) stratigraphy in Holy Joe Peak and Brandenburg Mountain quadrangles.

is below that unit. Krieger based her reinterpretation on correlation of Simons' upper andesite unit with her andesite of Table Mountain, which clearly overlies the Apsey Conglomerate Member in the Holy Joe Peak quadrangle. Also, the correlation of the upper tuff unit and the Hells Half Acre Tuff Member seems clear-cut. In addition, Krieger believes that what Simons called the upper andesite unit in Aravaipa Creek in the Klondyke quadrangle is the same as her upper andesite of Virgus Canyon in the Brandenburg Mountain quadrangle. She was able to walk the outcrop of the andesite from one locality to the other, a distance of about 2.5 km. Simons based his designation on the observation that the andesite in Aravaipa Creek in the Klondyke quadrangle overlies the upper rhyolite-obsidian unit. However, Krieger believes that the andesite actually underlies that unit. These relations and her correlations are shown in figure 4. More detailed information is presented in the geologic maps of Simons (1964) and Krieger (1968a).

LITHOLOGY

Andesite-rhyodacite and ash-flow tuff unit

The lava flow parts of the andesite-rhyodacite and ash-flow tuff unit are complex sequences of predominantly dark colored flows that contain minor tuff, agglomerate, rocks of vent areas, and intrusive rocks. Some flows have basal reddish flow breccia and scoriaceous tops, and about one-third of the flows are either vesicular or amygdaloidal or both. Most are porphyritic, but some are aphyric. Flow banding is

rare, but it was observed by Krieger (1968b) in some latite flows. These rocks range in chemical composition from rhyodacite to andesite (table 1, Nos. 1, 11, 13, 14); by some chemical classifications, rhyolite flows may be represented, but if so, they are atypical in appearance.

The appearance of the flows is deceptive. They are typically dark colored, commonly red, purple, gray, or brown, owing to finely disseminated iron in the groundmass, yet some of these rocks are chemically rhyodacite or rhyolite. The phenocryst content ranges from virtually 0 to an estimated 25 percent, but typically it is low, particularly in the andesitic flows. This low phenocryst content means that the only megascopic minerals are those that crystallized early and that under normal conditions some of these would have later reacted and disappeared. For example, some of these rocks that contain olivine phenocrysts are oversaturated with silica; that is, they contain normative quartz and are rich in alkalic elements, which are all in the microcrystalline groundmass. The rocks are not especially rich in iron, but iron is finely divided in the groundmass, and the rocks appear much darker than if the bulk of the iron were concentrated in megascopic minerals. These factors make it difficult to determine rock types from either megascopic or microscopic examination, and therefore the relative abundance of andesite, latite, or rhyodacite is unknown; the best determination of rock types is through chemical classifications (table 1).

The porphyritic andesite, known locally in southeastern Arizona as "turkey track" andesites because of the glomeroporphyritic habit of large tabular plagioclase phenocrysts, are a distinctive type. They occur at or near the top of the unit near lat 32°45′ and elsewhere in the section. The coarsely porphyritic andesite consists of large platy plagioclase phenocrysts (2–15 millimeters) and of smaller grains of olivine and magnetite(?) set in an intergranular or pilotaxitic groundmass composed of plagioclase microlites, pyroxene, magnetite, and potassium feldspar. In contrast, the common andesite flow in the unit is porphyritic (small phenocrysts) with a microcrystalline pilotaxitic groundmass. About 1 out of 10 andesite flows, however, is aphyric microgranular. Phenocrysts consists of plagioclase and lesser amounts of clinopyroxene and (or) altered olivine; the groundmass comprises plagioclase microlites, pyroxene, and iron oxide minerals that commonly so obscure the groundmass that resolution of minerals is difficult.

The more silicic flows in this unit differ from the more basic ones both in texture and phenocryst composition, and they typically ring when struck with a hammer. These flows are all conspicuously porphyritic; plagioclase phenocrysts are dominant, biotite is almost always present, and clinopyroxene occurs in about one out of every four flows. Groundmass textures are microgranular in marked contrast to the pilotaxitic and intergranular texture of the andesites, and the groundmass minerals consist of plagioclase, potassium feldspar, and mafic constituents including much iron oxide. Silica in some form is probably present to judge by the normative quartz content, but quartz was not recognized as a groundmass mineral.

Table 2 lists four chemical analyses (Nos. 11–14) from the andesite-rhyodacite and ash-flow tuff unit, and figure 2 shows the locations of the samples. Two of these (Nos. 13 and 14) are from Simons (1964); they were collected to represent the common andesite and the "turkey track" andesite, respectively. Of the other two analyses, one is from a rock selected for potassium-argon age determination (table 1, No. 11); it was selected because of the high content of large unaltered biotite books and therefore probably represents the most differentiated (quartzose and alkalic) rock in the unit; the other, a rhyodacite (Tlz of Krieger, 1968b), also represents a differentiated type. Table 1 lists four different chemical classifications for the analyzed rocks of the Galiuro Volcanics. By the classification of O'Connor (1965), the rocks are dominantly rhyolitic, whereas by the more recent classification of Irving and Barager (1971), developed for the Geological Survey of Canada, they range from andesite to rhyolite. In her previous publications, Krieger has used the American Geological Institute classification (Peterson, 1961), and, when using rock names in this report, we will use that system insofar as it is possible. However, volcanic rock names derived from megascopic and microscopic examination commonly differ significantly from those derived from chemical analyses. Some inconsistency is inevitable because rock descriptions in this report are derived from both microscopic examinations and chemical analyses.

The ash-flow tuff interbedded in the andesite-rhyodacite is light-pinkish-gray to pale-red-purple, predominantly welded tuff; the vitrophyre is brown to black. The tuff consists of phenocrysts of plagioclase, sanidine, and dark-red-brown biotite in a groundmass of partly to completely devitrified glass in which only feldspar microlites can be recognized. Iron ores, sphene, apatite, and zircon are accessory minerals.

A chemical analysis of one of these ash-flow tuffs is represented by number 9 (table 2); the location of the sample is shown in figure 2. It is higher in silica and alkalic metals than the most differentiated of the

TABLE 2.—*Chemical and spectrographic analyses and catanorms of Galiuro Volcanics*

[Major oxide analyses by standard methods described in Peck (1964): 1, 2, 5, 13, 14 by D. F. Powers; 6 by J. W. Goldsmith; by methods described in Shapiro (1967): 8, 9, 10, 11 by P. Elmore; by methods described in Shapiro and Brannock (1962), supplemented by atomic absorption: 3, 12 by P. Elmore, L. Artis, G. Chloe, J. Glenn, S. Botts, H. Smith, and D. Taylor; 4, 7 by P. Elmore, S. Botts, H. Smith, and D. Taylor. Minor-element analyses by semiquantitative spectrographic methods in parts per million to the nearest number in the series 1, 0.7, 0.5, 0.3, 0.2, 0.15, and 0.1; the numbers represent approximate midpoints of group data on a geometric scale. The assigned groups for semiquantitative results include the quantitative value about 30 percent of the time. N, not detected; d, barely detected, concentration uncertain; ---, not looked for. Looked for but not found: As, Au, Bi, Cd, Dy, Er, Eu, Ce, Hf, Ho, In, Li, Lu, Pd, Re, Sb, Sm, Ta, Tb, Te, Th, Tl, Tm, U, W. Dy, Er, Lu, Tb, Tm not looked for in 3, 8-12. Hf not looked for in 8-11]

	Andesite of Table Mountain	Upper rhyolite-obsidian unit		Aravaipa Member		Holy Joe Member			Ash-flow tuff unit[1]	Dike	Andesite-rhyodacite unit			
Lab. no.	F2678	F2679	M101317W	159531	F2680	G2965	159527	W182412	W182414	W182413	W182411	M101316W	F2681	[2]F2682
Loc. on fig. 2	1	2	3	4	5	6	7	8	9	10	11	12	13	14
SiO_2	53.95	72.83	74.6	73.4	72.92	65.17	68.5	68.4	64.2	66.9	63.4	64.6	57.59	52.45
Al_2O_3	17.06	12.94	13.5	13.6	13.37	14.67	15.2	15.70	17.7	16.0	17.2	16.4	16.70	16.99
Fe_2O_3	4.24	1.13	1.3	1.2	1.36	2.04	2.5	2.60	3.1	3.0	4.2	4.4	6.55	6.11
FeO	4.25	.19	.12	.08	.02	.22	.30	.16	.16	.24	.20	.28	.99	2.88
MgO	3.91	.18	.11	.47	.51	1.40	.80	.54	.92	1.1	1.5	1.1	2.15	3.10
CaO	8.04	.41	.38	.44	.53	1.44	1.3	1.60	1.6	1.5	.90	3.3	5.27	7.02
Na_2O	3.66	4.10	4.2	3.6	3.42	2.97	3.8	4.10	3.6	4.1	4.3	4.2	4.05	3.79
K_2O	1.60	4.69	4.5	5.2	5.29	4.73	5.7	4.80	5.7	4.5	5.4	3.2	2.87	2.71
H_2O+	.40	2.98	.42	.93	.63	2.73	.53	.70	1.0	1.9	.30	.61	.72	.86
H_2O-	.69	.18	.10	.93	1.04	3.43	.32	.42	.84	.22	.80	.39	1.02	1.08
TiO_2	1.39	.19	.21	.24	.22	.49	.56	.61	.59	.74	---	.85	1.37	1.79
P_2O_5	.29	.02	.03	.06	.03	.10	.16	.12	.19	.19	.30	.34	.38	.67
MnO	.13	.10	.10	.08	.07	.07	.08	.09	.16	.14	.13	.12	.10	.13
CO_2	.03	.01	<.05	<.05	.04	.01	<.05	.08	.30	.03	.06	<.05	.01	.13
Cl	.01	.06	---	---	.01	.05	---	---	---	---	---	---	.01	.01
F	.05	.10	---	---	.06	.11	---	---	---	---	---	---	.06	.07
Subtotal	99.70	99.61			99.52	99.68							99.84	99.79
less oxygen	.02	.05			.03	.05							.03	.03
Total	99.68	99.56	100	100	99.49	99.63	100	100	99	99	99	100	99.81	99.76
Powder density	2.84	2.40			2.57								2.71	2.79
SEMIQUANTITATIVE SPECTROGRAPHIC ANALYSES														
Ag	---	---	<0.7	<0.7	N	N	<0.7	N	N	N	N	<0.7	N	N
B	---	---	10	30	N	15	N	15	N	N	N	N	N	N
Ba	700	300	50	500	300	700	2,000	1,000	2,000	1,000	1,500	1,000	1,500	700
Be	N	3	5	5	3	30	3	3	3	2	2	2	N	1.5
Ce	N	d	100	100	d	150	300	N	N	N	N	70	d	d
Co	30	N	N	N	N	1.5	5	2	3	2	7	7	30	30
Cr	30	N	N	3	3	1.5	20	3	N	30	3	N	1.5	30
Cu	70	3	3	3	3	70	20	10	7	100	30	3	70	300
Ga	15	15	20	20	15	15	20	15	15	15	15	1.5	15	15
Gd	N	N	---	N	N	---	30	---	---	---	---	N	N	N
La	30	70	70	50	70	70	150	100	70	70	70	50	70	70
Mo	N	d	2	3	N	3	3	3	N	N	N	5	N	N
Nb	15	30	30	20	30	15	20	15	10	15	10	15	15	15
Nd	N	150	N	N	d	70	150	N	N	N	N	N	d	150
Ni	30	N	N	10	N	N	30	N	N	N	15	N	15	70
Pb	N	15	50	30	30	30	30	30	20	20	20	30	15	d
Sc	30	7	5	3	7	7	10	7	7	7	7	7	15	15
Sn	N	N	N	N	N	7	N	N	N	N	N	N	N	N
Sr	1,500	15	7	70	70	300	500	500	500	500	700	500	1,500	1,500
V	700	N	N	10	15	15	50	20	20	30	30	30	300	300
Y	30	30	30	30	30	30	70	30	30	30	15	30	30	30
Yb	3	3	3	3	7	3	7	3	2	3	1.5	3	3	3
Zn	---	---	N	N	---	N	N	N	N	N	N	---	---	---
Zr	150	300	200	200	300	300	1,000	500	500	500	200	200	300	300
MOLECULAR NORM CALCULATIONS (PERCENT)														
Si	50.99	70.04	70.18	69.59	69.63	65.09	64.39	64.33	60.56	63.10	59.89	61.00	54.83	50.13
Al	19.01	14.67	14.97	15.20	15.05	17.27	16.84	17.41	19.98	17.79	19.15	18.26	18.78	19.14
Fe^{3+}	3.02	.82	.93	.86	.98	1.54	1.77	1.85	2.21	2.13	2.99	3.13	4.71	4.40
Fe^{2+}	3.36	.16	.10	.07	.02	.19	.24	.13	.13	.19	.16	.23	.79	2.31
Mg	5.51	.26	.16	.67	.73	2.09	1.13	.76	1.30	1.55	2.12	1.55	3.06	4.42
Ca	8.15	.43	.39	.45	.55	1.55	1.31	1.62	1.62	1.52	.92	3.34	5.39	7.19
Na	6.71	7.65	7.66	6.62	6.34	5.76	6.93	7.48	6.59	7.50	7.88	7.69	7.49	7.03
K	1.93	5.76	5.40	6.29	6.45	6.03	6.84	5.76	6.86	5.42	6.51	3.86	3.50	3.31
Ti	.99	.14	.15	.18	.16	.37	.40	.44	.42	.53		.61	.99	1.29
P	.24	.02	.03	.05	.03	.09	.13	.10	.16	.16	.24	.28	.31	.55
Mn	.11	.09	.08	.07	.06	.06	.06	.08	.13	.12	.11	.10	.09	.11
C	.04	.02			.06	.02		.11	.39	.04	.08		.02	.17
H	(2.53)	(19.12)	(2.64)	(5.89)	(4.02)	(18.19)	(3.33)	(4.40)	(6.30)	(11.96)	(1.90)	(3.85)	(4.59)	(5.49)
Cl	(.02)	(.10)			(.02)	(.09)							(.02)	(.02)
F	(.15)	(.31)			(.19)	(.35)							(.19)	(.22)
Total Anions	160.48	181.22	173.09	174.35	173.71	178.64	169.06	170.21	168.96	173.37	165.15	168.85	165.12	161.98

[1]Ash-flow tuff in lower andesite-rhyodacite unit.

[2]"Turkey track" andesite.

TABLE 2.—*Chemical and spectrographic analyses and catanorms of Galiuro Volcanics*—Continued

	Andesite of Table Mountain	Upper rhyolite-obsidian unit		Aravaipa Member		Holy Joe Member			Ash-flow tuff unit	Dike	Andesite-rhyodacite unit			
Lab. no.	F2678	F2079	M101317W	159531	F2680	G2965	159527	W182412	W182414	W182413	W182411	M101316W	F2681	F2682
Loc. on fig. 2	1	2	3	4	5	6	7	8	9	10	11	12	13	14
						CATANORM (PERCENT)								
Quartz	5.79	29.42	30.16	29.47	29.90	25.48	19.80	21.17	16.99	20.37	13.77	19.05	10.26	4.27
Corundum		.90	1.23	1.56	1.57	3.13	.89	1.47	4.28	2.43	3.90	.94		
Orthoclase	9.65	28.77	27.00	31.45	32.22	30.14	34.18	28.80	34.20	27.08	32.54	19.28	17.47	16.53
Albite	33.45	37.74	38.30	33.09	31.58	28.34	34.63	37.39	32.93	37.49	39.38	38.45	37.37	35.04
Anorthite	25.96	1.17	1.72	1.84	1.82	6.14	5.49	6.76	4.89	6.13	2.17	14.43	19.52	22.07
Halite	.04	.20			.04	.17							.04	.04
Wollastonite	4.98												1.62	3.38
Enstatite	11.02	.52	.31	1.33	1.46	4.17	2.25	1.52	2.59	3.10	4.23	3.10	6.12	8.84
Ferrosilite	1.94													
Magnetite	4.53	.30	.08								.79			3.37
Hematite		.63		.86	.98	1.54	1.77	1.85	2.21	2.13	2.47	3.13	4.71	2.16
Ilmenite	1.98	.28	.30	.26	1.15	.49	.59	.40	.51	.61		.64	1.75	2.58
Rutile				.05	.09	.13	.11	.24	.17	.23		.29	.34	
Apatite	.62	.05	.07	.13	.07	.23	.34	.26	.41	.41	.64	.73	.82	1.45
Fluorite	.11	.45			.26	.48							.12	.05
Calcite	.08	.03			.11	.03		.21	.78	.08	.16		.03	.34
Total	100.09	100.40	100.01	100.01	100.19	100.41	100.01	100.01	100.01	100.01	100.01	100.01	100.10	100.05
Diopside	9.96												3.23	6.75
Di-Wo	4.98												1.62	3.38
Di-En	4.24												1.62	3.38
Di-Fs	.75													
Hypersthene	7.98	.52	.31	1.33	1.46	4.17	2.25	1.52	2.59	3.10	4.23	3.10	4.51	5.46
Hy-En	6.79	.52	.31	1.33	1.46	4.17	2.25	1.52	2.59	3.10	4.23	3.10	4.51	5.46
Hy-Fs	1.20													
Percent An	43.70	3.0	4.29	5.26	5.44	17.80	13.68	15.30	12.94	14.04	5.22	27.29	34.32	38.65
D.I.	46.9	92.6	94.7	92.9	92.8	81.3	87.4	86.0	82.8	82.6	84.7	75.1	62.6	53.2
k-value	.224	.430	.414	.488	.505	.512	.497	.436	.511	.420	.453	.334	.318	.320
mg-value	.460	.197	.124	.404	.409	.540	.353	.271	.346	.389	.395	.311	.355	.394
c/a-value	.427	.232	.153	.139	.166	.202	.263	.245	.136	.201	.084	.301	.385	.410
Alk/fm value	.419	.911	.913	.887	.878	.754	.813	.826	.782	.765	.729	.699	.561	.480

flows in the unit, and, as will be discussed later, its source probably differed from that of the flows. By chemical classification, the tuff is either a quartz latite or a rhyolite (table 1).

Lower rhyolite-obsidian unit

The lower rhyolite-obsidian unit consists of domes, stubby flows, and subordinate tuffs and breccias. The color ranges widely: the stony (devitrified) and the originally microcrystalline rhyolites are off-white, pale red, pink, and orange, and the obsidians are dark hues of nearly black, brown, red-brown, green, and yellow. Contorted flow banding is common but not ubiquitous. Spherulites and lithophysae are common.

The rhyolite-obsidian is composed of phenocrysts and sanidine (most abundant) and quartz and sparse biotite and albite. The groundmass of the obsidian is either glass or devitrified glass, and that of the rhyolite is microcrystalline, containing feldspar microlites.

A sedimentary breccia (fig. 3) that is part of the lower rhyolite-obsidian unit crops out in the central part of the Galiuro Mountains. It represents rhyolite debris transported eastward from the topographically higher rhyolite-obsidian domes and flows and deposited against the fault scarp of the longitudinal fault in the central Galiuro Mountains. The breccia is crudely bedded, the beds typically dipping gently eastward except near the fault on the eastern margin of the breccia, where dips are as steep as 80° E.; these steep dips are attributed to movement along the fault during accumulation of the breccia. Individual beds are disordered accumulations of angular clasts ranging in size from microscopic to 1 or 2 m in diameter. Sorting within beds appears to be nonexistent and is only crude between beds. Rounding of fragments is minimal. Although the source of the fragments is primarily the underlying lower rhyolite-obsidian unit, fragments of ash-flow tuff are common, and here and there fragments of andesite occur.

Ash-flow tuff and andesite unit

Both Krieger (1968a,b) and Simons (1964) mapped the Galiuro Volcanics in detail, and both recognized two sequences of ash-flow tuffs, the Holy Joe and Aravaipa Members of Krieger and the lower and upper welded tuff and white tuff units of Simons. Both sequences probably extend into the central part of the Galiuro Mountains, but Creasey made no attempt to divide them.

The Holy Joe Member has a white- to cream-colored, nonwelded tuff base that grades upward into brown, partly welded tuff, black vitrophyre, and typical reddish, strongly welded devitrified tuff. It is composed of phenocrysts or fragments of phenocrysts (about 10 percent) of plagioclase, biotite (oxidized in devitrified rock), quartz, sanidine, and sparse clinopyroxene and magnetite; rock fragments and pumice lapilli are common. Except for the nonwelded base and the vitrophyre, the matrix has devitrified to a cryptocrystalline mass. As seen in thin sections, shard structure is not well preserved in some welded tuff south of lat 32°45′ but is generally well preserved in welded tuff north of that latitude. In the Holy Joe Peak quadrangle, the member was erupted as very hot ash flows that became densely welded and cooled as a unit.

Three samples of welded devitrified ash-flow tuff from the Holy Joe Member were analyzed (table 2, Nos. 6–8; geographic locations shown in fig. 2). The classification from the chemical analyses is either quartz latite or rhyolite (table 1). Quartz latite would be the more appropriate field term, as plagioclase and quartz phenocrysts are ubiquitous and sanidine sparse.

Between the Holy Joe Member and the next overlying major rock unit (Aravaipa Member) is a sequence of local tuffs, conglomerates, and andesitic to dacitic flows. North of lat 32°45′ and west of long 110°30′, Krieger (1968a,b) recognized a white to grayish-orange-pink rhyolitic tuff containing crystal fragments of quartz, feldspar, and biotite and pumice lapilli and accidental rock fragments (tuff of Oak Springs Canyon). Above this tuff, a sequence from top to bottom of conglomerate, vesicular and amygdaloidal andesite, and conglomerate (andesite and conglomerate of Depression Canyon) is exposed.

The andesite consists of phenocrysts of plagioclase, altered olivine, clinopyroxene, and magnetite in a pilotaxitic groundmass of plagioclase microlites, clinopyroxene, iron ores, some potassium feldspar, and alteration products. The conglomerates contain clasts from Paleozoic rocks, from older members of the Galiuro Volcanics, and locally from Late Cretaceous and (or) early Tertiary volcanic and intrusive rocks.

The next overlying unit (tuff and conglomerate of Bear Springs Canyon) consists of a thin, light-colored, rhyolitic ash-flow tuff that is both overlain and underlain by thin conglomerate beds. The tuff is composed of pumice lapilli, and crystal and accidental rock fragments. The clast in the conglomerate were derived from Paleozoic and older rocks and from older members of the Galiuro Volcanics. East of long 110°30′, in the same stratigraphic interval between the Holy Joe and Aravaipa Members, Simons (1964) recognized, from bottom to top, a biotite dacite, hornblende andesite, silicic tuff, silicic welded tuff, olivine andesite, and porphyritic rhyolite. Not all of these units occur in one place, and the tuffs, which are rhyolitic, differ from place to place in induration and color. The hornblende andesite consists of long phenocrysts of brown hornblende (oxidized) and plagioclase in a groundmass of plagioclase microlites, iron ore, and interstitial devitrified glass. The olivine andesite consists of small phenocrysts of clinopyroxene and red olivine in an intergranular groundmass of plagioclase laths and interstitial iron ores, olivine, and pyroxene. Figure 3 shows the correlation between Simons' and Krieger's map units in the stratigraphic interval between the two major ash-flow tuffs.

In the central part of the Galiuro Mountains within the ash-flow tuff unit between lat 32°30′ and 32°45′, Creasey mapped about five andesite flows separated by tuffs and welded tuffs. Some crystal-lithic andesitic tuffs associated with the andesite consist of lithic fragments of andesite and welded tuff and crystal fragments of plagioclase, quartz, and biotite in a tuff matrix. The andesite flows consist of phenocrysts of plagioclase and clinopyroxene in a pilotaxitic groundmass of plagioclase microlites and interstitial iron ores, pyroxene, and unidentified material.

The upper ash-flow tuff, the Aravaipa Member of Krieger (1968a,b) and the white tuff and upper welded tuff units of Simons (1964), is a simple cooling unit and probably a single ash flow. It is composed of pumice lapilli, crystal fragments (totaling about 6 percent of the rock) of feldspar (sanidine and plagioclase), quartz, and biotite, and sparse exotic fragments, chiefly dark volcanic rocks, in a matrix of shards. In the Holy Joe Peak quadrangle, the ash flow typically has a light-colored nonwelded base, a brown-to-black vitrophyre, a densely welded devitrified zone that in the lower part contains large vugs and silica-lined lithophysae, a somewhat lighter colored columnar-jointed zone, and a slope-forming very light gray to white slightly welded top. The two upper units show both devitrification and vapor-phase crystallization. The transition from the interior of the ash flow, which shows pronounced vertical zonation, to the distal end of the ash flow, is completely exposed in the east-central part of the Holy Joe Peak quadrangle. The distal end is nonwelded; it has been completely zeolitized. Table 2 lists two chemical analyses (Nos. 4 and 5) of the Aravaipa Member, which by chemical classification is a rhyolite (table 1).

Upper rhyolite-obsidian unit

Above the Aravaipa Member and below the rhyolite-obsidian member and north of lat 32°45′, Krieger (1968a,b) recognized an upper and lower andesite separated by a conglomerate (andesite and conglomerate of Virgus Canyon), whereas Simons (1964) also recognized two andesites (intermediate and upper andesite units) but not the conglomerate. In the northwest part of the Klondyke quadrangle, a tuff unit (tuff of Hawk Canyon) lies between his intermediate andesite and rhyolite-obsidian.

The lower andesite, a "turkey track" andesite, is medium gray on fresh fractures and light brown on weathered surfaces. It is composed of large plagioclase laths as long as 20 mm and small altered olivine and clinopyroxene in an intersertal or pilotaxitic groundmass of plagioclase microlites, clinopyroxene, iron ores, altered olivine, apatite needles, and glass.

The conglomerate between the two andesites consists of clasts derived from underlying "turkey track" andesite and from older rocks in a sand matrix. It thins and is largely absent in the Klondyke quadrangle. The upper andesite is dark colored, fine grained, and amygdaloidal. It consists of small phenocrysts of plagioclase, altered olivine, and clinopyroxene in an intergranular groundmass of andesine microlites and granules of clinopyroxene and sparse olivine and iron ore.

The tuff unit of Hawk Canyon of Simons is a cream-colored or pink massive coarse-grained rough-weathering rock composed of crystals of feldspar and quartz and fragments of volcanic rock in a glassy or pumiceous matrix.

The rhyolite-obsidian part of the unit is composed chiefly of domes and stubby flows and subordinate breccia, agglomerate, and cinder cones. Color of the obsidian ranges from gray to black; rhyolite is gray. Obsidian is perlitic to lithophysal. Both rhyolite and obsidian are characterized by finely laminated to contorted flow layering. Some breccia consists of angular fragments of vesicular rhyolite and obsidian. Rhyolite and obsidian contain sparse sanidine, quartz, plagioclase, pyroxene, hornblende, iron oxide, sphene, and scattered accidental fragments. Lithophysae, generally 10–30 mm in diameter, are strung out in places, giving large outcrops a steeply dipping bedded appearance. Table 2 lists two chemical analyses (Nos. 2 and 3) for the rhyolite-obsidian, which by chemical classification is a rhyolite (table 1).

Crystal, vitric, and lithic tuff unit

Overlying the upper rhyolite-obsidian and andesite unit is latite (quartz latite of Hawk Canyon of Simons, 1964) and tuff (Hells Half Acre Tuff Member of Krieger 1968 a, b, d; upper tuff unit of Simons, 1964; and tuff of Willden, 1964). The quartz latite of Hawk Canyon occurs only east of long 110°30′. It is a massive reddish rock composed of abundant phenocrysts from 1 to 5 mm long of pink potassium feldspar, gray plagioclase, quartz, and biotite in a stony groundmass.

The lowest subunit of the Hells Half Acre Tuff Member is a cliff-forming rhyolite tuff. In the Klondyke quadrangle, it is predominately coarse grained but contains interbeds of fine-grained crystal-rich tuff; the lithic fragments are chiefly rhyolite derived from the rhyolite-obsidian. In the Holy Joe Peak 15′ quadrangle, the lowest subunit is a water-laid tuff, deposited in water impounded behind rhyolite flows; it is fine grained and contains fragments of pumice lapilli and crystals of quartz, feldspar, and biotite. Here it locally appears to be contemporaneous with the rhyolite-obsidian.

Resting on the lowest subunit is a massive, white, cliff-forming tuff composed of pumice lapilli, obsidian, and grains of quartz, feldspar, and biotite in a matrix of white ash. At least part of the subunit is probably a nonwelded to slightly welded ash-flow tuff. Pumice lapilli and some of the shard matrix have been altered to clinoptilolite.

The upper subunit is a variable vitric, lithic, and crystal tuff. It ranges in color from white to yellow-brown to brown. Some beds are cliff forming, and some are slope forming. It ranges from coarse to fine grained, and local beds are water laid. Lithic fragments comprise rhyolite, obsidian, pumice lapilli, and stony vitrophyre. Crystal fragments are quartz, feldspar, and biotite.

Apsey Conglomerate Member

The Apsey Conglomerate Member crops out prominently in the Brandenburg and Holy Joe Peak quadrangles, but it laps out eastward against the rhyolite-obsidian; it was not a mappable unit in the Klondyke quadrangle. It is a light-colored cliff-forming conglomerate and conglomeratic tuff containing pebbles, cobbles, and scattered boulders derived from the rhyolite-obsidian member. It also contains sparse to locally abundant clasts of older rocks including members of the Galiuro Volcanics older than the upper rhyolite-obsidian unit. The indurated and sandy matrix consists of quartz, feldspar, and many small lithic fragments. Pumice lapilli and shards are locally common, especially in the lower part.

Upper andesite unit

The andesite of Table Mountain of Krieger (1968b) and part of the upper andesite unit of Simons (1964), and possibly "basalt of Gila Conglomerate" of Willden (1964) that rests on the upper rhyolite-obsidian unit, are composed of dark-colored fine-grained amygdaloidal lavas, in which individual flows commonly have scoriaceous tops and flow breccia or agglomeratic bottoms. The andesite consists of small phenocrysts of plagioclase, red-altered olivine, and sparse clinopyroxene set in an intergranular groundmass of plagioclase microlites, and granules of clinopyroxene, olivine, and iron ores. Staining of the groundmass with sodium cobaltinitrite shows some potassium feldspar. Its chemical classification (table 2, No. 1) indicates it is either an andesite or olivine andesite (table 1).

CHEMISTRY

The chemical characteristics of the Galiuro Volcanics were obtained from 14 chemical and spectrographic analyses. Six of the analyses, from Simons (1964), were made to characterize the rocks in the Klondyke quadrangle. Four, from M. H. Krieger, were made to study the ash-flow tuffs. Four were made from samples used in this report, but only for dating purposes. The analyzed samples, therefore, are not a suite selected to represent the Galiuro Volcanics; rather, they are the available analyses most of which were made for other purposes. Nevertheless, they give considerable information about the chemical character of the rocks. Table 2 contains the 14 chemical and spectrographic analyses, as well as ionic percentages of the elements, catanorms, and differentiation indices (D.I.).

Numbers 11–14 (table 2) are from flows from the andesite-rhyodacite unit, and they probably represent the compositional range of the flows. Number 14 is a "turkey track" andesite and represents the most mafic of these lower flows. Number 13 is typical of the more common andesite flows and numbers 11 and 12 of the more silicic and alkalic flows. In consideration of the generation of the magmas responsible for the andesite-rhyodacite in the lower part of the Galiuro Volcanics, it is significant that the most mafic flow (No. 14) is at the top and the most salic (No. 11) is near the bottom. These relations imply more than one magma source, an implication supported by the intercalation of ash-flow tuffs in the lower flow unit. The only other analysis of a mafic flow is number 1 (discussed below), which is from andesite of Table Mountain. It is the most mafic rock analyzed, and it is at the very top of the volcanic pile. Number 9 is from an ash-flow tuff intercalated in the flows of the lower part of the Galiuro Volcanics, and number 10 is from a dike that cuts flows near the ash-flow tuff. The chemical analyses of the ash-flow tuff and the dike are like those for the Holy Joe Member.

The chemical composition of rhyolite-obsidian is represented by two analyses (Nos. 2 and 3). Both samples came from the upper rhyolite-obsidian unit. The Holy Joe and Aravaipa Members are ash-flow tuffs characterized by three (Nos. 6–8) and two (Nos. 4 and 5) analyses, respectively. All five analyses represent devitrified parts of the ash-flow tuff, which hydrate less than the glassy parts and are therefore closer to the composition at the time of eruption.

The abundance of calcium, sodium, potassium, magnesium, and ferrous iron relative to that of silicon are shown in figure 5. Calcium shows a reasonably inverse relation with silicon. A similar linear curve results when calcium is plotted against the D.I. Magnesium and, to some extent, ferrous iron also show an inverse relation to silicon, whereas potassium shows a direct relation, and sodium is nearly constant. These variation curves and the D.I. suggest a differentiating magma that produced early andesite and late rhyolite, but the elements do not vary systematically with stratigraphic position. The youngest rock in the volcanic pile has the lowest D.I. and the next to lowest silicon content. The rhyolite-obsidian, which is the most differentiated, occurs at two separate localities at different stratigraphic positions. Generally, however, the lower part of the Galiuro Volcanics is dominated by flows and contains the bulk of the andesite, and the upper part by ash-flow tuff and tuff. Probably there were two or more magma chambers in each of which differentiation occurred, and certainly there were several or many vent sites. From the similarities in geographic distribution, the Holy Joe and Aravaipa Members could have come from the same vent areas. The chemical analyses and the variation diagrams (table 2, fig. 5) show that the chemical compositions of the two ash-flows tuffs are distinctly different, those from the Aravaipa Member being significantly higher in silica and in D.I. If they came from the same magma chamber, differentiation was taking place.

The occurrence of the mafic andesite of Table Mountain at the top of the volcanic pile and of andesite intercalated in the predominantly ash-flow tuff parts of the volcanic pile suggests that within the limits of observation andesite was the parent magma and that periodically new andesitic magma was generated.

The tendency for the amounts of the individual elements to change systematically (smooth curves) on the silicon variation diagrams suggests that all of the

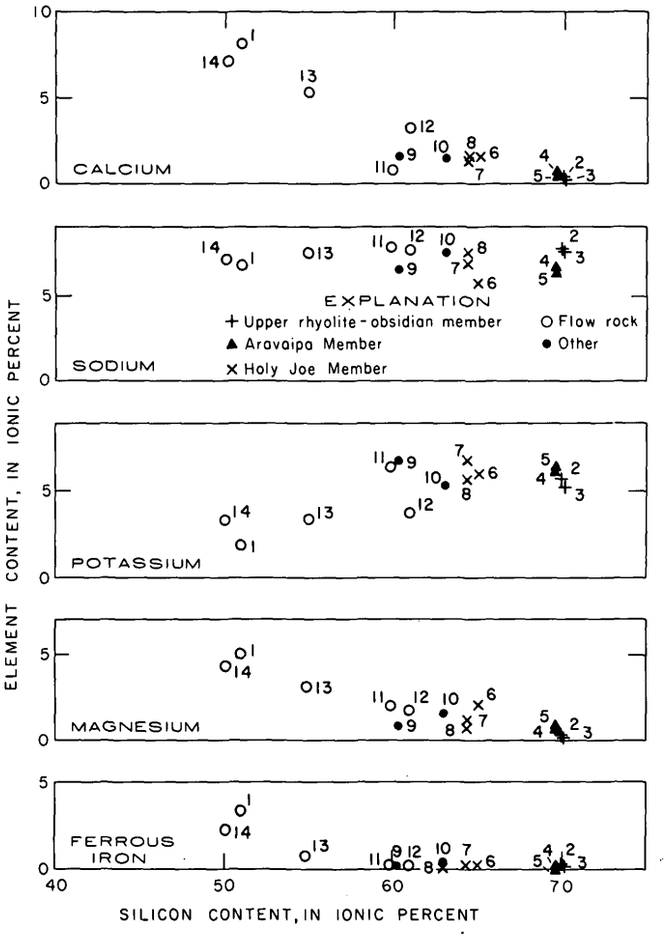

FIGURE 5.—Silicon variation curves for calcium, sodium, potassium, magnesium, and ferrous iron. Numbers refer to sample localities in figure 2.

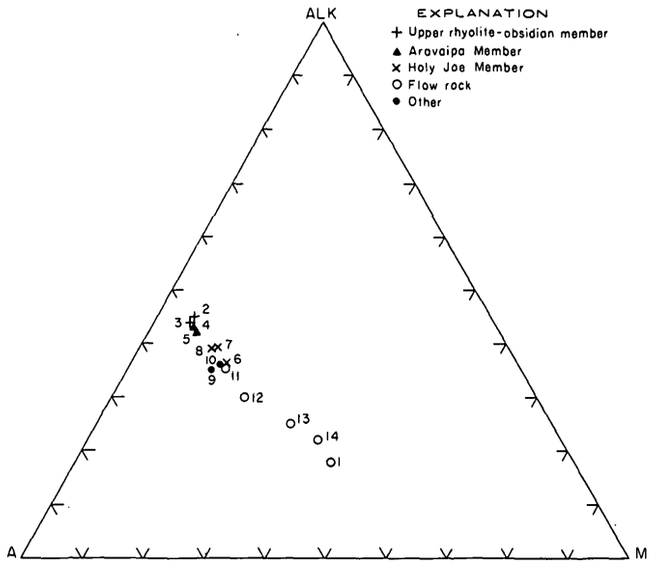

FIGURE 6.—Ternary Alk-A-M diagram for chemically analyzed samples of Galiuro Volcanics. Alk=Na+K, A=Al, M=Fe^{3+} +Fe^{2+}+Mg+Ca+Mn+Ni+Ba. Numbers refer to sample localities in figure 2.

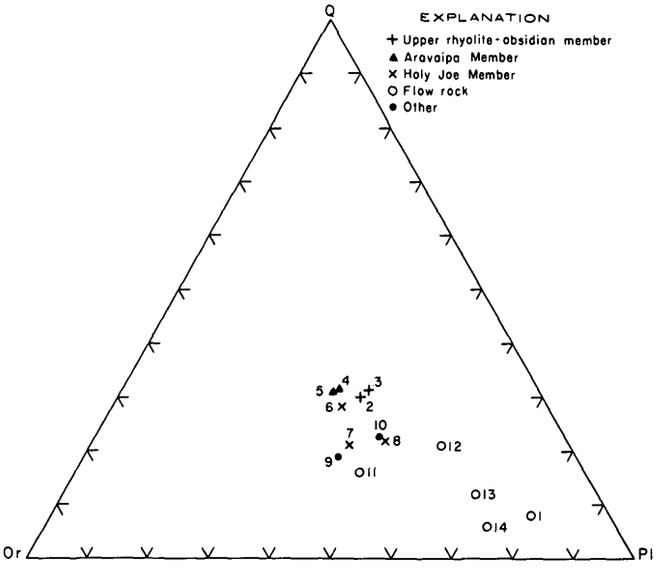

FIGURE 7.—Ternary Pl-Q-Or (plagioclase-quartz-orthoclase) diagram for chemically analyzed samples of Galiuro Volcanics. Numbers refer to sample localities in figure 2.

rocks in the Galiuro Volcanics are related and that the differences in composition probably represent different stages of differentiation for individual magma chambers. The suite of rocks is calc-alkaline, and all the rocks are somewhat high in alkalic elements.

The systematic relation of the elements in the volcanic rocks is indicated further by the Alk-A-M (sodium and potassium-aluminum-mafic elements) ternary diagram (fig. 6). Here the plots for the analyzed rocks aline remarkably well, showing a systematic variation in sodium and potassium (Alk), aluminum (A), and the "mafic" elements (M:Fe, Mg, Ca, Mn, Ni, and Ba). Plots of the molecular normative quartz (Q), orthoclase (Or), and plagioclase (Pl) (fig. 7) lie along a poorly defined differentiation trend line extending from the Pl corner to the center of the diagram, which is the approximate final composition of a granitic differentiate. Similar trend lines have been recorded for the Laramide stocks in Arizona, and it is believed to be characteristic of the granitic rocks in this region. Like the variation diagrams, figure 7 shows that the rhyolite-obsidian and the ash-flow tuff are the products of highly differentiated magmas.

AGE

The age of the Galiuro Volcanics generally ranges from about 23 to about 29 m.y. (Oligocene and Miocene) (fig. 8, table 3). In figure 8, they are arranged

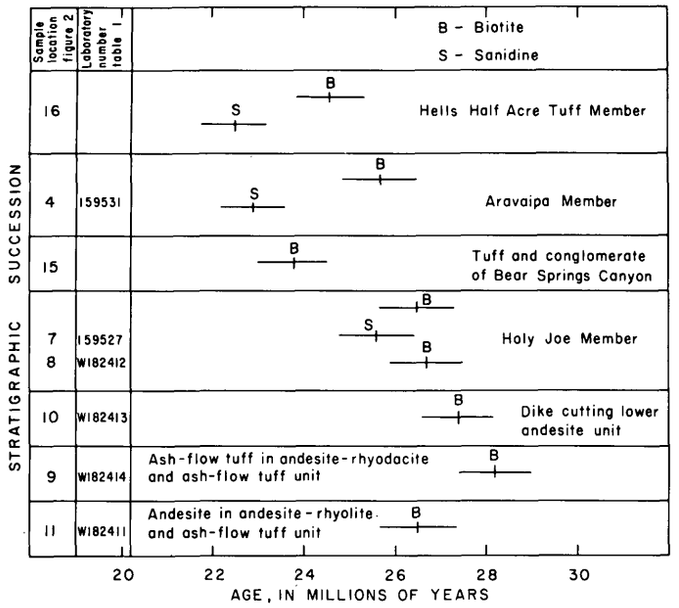

FIGURE 8.—Potassium-argon ages of the Galiuro Volcanics.

from top to bottom in the order of descending stratigraphic succession of the volcanics dated. The ages from about 24 to 28 m.y. are alined, and, if sanidine ages are accepted for the youngest ages, the linearity extends to 23 m.y. However, the two youngest biotite ages and the oldest age, which is also from biotite, each fall about 2 m.y. off the trend of the other ages. The discrepancies of these three ages are beyond the analytical uncertainty. To fix the age range more closely would require dating more samples, but because the approximate range from 23 to 29 m.y. is more than adequate to fit the Galiuro Volcanics into the mid-Tertiary volcanic and plutonic event in Arizona, there is no compelling geologic reason to do so.

Damon (1968) compiled a histogram of potassium-argon ages of volcanic and hypabyssal plutonic rocks younger than 90 m.y. in the Basin and Range province south of lat 36° N. His histogram is bimodal, one peak extending from 10 to 40 m.y., with a maximum at 25–30 m.y., and the other peak extending from 50 to 80 m.y., with a maximum of about 65 m.y. The age of the Galiuro Volcanics falls about in the middle of the younger igneous event.

In the Santa Catalina Mountains, which lie southwest of the Galiuro Mountains on the opposite side of the San Pedro valley (fig. 1), a mid-Tertiary quartz-monzonite composite batholith ranges in cooling age from 21 to 28 m.y. (Creasey and others, 1977). The chemical and normative composition of the batholith lies in the same range as the tuffs of the Holy Joe and Aravaipa Members. The combination of proximity, contemporaneity, and similar composition of the batholith and the Galiuro Volcanics indicates that both are part of the same igneous event and explains the general absence through uplift and erosion of the Galiuro Volcanics west of the San Pedro valley.

REFERENCES CITED

Blake, W. P., 1902, Geology of the Galiuro Mountains, Arizona, and of the gold-bearing ledge known as Gold Mountain: Eng. and Mining Jour., v. 73, p. 546–547.

Cooper, J. R., and Silver, L. T., 1964, Geology and ore deposits of the Dragoon quadrangle, Cochise County, Arizona: U.S. Geol. Survey Prof. Paper 416, 196 p.

Creasey, S. C., Banks, N. G., Ashley, R. P., and Theodore, T. G., 1977, Middle Tertiary plutonism in the Santa Catalina and Tortolita Mountains, Arizona: U.S. Geol. Survey Jour. Research, v. 5, no.6, p.705–717.

Creasey, S. C., Jackson, E. D., and Gulbrandsen, R. A., 1961, Reconnaissance geologic map of parts of the San Pedro and Aravaipa valleys, south-central Arizona: U.S. Geol. Survey Mineral Inv. Field Studies Map MF-238, scale 1:125 000.

TABLE 3.—*Analytical data for radiometric ages for the Galiuro Volcanics*

[$\lambda_\varepsilon = 0.585\times10^{-10}$/yr. $\lambda_\beta = 4.72\times10^{-10}$/yr. $K^{40}/K_{total} = 1.19\times10^{-4}$]

K-Ar lab no.	Sample loc. fig. 2	Mineral	K_2O (percent)	Ar^{40} (moles/g $\times10^{-10}$)	$Ar^{40}/\Sigma Ar^{40}$ (percent)	Age ($\times10^6$ years)
65I096	16	Biotite	8.82	3.233	63.3	24.6±0.7
65I094	16	Sanidine	6.66	2.230	89.4	22.5±0.7
KA418	4	Biotite	8.51	3.260	77.4	25.7±0.8
KA427	4	Sanidine	8.03	2.732	92.0	22.9±0.7
65I099	15	Biotite	8.47	3.000	62.0	23.8±0.7
KA154	7	do	8.14	3.212	74.5	26.5±0.8
65I095	7	Sanidine	8.68	3.305	97.1	25.6±0.8
75I316	8	Biotite	7.99, 8.00	3.178	87.2	26.7±0.8
75I310	10	do	8.42, 8.40	3.424	17.0	27.4±0.8
75I307	9	do	8.53, 8.58	3.590	81.3	28.2±0.8
75I314	11	do	8.45, 8.50	3.339	49.7	26.5±0.8

Creasey, S. C., Peterson, D. W. and Gambell, N. A., 1975, Preliminary geologic map of the Teapot Mountain quadrangle, Pinal County, Arizona: U.S. Geol. Survey Open-File Rept. 75–314.

Damon, P. E., 1968, Application of the potassium-argon method to the dating of igneous and metamorphic rock within the Basin Ranges of the southwest, *in* Southern Arizona Guidebook 3—Geol. Soc. America, Cordilleran Sec., 64th Ann. Mtg., Tucson. 1968: Tucson, Ariz., Arizona Geol. Soc., p. 7–20.

Damon, P. E., and Bikerman, Michael, 1964, Potassium-argon dating of post-Laramide plutonic and volcanic rocks within the Bason and Range province of southeastern Arizona and adjacent areas: Arizona Geol. Soc. Digest, v. 7, p. 63–78.

Darton, N. H., 1925, A resume of Arizona geology: Arizona Bur. Mines, Bull. 119, 298 p.

Drewes, Harald, 1971a, Geologic map of the Sahuarita quadrangle, southeast of Tucson, Pima County, Arizona: U.S. Geol. Survey Misc. Inv. Map I–613, scale 1:48 000.

———1971b, Geologic map of the Mount Wrightson quadrangle, southeast of Tucson, Santa Cruz, and Pima Counties, Arizona.: U.S. Geol. Survey Misc. Geol. Inv. Map I–614, scale 1:48 000.

Irving, T. N., and Barager, W. R., 1971, A guide to the chemical classification of the common volcanic rocks: Canadian Jour. Earth Sci., v. 8, p. 523–548.

Krieger, M. H., 1968a, Geologic map of the Brandenburg Mountain quadrangle, Pinal County, Arizona: U.S. Geol. Survey Quad. Map GQ–668, scale 1:24 000.

———1968b, Geologic map of the Holy Joe Peak quadrangle, Pinal County, Arizona: U.S. Geol. Survey Geol. Quad. Map GQ–669, scale 1:24 000.

———1968c, Geologic map of the Lookout Mountain quadrangle, Pinal County, Arizona: U.S. Geol. Survey Geol. Quad. Map GQ–670, scale 1:24 000.

———1968d, Geologic map of the Saddle Mountain quadrangle, Pinal County, Arizona: U.S. Geol. Survey Geol. Quad. Map GQ–671, scale 1:24 000.

O'Connor, J. T., 1965, A classification for quartz-rich igneous rocks based on feldspar ratios, *in* Geological Survey Research 1965: U.S. Geol. Survey Prof. Paper 525–B, p. B79–B84.

Peck, L. C., 1964, Systematic analysis of silicates: U.S. Geol. Survey Bull. 1170, 89 p.

Peterson, D. W., 1961, Descriptive modal classification of igneous rocks, AGI Data Sheet 23: Geotimes, v. 5, no. 6, p. 30–36.

———1969, Geologic map of the Superior quadrangle, Pinal County, Arizona: U.S. Geol. Survey Geol. Quad. Map GQ–818, scale 1:24 000.

Peterson, N. P., 1938, Geology and ore deposits of the Mammoth mining camp area, Pinal County, Arizona: Arizona Bur. Mines Bull. 144, Geol. ser. 11, 63 p.

Rittmann, A., 1952, Nomenclature of volcanic rocks: Bull. Volcanol., ser. 2, v. 12, p. 75–102.

Shapiro, Leonard, 1967, Rapid analyses of rocks and minerals by a single-solution method, *in* Geological Survey research 1967: U.S. Geol. Survey Prof. Paper 575–B, p. B187–B191.

Shapiro, Leonard, and Brannock, W. W., 1962, Rapid analysis of silicate, carbonate, and phosphate rocks: U.S. Geol. Bull. 1144–A, 56 p.

Simons, F. S., 1964, Geology of the Klondyke quadrangle, Graham and Pinal Counties, Arizona: U.S. Geol. Survey Prof. Paper 461, 173 p.

———1974, Geologic map and sections of the Nogales and Lochiel quadrangles, Santa Cruz County, Arizona: U.S. Geol. Survey Mineral Inv. Field Studies Map I–762, scale 1:48 000.

Willden, Ronald, 1964, Geology of the Christmas quadrangle, Gila and Pinal Counties, Arizona: U.S. Survey Bull. 1161–E, 64 p.

Jour. Research U.S. Geol. Survey
Vol. 6, No. 1, Jan.–Feb. 1978, p. 133–147

PLEISTOCENE RHYOLITE OF THE MINERAL MOUNTAINS, UTAH–GEOTHERMAL AND ARCHEOLOGICAL SIGNIFICANCE

By P. W. LIPMAN; P. D. ROWLEY, H. H. MEHNERT;
S. H. EVANS, Jr., W. P. NASH, and F. H. BROWN;[1]
Hawaiian Volcano Observatory, Hawaii; Denver, Colo.; and Salt Lake City, Utah
With sections by G. A. IZETT and C. W. NAESER
and by IRVING FRIEDMAN, Denver, Colo.

Abstract.—Little-eroded rhyolitic tuffs, flows, and domes extend over about 25 km² along the western side of the Mineral Mountains, southwestern Utah, which is along the eastern edge of the Roosevelt KGRA (Known Geothermal Resource Area). Initial eruptions resulted in two low-viscosity lava flows of nonporphyritic rhyolite. These were followed by bedded pumice falls and nonwelded ash flows. The youngest activity produced at least nine viscous domes and small lava flows of rhyolite that contain 1–5 percent phenocrysts of quartz, plagioclase, sodic sanidine, and biotite; distinction between domes and eroded flow segments locally is difficult.

Potassium-argon ages indicate that all the rhyolite of the Mineral Mountains was erupted between 0.8 and 0.5 m.y. ago. The rhyolite rests on dissected granite of the Mineral Mountains pluton, the largest intrusion in Utah, which has yielded published K-Ar ages of 9 and 15 m.y. A small older dissected rhyolite dome, about 8 m.y. old, occurs just west of the range front. Whether the young ages of the pluton represent time of intrusion or of later reheating, they, in conjunction with the Pleistocene rhyolite in the Mineral Mountains, do indicate a major late Cenozoic thermal anomaly, the size and age of which is significant to evaluation of the Roosevelt KGRA. The rhyolite is also the only known source of implement-grade obsidian in the southwest between eastern California and northern New Mexico.

As part of the U.S. Geological Survey's geothermal energy program, age, composition, and distribution data are being obtained for upper Cenozoic volcanoes in the western United States that have erupted significant amounts of silicic rocks. Such silicic rocks, mostly rhyolites, are considered possible indicators of the subsurface presence of shallow magma chambers still sufficiently hot to have potential for geothermal resources. A rationale for this approach is outlined by Smith and Shaw (1975).

Large volumes of rhyolite associated with known geothermal resources have been described from Yellowstone National Park (Allen and Day, 1935; Christiansen and Blank, 1972), in the Jemez Mountains in New Mexico (Smith, Bailey, and Ross, 1970), and in the Long Valley area, California (Bailey, Dalrymple, and Lanphere, 1976). Around the margins of the Colorado Plateau, small volumes of similar silicic rocks that also seem worthy of reconnaissance evaluation in terms of geothermal signifiance occur in the San Francisco Mountains volcanic field, Arizona (Robinson, 1913; Moore, Wolfe, and Ulrich, 1974), in the Mount Taylor and Taos Plateau volcanic fields of New Mexico (Hunt, 1938; Lambert, 1966), and in the Mineral Mountains, Utah.

In the Mineral Mountains, southwestern Utah, young rhyolite masses extend discontinuously for about 15 km along the range crest and cover an area of less than 25 km²; these have been little studied and previously were interpreted as erosional remnants of a single large silicic volcano of late Tertiary age (Earll, 1957; Liese, 1957). This brief report presents new geologic data, including K-Ar ages which demonstrate that many separate lava domes, flows, and tuffs were erupted from vents along the range crest between 0.8 and 0.5 m.y. ago. Along one of the western range-front faults, about 2 km northwest of the nearest rhyolitic volcanic rocks, Roosevelt Hot Springs is located within a KGRA (Known Geothermal Resource Area) that is actively being developed for geothermal power production. The youthful silicic volcanism recorded by the rhyolite of the Mineral Mountains suggests the presence of a still-hot buried magma chamber that may be the heat source for the KGRA.

Acknowledgments.—Discussions with Glenn A. Izett and Irving Friedman, who examined the rhyolites, and Sr-Rb data on granite from the Mineral Mountains pluton by Carl E. Hedge aided the evolution of ideas on the rhyolite of the Mineral Mountains. We thank John S. Pallister and Alan Martz for assistance

[1] Department of Geology and Geophysics, University of Utah.

in the field and for making mineral separations for K-Ar dating and microprobe analyses, respectively. We also thank Gary L. Galyardt for information on the Roosevelt KGRA.

Research by authors from the University of Utah was supported by National Science Foundation Grant GI-43741 and U.S. Energy Research and Development Administration Contract no. EY-76-S-07-1601.

GENERAL GEOLOGIC SETTING

The Mineral Mountains, in west-central Utah (fig. 1), are a typical basin-range horst, which rises about 1 km above the adjacent alluviated basins, the Escalante Desert to the west and an unnamed valley to the east. The horst extends nearly 50 km in a northerly direction and is in general about 10 km wide.

On the western and northern sides of the range, metamorphic rocks of the Wildhorse Canyon Series of Condie (1960), of probable Precambrian age, are the dominant rocks, but on the southern, northern, and eastern sides of the range, Paleozoic and Mesozoic sedimentary rocks are exposed widely. These layered rocks are intruded by a distinctive body of granite, the Mineral Mountains pluton, which is the largest single exposed intrusive body in Utah, covering nearly 250 km^2. This granite and associated pegmatite and aplite may be as young as late Miocene, having yielded two K-Ar ages on feldspars of 15 and 9 m.y. from different sample sites (Park, 1968; Armstrong, 1970). These young apparent ages are supported in a general way by results of a Rb-Sr isotopic study. A Rb-Sr isochron, based on 11 analyses of whole-rock samples ranging in composition from diorite to aplite, shows exceptionally bad scatter but suggests that the age of the main batholith is about 35 m.y., with sizable chemical modification—especially Sr loss—having occurred 7–15 m.y. ago (C. E. Hedge, written commun., 1976).

Prior to the onset of late Cenozoic rhyolitic volcanism in the Mineral Mountains, the Mineral Mountains pluton and its country rocks were deeply dissected to form a rugged erosional topography with towering pinnacles rising above narrow usually dry valleys.

The Mineral Mountains are bounded on the west, and probably on the east side, by north-striking normal faults. The trend of the bounding faults on the west is marked locally in the Roosevelt KGRA by discontinuous elongate mounds of opaline sinter and other hot-spring deposits. Near the northern end of this trend is Roosevelt Hot Springs (Petersen, 1975). Water temperatures as high as 90°C have been recorded from Roosevelt Hot Springs, but sometime prior to 1966 the springs dried up (Mundorff, 1970). Phillips Petroleum Co., the successful bidder on the KGRA in 1974, is continuing exploration on the property. Numerous test wells so far drilled in the KGRA have documented the presence of a low-salinity liquid-dominated geothermal system (Berge, Crosby, and Lenzer, 1976; Greider, 1976). The thermal anomaly covers approximately 32 km^2, and reservoir temperatures exceed 250°C.

RHYOLITE OF THE MINERAL MOUNTAINS

Rhyolitic rocks in the Mineral Mountains include three stratigraphically distinct sequences. Lowermost are two nearly nonporphyritic obsidian-rich lava flows. These are overlain by a pyroclastic sequence, including both ash-fall and ash-flow tuffs. Stratigraphically highest are porphyritic rhyolite lava domes erupted from at least nine separate vents, most of which are along the range crest.

Flows of Bailey Ridge and Wildhorse Canyon

The oldest rhyolitic rocks in the Mineral Mountains are two lava flows of virtually nonporphyritic flow-layered rhyolite. One flow is exposed for about 3 km along Bailey Ridge and in Negro Mag Wash (fig. 2) northwest of Bearskin Mountain. The other is exposed for about 3.5 km along Wildhorse Canyon, west of Bearskin Mountain. Both flows were originally as much as 100 m thick and followed pre-existing valleys that drained the western side of the Mineral Mountains, with relief much like the present, and that were graded nearly to the present levels at valley fronts. Both flows are only slightly dissected, and much of their primary upper surfaces of frothy pumiceous perlitic rubble is preserved.

Where deeply dissected, both flows display similar cooling and crystallization zonations. The basal few meters of the flow, resting directly on medium- to coarse-grained Tertiary granite of the Mineral Mountains pluton, consists of dense black obsidian. The obsidian has well-developed flow lamination defined by alined microlites of feldspars and opaque oxides (fig. 3*A*). The basal obsidian zone grades upward within a meter or two into a well-layered zone, in which dark obsidian and light-gray or brown finely crystallized flow-layered lava alternate. The interior of the flow is as much as 10–30 m thick and consists of gray relatively structureless devitrified rhyolite, in places containing concentrations of ovoid gas cavities locally filled with vapor-phase crystallization products.

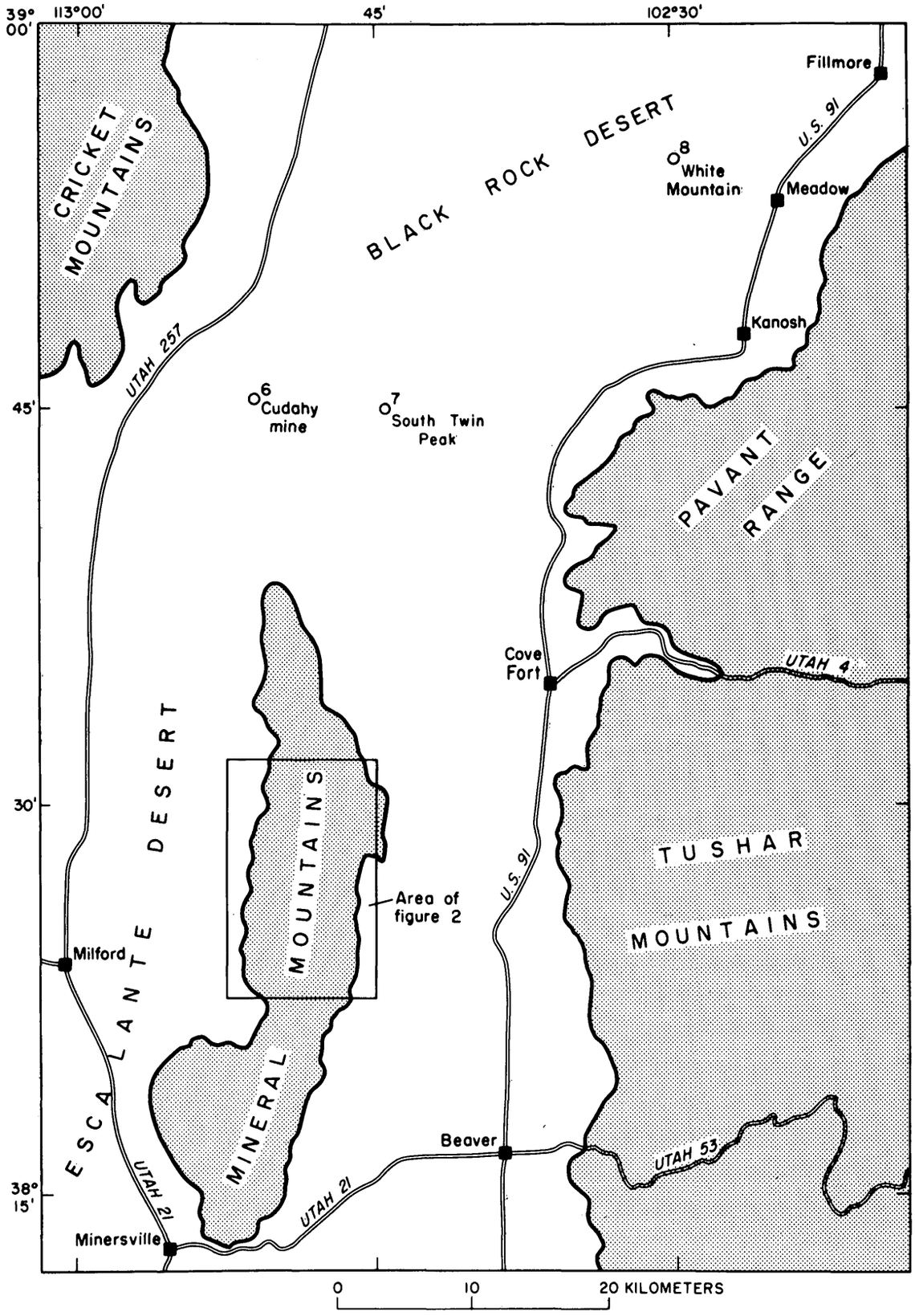

FIGURE 1.—Index map showing location of the Mineral Mountains and nearby areas, Utah. Numbers indicate locations of some dated samples (table 3); the others are shown on figure 2.

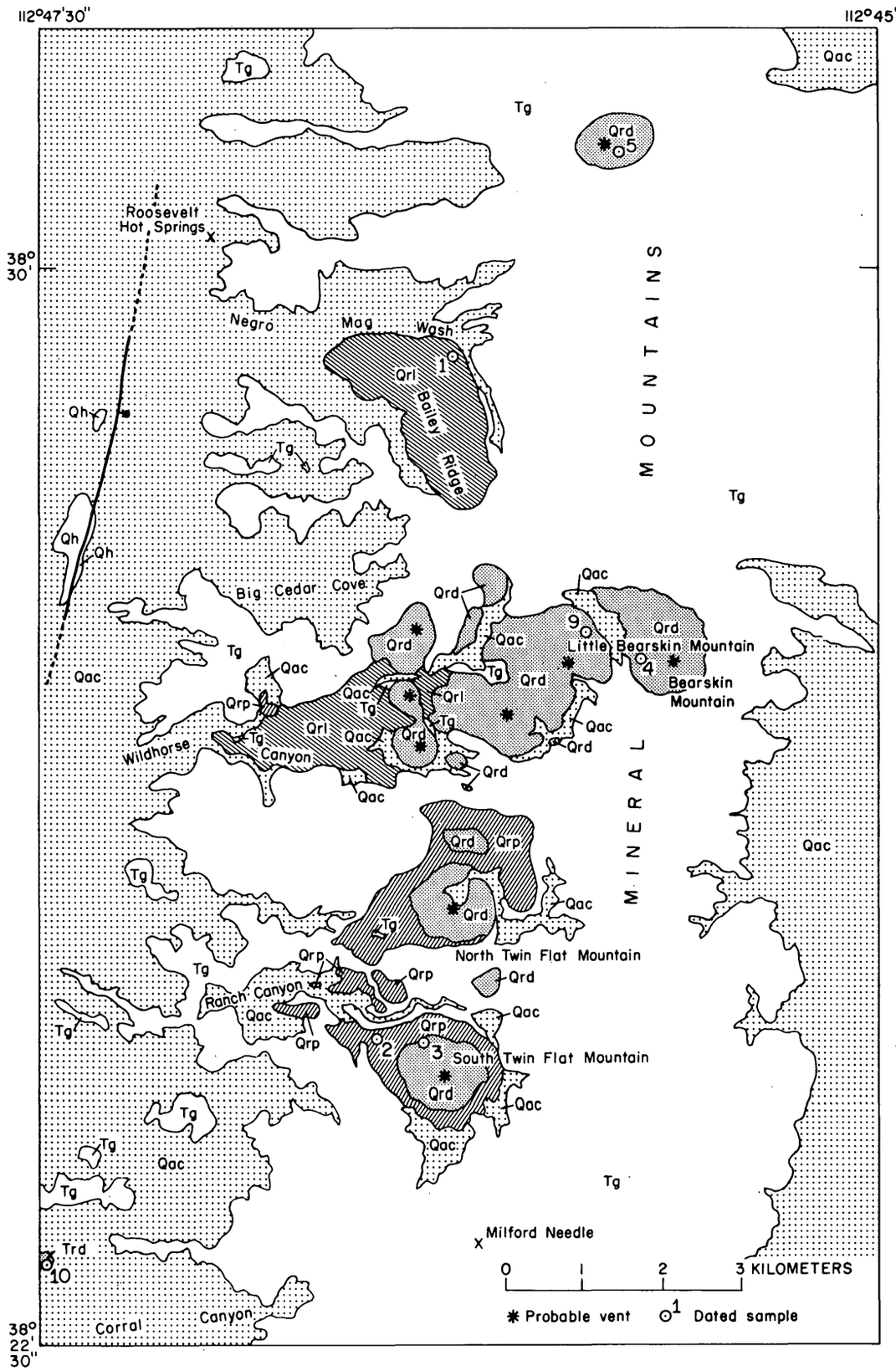

FIGURE 2.—Generalized geologic map of the central Mineral Mountains, Utah, showing distribution of Pleistocene rhyolitic rocks and locations of dated samples (table 3). Rock units, from oldest to youngest: **Tg**, Tertiary granite of Mineral Mountains; **Trd**, Tertiary rhyolite dome of Corral Canyon; **Qrl**, lava flows of Bailey Ridge and Wildhorse Canyon; **Qrp**, pyroclastic rocks; **Qrd**, lava domes; **Qac**, surficial deposits, primarily alluvium and colluvium; **Qh**, hot-spring deposits. Fault shown (bar and ball on downthrown side), named the Dome fault by Petersen (1975), is only one of many along the western range front.

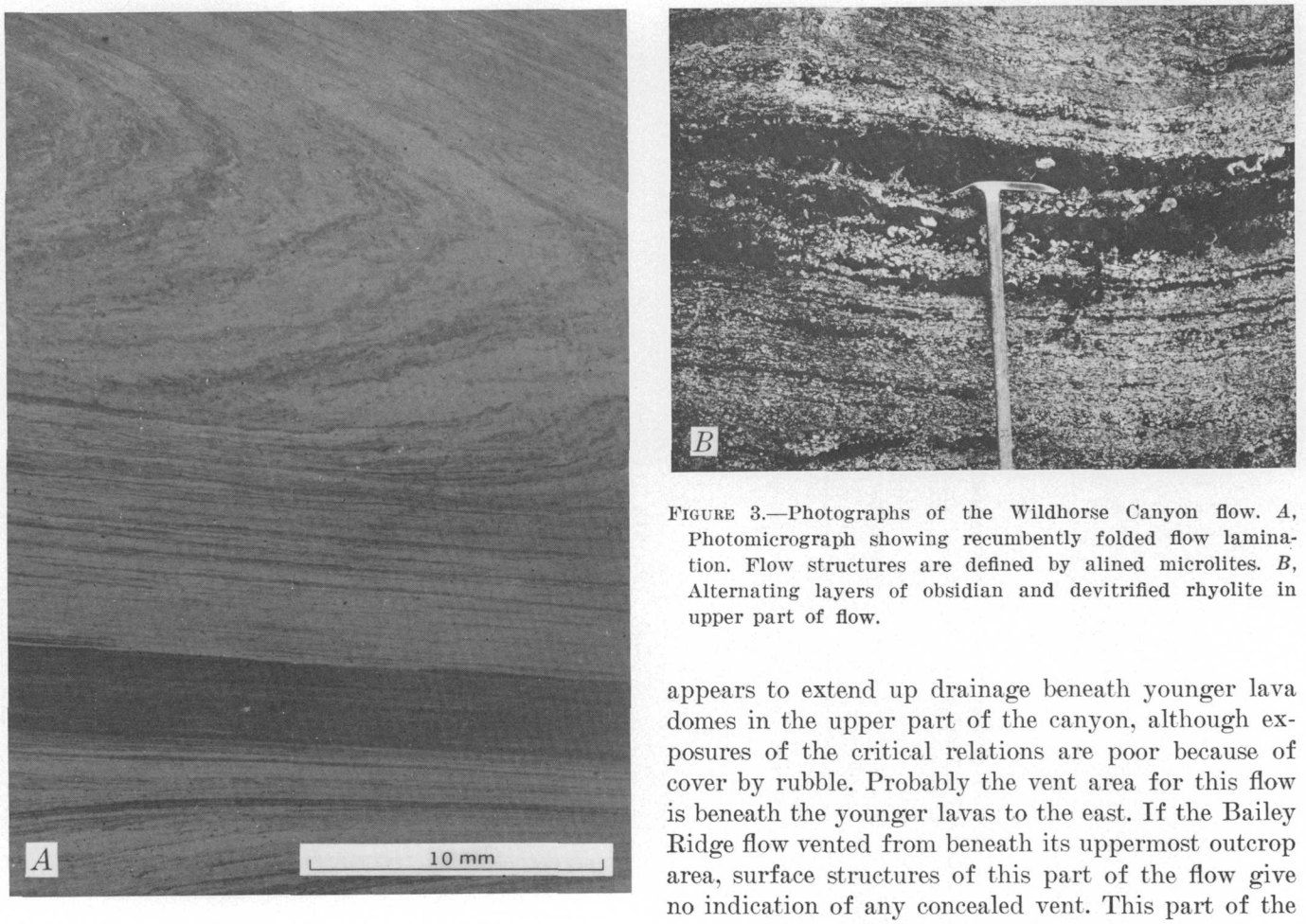

FIGURE 3.—Photographs of the Wildhorse Canyon flow. *A*, Photomicrograph showing recumbently folded flow lamination. Flow structures are defined by alined microlites. *B*, Alternating layers of obsidian and devitrified rhyolite in upper part of flow.

In upper parts of the flow a few meters of flow-layered obsidian are interlayered with devitrified rock (fig. 3*B*), passing upward into a more uniform dark glass zone or grading directly into a frothy rubbly breccia of tan perlitic pumice as much as 10 m thick at the top of the flow.

The flow layering and lamination in these rhyolitic lavas is remarkably planar and uncontorted as compared to the swirly internal structures typical of many rhyolitic lava flows. The "ramp structures" that occur commonly in upper parts of silicic flows (Christiansen and Lipman, 1966), are absent or poorly developed, and subhorizontal layering is typical throughout the Bailey Ridge and Wildhorse Canyon flows. The most common deviations from planar layering are small, typically rootless recumbent folds (fig. 3*A*), most limbs of which are less than 1 m long. These flowage features, as well as the relatively slight thickness of each lava flow as compared to its longitudinal extent, indicate that they were characterized by lower emplacement viscosities than many silicic lava flows.

Vents for these oldest flows of the Mineral Mountains have not been found. The Wildhorse Canyon flow appears to extend up drainage beneath younger lava domes in the upper part of the canyon, although exposures of the critical relations are poor because of cover by rubble. Probably the vent area for this flow is beneath the younger lavas to the east. If the Bailey Ridge flow vented from beneath its uppermost outcrop area, surface structures of this part of the flow give no indication of any concealed vent. This part of the flow is little dissected, however, and the vent area could be completely buried. Alternatively, the Bailey Ridge flow, and also the Wildhorse Canyon flow, might have come from higher on the slope, underneath the area now covered by the Bearskin and Little Bearskin Mountain lava domes. However, this would require that the upper portions of the flows be largely removed by erosion while the lower portions were left relatively undissected.

The Bailey Ridge and Wildhorse Canyon flows are petrographically similar. They contain less than 0.5 percent total phenocrysts, the majority of which are alkali feldspar (table 1). There are trace amounts of oligoclase, biotite, titanomagnetite, and ilmenite. The two flows are virtually identical in chemical composition (table 2). They are typical silicic rhyolites, containing about 76.5 percent SiO_2 and just over 9 percent total alkalis. The fresh obsidians contain more fluorine than water; secondarily hydrated pumice from the Bailey Ridge flow contains 2.4 percent total H_2O. The magmatic temperatures of these flows were about 750°C, as determined from compositions of iron-titanium oxides and coexisting plagioclase and alkali

TABLE 1.—*Modal compositions of radiometrically dated samples*
[Est., estimate; tr., trace; leaders (--), not present; *, microphenocrysts]

Field No.	Unit	Ground-mass	Plagio-clase	K-feldspar	Quartz	Biotite	Horn-blende	Clino-pyroxene	Opaques	Points counted
75L-17	Bailey Ridge flow, obsidian	99.9	--	tr.	tr.	--	--	--	--	Est.
75L-15	Tuff of Ranch Canyon obsidian block	98.2	0.6	0.8	0.4	tr.	--	--	tr.	3,615
75L-16	South Twin Flat Mountain dome, obsidian with patchy devitrification	92.6	1.2	3.9	2.3	tr.	--	--	tr.	3,034
75L-56	Bearskin Mountain, obsidian	97.2	.3	1.2	1.2	0.1	--	--	tr.	4,725
75R-53	Little Bearskin Mountain dome, obsidian	96.0	.9	1.9	1.0	--	--	--	0.1	2,000
75L-18A	Northern dome, frothy perlite	97.4	.4	1.3	.7	.1	--	--	.1	2,642
75L-19	Rhyolite of the Cudahy mine, obsidian	100	--	--	--	--	--	--	--	Est.
75L-21	Black Rock desert felsite plug	91.2	5.8	1.2	--	tr.	--	1.2	.6	3,188
75L-23	Rhyolite of White Mountain, obsidian	94	--	--	--	--	*6	--	--	Est.

TABLE 2.—*Chemical analyses and CIPW norms of rhyolites of the Mineral Mountains*

[Analyses by S. H. Evans, Jr., by standard wet chemical techniques. Key to analyses; 74-3A, Obsidian, Bailey Ridge flow; 74-8, Obsidian, Wildhorse Canyon flow; 75-14, Obsidian, Little Bearskin Mountain dome; 75-20, Basal Obsidian, North Twin Flat Mountain dome. Leaders (---) not present; tr., trace]

	Chemical Analyses					CIPW Norms			
	74-3A	74-8	75-14	75-20		74-3A	74-8	75-14	75-20
SiO_2	76.52	76.51	76.42	76.45	Q	33.40	33.28	33.22	32.48
TiO_2	.12	.12	.08	.08	c	---	.26	.41	.45
Al_2O_3	12.29	12.29	12.79	12.79	or	30.96	31.20	27.89	27.95
Fe_2O_3	.31	.23	.20	.30	ab	32.15	31.90	37.40	37.15
FeO	.46	.51	.38	.29	an	1.00	1.02	---	---
MnO	.05	.05	.09	.10	di-wo	.37	.47	---	---
MgO	.08	.08	.11	.12	di-en	.11	.12	---	---
CaO	.64	.65	.44	.40	di-fs	.27	.38	---	---
Na_2O	3.80	3.77	4.42	4.39	hy-en	.09	.08	.27	.30
K_2O	5.24	5.28	4.72	4.73	hy-fs	.21	.26	.57	.34
P_2O_5	.02	.01	tr.	.06	mt	.45	.33	.29	.43
H_2O+	.12	.06	.13	.10	il	.23	.23	.15	.15
H_2O-	.06	.06	.01	---	ap	.05	.02	---	.14
F	.16	.15	.42	.44	fr	.33	.29	.61	.45
Sum	99.87	99.77	100.21	100.25	rest	.18	.12	.14	.10
Less F=O	.07	.06	.18	.19	Total	99.80	99.96	99.95	99.94
Total	99.80	99.71	100.03	100.06					

feldspar. The relatively low emplacement viscosities, indicated by the planar flow structures of these rhyolites, do not therefore seem related to exceptionally high emplacement temperatures.

A single K-Ar radiometric age determination of 0.79±0.08 m.y. (table 3, no. 1), from the toe of the Bailey Ridge flow, is the oldest age obtained from any rhyolite of the Mineral Mountains. The Bailey Ridge flow has a reversed paleomagnetic pole position (table 4) indicating, in conjunction with K-Ar data, that it was erupted toward the end of the Matuyama polarity epoch. The Wildhorse Canyon flow has not yet been dated radiometrically, but it also is characterized by a reversed polarity, which, in conjunction with morphological and chemical resemblance to the Bailey Ridge flow and its position beneath some of the pyroclastic rocks, suggests a similar age.

Pyroclastic rocks

South of Wildhorse Canyon, pyroclastic rocks of ash-fall and ash-flow origin are the lowest exposed rhyolitic rocks. The main area of pyroclastic rocks is in Ranch Canyon, where tuffs bury rugged paleotopography much like the present land surface.

The pyroclastic rocks are only weakly consolidated and are mostly poorly exposed, underlying alluviated slopes. All the pyroclastic deposits, both ash-fall and and ash-flow, are white to light tan. They occur over an altitude range from 1950 m in valley-bottom exposures in Ranch Canyon to as high as 2540 m on the surrounding slopes. They also occur in the Cove Fort area, where they are overlain by basalt lava flows (Nash and Smith, 1977). Much of the pyroclastic sequence has been removed by erosion in Ranch Canyon, and it is not clear to what extent this altitude range reflects an actual total thickness of the original deposit and to what extent the pyroclastic rocks were thinner but blanketed the preexisting topography. In Ranch Canyon these rocks are overlain by the large lava domes on North and South Twin Flat Mountains and by smaller masses of rhyolitic lava on adjacent ridges. Although contacts between these domes and the pyroclastic rocks are nowhere well exposed, this stratigraphic sequence is indicated by structural zones in the rhyolite domes of North and South Twin Flat Mountains. The lowest exposures are of a subhorizontal

TABLE 3.—K-Ar *age determinations on upper Cenozoic rhyolites of the Mineral Mountains, Utah, and adjacent areas*

[Constants: $K^{40}\lambda_\varepsilon = 0.581 \times 10^{-10}$/yr, $\lambda_\beta = 4.963 \times 10^{-10}$/yr; atomic abundance: $K^{40}/K = 1.167 \times 10^{-4}$; *Radiogenic argon; Potassium determinations made with an Instrumentation Laboratories flame photometer with a Li internal standard. Figures 1 and 2 give sample locations. Ages of WM76-3 and MR76-26 determined by S. H. Evans, Jr., and F. H. Brown; other ages determined by H. H. Mehnert]

Sample	Field No.	Unit	Material dated	Location (Lat N Long W)	K_2O (percent)	$*Ar^{40}$ (10^{-10}) (moles/gram)	$*Ar^{40}$ (percent)	Age (m.y.±2σ)
1	75L-17	Bailey Ridge flow-------	Obsidian--------	38°29′, 112°49′	5.10, 5.10	0.058	25.8	0.79±0.08
2	75L-15	Tuff of Ranch Canyon----	Obsidian block--	38°25′, 112°50′	4.63, 4.66	.047	47.1	0.70±0.04
3	75L-16	South Twin Flat Mountain dome---------	Sanidine--------	38°25′, 112°49′	8.14, 8.08	.059	18.1	0.50±0.07
4	75L-56	Bearskin Mountain dome--	Obsidian--------	38°27′, 112°47′	4.48, 4.49	.048	20.2	0.75±0.10
						.039	13.5	0.60±0.12
5	75L-18A	North Dome----------	Sanidine--------	38°31′, 112°47′	9.36, 9.35	.073	24.5	0.54±0.06
6	75L-19	Cudahy mine----------	Obsidian--------	38°45′, 112°51′	4.91, 4.93	.168	46.0	2.38±0.15
7	75L-21	South Twin Peak---------	Sanidine--------	38°45′, 112°47′	11.13, 11.12	.373	54.3	2.33±0.12
8	75L-23	White Mountain----------	Obsidian--------	38°55′, 112°30′	4.63, 4.70	.029	15.9	0.43±0.07
	WM76-3		Obsidian--------		5.23, 5.25	.030	21.5	0.39±0.02
9	75R-23	Little Bearskin Mountain dome---------	Sanidine--------	38°27′, 112°48′	9.31, 9.15 [1]9.26	.080	31.8	0.61±0.05
10	MR76-26	Corral Canyon dome------	Biotite---------	38°24′, 112°53′	8.72, 8.75	1.011	61.6	7.90±0.30

[1]Isotope dilution determination

TABLE 4.—*Preliminary data on magnetic polarities of rhyolites of the Mineral Mountains*

Unit	Number of samples	Declination	Inclination	Standard error (percent)
Normal samples:				
Northern dome----------	9	350	62	3
Big Cedar Cove dome------	4	23	67	4
Ranch Canyon dome--------	5	22	44	5
Corral Canyon dome-------	3	332	25	20
Ranch Canyon ash---------	2	356	46	29
Wildhorse Canyon ash-----	6	349	48	5
Reversed samples:				
Bailey Ridge flow--------	6	173	-63	6
Wildhorse Canyon flow----	4	168	-61	2

zone of basal flow breccia below the basal obsidian zone; this is the typical zonation expectable at the base of a lava flow or dome and would be an improbable relation if the pyroclastic rocks had been plastered against older lava domes. Thus, the lava dome of South Twin Flat Mountain overlies pyroclastic rocks that are at least 60 m and probably as much as 180 m thick, and these figures suggest minimum thicknesses of the pyroclastic unit.

The lower pyroclastic rocks are beds of air-fall pumice and ash at least 10 m thick and probably much thicker. Individual beds are a few centimeters to about a meter thick. Variable dips indicate that the ash was deposited on the underlying granite, on a surface as rugged as the present one. The pumice and ash contain several percent of small phenocrysts of quartz, oligoclase, alkali feldspar, biotite, magnetite, ilmenite, sphene, and allanite. This mineral assemblage is generally characteristic of the youngest rhyolite flows as well. Associated with the pumice and ash are a few percent of rhyolitic lithic debris, including devitrified rhyolite, perlite, and sparse obsidian fragments. Phenocrysts in the lithic debris are sparse, generally similar to those in the flows of Bailey Ridge and Wildhorse Canyon.

Ash-flow deposits widely overlie the ash-fall beds in Ranch Canyon. The ash-flow deposits locally are at least 50 m thick; probably the total thickness is much greater, but accurate estimates are difficult because of the poor exposures. The ash-flow deposits are everywhere nonwelded and only weakly consolidated; they tend to weather to small conical hills. On especially

steep slopes the ash-flow deposits rest directly against granite, with no intervening ash-fall material (fig. 4). In exceptionally good exposures, several flow units —each a few meters thick—can be recognized in the ash-flow deposits, with partings between the flow units marked by local concentrations of pumice, lithic debris, or better sorted ash.

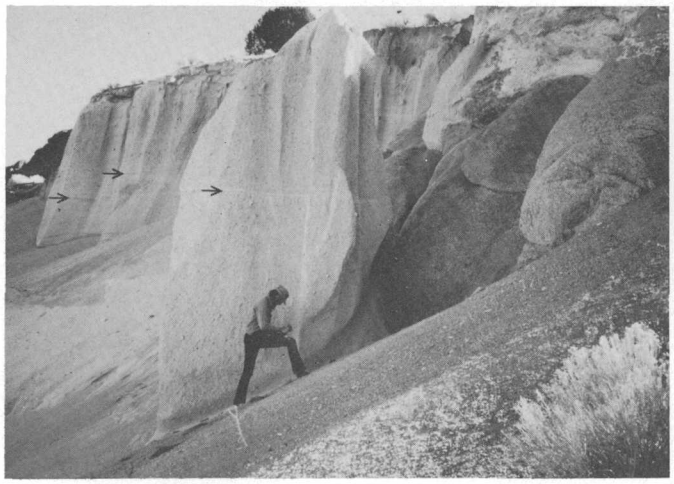

FIGURE 4.—Ash-flow tuff, resting on a rugged erosion surface cut on granite of the Mineral Mountains pluton. Arrows indicate faint parting between flow units of tuff. From northern side of Ranch Canyon at about 2105-m elevation.

On the northern side of lower Wildhorse Canyon, an isolated patch of pyroclastic material about 150 m across consists of finely laminated white fine-grained ash of lacustrine origin. These beds of water-reworked ash are younger than the Wildhorse Canyon flow and were deposited in a local basin dammed by the flow. The ash has a refractive index similar to that of the pyroclastic rocks in Ranch Canyon, one valley to the south, suggesting to us that it represents a reworked marginal facies of this deposit. In contrast, this patch of lacustrine tuff is interpreted by Glenn Izett (written commun., 1976) as airborne Bishop ash, from the Long Valley caldera in California, on the basis of small compositional differences with other rhyolites of the Mineral Mountains.

A single whole-rock K-Ar age on an obsidian clast from ash-flow tuff in Ranch Canyon yielded an age of 0.70 ± 0.04 m.y. (table 3, no. 2), providing an older limit for the age of the pyroclastic rocks. The pyroclastic deposits in Ranch Canyon, as well as the local lake beds in Wildhorse Canyon. have normal magnetic polarities in contrast to the reverse polarities of Bailey Ridge and Wildhorse Canyon flows. Thus, the pyroclastic rocks have been deposited during the Brunhes polarity epoch.

Porphyritic lava domes

The stratigraphically highest part of the upper Cenozoic volcanic assemblage in the Mineral Mountains is a group of at least nine separate perlite-mantled lava domes and small flows of porphyritic rhyolite. The domes tend to occur along the crest of the range, discontinuously over a zone about 15 km long. These domes form some of the highest topographic points in the Mineral Mountains, including Bearskin Mountain with an elevation of 2772 m (9095 ft). Individual domes are as much as 1 km across at their bases and stand as much as 250 m high, although dimensions are difficult to determine precisely because of the irregular pre-existing topography and subsequent erosion. Small stubby flows extend out from some of the domes, and some small isolated patches of rhyolite (fig. 2) may represent either eroded flow remnants or small separate domes.

The larger domes, such as Bearskin and Little Bearskin Mountains, are little eroded, and surface exposures consist largely of blocks of tan perlitic glass that are slightly modified remnants of the original brecciated frothy carapaces of the domes. Scattered fragments of dense black obsidian, derived from beneath the perlitic breccia, occur about a third of the way above the base of these domes. Float of well-layered devitrified rhyolite is exposed locally just above the zone of obsidian fragments. Pumiceous material, that in places ravels out from below the level of the obsidian zone, may represent an initial pyroclastic fall that is not well exposed.

Other domes, such as those of North and South Twin Flat Mountains (fig. 5), have been more deeply dissected, in this case by the reexcavation of Ranch Canyon, and their internal structural and crystallization features are better exposed. The internal features of all these late domes are in general similar. A basal black vitrophyric zone is everywhere well developed, in places resting on lighter colored glassy basal flow breccia. The vitrophyre zone, which is as much as 5–10 m thick, grades upward into devitrified rock through a transition zone a few meters thick in which flow-layered obsidian alternates with devitrified rock that is commonly highly spherulitic. The devitrified interiors of the flows tend to be light gray and contain conspicuous spherulites. In places, gas cavities several centimeters across contain lithophysal fillings. The interiors of the flows tend to be crudely flow layered, with the layering subhorizontal just above the basal glass zone, but becoming steeper in upper parts of the lava dome. Near-vertical riblike masses of flow-layered devitrified rock are commonly exposed high on the

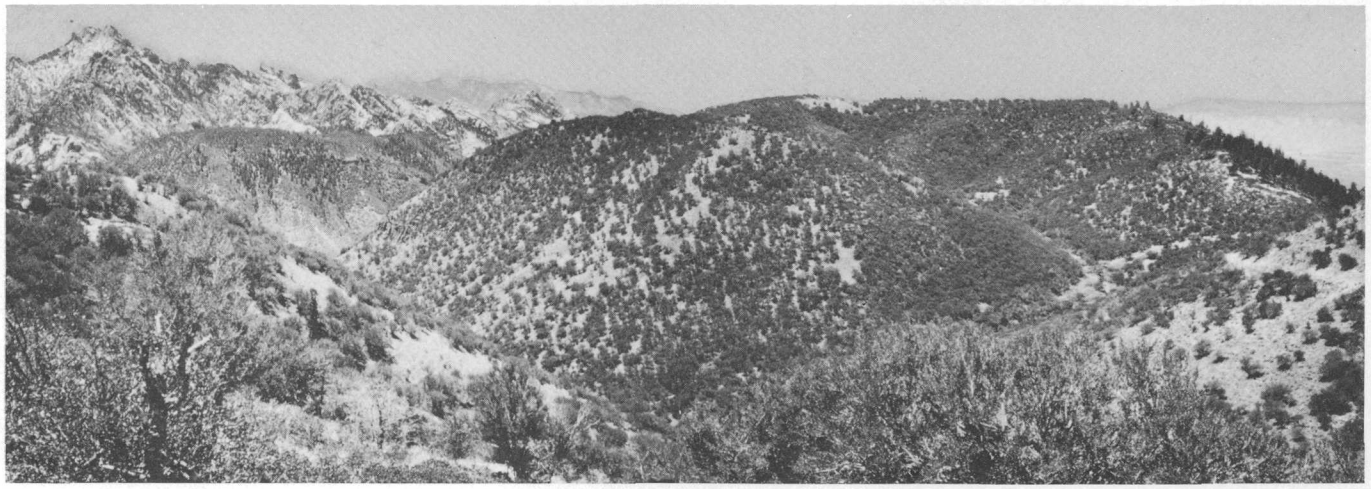

FIGURE 5.—Rhyolite domes of North and South Twin Flat Mountains. Rugged terrain in distance, including Milford Needle (elev. 2920 m) on the left side of the picture, is underlain by granite of the Mineral Mountains pluton. Photographed from ridge between Ranch and Wildhorse Canyons.

domes, where erosion has stripped away the surface mantle of frothy perlite. The steeply dipping flow layering and ramp structures of these domes thus are in contrast to structures in the older lava flows of Wildhorse Canyon and Bailey Ridge.

The porphyritic domes typically lack well-developed central craters (for example, the South Twin Flat Mountain dome) although several have slight central depressions that have been breached and accentuated by erosion. Breached depressions are especially evident for the unnamed northern dome, which is on the range crest northeast of Negro Mag Wash (fig. 2), Bearskin Mountain dome, and North Twin Flat Mountain dome (fig. 5).

All the domes contain several percent phenocrysts of quartz, oligoclase, alkali feldspar, biotite, and iron-titanium oxides (table 1). Trace amounts of sphene and allanite occur in some domes. Hornblende, zircon, and allanite are present in the Corral Canyon dome, the southernmost exposure of rhyolitic volcanic rocks. The North and South Twin Flat Mountain domes have 5–8 percent total phenocrysts, distinctly more than any of the others. The obsidian zones of these two domes appear even more phenocryst-rich, because of the presence of small "snowflake" devitrification spots. The flows in upper Wildhorse Canyon and to the north contain only 2–3 percent total phenocrysts.

Two analyzed samples of the porphyritic domes (table 2) are chemically similar silicic alkalic rhyolite. In comparison with the older flows of Bailey Ridge and Wildhorse Canyon, the domes are slightly but significantly higher in Na_2O and F; they are lower in K_2O and CaO.

Lack of continuity, and thus absence of contact relations, between the domes makes relative ages of the domes difficult to determine. On the basis of amount of dissection, North and South Twin Flat Mountains may be among the oldest, and Bearskin Mountain among the youngest of the domes. The K-Ar ages (table 1), petrographic and chemical similarities, and the generally similar degree of erosional dissection indicate that the domes are about the same age. Stratigraphic relations on the northern side of the North Twin Flat Mountain dome suggest that this dome is older than the unnamed ridge-capping flow 0.5 km north of it (fig. 2). Bearskin Mountain and the three domes extending southwest from it appear compositionally homogeneous, consisting of phenocryst-poor rhyolite similar to the rhyolite that overlies the North Twin Flat Mountain dome. The Bearskin Mountain dome has yielded K-Ar ages on obsidian of 0.60 ± 0.12 and 0.75 ± 0.10 m.y. (table 3, no. 4), and the Little Bearskin Mountain dome has an indicated sanidine age of 0.61 ± 0.05 m.y. (table 3, no. 9). Sanidines from obsidian of South Twin Flat Mountain and the unnamed northern dome have yielded K-Ar ages of 0.50 ± 0.07 and 0.54 ± 0.06 m.y. respectively (table 3, nos. 3, 5). Magnetic-polarity determinations for several domes of this group are normal (table 4) indicating, in conjunction with the K-Ar ages, that they were erupted during the Brunhes polarity epoch.

One small dome of mostly devitrified alkalic rhyolite and minor vitrophyre in Corral Canyon, shown as Trd in the lower left corner of figure 2, has been dated at 7.90 ± 0.30 m.y. (table 3, no. 10). These volcanic rocks appear to be unrelated to the young rhyolites higher in the Mineral Mountains; the rhyolite in Corral Canyon is more eroded and contains a different

phenocryst assemblage than the other rhyolites. The thermal event about 8 m.y. ago, as represented by these lavas, may have been responsible for producing the anomalously young ages of 14 and 9 m.y. measured on the Mineral Mountains pluton.

DISCUSSION

The stratigraphic relations and K-Ar ages of rhyolites of the Mineral Mountains, newly reported here, indicate that these rocks were emplaced during a relatively brief period in the Pleistocene, between about 0.8 and 0.5 m.y. ago, but an older rhyolitic event occurred about 8 m.y. ago. The Mineral Mountains are flanked on the northern and eastern sides by upper Cenozoic basalt flows (Condie and Barsky, 1972; Hoover, 1974), roughly contemporaneous with and younger than the rhyolite of the Mineral Mountains, and this association of rhyolite and basalt constitutes a bimodal volcanic assemblage of a type that is being recognized widely in the western United States in upper Cenozoic volcanic sequences (Christiansen and Lipman, 1972).

A significant question is whether the thermal anomaly of the Roosevelt KGRA is due to proximity to the late Cenozoic volcanic centers in the Mineral Mountains. Roosevelt Hot Springs and other inactive hot springs are located along the mountain-front fault on the western side of the Mineral Mountains, about 2 km west of the nearest exposed rhyolite (fig. 2). The size and shape of the Pleistocene magmatic system underlying the Mineral Mountains cannot be determined with any precision from the surface distribution of rhyolite vents, yet the extent of the vents for 15 km along the crest of the range suggests the possibility of a sizable magmatic system at depth. The elongate trend of rhyolite vents might even mark a segment of a large evolving circular igneous structure, such as interpreted for the Coso rhyolite domes in California (Duffield, 1975). The rhyolites of the Mineral Mountains were extruded along the eroded core of the large Mineral Mountains pluton, itself a late Cenozoic intrusion of remarkably large size for so young an age. Proximity in space and time suggests that the rhyolite of the Mineral Mountains represents a late stage in the evolution of a complex magmatic system that earlier gave rise to the granite of the Mineral Mountains. Alternatively, the rhyolite volcanism might have evolved independently of the granite, but has been partly localized where the crust was still hot from an earlier plutonic event. It seems likely, though not provable, that this large complex magmatic system has also been the heat source for the Roosevelt KGRA, with the shallow thermal anomaly enhanced along the range front by deep fault-controlled convective circulation of hot water.

This interpretation of a complex shallow magmatic system is supported by limited available rare-earth element data (table 5), which indicate that the rhyolite of the Mineral Mountains had a magmatic residence time in a shallow environment for a sufficiently long time to undergo major low-pressure fractional

TABLE 5.—*Rare-earth element analyses of rhyolites of the Mineral Mountains*

[Analyses by J. S. Pallister and H. T. Millard by neutron activation, using a chemical concentration technique. (See Zielinski and Lipman, 1976.)]

	Bailey Ridge flow	Wildhorse Canyon flow	South Twin Flat Mountain dome	Bearskin Mountain dome
	(75L-17)	(75L-60A)	(75L-16)	(75L-56)
La------	43.5	44.3	24.9	25.0
Ce------	95.6	94.3	51.5	44.2
Nd------	27.0	25.5	9.6	7.5
Sm------	3.6	3.5	1.3	.90
Eu------	.42	.40	.037	.035
Gd------	2.8	2.5	1.3	.88
Tb------	.52	.49	.30	.20
Tm------	.38	.35	.47	.31
Yb------	2.9	2.9	4.2	3.0
Lu------	.52	.49	.79	.57

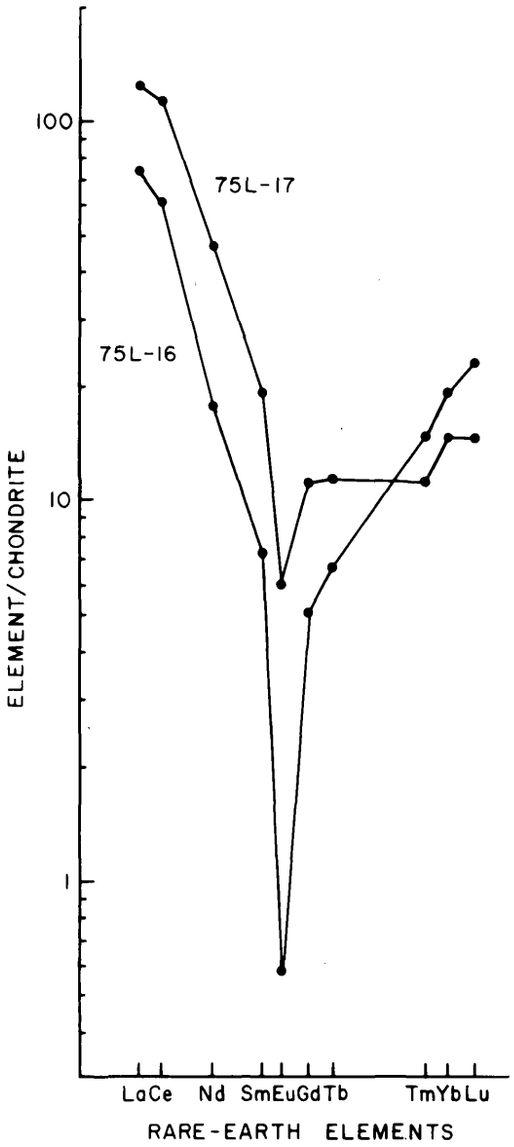

FIGURE 6.—Chrondite-normalized rare-earth-element plot for two rhyolites of the Mineral Mountains (75L–16 and 75L–17), showing negative Eu anomalies.

crystallization involving removal of feldspar. Chondrite-normalized analyses of two whole-rock samples show large negative Eu anomalies (fig. 6), indicative of major feldspar removal (Arth, 1976). This pattern contrasts with that of some other voluminous Cenozoic silicic rocks in the western United States (Zielinski and Lipman, 1976; P. W. Lipman, unpub. data, 1976) which show small or no Eu anomalies and appear to have developed their silicic compositions by processes not involving major feldspar fractionation, probably because the environment of differentiation was at pressures too high for feldspar to be stable.

Occurrences of upper Cenozoic alkalic rhyolite of possible geothermal significance in southwestern Utah are not restricted to the Mineral Mountains. We dated obsidian "Apache tears" from an eroded rhyolite flow at the Cudahy mine about 25 km north of the Mineral Mountains (fig. 1), as 2.38±0.15 m.y. (table 3, no. 6). A large rhyolite plug (South Twin Peak) in the Black Rock desert about 10 km east of the Cudahy mine yielded a similar K-Ar age of 2.33±0.12 m.y. (table 3, no. 7). Marginal obsidian from a small body of rhyolite at White Mountain, about 50 km northeast of the Mineral Mountains (fig. 1), yielded ages of 0.43±0.07 and 0.39±0.02 m.y. (table 3, no. 8), the youngest of any of our ages. The rhyolite at White Mountain contains inclusions of a distinctive dated basalt, indicating a maximum age for the dome of about 1 m.y. (Hoover, 1974). This rhyolite occurs less than 1 km from the nearest exposure of upper Pleistocene basalt of the Tabernacle volcanic field estimated to be 10 000–20 000 yr old (Hoover, 1974). Basalts of the Ice Springs volcanic field, 3 km north of White Mountain, are post-Lake Bonneville in age, that is, less than 12 000 yr old. These basaltic and rhyolitic rocks together offer another example of a bimodal basalt-rhyolite association in Utah. Thus, the potential for volcanic-related thermal anomalies in southwestern Utah is not confined to the Mineral Mountains. In fact, White Mountain is about 7 km north of Meadow and Hatton hot springs (Mundorff, 1970).

Another intriguing aspect of the rhyolites in the Mineral Mountains is their significance as a source of artifact obsidian. Implement-grade obsidian is relatively scarce in the southwestern United States, yet obsidian artifacts occur widely in archeological sites. Well-known sources of archeological obsidian include the Jemez Mountains in New Mexico, Coso Mountains and Long Valley areas in east-central California, Medicine Lake Highlands and associated rhyolitic centers in northeastern California, Newberry volcano and numerous small areas of rhyolite in eastern Oregon, and Yellowstone rhyolite plateau in Wyoming (fig. 7). The little known Mineral Mountains locality is in a region where high-quality obsidian is scarce, nearly equidistant from better known sources, yet it contains abundant obsidian suitable for implement manufacture. Individual blocks of nonporphyritic obsidian from the Bailey Ridge and Wildhorse Canyon flows are as much as 0.5 m across. Obsidian from the Mineral Mountains has recently been recognized in several archeological sites in southwestern Utah and adjacent parts of Nevada (Umshler, 1975), but how widely it has been distributed has yet to be established.

FIGURE 7.—Well-known sources for archeological obsidian in the western United States.

Available compositional data indicate that obsidian artifacts derived from the Mineral Mountains should be distinguishable, especially by minor-element compositions, from those of most of the better known obsidian sites.

Fission-track age dating, by G. A. Izett and C. W. Naeser, and obsidian-hydration age dating, by Irving Friedman, were conducted—independently of our study—on selected samples of rhyolite from the Mineral Mountains. The ages determined by these two other techniques provide a cross-check on the ages presented above that were determined by the K-Ar isotope method. Comparisons of the results of the three techniques are presented separately, in the sections that follow.

FISSION-TRACK DATING

By G. A. Izett and C. W. Naeser

Fission-track age determinations were made on samples of obsidian from the Bailey Ridge flow and the Bearskin Mountain dome. The fission-track age of the Bailey Ridge obsidian is in fair agreement with the K-Ar age of the obsidian, but the fission-track age of the Bearskin Mountain obsidian is anomalously younger than the K-Ar age. Th sample we dated of the Bearskin Mountain obsidian contains no fossil fission tracks; however, the age can be estimated by assuming the presence of one fossil track as shown in the table below. The anomalously young fission-track age of the Bearskin Mountain obsidian probably is due to the annealing of fossil tracks from a recent thermal event. The fission-track analytical data follow:

Fission-track analytical data

[Fission tracks etched for about 10 seconds in 48 percent hydrofluoric acid; ± 1 sigma about the mean. $\lambda f = 6.85 \times 10^{-17} yr^{-1}$]

Locality	ϕ (neutrons cm^{-2})	ρ_s (tracks cm^{-2})	ρ_i (tracks cm^{-2})	Fission track glass age x 10^6 years	K-Ar glass age x 10^6 years[1]
Bearskin Mountain dome	8.72×10^{14}	$<3.37 \times 10^1$ (1)	1.25×10^5 (309)	<0.02	0.75 ± 0.1 0.60 ± 0.12
Bailey Ridge flow	0.5×10^{15}	7.89×10^2 (3)	4.40×10^4 (213)	0.55 ± 0.30	0.79 ± 0.08

[1]See table 3.

OBSIDIAN-HYDRATION DATING

By Irving Friedman

Four rhyolite lava flows or domes from the Mineral Mountains, Utah, were dated by the obsidian-hydration technique. Most of the results agree with K-Ar and fission-track dates of the same flows.

Obsidian-hydration dating depends upon the fact that a newly formed surface on obsidian, such as a cooling crack, adsorbs water from the atmosphere. This adsorbed water slowly diffuses into the obsidian, and the depth of penetration of the water can be measured under the microscope in a thin section cut normal to the surface (Friedman and Smith, 1960). The rate at which the water diffuses into the obsidian is dependent upon temperature and glass composition (Friedman and Long, 1976).

The thickness of the hydrated layer (in micrometers) for the rhyolite units is tabulated below. Also listed is the expected rate of hydration (in $\mu m^2/10^3$ yr) for each flow, calculated for an estimated effective hydration temperature of 8°C and from the chemical composition of the obsidian. (See Friedman and Long, 1976.) The calculated obsidian-hydration age is also given, as is the K-Ar age.

Although the effective hydration temperature is assumed to be the same for all the flows sampled, the differing whole-rock chemistry of the obsidian gives different calculated hydration rates. Compositions of two of the obsidians are from table 2 in this paper; the analysis of the Bearskin Mountain dome is from S. H. Evans (written commun., 1976). No analysis is available for the South Twin Flat Mountain dome. An analysis for the North Twin Flat Mountains (table 2) was used instead; the hydration rate and calculated age are accordingly uncertain.

The calculated hydration rates vary by a factor of 2.5, owing mainly to differences in the amount of CaO+MgO. The chemical analyses were on whole-rock samples, but the hydration-rate calculation should be based on glass compositions. The Wildhorse Canyon and the Bailey Ridge glasses are almost free of phenocrysts, but the Bearskin Mountain and particularly the

Rhyolite	Thickness of hydration μm (± 1 μm)	Chemical index	Calculated hydration rate $\mu m^2/10^3$ yrs	Calculated age 10^6 yrs	Corrected age	K/Ar age
Wildhorse Canyon flow	41	42.5	2	0.85	0.85	([1])
Bailey Ridge flow	40	41.7	2	.80	.80	0.79 .75
Bearskin Mountain dome	31	47.4	4	.24	.48	.60
South Twin Flat Mountain dome	22	51.1(?)	5(?)	.10(?)	.25	.50

[1]No determination

South Twin Flat Mountain glasses are porphyritic. Obsidian from Wildhorse Canyon, Bailey Ridge, and South Twin Flat Mountain all have refractive indices of 1.4847 ± 0.0005, whereas Bearskin Mountain dome has a slightly higher index, 1.4856 ± 0.0005. The similarity in index of all four glasses makes any assumption of greatly differing hydration rates for these samples unrealistic. If we assume that the chemical compositions of the glass phase of all four samples are similar, then the hydration rates also will be similar and the dates shown in the column "Corrected age" should apply.

The corrected ages agree with the K-Ar dates, except for the date for the South Twin Flat Mountain dome, where the hydration date is about half that derived by K-Ar dating. The reasons for this discrepancy are not known, but we may not have sampled sufficiently to find an original surface on the samples from this site. Alternatively, the discrepancy may be due to some inherited argon in the sanidine used for K-Ar dating.

REFERENCES CITED

Allen, E. T., and Day, A. L., 1935, Hot spring of the Yellowstone National Park: Carnegie Inst. Washington Pub. 466, 525 p.

Armstrong, R. L., 1970, Geochronology of Tertiary igneous rocks, eastern Basin and Range province, western Utah, eastern Nevada, and vicinity, U.S.A.: Geochim. et Cosmochim. Acta, v. 34, p. 203–232.

Arth, J. G., 1976, Behavior of trace elements during magmatic processes—A summary of theoretical models and their application: U.S. Geol. Survey Jour. Research, v. 4, no. 1, p. 41–48.

Bailey, R. A., Dalrymple, G. B., and Lanphere, M. A., 1976, Volcanism, structure, and geochronology of Long Valley caldera, Mono County, California: Jour. Geophys. Research, v. 81, p. 725–744.

Berge, C. W., Crosby, G. W., and Lenzer, R. C., 1976, Geothermal exploration of Roosevelt KGRA, Utah [abs.]: Rocky Mtn. Section, AAPG and SEPM 25th Annual Mtg., Billings, Mont., Program, p. 52–53.

Christiansen, R. L., and Blank, H. R., 1972, Volcanic stratigraphy of the Quaternary rhyolite plateau in Yellowstone National Park: U.S. Geol. Survey Prof. Paper 729–B, 18 p.

Christiansen, R. L., and Lipman, P. W., 1966, Emplacement and thermal history of rhyolite lava flow near Fortymile Canyon, southern Nevada: Geol. Soc. American Bull., v. 77, no. 7, p. 671–684.

———1972, Late Cenozoic, Pt. 2 *of* Cenozoic volcanism and plate-tectonic evolution of the western United States: Royal Soc. London Philos. Trans., ser. A., v. 217, p. 249–284.

Condie, K. C., 1960, Petrogenesis of the Mineral Range pluton, southwestern Utah: Utah Univ., M.S. thesis, 94 p.

Condie, K. C., and Barsky, C. K., 1972, Origin of quaternary basalts from the Black Rock Desert Region, Utah: Geol. Soc. America Bull., v. 84, no. 2, p. 333–352.

Duffield, W. A., 1975, Late Cenozoic ring faulting and volcanism in the Coso Range area of California: Geology, v. 3, p. 335–338.

Earll, F. N., 1957, Geology of the central Mineral Range, Beaver County, Utah: Utah Univ., Ph. D. thesis, 112 p.

Friedman, Irving, and Long, W. D., 1976, Hydration rate of obsidian: Science, v. 191, no. 4225, p. 347–352.

Friedman, Irving, and Smith, R. L., 1960, A new dating method using obsidian: Part 1, the development of the method: Am. Antiquity, v. 25, no. 4, p. 476–522.

Greider, B., 1976, Geothermal energy, Cordilleran hingeline—West, *in* Hill, J. G., ed., Geology of the Cordilleran hingeline: Denver, Rocky Mountain Assoc. Geologists, p. 351–362.

Hoover, J. D., 1974, Periodic Quaternary volcanism in the Black Rock Desert, Utah: Brigham Young Univ., Geology studies, v. 21, p. 3–72.

Hunt, B. B., 1938, Igneous geology and structure of the Mount Taylor volcanic field, New Mexico: U.S. Geol. Survey Prof. Paper 189–B, p. 51–80.

Lambert, Wayne, 1966, Notes on the late Cenozoic geology of the Taos–Questa area, New Mexico, *in* Guidebook of Taos Raton Spanish Peaks country, New Mexico and Colorado, New Mexico Geol. Soc. 17th Field Conf., 1966: Socorro, N. Mex., New Mexico Bur. Mines and Mineral Resources, p. 43–50.

Liese, H. C., 1957, Geology of the northern Mineral Range, Millard and Beaver Counties, Utah: Utah Univ., M.S. thesis, 88 p.

Moore, R. B., Wolfe, E. W., and Ulrich, G. E., 1974, Geology of the eastern and northern parts of the San Francisco volcanic field, Arizona, *in* Geology of Northern Arizona: Geol. Soc. America, Rocky Mtn. Section Mtg., p. 465–494.

Mundorff, J. C., 1970, Major thermal springs, Utah: Utah Geol. and Mineralog. Survey Water-Resources Bull. 13, 60 p.

Nash, W. P., and Smith, R. P., 1977, Pleistocene volcanic ash deposits in Utah: Utah Geology, v. 4, no. 1, p. 35–42.

Park, G. M., 1968, Some geochemical and geochronologic studies of the beryllium deposits in western Utah: Utah Univ., M.S. thesis, 195 p.

Petersen, C. A., 1975, Geology of the Roosevelt hot springs area, Beaver County, Utah: Utah Geology, v. 2, no. 2, p. 109–116.

Robinson, H. H., 1913, The San Francisco volcanic field, Arizona: U.S. Geol. Survey Prof. Paper 76, 213 p.

Smith, R. L., Bailey, R. A., and Ross, C. S., 1970, Geologic map of the Jemez Mountains, New Mexico: U.S. Geol. Survey Misc. Geol. Inv. Map I–571.

Smith, R. L., and Shaw, H. R., 1975, Igneous-related geothermal systems: U.S. Geol. Survey Circ. 726, p. 58–83.

Umshler, D. B., 1975, Source of the Evan's Mound obsidian: Socorro, New Mexico Inst. Mining and Technology, M.S. thesis, 38 p.

Zielinski, R. A., and Lipman, P. W., 1976, Trace-element variations at Summer Coon volcano, San Juan Mountains, Colorado, and the orign of continental-interior andesite: Geol. Soc. America Bull., v. 87, p. 1477–1485.

*U.S.GOVERNMENT PRINTING OFFICE: 1977--261-198/1

RECENT PUBLICATIONS OF THE U.S. GEOLOGICAL SURVEY

(The following books, except TWI 5–A4, may be ordered from the Branch of Distribution, U.S. Geological Survey, 1200 South Eads Street, Arlington, VA 22202 (an authorized agent of the Superintendent of Documents, Government Printing Office). Prepayment is required. Remittances should be sent by check or money order payable to U.S. Geological Survey. Give series designation and number, such as Bulletin 1368–A, and the full title. Prices of Government publications are subject to change. Increases in costs make it necessary for the Superintendent of Documents to increase the selling prices of many publications offered. As it is not feasible for the Superintendent of Documents to correct the prices manually in all the previous announcements and publications stocked, the prices charged on your order may differ from the prices printed in the announcements and publications)

Professional Papers

P 655–O. Calculation of evapotranspiration using color-infrared photography, by J. E. Jones. 1977. p. O1–O45. $2.50.

P 902. Precambrian geology of the United States; An explanatory text to accompany the Geologic Map of the United States, by P. B. King. 1976. 85 p. $2. (Reprint.)

P 992. Otarioid seals of the Neogene, by C. A. Repenning and R. H. Tedford. 1977. 93 p.; 24 plates. $3.75.

P 1004. Cooling and crystallization of tholeiitic basalt, 1965, Makaopuhi lava lake, Hawaii, by T. L. Wright and R. T. Okamura. 1977. 78 p. $2.75.

P 1015. Proceeding of the first annual William Pecora Memorial Symposium, October 1975, Sioux Falls, South Dakota, by P. W. Woll and W. A. Fischer, editors. 1977. 370 p. $6.50.

P 1020. Ordovician and Silurian graptolite succession in the Trail Creek area, central Idaho—A graptolite zone reference section, by Claire Carter and Michael Churkin, Jr. 1977. 37 p., 7 plates. $2.40.

Bulletins

B 1278–E. Geochemical exploration techniques based on distribution of selected elements in rocks, soils, and plants, Vekol porphyry copper deposit area, Pinal County, Arizona, by M. A. Chaffee. 1977. p. E1–E78. $1.90.

Techniques of Water Resources Investigations

TWI 5–A4. Methods for collection and analysis of aquatic biological and microbiological samples, edited by Task Group on Biology and Microbiology, P. E. Greeson, Chairman, T. A. Ehlke, G. A. Irwin, B. W. Lium, and K. V. Slack. 1977. 332 p. (loose leaf format in notebook binder). $20 domestic, $25 foreign; supplements to be prepared as need arises, will be issued to purchasers at no charge as they become available. (Available only through Superintendent of Documents, Government Printing Office, Washington, DC 20402.)

ANNOUNCEMENT

DIRECT-MAIL SALES OF USGS OPEN-FILE REPORTS

By the U.S. Geological Survey

Purpose of Program

- To furnish microfiche or paper-duplicate copies of open-file reports from a single, centrally located facility.
- To provide faster order-filling service to the public for copies of open-file reports.
- To increase the availability of earth-science information to the scientific community.

Order USGS Open-File Reports From:

Open-File Services Section, Branch of Distribution, U.S. Geological Survey, Box 25425, Federal Center, Denver, CO 80225. (Telephone: 303-234-5888.)

Price information will be published in the monthly listing "New Publications of the Geological Survey."

This facility will stock open-file reports only. Please do not mix orders for open-file reports with orders for any other USGS products. Checks or money orders, in exact amount for open-file reports ordered, should be made payable to U.S. Geological Survey. Prepayment is required.

Order by series and number (such as Open-File Report 77-123) and complete title.

Inquiries concerning this new program should be sent to the address given above.

TECHNICAL INFORMATION OFFI
U S GEOLOGICAL SURVEY TOPO DI
NATIONAL CENTER STOP 520
RESTON VA 22092